
ORDRE : 41070

THÈSE

Présentée à

Université Lille 1 - Sciences et Technologies

**(Ecole Doctorale des Sciences de la Matière, du Rayonnement et de
l'Environnement)**

East China Normal University

pour l'obtention du

Docteur

(Discipline : Molécules et Matière Condensée)

par

Ming SHEN

**Nouvelles méthodes de RMN des solides pour les corrélations homo- et
hétéro-nucléaires et l'observation des noyaux de spin 1**

**(New Solid-State NMR methods for homo-/hetero-nuclear correlations
and spin=1 nucleus)**

Soutenance prévue le 15 Août 2015

Composition du Jury :

Directeurs de Thèse:

Jean-Paul Amoureux, Professeur, Université de Lille 1

Olivier Lafon, Professeur, Université de Lille 1

Qun Chen, Professeur, East China Normal University

Bingwen Hu, Professeur, East China Normal University

Rapporteurs :

Francis Taulelle, Directeur de Recherche CNRS, Université de Versailles, St Quentin en Yvelines

Heyong He, Professeur, Fudan University

Examineur :

Charlotte Martineau, Maître de Conférences, Université de Versailles, St Quentin en Yvelines

Acknowledgements

The past five years I spent in the highest education have been a long long journey. This journey was full of depression, doubt and failure.

Nevertheless, I survived and I built self-confidence from the work that I have done through this journey. These work could not been fulfilled without many encouraging people's help.

I would like to express my gratitude to all the supervisors who guided me in the NMR lab in Shanghai and Lille. Thanks to Prof. Qun CHEN for introducing me to study Solid-State NMR after I graduated from college. Thanks to Prof. Bingwen HU who gave me a lot of guidance on NMR simulations and experimental techniques. He also gave me many new ideas. I also thank him for introducing me to apply for the Ph.D. position in Prof. Jean-Paul Amoureux's group. I would like to thank Prof. Jean-Paul Amoureux for his organization and instructions on my research projects and help in writing the manuscripts. Thanks to Prof. Olivier Lafon for his patient guidance on my projects and his help in improving the manuscripts. Thanks to Julien Trebosc for his help in the NMR experiments and many useful suggestions and guidance. All my supervisors' dedication and passion to the scientific work were very impressive. I was so lucky to study from different perspectives under their direction.

Thanks to Fr  rique Pourpoint and Delevoye Laurent for their help in my study and life in Lille. Thanks to Xingyu Lu, Aany Sophie Thankmony, Qinghua Liu, Siyong Zhang, Yixuan Li for their help and useful discussions.

I would like to thank all other colleges in Shanghai and Lille: Huawei Liu, Taiqiang Chen, Guoyi Zhang, Esperanza Pavon, Guillaume Girard, Hiroki Nagashima, Denis Grekov, Carlier Thibault for the very nice working atmosphere.

I would like to thank my parents for their support and trust within so many years.

Finally, I am the most grateful to my wife for her selfless support, encourage and love in my life.

Contents

ABSTRACT	I
Chapter 1: Introduction	1
1.1 Nuclear Spin Interactions in Solids	2
1.1.1 Chemical shift and Chemical shift anisotropy	3
1.1.2 <i>J</i> -coupling	4
1.1.3 Dipolar Coupling	5
1.1.4 Quadrupolar interaction	6
1.2 Through-space Homo-nuclear Correlation Spectroscopy	7
1.2.1 SQ-SQ approach	9
1.2.2 DQ-SQ approach	11
1.3 Through-space Hetero-nuclear Correlation Spectroscopy	13
Chapter 2: Through-space Homo-nuclear Correlation Spectroscopy: fp-RFDR with (XY8)⁴ super-cycling	21
2.1 Pulse sequence	23
2.2 Numerical simulations	27
2.2.1 Two spin-system	28
2.2.2 Three spin-system: choice of rf-field.....	29
2.2.3 Three spin-system: rf-inhomogeneity	32
2.3 Experimental section	35
2.4 Results and Discussion	36
2.4.1 ¹³ C- ¹³ C correlation	36
2.4.2 ³¹ P- ³¹ P correlations.....	42
2.5 Conclusions	43
Chapter 3: Through-space Homo-nuclear Correlation Spectroscopy: SHANGHAI+	51
3.1 Numerical simulations	53
3.2 Experimental verifications	57
3.3 Conclusion	60
Chapter 4: Through-space Hetero-nuclear Correlation Spectroscopy: improving the	

resolution	63
4.1 Pulse sequence and theory.....	65
4.1.1 The <i>D</i> -HMQC sequence	65
4.1.2 The decoupling sequences	68
4.1.3 Time increment optimization.....	73
4.2 Numerical simulations	74
4.2.1 Simulation parameters	74
4.2.2 Decoupling efficiency.....	75
4.3 Experimental demonstrations.....	78
4.3.1 Sample and experimental conditions	78
4.3.2 $^1\text{H}\{-^{13}\text{C}\}$ <i>D</i> -HMQC 2D experiments at 9.4 T and $\nu_R = 32.3$ kHz.....	80
4.3.3 $^1\text{H}\{-^{13}\text{C}\}$ <i>D</i> -HMQC 2D experiments at 18.8 T and 21.1 T using $\nu_R \approx 62$ kHz	82
4.3.4 Application to $^1\text{H}\{-^{14}\text{N}\}$ DANTE- <i>D</i> -HMQC at 21.1 T and $\nu_R = 62.1$ kHz	89
4.4 Conclusions	91

Chapter 5: Through-space Hetero-nuclear Correlation Spectroscopy: detection of nuclei experiencing large anisotropic interactions using frequency-selective pulses 99

5.1 Pulse sequence	102
5.2 Theory	103
5.2.1 Coherence transfer	103
5.2.2 Broadband excitation.....	104
5.2.3 Sideband selective excitation.....	105
5.2.4 Excitation of 2Q coherences.....	107
5.3 Numerical simulations	108
5.3.1 Simulation parameters	108
5.3.2 Simulations for ^{195}Pt nucleus	109
5.3.3 Simulations for ^{14}N nucleus.....	117
5.4 Experimental demonstration for $^1\text{H}\{-^{14}\text{N}\}$ 1Q-HMQC.....	129
5.4.1 Samples and experimental conditions.....	129
5.4.2 Effect of rf-field and pulse length.....	130
5.4.3 Sensitivity to rotor-synchronization.....	132
5.4.4 Robustness to ^{14}N offset.....	132
5.5 Conclusions	134

Chapter 6: Revisiting NMR composite pulses for broadband ^2H excitation..... 142

6.1 Pulse sequence and its implementation with composite pulse.....	142
6.2 Numerical simulations	145
6.3 Experimental	146
6.4 Conclusions	149
Chapter 7: Revisiting NMR composite pulses for broadband ^2H excitation:	
Theoretical calculation by average Hamiltonian theory	152
7.1 Analytical calculations of COM-II.....	152
7.2 Numerical simulations	158
7.3 Conclusions	159
Chapter 8: Resume	161
Paper list	163

ABSTRACT

The main aim of this thesis is to develop new methods of homo- and hetero-nuclear correlation spectroscopy that allows probing proximities between active nuclei in Solid-State NMR. Minor parts of this thesis concern the broadband excitation of ^2H nuclei with composite pulses.

In Chapter 1, a brief introduction of spin Hamiltonians in solids is given. Common methods of homo- and hetero-nuclear correlation spectroscopy are also explained in detail. Some of these methods are employed and improved in the following chapters.

In Chapter 2, a broadband first-order finite-pulse radio-frequency-driven recoupling (fp-RFDR) NMR sequence with a nested $(\text{XY8})_4^1$ super-cycling for very high magnetic fields is presented. At fast to ultra-fast magic-angle spinning (MAS), this super-cycling, formed by combining phase inversion and a global four-quantum phase cycle, improves the robustness of fp-RFDR to (i) chemical shift anisotropy (CSA), (ii) spread in isotropic chemical shifts, (iii) rf-inhomogeneity and (iv) hetero-nuclear dipolar couplings for long recoupling times. The performances of fp-RFDR-XY8, fp-RFDR-XY16 and fp-RFDR- $(\text{XY8})_4^1$ have been compared using simulations and experiments with very large offsets and/or CSAs. In all cases, fp-RFDR- $(\text{XY8})_4^1$ is superior to the two other types of sequences, especially in case of very large CSAs and long recoupling times. The robustness of fp-RFDR- $(\text{XY8})_4^1$ to offset is demonstrated by the analysis of ^{13}C - ^{13}C proximities in a solid-state tetra-peptide *sans* ^1H decoupling at MAS frequency of 60 kHz and the high magnetic field of 21.1 T, for which the difference in ^{13}C resonance frequencies can differ by 36 kHz. The increased efficiency of this super-cycling on phosphorous atoms submitted to very large CSAs of ca. 80 kHz at 21.1 T is also demonstrated. The stability of the transfer efficiency for long recoupling times in fp-RFDR- $(\text{XY8})_4^1$ facilitates the enhancement of ^{13}C - ^{13}C long-range correlations in uniformly labeled samples, especially at very high magnetic fields.

In Chapter 3, modulation-sideband recoupling conditions of the ^{13}C - ^{13}C Second-order

Hamiltonian among Analogous nuclei plus (SHA+) is discussed, and it is shown that this sequence can be used in two different recoupling regimes, depending on the ratio between the spinning speed and the carbon frequency range, $\Delta\nu_{\text{iso}}^{\text{max}}$. The first regime, $\nu_{\text{R}} > \Delta\nu_{\text{iso}}^{\text{max}}$, is recommended for *broad-band* recoupling to avoid any rotational resonance broadening. In this regime, the spinning speed should be only slightly larger than $\Delta\nu_{\text{iso}}^{\text{max}}$, to obtain the best transfer efficiency. This condition could be used in most cases. The second regime, $\nu_{\text{R}} < \Delta\nu_{\text{iso}}^{\text{max}}$, benefits from higher transfer efficiency and S/N ratio owing to the use of slower spinning speed. It can be used *selectively* to observe long-range constraints with lower spinning speed, which increases the transfer efficiency, and may allow using bigger rotors to increase the S/N ratio. It also leads to lower proton rf-power, which facilitates the use of longer mixing time, and avoids the denaturation of temperature-sensitive proteins.

In Chapter 4, a systematic comparison of the performances of various decoupling schemes during the indirect t_1 evolution period of dipolar-mediated HMQC (*D*-HMQC) experiment is presented. It is shown that the spectral resolution along the indirect dimension of proton-detected HMQC spectra can be enhanced by applying decoupling schemes during the t_1 period to a level close to best directly observed decoupled CP spectra. It is also demonstrated that ^1H - ^1H dipolar decoupling sequences during t_1 , such as symmetry-based schemes, phase-modulated Lee-Goldburg (PMLG) and Decoupling Using Mind-Boggling Optimization (DUMBO), provide better resolution than continuous wave ^1H irradiation. When observing indirectly broad spectra presenting numerous spinning sidebands, the *D*-HMQC sequence must be fully rotor-synchronized owing to the rotor-synchronized indirect sampling and dipolar recoupling sequence employed. In this case, a solution to reduce artifactual sidebands caused by the modulation of window delays before and after the decoupling application during the t_1 period is proposed. The performances of the various decoupling schemes are assessed via numerical simulations and compared to 2D ^1H - $\{^{13}\text{C}\}$ *D*-HMQC experiments on $[\text{U-}^{13}\text{C}]\text{-L-histidine.HCl.H}_2\text{O}$ at various magnetic fields and Magic Angle Spinning (MAS) frequencies. At $\nu_{\text{R}} \approx 32$ kHz, similar spectral resolutions were obtained using $\text{C14}^{7_2}(\alpha_0\alpha_{180})$, $\text{SAM}_{3.5}$ and SAM_4 since all decoupling schemes were applied

at optimal rf field value. Hardware limitations of Avance-II consoles did not allow using non rotor synchronized sequences like PMLG or DUMBO. At $\nu_R = 62$ kHz, we recorded a *D*-HMQC spectrum using PMLG sequence, the resolution of which matches the resolution of directly observed ^{13}C . Resolution improvement for SAM sequences was limited by the specifications of the 1.3 mm probe, since the optimal peak rf field amplitude for SAM_{3.5} and SAM₄ exceeds the maximal rf field the probe can deliver. Thanks to transient free pulses, Smoothed Amplitude Modulation (SAM) generally produced spectra with reduced t_1 noise levels, which is beneficial for the observation of weak long-range correlations. Experimentally, the independent execution of pulse sequences on each channel using Bruker Avance III spectrometer greatly facilitates the implementation of decoupling schemes, especially the unsynchronized ones. Great resolution and sensitivity enhancements resulting from decoupling during t_1 period enable the detection of hetero-nuclear correlation between aliphatic protons and ammonium ^{14}N sites in L-histidine.HCl.H₂O.

In Chapter 5, we demonstrate how frequency-selective radio-frequency (rf) long pulses allow one to achieve an efficient excitation of nuclei experiencing large anisotropic NMR interactions. It is shown that these rf pulses can be applied on the indirect channel of Hetero-nuclear Multiple-Quantum Correlation (HMQC) experiments, which facilitate the detection of nuclei exhibiting wide spectra via spin-1/2 isotopes. Selective excitation is achieved using long pulses as well as trains of long pulses in the manner of Delays Alternating with Nutation for Tailored Excitation (DANTE). Numerical simulations show that this indirect excitation method is applicable to spin-1/2 nuclei experiencing large chemical shift anisotropy, as well as to spin-1 isotopes subject to large quadrupolar interaction, such as ^{14}N . The performances of selective pulses are analyzed by numerical simulations of scalar-mediated HMQC experiments indirectly detecting spin-1/2 or spin-1 nuclei, as well as by dipolar-mediated HMQC experiments between ^1H and ^{14}N nuclei in solid-state α -glycine amino-acid at 21.1 T and Magic Angle Spinning (MAS) frequency of 60 kHz. It is shown that the efficiency of selective excitation is comparable to that of broadband excitation given the rf field delivered by common solid-state NMR probes. Furthermore, selective excitation: (i)

requires moderate rf field, (ii) can be easily optimized, and (iii) displays high robustness to offset, rf field inhomogeneity, and fluctuations in MAS frequencies. The choice in between the selective excitation with two long pulses or two DANTE trains depends on a compromise in between the sensitivity to offsets and the required rf field strength. However, it must be noted that even with long pulse selective excitations the required rf field strength is weak and smaller than the spinning speed. More globally, the selective excitation with two long pulses looks to be the most appropriate way to perform $^1\text{H}\{-^{14}\text{N}\}$ *D*-HMQC experiments, except when the ^{14}N frequency range is small or moderate where DANTE trains provide a slightly larger efficiency than selective long pulses.

In Chapter 6, a revision of four well-known composite pulses (COM-I, II, III, and IV) for broadband excitation in deuterium quadrupolar echo (solid-echo) spectroscopy is presented. These composite pulses are combined with several phase cycling schemes that were previously shown to decrease finite pulse width distortions in deuterium solid-echo experiments performed with two single pulses. The simulations and experiments shown COM-II and -IV are superior to the other composite 90° pulses studied as they reduce the requisite RF fields for uniform excitation, but also give undistorted spectra without baseline artifacts. COM-III was found to yield a distorted powder pattern due to its much longer pulse duration. Our results show that the full 8-step phase cycling is robust in mitigating undesired finite pulse width effects that result in spectral distortions and should be applicable for quadrupolar echo spectroscopy based on composite pulses.

In Chapter 7, a theoretical analysis of COM-II with 8-step phase cycling by average Hamiltonian theory is given, which allows us to understand the experiment results we obtained in Chapter 6. Analytical results, to first order of the Magnus expansion, highlight the performance of this composite pulse with an 8-step phase cycling scheme. By applying the fictitious spin-1 operators, this chapter highlights the mechanism of the 8-step phase cycling that minimizes spectral distortions.

Keywords: Solid-State NMR, Homo-nuclear Correlation Spectroscopy, Hetero-nuclear

Correlation Spectroscopy, ^2H Quadrupolar Echo Spectroscopy, Dipolar Recoupling, Dipolar Decoupling

Chapter 1: Introduction

Since the first observation of nuclear magnetic resonance (NMR) signal by Purcell^[1] and Bloch^[2] in 1940s, NMR has become a very important analytical technique and has been applied in many different domains of science.

In the early stage of Solid-State NMR (SS-NMR), the resolution was not satisfying due to the large anisotropic interactions existed in the solid samples. High-resolution spectra was not possible until 1950s when the magic angle spinning (MAS) technique was developed by Andrew et al.^[3] and Lowe^[4]. It has been shown that MAS greatly removes the orientation-dependent interactions by mechanical rotation around the magic angle, resulting in the spectra with narrow lines. At the same time, multiple-pulse pulse sequences technique was also developed to enhance the resolution by manipulating the spin part of the Hamiltonian interactions through irradiation of the radio frequency pulses. At present, MAS and multiple-pulse technique are often combined in SS-NMR, which allows partially removing the homo-nuclear and hetero-nuclear dipolar couplings. Another important breakthrough in SS-NMR is the development of Cross-Polarization technique by Hartman and Hahn^[5] in 1960s. CP technique transfers the nuclear polarization from ^1H with the greatest gyromagnetic ratio to the dilute spins with much smaller gyromagnetic ratio, which enables the detection of insensitive spins with improved sensitivity. With the development of modern MAS probe, spinning speed of up to 80 kHz^[6] was achievable. This also aids in the resolution improvement by removing very large proton-proton homo-nuclear dipolar couplings.

This chapter will be organized as following: The first section will address the basic interactions encountered in SS-NMR. The second section will describe some common methods of through-space Homo-nuclear and Hetero-nuclear Correlation Spectroscopy related to this thesis.

1.1 Nuclear Spin Interactions in Solids

To fully describe and understand the physics phenomenon in Solid State NMR, one often refers to the *nuclear spin Hamiltonian*, which obeys the time-dependent Schrödinger equation:

$$\frac{d}{dt} |\psi_{\text{spin}}(t)\rangle = -i\hat{\mathcal{H}}_{\text{spin}} |\psi_{\text{spin}}(t)\rangle \quad (1)$$

In this equation, $|\psi_{\text{spin}}(t)\rangle$ is the spin state of the nuclei and the *nuclear spin Hamiltonian* $\hat{\mathcal{H}}_{\text{spin}}$ describes all the interactions involved in the system.

Nuclear spins interact with their surroundings and with each other. In general, the interactions may be divided into external spin interactions and internal spin interactions:

$$\hat{\mathcal{H}}_{\text{spin}} = \hat{\mathcal{H}}_{\text{Ext}} + \hat{\mathcal{H}}_{\text{Int}} \quad (2)$$

The external spin interactions correspond to the interaction of the nuclear spins with the external static magnetic field and the oscillating radio-frequency field. This term can be written as:

$$\hat{\mathcal{H}}_{\text{Ext}} = \hat{\mathcal{H}}_{\text{Z}} + \hat{\mathcal{H}}_{\text{RF}} \quad (3)$$

where $\hat{\mathcal{H}}_{\text{Z}}$ is the Zeeman interaction term, $\hat{\mathcal{H}}_{\text{RF}}$ the radiofrequency interaction term.

NMR is conducted in a superconducting magnet containing a strong, homogeneous and static magnetic field, called \mathbf{B}^0 . The Zeeman term, $\hat{\mathcal{H}}_{\text{Z}}$, describing the interaction of each spin with the static field \mathbf{B}^0 , can be written as:

$$\hat{\mathcal{H}}_{\text{Z}} = -\gamma B^0 \hat{I}_z \quad (4)$$

where γ is gyromagnetic ratio between the nuclear magnetic moment, $\hat{\boldsymbol{\mu}}$, and the spin angular momentum, $\hat{\mathbf{I}}$:

$$\hat{\boldsymbol{\mu}} = \gamma \hat{\mathbf{I}} \quad (5)$$

The strength of Zeeman interaction can also be indicated by the Larmor frequency, ω_0 , which can be written as:

$$\omega_0 = -\gamma B^0 \quad (6)$$

In many modern pulsed NMR experiments, radiofrequency pulses are employed to manipulate the internal spin interactions. This imposes another Hamiltonian term on the system as included in Eq.3. This Hamiltonian, $\hat{\mathcal{H}}_{\text{RF}}$, can be written as:

$$\hat{\mathcal{H}}_{\text{RF}} = -\frac{1}{2}\gamma B_{\text{RF}}(\cos(\omega_{\text{ref}}t + \phi_p) I_x + \sin(\omega_{\text{ref}}t + \phi_p) I_y) \quad (7)$$

where ω_{ref} is the reference frequency of the spectrometer, ϕ_p the phase of the radio frequency pulse, B_{RF} the maximum radiofrequency amplitude during the pulse.

In the *rotating frame* as often used to describe the spin evolution, Eq.7 can be simplified to have the form:

$$\hat{\mathcal{H}}_{RF}^{rot} = -\frac{1}{2}\gamma B_{RF}(\cos(\phi_p) I_x + \sin(\phi_p) I_y) \quad (8)$$

Internal spin interactions as included in Eq.2 correspond to the interactions of the nuclear spins with the molecular surroundings and other nuclear spins. Internal spin interactions mainly contains chemical shift term: $\hat{\mathcal{H}}_{CS}$, dipolar coupling term: $\hat{\mathcal{H}}_D$, J-coupling term: $\hat{\mathcal{H}}_J$, and quadrupolar coupling term: $\hat{\mathcal{H}}_Q$:

$$\hat{\mathcal{H}}_{Int} = \hat{\mathcal{H}}_{CS} + \hat{\mathcal{H}}_D + \hat{\mathcal{H}}_J + \hat{\mathcal{H}}_Q \quad (9)$$

In the following part, further explanations of these terms will be given in detail.

1.1.1 Chemical shift and Chemical shift anisotropy

The chemical shift term represents the indirect magnetic interaction of the external magnetic field and the nuclear spins through the electrons. The external magnetic field B^0 induces currents in the electron clouds in the molecule. Then the circulating molecular currents in turn generate a magnetic field, called the induced field $B^{induced}$.

As a result, the nuclear spins sense not only the static external field, but also the induced field generated by the molecular electrons:

$$B^{loc} = B^0 + B^{induced} \quad (10)$$

To a very good approximation, the induced field is linearly dependent on the static field, and may be written as:

$$B^{induced} = \sigma \cdot B^0 \quad (11)$$

Thus, the chemical shielding Hamiltonian acting on a spin can be written as:

$$\hat{H}_{CS} = -\gamma \hbar \hat{I} \cdot \sigma \cdot B^0 \quad (12)$$

where the shielding tensor σ is represented by a matrix:

$$\sigma = \begin{pmatrix} \sigma_{xx} & \sigma_{xy} & \sigma_{xz} \\ \sigma_{yx} & \sigma_{yy} & \sigma_{yz} \\ \sigma_{zx} & \sigma_{zy} & \sigma_{zz} \end{pmatrix} \quad (13)$$

It is possible to choose the axis frame that σ is defined with respect to so that the shielding tensor is diagonal. We call this axis frame as principal axis frame, in which

only three diagonal numbers σ_{xx}^{PAF} , σ_{yy}^{PAF} , σ_{zz}^{PAF} left:

$$\sigma^{PAF} = \begin{pmatrix} \sigma_{xx}^{PAF} & 0 & 0 \\ 0 & \sigma_{yy}^{PAF} & 0 \\ 0 & 0 & \sigma_{zz}^{PAF} \end{pmatrix} \quad (14)$$

The orientation of the principal axis frame is determined by the electronic structure of the molecule and is fixed with respect to the molecule.

The isotropic chemical shift σ^{iso} is defined as the mean of the three principal values:

$$\sigma^{iso} = \frac{1}{3} (\sigma_{xx}^{PAF} + \sigma_{yy}^{PAF} + \sigma_{zz}^{PAF}) \quad (15)$$

The anisotropy Δ is defined as:

$$\Delta = \sigma_{zz}^{PAF} - \sigma_{iso} \quad (16)$$

The asymmetry η is defined as:

$$\eta = (\sigma_{xx}^{PAF} - \sigma_{yy}^{PAF}) / \sigma_{zz}^{PAF} \quad (17)$$

with the principal elements ordered according to $|\sigma_{zz}^{PAF} - \sigma_{iso}| \geq |\sigma_{xx}^{PAF} - \sigma_{iso}| \geq |\sigma_{yy}^{PAF} - \sigma_{iso}|$.

1.1.2 J -coupling

Nuclear spins magnetically interact via electrons to perturb the nuclear spin Hamiltonian. This kind of interaction is called J -coupling. J -coupling is generated through chemical bonds and depends on the structural configuration.

The isotropic form of the J -coupling Hamiltonian between spin j and k can be written as:

$$\hat{H}_{jk}^{iso} = 2\pi \hat{I}_j \cdot J_{jk} \cdot \hat{I}_k \quad (18)$$

Note here that this term doesn't depend on the Larmor frequency.

In solids, the anisotropic part of the J -coupling survives, but is often ignored, as it is too small compared to other nuclear spin interactions.

The secular homo-nuclear and hetero-nuclear J -coupling can be written as:

$$\text{homonuclear} : \hat{H}_{jk} = 2\pi \hat{I}_j \cdot J_{IS} \cdot \hat{I}_k \quad (19)$$

$$\text{hetero-nuclear} : \hat{H}_{jk} = 2\pi \hat{I}_{jz} \cdot J_{IS} \cdot \hat{I}_{kz} \quad (20)$$

1.1.3 Dipolar Coupling

The dipolar coupling is the interaction between the nuclear spins through the space. This interaction occurs when a magnetic nuclear spin generates a magnetic field looping around in the surrounding space. The second nuclear spin interacts with this magnetic field.

The spin Hamiltonian of dipolar coupling between spin j and k has the form:

$$\hat{H}_{jk}^D = b_{jk}(3(\hat{I}_j \cdot e_{jk})(\hat{I}_k \cdot e_{jk}) - \hat{I}_j \cdot \hat{I}_k) \quad (21)$$

where e_{jk} is a unit vector parallel to the line joining the centres of the two nuclei, and b_{jk} is the dipolar coupling constant defined as

$$b_{jk} = -\frac{\mu_0 \gamma_j \gamma_k \hbar}{4\pi r_{jk}^3} \quad (22)$$

where γ_j and γ_k are the gyromagnetic ratios of the two spins and r_{jk} is the distance between the two spins, μ_0 is equal to $4\pi \times 10^{-7} \text{ Hm}^{-1}$. Eq.21 and Eq.22 indicate that dipolar interaction is inverse proportional to the cube of the internuclear distance and is proportional to the gyromagnetic ratio of each spin. Since the vector e_{jk} changes direction as the molecule rotates, the dipolar Hamiltonian in Eq.21 is orientation dependent.

In solids, the secular part of the mononuclear and hetero-nuclear dipolar spin Hamiltonians are given by

$$\text{homo} - \text{nuclear} : \hat{H}_{jk}^D(\Theta_{jk}) = d_{jk}(3\hat{I}_{jz}\hat{I}_{kz} - \hat{I}_j \cdot \hat{I}_k) \quad (23)$$

$$\text{hetero} - \text{nuclear} : \hat{H}_{jk}^D(\Theta_{jk}) = d_{jk}2\hat{I}_{jz}\hat{I}_{kz} \quad (24)$$

where d_{jk} is given by

$$d_{jk} = b_{jk} \frac{1}{2} (3\cos^2\Theta_{jk} - 1) \quad (25)$$

and Θ_{jk} the angle between the vector joining the spins and the external magnetic field:

$$\cos^2\Theta_{jk} = e_{jk}e_z \quad (26)$$

Note here that d_{jk} is orientation-dependent through the angle Θ_{jk} . The secular dipolar coupling d_{jk} is equal to zero when Θ_{jk} satisfies this equation:

$$(3\cos^2\Theta_{jk} - 1) = 0 \quad (27)$$

then we get the so-called *magic angle* :

$$\Theta_{magic} = \arctan\sqrt{2} \cong 54.74^\circ \quad (28)$$

1.1.4 Quadrupolar interaction

Quadrupolar nuclei represent more than 70% of nuclei in the Periodic Table. Their electric quadrupole moment interacts with the electric field gradients generated by the surrounding electron clouds. We call this interaction as the quadrupolar coupling.

The form of the nuclear quadrupole Hamiltonian can be written as

$$\hat{H}_Q(\Theta) = \frac{eQ}{2I(2I-1)\hbar} \hat{I} \cdot V(\Theta) \cdot \hat{I} \quad (29)$$

where Q is the nuclear quadrupole moment, $V(\Theta)$ the electric field gradient tensor, I the nuclear spin quantum number.

$V(\Theta)$ is diagonal in the principal axis (PAS) of the electric field gradient.

$$V^{PAS} = \begin{pmatrix} V_{XX} & 0 & 0 \\ 0 & V_{YY} & 0 \\ 0 & 0 & V_{ZZ} \end{pmatrix} \quad (30)$$

with three numbers ordered by $|V_{ZZ}| \geq |V_{YY}| \geq |V_{XX}|$.

Then we can define two independent parameters: eq and η as following:

$$eq = V_{zz} \quad (31)$$

$$\eta = \frac{V_{XX} - V_{YY}}{V_{ZZ}} \quad (32)$$

Since the quadrupolar interaction is very large, secular approximation can't applied. As a result, it is necessary to include more than one term in the following series:

$$\hat{H}_Q = \hat{H}_Q^1 + \hat{H}_Q^2 + \dots \quad (33)$$

where \hat{H}_Q^1 is the first-order quadrupolar Hamiltonian and \hat{H}_Q^2 the second-order quadrupolar Hamiltonian.

In solids, the first-order quadrupolar Hamiltonian can be written as:

$$\hat{H}_Q^1(\Theta) = \omega_Q^1(\Theta) \times \frac{1}{6} (3\hat{I}_z^2 - I(I+1)\hat{1}) \quad (34)$$

where Θ is the molecular orientation. If $\eta = 0$, the first-order quadrupolar coupling can be written as:

$$\hat{H}_Q^1(\Theta) = \frac{3\pi C_Q}{I(2I-1)} \times \frac{1}{2} (3 \cos^2 \theta_Q - 1) \quad (35)$$

where θ_Q is the angle between the principal Z-axis of the EFG tensor and the static

magnetic field, and the quadrupolar coupling constant C_Q is defined as:

$$C_Q = \frac{e^2qQ}{h} \quad (36)$$

1.2 Through-space Homo-nuclear Correlation Spectroscopy

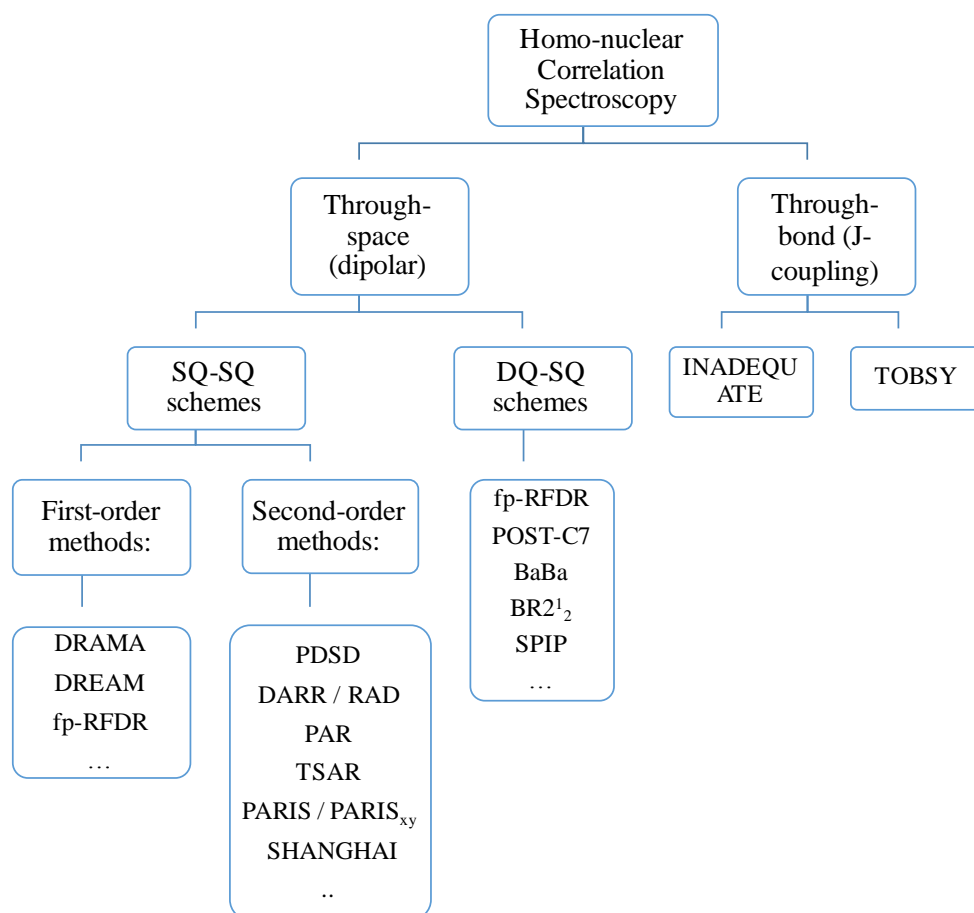


Fig.1. Schematic classification of Two-dimensional Homo-nuclear correlation experiments.

Two-dimensional homo-nuclear correlation spectroscopy is a powerful tool for the characterization of solid-state samples under MAS. There are mainly two ways for building up internuclear high resolution correlation spectra. As shown in Fig.1, the first method, called *through-bond* homo-nuclear correlation spectroscopy, is realized through *J*-coupling based on chemical bonds. Several experimental techniques, such as TOBSY^[7] and INADEQUATE^[8, 9] have been well established to help the identification of chemical shift in powdered solids. A detailed review can be found elsewhere^[10].

The second method, called *through-space* homo-nuclear correlation spectroscopy relies on restoring the through-space dipolar interaction averaged out by very fast MAS. As mentioned in Section 1.1.3, the homo-nuclear dipolar interaction conveys information about the distance of a homo-nuclear pair of nuclei. There are two types of experiment that can be performed to establish spatial correlations of coupled spins.

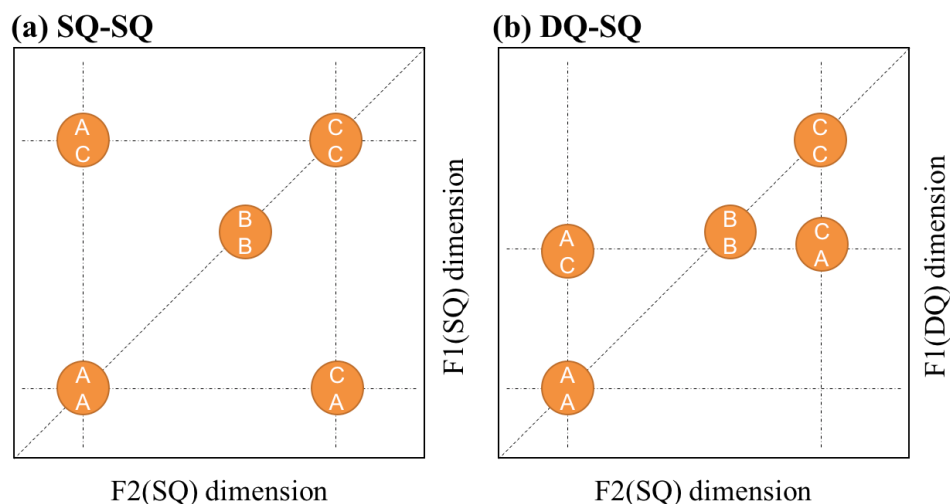


Fig.2 Illustration of two-dimensional (a) SQ-SQ and (b) DQ-SQ homo-nuclear correlation spectrum.

The first type of two-dimensional dipolar correlation experiments is so-called SQ-SQ approach that correlates two single-quantum spectra with cross-peaks occurring between signals from spins that are close in space. In the resulting SQ-SQ spectra (shown in Fig.2a), the signal of two coupled spins A and C with different chemical shifts is distributed over four resonance positions in the 2D spectrum, namely AA, AC, CA and CC, where AA and CC correspond to diagonal peaks and AC and CA to the cross-peaks.

The second type of two-dimensional dipolar correlation experiments, called DQ-SQ approach, requires the excitation and reconversion of double-quantum coherence. The resulting two-dimensional frequency spectrum correlates the double-quantum spectrum in F1 dimension with a double-quantum filtered single-quantum spectrum in F2 dimension. In the double-quantum dimension (F1), the chemical shift of the signals corresponds to the sum of the chemical shifts to the two coupled nuclei: $\omega_{AC} = \omega_A + \omega_C$. As a result, signals located at $(\omega_A, \omega_A + \omega_C)$ and $(\omega_C, \omega_A + \omega_C)$ can be observed in the DQ (F1) dimension, while diagonal signals, denoted as CC and AA in the figure, can be observed

at $(\omega_C, 2\omega_C)$ and $(\omega_A, 2\omega_A)$.

In this section, we will focus on the ^{13}C - ^{13}C through-space homo-nuclear correlation spectroscopy that has been widely used in the structural determination of biological samples. A brief summary of pulse sequences available for this type of experiments will be given in the following.

1.2.1 SQ-SQ approach

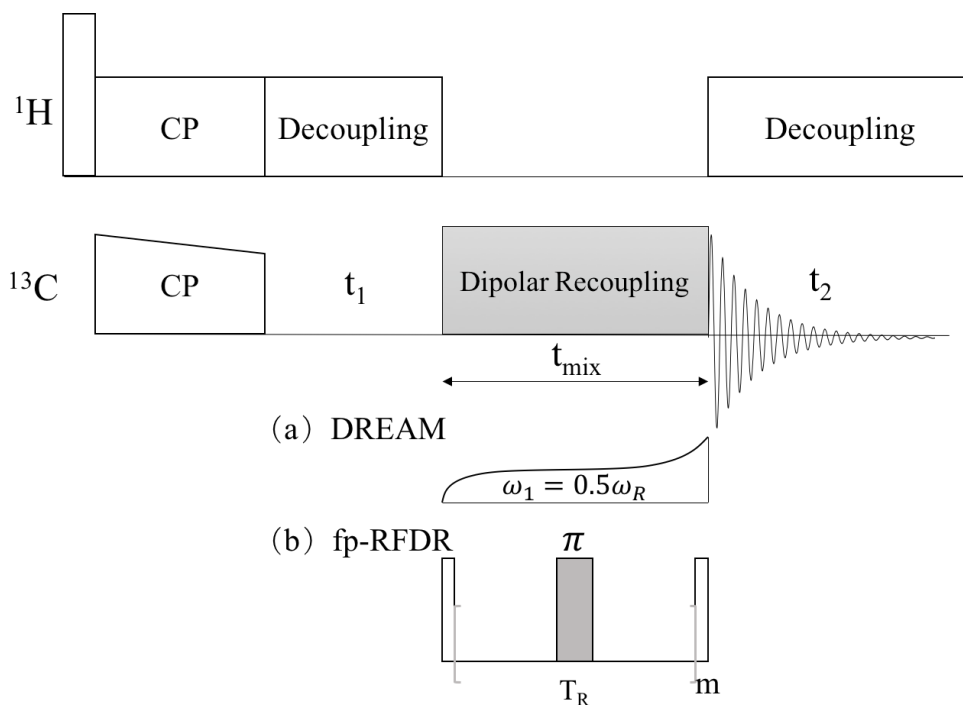


Fig.3. General pulse sequence for first-order ^{13}C - ^{13}C SQ-SQ Homo-nuclear Correlation Experiment with (a) DREAM and (b) fp-RFDR recoupling during mixing time.

Under fast MAS, the SQ-SQ correlation experiments can be implemented by using either first-order or second-order dipolar recoupling sequences.

DREAM^[11] and finite-pulse RFDR^[12] are the two most common first-order dipolar recoupling sequences. The coherence transfer in these two methods relies on the homo-nuclear dipolar interaction in the first term of the Magnus expansion, which makes the transfer efficiencies independent on the MAS frequency. The first-order recoupling sequences are prone to dipolar truncation^[13] and they allow mainly the observation of proximities between closet neighbors for short recoupling times. In uniformly ^{13}C -labeled

proteins, these close contacts correspond to one-bond restraints, which are useful for spectral assignment. At longer recoupling times, cross-peaks corresponding to two or three-bond transfers can be observed. Fig.3 gives the pulse sequence of ^{13}C - ^{13}C SQ-SQ Homo-nuclear Correlation Experiment using DREAM and fp-RFDR as dipolar recoupling. The DREAM scheme, as shown in Fig.3a, relies on the adiabatic amplitude sweep through the HORROR^[14] recoupling condition, which makes it less sensitive to the rf-field inhomogeneity. It has been shown that this method can be applied without proton decoupling during the dipolar recoupling period and with low-power XiX decoupling during the t_1 and t_2 evolution period.^[15] The fp-RFDR scheme, as shown in Fig.3 (b), corresponds to a train of π pulses of finite duration applied every rotor period, T_R . The most two common basic phase cycles of fp-RFDR are XY-4 and XY-8^[16], which corresponds to the symmetry $[R4_4^{-1}]_{45}$ (a 45° phase shift of $[R4_4^{-1}]$) and $[R4_4^{-1}R4_4^1]_{45}$. These two symmetries achieve zero-quantum homo-nuclear recoupling with suppression of CSA, hetero-nuclear J and dipolar couplings and isotropic chemical shift in the first-order Average Hamiltonian.^[17] The XY-8 phase cycle using super cycling suppressed the second order cross-terms proportional to zero-quantum spin operators, which are responsible for the depolarization in zero-quantum homo-nuclear dipolar recoupling. In order to prevent the interference of ^1H - ^{13}C dipolar coupling with ^{13}C - ^{13}C dipolar recoupling, strong ^1H decoupling should be applied during the dipolar recoupling time. However, it was shown that this kind of interference can be minimized by employing high rf-fields of recoupling pulses on ^{13}C channel and very fast magic angle spinning.

The second-order recoupling sequences include the Proton Driven Spin Diffusion (PDSD)^[18] (Fig.2a), the Dipolar Assisted Rotational Resonance (DARR)^[19] (Fig.2b), Rf-Assited Diffusion (RAD)^[20] (Fig.2b), the Phase-Alternated Recoupling Irradiation Schemes: PARIS^[21] (Fig.2c) and PARIS_{xy}^[22, 23] (Fig.2d), and Second-order Hamiltonian among Analogous Nuclei Generated by Hetero-nuclear Assistance Irradiation (SHANGHAI)^[24] (Fig.2e). These methods requires the presence of protons and are not applicable to perdeuterated proteins. Unlike those first-order recoupling schemes, the second-order recoupling schemes are less affected by the dipolar truncation and they allow the measurement of long-range ^{13}C - ^{13}C distance restraints in uniformly ^{13}C -labeled biomolecules. For PDSD scheme, no rf irradiation during mixing time on the ^1H channel

is required, and it mainly achieves polarization transfer through high-order Hamiltonians. The DARR and RAD experiments employ rf nutation frequency, ν_1 , equals to ν_R or $2\nu_r$, which promotes magnetization transfers owing to the resonance interference recoupling, also called MIRROR^[25] conditions. For the PARIS_{xy} scheme, the m parameter is the number of alternations between opposite phase comprised between two $\pi/2$ phase shifts. If the rf-field is equal to ν_R , then PARS, PARIS_{xy}(m=1) and PARIS_{xy}(m=2) schemes correspond to the symmetries $[R2_1^1]_{270}$, $[R2_1^1]_{270}[R2_1^1]_{180}$, $[R4_2^2]_{270}[R4_2^2]_{180}$. SHANGHAI scheme is close to the PARS_{xy}, and the only difference is that the four phases are ordered as x, y, -x and -y.

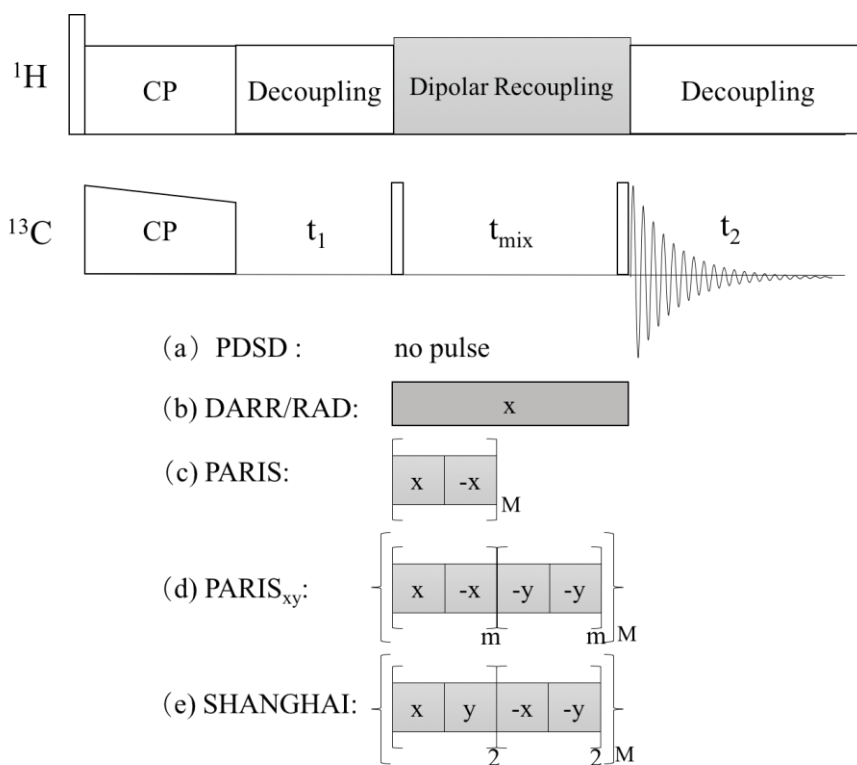


Fig.4. General pulse sequence for second-order ^{13}C - ^{13}C SQ-SQ Homo-nuclear Correlation Experiment with (a) PDSD (b) DARR/RAD (c) PARIS (d) PARIS_{xy} (e) SHANGHAI schemes.

1.2.2 DQ-SQ approach

The two-dimensional DQ-SQ correlation spectroscopy is revealed through the generation of Double-quantum coherences via homo-nuclear dipolar couplings. For this

purpose, dipolar recoupling schemes are required to excite DQ coherences and reconvert them back into observable magnetization. Compared to the SQ-SQ correlation experiments, the DQ-SQ correlation experiments permit to probe correlation between equivalent sites.

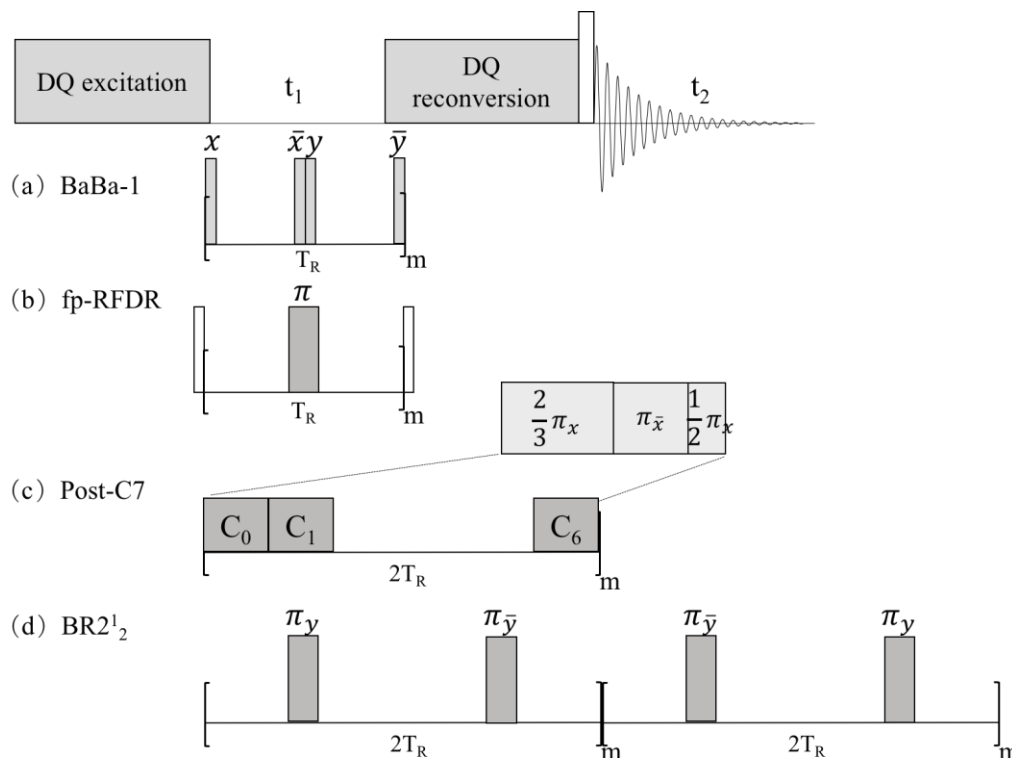


Fig.5. General pulse sequence for DQ-SQ Homo-nuclear Correlation Experiment. The excitation and reconversion are achieved using (a) Baba-1, (b) fp-RFDR, (c) POST-C7, (d) BR2¹₂.

Fig.5 shows the general pulse sequence for DQ-SQ homo-nuclear correlation experiment with several DQ dipolar recoupling schemes. In this pulse sequence, a first recoupling sequence is applied in order to transform the longitudinal magnetization into DQ coherences. A second recoupling period followed by a $\pi/2$ pulse transforms the DQ coherences into observable transverse magnetization. Different homo-nuclear dipolar recoupling sequences can be applied in this experiment.

For BABA^[26] (back-to-back) recoupling (Fig.5a), different variants have been proposed. One of the key features of BABA is its large scaling factor of DQ operators, which means that the optimal recoupling times for BABA sequence is much shorter than other recoupling schemes. However, the BABA method is quite sensitive to resonance offsets and CSA. The fp-RFDR scheme (Fig.5b), as mentioned in Section 1.2.1, achieves

zero quantum dipolar recoupling. The usual phase cycle of fp-RFDR is XY4, which corresponding to the $R4_4^1$. The performance of this scheme can be further improved by using super-cycling, such as XY-8 and XY-16. It should be noted here that the excitation and reconversion of DQ coherences are realized by insertion of bracket $\pi/2$ pulse at the beginning and at the end of fp-RFDR. The POST-C7^[27] scheme (Fig.5c) utilizes the CN_n^v symmetry to achieve efficient excitation. However, it can't be employed under fast MAS frequencies, since the requisite rf-field has to be seven times the spinning frequency. The $BR2_2^{1,2}$ ^[28, 29] scheme is derived from the $R2_2^1$. The $R2_2^1$ symmetry provides zero-quantum and double-quantum dipolar recoupling. However, it does not eliminate the unwanted CSA and offset terms in the first-order average Hamiltonian. The $BR2_2^1$ scheme increases the robustness to CSA and offset effect by applying an overall phase of 180° from the middle of the recoupling sequence. It has been shown that the $BR2_2^1$ can be employed to characterization of ^{31}P species submitted to very large chemical shift anisotropic interaction.^[28]

In fact, the DQ-SQ can be used in a one-dimensional fashion where the recoupling schemes act as an T_2 (spin-spin relaxation time) filter. Such kind of experiment is often called the DQ filtered 1D experiment. In this kind of experiment, the signals are more suppressed by the strong homo-nuclear dipolar couplings, which provides us information whether a certain spin is subject to dipolar interaction. Moreover, the build-up curve of DQ coherence is modulated by the recoupled dipolar coupling and evolves as a function of the recoupling time. This approach permits estimation of dipolar coupling between spin pair of interest in materials.^[30]

1.3 Through-space Hetero-nuclear Correlation Spectroscopy

Two-dimensional hetero-nuclear correlation experiments (HECTOR) are very important tools of SS-NMR spectroscopy to probe through-bond connectivities or through-space proximities between distinct isotopes. As shown in Fig.6, the connectives and proximities are revealed through coherence transfer via dipolar couplings or J -coupling, respectively. The through-bond HECTOR makes use of the non-vanishing isotropic terms of J -coupling, which reveals the existence of chemical bond between two

distinct nuclei. The through-space HECTOR technique relies on restoring the dipolar interaction, which indicates the proximities in space.

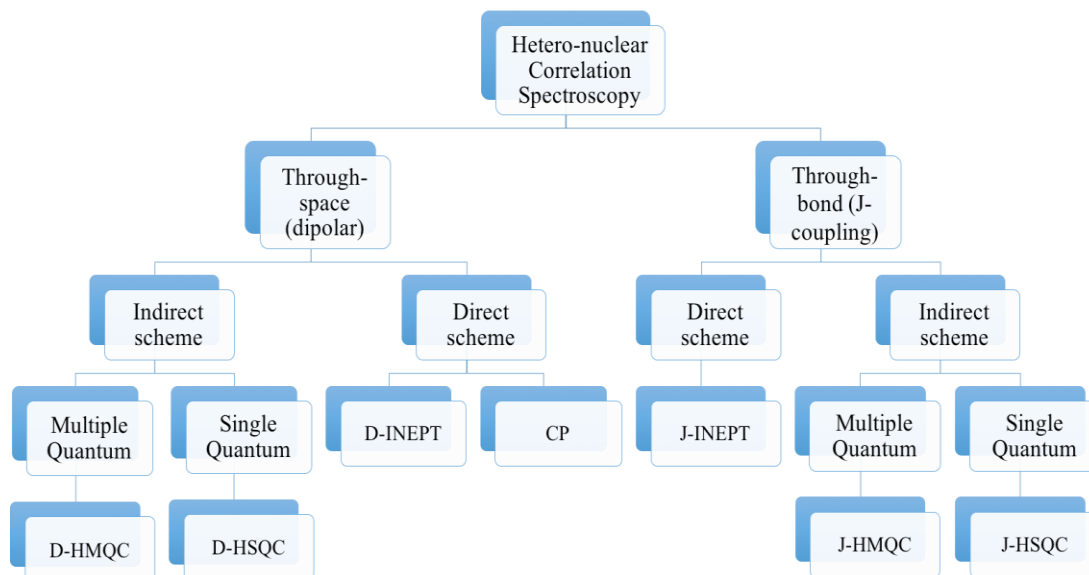


Fig.6. Schematic classification of Two-dimensional Hetero-nuclear correlation experiments.

Fig.6 summarizes the main properties of available pulse sequences for hetero-nuclear correlation experiments. This classification is based on the mode of detection and the order of coherences during the t_1 evolution period. The through-bond hetero-nuclear correlation can be realized through directly detected J -INEPT^[31], indirectly detected J -HSQC^[32] and J -HMQC^[33-35] methods. However, through-space HECTOR experiments are generally more efficient than the through-bond HECTOR due to the fact that the dipolar couplings are much larger than the J -couplings. This allows the use of short recoupling times in through-space HECTOR experiments, thus prevents the fast decay of signals due to T_2 relaxation. The through-space hetero-nuclear correlation experiments include the directly detected D-INEPT^[36], CP^[37], and indirectly detected D-HMQC^[36, 38] and D-HSQC^[39] methods. It should be noted here that the indirect detection can enhance the sensitivity of through-space HECTOR experiments at high MAS frequency.

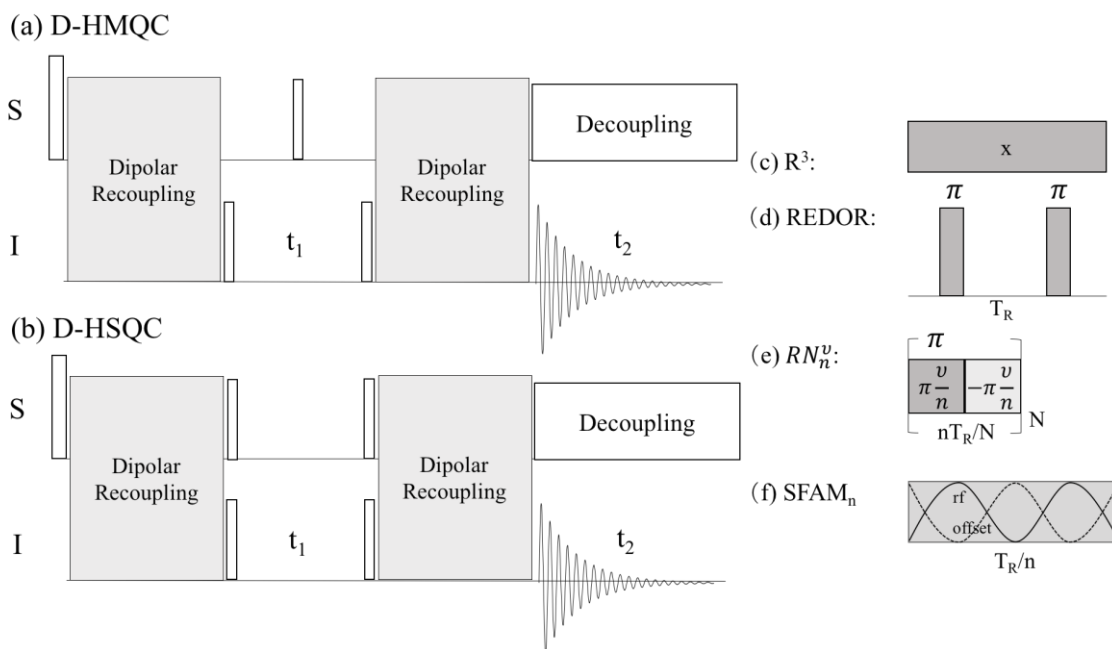


Fig.7. General pulse sequence for (a) *D*-HMQC and (b) *D*-HSQC experiment. Hetero-nuclear dipolar recoupling can be applied on either *S* channel or *I* channel by using (a) Baba-1, (b) fp-RFDR, (c) POST-C7, (d) BR2¹₂.

The general pulse sequence for *D*-HMQC and *D*-HSQC experiments are shown in Fig.7a and Fig.7b respectively. During the first recoupling block, the *S*-spin magnetization for a coupled *IS* spin system evolves from in-phase (S_x) in to antiphase ($2I_zS_y$) coherence with respect to *I*. In the *D*-HMQC experiment, this antiphase coherence is converted into a hetero-nuclear MQ coherence ($2I_xS_y$) by the $\pi/2$ pulse on the *I* channel. In the *D*-HSQC experiment, this antiphase coherence is converted into an antiphase hetero-nuclear 1Q *I*-spin coherence ($2I_xS_z$) by applying two simultaneous $\pi/2$ pulses. At the end of t_1 , the MQ and 1Q coherences are converted back into antiphase *S*-spin coherences by the $\pi/2$ pulses, and these coherences evolve during the second recoupling block to become observable transverse *S*-spin magnetization. A 2D Fourier transform of the time domain signal provides isotropic shift correlations between pairs of *I* and *S* nuclei.

The hetero-nuclear dipolar couplings are recoupled by applying hetero-nuclear dipolar recoupling techniques such as $R^{3[40]}$ (Fig.7c), REDOR^[41] (Fig.7d), R symmetry sequences^[17] (Fig.7e), and $SFAM_n$ ^[42] (Fig.7f) sequences. Rotary resonance recoupling has been shown to recover various anisotropic interactions under MAS with resonance

conditions described by a number $q = \nu_1/\nu_R$, where ν_1 is the rf field and ν_R is the sample spinning speed. For CSA and hetero-nuclear dipolar coupling, the reintroduction occurs at $q = 1$ and 2 . For homo-nuclear dipolar coupling it occurs at $q = 1/2$ and 1 . Therefore, the $q = 2$ condition should be used in the case of nuclei submitted to strong homo-nuclear dipolar couplings. In other cases, the $q = 1$ condition should be used to provide better experimental efficiency. The rotational echo double resonance (REDOR) applies two spaced π pulses every rotor cycle to recouple dipolar interaction. Different variations of REDOR sequences (XY4, XY8, XY16)^[16, 43] have been proposed to compensate the flip angle error and the offset effect. However, it has been shown that in case of weak dipolar recoupling, a very tiny 0.1 Hz change of MAS frequency can attenuate signal intensities if REDOR pulses are sent on the observable channel.^[43] REDOR suffers from artifacts because of the finite π pulse lengths, which represent a non-negligible fraction of the rotor period. The simultaneous frequency and amplitude modulation (SFAM) was proposed to overcome this limitation. The carrier frequency of the rf field is modulated cosinusoidally, while its amplitude is modulated sinusoidally. It has been shown that the SFAM₁ method leads to the efficiency with the modulation frequency of rf field equals to the spinning speed.

$$\begin{aligned}\Delta\nu_0(t) &= \Delta\nu_0^{max} \cos(2\pi\nu_R t) \\ \nu_1(t) &= \nu_1^{max} \sin(2\pi\nu_R t)\end{aligned}$$

However, SFAM₁ also recouples the homo-nuclear dipolar coupling. Thus, in a similar way as with R³ to suppress the homo-nuclear dipolar coupling, the modulate frequency should be twice the spinning speed, leading to the SFAM₂ method.

$$\begin{aligned}\Delta\nu_0(t) &= \Delta\nu_0^{max} \cos(4\pi\nu_R t) \\ \nu_1(t) &= \nu_1^{max} \sin(4\pi\nu_R t)\end{aligned}$$

Symmetry sequences can also be applied to recoupling the hetero-nuclear dipolar interaction as long as the hetero-nuclear dipolar interaction associated with the quantum numbers $\{l, m, \lambda, \mu\}$ is selected according to the selection rules. The basic block of these sequences extends over n rotor periods and is composed of N rotor-synchronized π pulses. In this thesis, we have chosen the $SR4_1^2$ symmetry, which has been proposed to measure ¹H-¹⁷O distances in protonated sample^[44]. $SR4_1^2$ Symmetry only requires the rf-field to be only twice the spinning frequency, which means it can be employed under

very fast MAS frequency. This method also suppresses the un-wanted homo-nuclear dipolar couplings.

References

- [1] E.M. Purcell, H.C. Torrey, R.V. Pound, Resonance Absorption by Nuclear Magnetic Moments in a Solid, *Physical Review*, 69 (1946) 37-38.
- [2] F. Bloch, W.W. Hansen, M. Packard, Nuclear Induction, *Physical Review*, 69 (1946) 127-127.
- [3] E.R. Andrew, A. Bradbury, R.G. Eades, Removal of Dipolar Broadening of Nuclear Magnetic Resonance Spectra of Solids by Specimen Rotation, *Nature*, 183 (1959) 1802-1803.
- [4] I.J. Lowe, Free Induction Decays of Rotating Solids, *Physical Review Letters*, 2 (1959) 285-287.
- [5] S.R. Hartmann, E.L. Hahn, Nuclear Double Resonance in the Rotating Frame, *Physical Review*, 128 (1962) 2042-2053.
- [6] Y. Nishiyama, Y. Endo, T. Nemoto, H. Utsumi, K. Yamauchi, K. Hioka, T. Asakura, Very fast magic angle spinning 1H-14N 2D solid-state NMR: Sub-micro-liter sample data collection in a few minutes, *Journal of Magnetic Resonance*, 208 (2011) 44-48.
- [7] M. Baldus, R.J. Iulucci, B.H. Meier, Probing Through-Bond Connectivities and Through-Space Distances in Solids by Magic-Angle-Spinning Nuclear Magnetic Resonance, *Journal of the American Chemical Society*, 119 (1997) 1121-1124.
- [8] A. Lesage, C. Auger, S. Caldarelli, L. Emsley, Determination of Through-Bond Carbon–Carbon Connectivities in Solid-State NMR Using the INADEQUATE Experiment, *Journal of the American Chemical Society*, 119 (1997) 7867-7868.
- [9] A. Lesage, M. Bardet, L. Emsley, Through-Bond Carbon–Carbon Connectivities in Disordered Solids by NMR, *Journal of the American Chemical Society*, 121 (1999) 10987-10993.
- [10] A. Lesage, Indirect Coupling and Connectivity, in, John Wiley & Sons, Ltd, 2007.
- [11] R. Verel, M. Ernst, B.H. Meier, Adiabatic dipolar recoupling in solid-state NMR: the DREAM scheme, *Journal of Magnetic Resonance*, 150 (2001) 81-99.
- [12] Y. Ishii, [¹³C–¹³C dipolar recoupling under very fast magic angle spinning in solid-state nuclear magnetic resonance: Applications to distance measurements, spectral assignments, and high-throughput secondary-structure determination, *J. Chem. Phys.*, 114 (2001) 8473.

- [13] M.J. Bayro, M. Huber, R. Ramachandran, T.C. Davenport, B.H. Meier, M. Ernst, R.G. Griffin, Dipolar truncation in magic-angle spinning NMR recoupling experiments, *J. Chem. Phys.*, 130 (2009) 114506.
- [14] N.C. Nielsen, H. Bildsoe, H.J. Jakobsen, M.H. Levitt, Double-quantum homonuclear rotary resonance: Efficient dipolar recovery in magic-angle spinning nuclear magnetic resonance, *J. Chem. Phys.*, 101 (1994) 1805.
- [15] M. Ernst, M.A. Meier, T. Tuhem, A. Samoson, B.H. Meier, Low-power high-resolution solid-state NMR of peptides and proteins, *J. Am. Chem. Soc.*, 126 (2004) 4764-4765.
- [16] T. Gullion, D.B. Baker, M.S. Conradi, New, compensated Carr-Purcell sequences, *Journal of Magnetic Resonance*, 89 (1990) 479-484.
- [17] M.H. Levitt, Symmetry-Based Pulse Sequences in Magic-Angle Spinning Solid-State NMR, in: *eMagRes*, John Wiley & Sons, Ltd, 2007.
- [18] A. Grommek, B.H. Meier, M. Ernst, Distance information from proton-driven spin diffusion under MAS, *Chemical Physics Letters*, 427 (2006) 404-409.
- [19] K. Takegoshi, S. Nakamura, T. Terao, C-13-H-1 dipolar-assisted rotational resonance in magic-angle spinning NMR, *Chemical Physics Letters*, 344 (2001) 631-637.
- [20] C.R. Morcombe, V. Gaponenko, R.A. Byrd, K.W. Zilm, Diluting abundant spins by isotope edited radio frequency field assisted diffusion, *J. Am. Chem. Soc.*, 126 (2004) 7196-7197.
- [21] M. Weingarth, D.E. Demco, G. Bodenhausen, P. Tekely, Improved magnetization transfer in solid-state NMR with fast magic angle spinning, *Chemical Physics Letters*, 469 (2009) 342-348.
- [22] M. Weingarth, G. Bodenhausen, P. Tekely, Broadband magnetization transfer using moderate radio-frequency fields for NMR with very high static fields and spinning speeds, *Chemical Physics Letters*, 488 (2010) 10-16.
- [23] M. Weingarth, Y. Masuda, K. Takegoshi, G. Bodenhausen, P. Tekely, Sensitive ^{13}C - ^{13}C correlation spectra of amyloid fibrils at very high spinning frequencies and magnetic fields, *J Biomol NMR*, 50 (2011) 129-136.
- [24] B. Hu, O. Lafon, J. Trépo, Q. Chen, J.-P. Amoureux, Broad-band homo-nuclear correlations assisted by ^1H irradiation for bio-molecules in very high magnetic field at fast and ultra-fast MAS frequencies, *Journal of Magnetic Resonance*, 212 (2011) 320-329.
- [25] I. Scholz, M. Huber, T. Manolikas, B.H. Meier, M. Ernst, MIRROR recoupling and its application to spin diffusion under fast magic-angle spinning, *Chemical Physics Letters*, 460 (2008) 278-283.
- [26] M. Feike, D.E. Demco, R. Graf, J. Gottwald, S. Hafner, H.W. Spiess, Broadband multiple-quantum NMR spectroscopy, *J Magn Reson Ser A*, 122 (1996) 214-221.

- [27] M. Hohwy, H.J. Jakobsen, M. Eden, M.H. Levitt, N.C. Nielsen, Broadband dipolar recoupling in the nuclear magnetic resonance of rotating solids: A compensated C7 pulse sequence, *J Chem Phys*, 108 (1998) 2686-2694.
- [28] B. Hu, L. Delevoye, O. Lafon, J. Trébosc, J.P. Amoureux, Double-quantum NMR spectroscopy of ^{31}P species submitted to very large CSAs, *Journal of Magnetic Resonance*, 200 (2009) 178-188.
- [29] B. Hu, Q. Wang, O. Lafon, J. Trébosc, F. Deng, J.P. Amoureux, Robust and efficient spin-locked symmetry-based double-quantum homonuclear dipolar recoupling for probing ^1H - ^1H proximity in the solid-state, *Journal of Magnetic Resonance*, 198 (2009) 41-48.
- [30] J. Huang, M. Wang, S. Zhang, B. Hu, H. Li, Influence of the Pd(II) Coordination Model on the Catalytic Performance of Pd-PPh₂-SBA-15 in C-C Bond Forming Reactions, *The Journal of Physical Chemistry C*, 115 (2011) 22514-22522.
- [31] D.C. Finster, W.C. Hutton, R.N. Grimes, Two-dimensional correlated nuclear magnetic resonance of spin-coupled boron-11-proton systems, *J. Am. Chem. Soc.*, 102 (1980) 400-401.
- [32] S. Cavadini, A. Abraham, G. Bodenhausen, Coherence transfer between spin nuclei and nitrogen-14 in solids, *Journal of Magnetic Resonance*, 190 (2008) 160-164.
- [33] D. Massiot, F. Fayon, B. Alonso, J. Trébosc, J.-P. Amoureux, Chemical bonding differences evidenced from J-coupling in solid state NMR experiments involving quadrupolar nuclei, *Journal of Magnetic Resonance*, 164 (2003) 160-164.
- [34] L. Mueller, Sensitivity enhanced detection of weak nuclei using heteronuclear multiple quantum coherence, *J. Am. Chem. Soc.*, 101 (1979) 4481-4484.
- [35] A. Lesage, L. Emsley, Through-Bond Heteronuclear Single-Quantum Correlation Spectroscopy in Solid-State NMR, and Comparison to Other Through-Bond and Through-Space Experiments, *Journal of Magnetic Resonance*, 148 (2001) 449-454.
- [36] J. Trébosc, B. Hu, J.-P. Amoureux, Z. Gan, Through-space R₃-HETCOR experiments between spin-1/2 and half-integer quadrupolar nuclei in solid-state NMR, *Journal of Magnetic Resonance*, 186 (2007) 220-227.
- [37] P. Caravatti, G. Bodenhausen, R.R. Ernst, Heteronuclear solid-state correlation spectroscopy, *Chemical Physics Letters*, 89 (1982) 363-367.
- [38] Z. Gan, $^{13}\text{C}/^{14}\text{N}$ heteronuclear multiple-quantum correlation with rotary resonance and REDOR dipolar recoupling, *Journal of Magnetic Resonance*, 184 (2007) 39-43.
- [39] M. Hong, R.G. Griffin, Resonance Assignments for Solid Peptides by Dipolar-Mediated $^{13}\text{C}/^{15}\text{N}$ Correlation Solid-State NMR, *Journal of the American Chemical Society*, 120 (1998) 7113-7114.

-
- [40] T.G. Oas, R.G. Griffin, M.H. Levitt, Rotary resonance recoupling of dipolar interactions in solid - state nuclear magnetic resonance spectroscopy, *J. Chem. Phys.*, 89 (1988) 692-695.
- [41] T. Gullion, J. Schaefer, Rotational-echo double-resonance NMR, *Journal of Magnetic Resonance* (1969), 81 (1989) 196-200.
- [42] R.Q. Fu, S.A. Smith, G. Bodenhausen, Recoupling of heteronuclear dipolar interactions in solid state magic-angle spinning NMR by simultaneous frequency and amplitude modulation, *Chemical Physics Letters*, 272 (1997) 361-369.
- [43] T. Gullion, J. Schaefer, Elimination of resonance offset effects in rotational-echo, double-resonance NMR, *Journal of Magnetic Resonance*, 92 (1991) 439-442.
- [44] A. Brinkmann, A.P.M. Kentgens, Proton-Selective ^{17}O - ^1H Distance Measurements in Fast Magic-Angle-Spinning Solid-State NMR Spectroscopy for the Determination of Hydrogen Bond Lengths, *Journal of the American Chemical Society*, 128 (2006) 14758-14759.

Chapter 2: Through-space Homo-nuclear Correlation Spectroscopy: fp-RFDR with (XY8)₄¹ super-cycling

Solid-State Nuclear Magnetic Resonance (SS-NMR) is a powerful tool for structural determination of biomolecules.^[1-4] In particular, SS-NMR is especially qualified for non-crystalline and insoluble systems, such as amyloid fibrils or membrane proteins.^[5-8] Furthermore, the recent development of commercial Magic-Angle Spinning (MAS) probes with rotor outer diameter of less than 2.0 mm, and hence spinning speed, ν_R , faster than 40 kHz (up to 110 kHz presently), has been decisive for (i) the study of paramagnetic proteins,^[9,10] (ii) the use of long-range ¹H-¹H restraints,^[11-15] or (iii) the investigation of temperature-sensitive bio-molecules in aqueous matrices with high salt concentration and high dielectric constant.^[16-19] These fast MAS speeds allow enhancing the resolution and the sensitivity of paramagnetic compounds as well as of ¹H spectra by averaging the electron-nuclei or the ¹H-¹H dipolar interactions. Two other important consequences of these fast-MAS speeds, are the increase in sensitivity using indirect detection via ¹H nuclei,^[15,20] and the possibility of low-power ¹H decoupling in order to avoid radio-frequency (rf) heating in the case of temperature-sensitive systems.^[16-18,21] Furthermore, small outer rotor diameters permit the use of small detector coils, hence increasing the sensitivity per spin, which is beneficial for samples of limited volume, such as isotopically labeled biological systems.^[22,23] At high magnetic fields, fast MAS speeds are also required to eliminate the spinning sidebands of nuclei experiencing large chemical shift anisotropy (CSA), such as ¹³C and ¹⁵N. As the aromatic ¹³C sites display CSA as large as 120 ppm, their spinning sidebands can only be eliminated by using MAS frequencies higher than ca. 24 kHz at $B_0 = 18.8$ T and 36 kHz at 28.2 T, a targeted magnetic field for forthcoming NMR commercial spectrometers.

The observation in proteins of spatial proximities between identical isotopes using multidimensional NMR experiments represents an essential step for the spectral assignment and structure determination. In particular, ¹H-¹H^[11-15] and ¹³C-¹³C^[18,24-30] homo-nuclear distance restraints in peptides and proteins have been detected at MAS

speeds faster than 40 kHz. Under fast MAS, the homo-nuclear dipolar couplings can be reintroduced using either first-order or second-order dipolar recoupling sequences.

The second-order recoupling methods comprise: (i) ^{13}C - ^{13}C or ^{15}N - ^{15}N spin-diffusion types of experiments, including Proton Driven Spin Diffusion (PDS),^[31-34] and its variants assisted by ^1H irradiation, such as the Dipolar Assisted Rotational Resonance (DARR)^[35,36] and its closely related version Rf-Assisted Diffusion (RAD),^[37] the resonance interference recoupling,^[36] also called MIXed Rotational and ROTary Resonance (MIRROR),^[29] or more robust versions incorporating phase shifts of ^1H irradiation: the Phase-Alternated Recoupling Irradiation Schemes (PARIS^[38-40] and PARIS_{xy}^[26,28]) or the Second-order Hamiltonian among Analogous Nuclei Generated by Hetero-nuclear Assistance Irradiation (SHANGHAI);^[27] (ii) the methods based on ^1H - ^1H spin-diffusion, such as CHHC;^[41] (iii) the techniques based on rotational resonance (R^2);^[42] (iv) the sequences relying on Third-Spin Assisted Recoupling (TSAR), such as Proton Assisted Recoupling (PAR), which uses two simultaneous ^1H and ^{13}C rf-irradiations.³⁰ These second-order methods are less affected by the dipolar truncation than the first-order recoupling sequences and in particular they allow the measurement of long-range ^{13}C - ^{13}C distance restraints in uniformly ^{13}C -labeled biomolecules.^[19,28,43-45] However, these methods require the presence of protons and are not applicable to perdeuterated proteins.^[46] Furthermore, except CHHC, these methods do not allow to probe ^1H - ^1H distances. While MIRROR, PARIS, PARIS_{xy} and SHANGHAI have been demonstrated experimentally at MAS speeds faster than 40 kHz,^[26-29] their efficiency is inverse proportional to the MAS frequency. On the contrary, with the PAR method the choice of the two rf-fields permits to compensate the increase in MAS frequency.^[30]

The first-order homo-nuclear recoupling sequences are complementary of the previous second-order ones. These methods comprise SPC-5,^[47,48] DREAM,^[24,49] CMpRR,^[43] COMICS,^[43] Radio-Frequency-Driven Recoupling (RFDR),^[50] finite-pulse RFDR (fp-RFDR),^[51,52] BR2₂¹,^[25,53,54] *etc.* However, only methods requiring low rf power, such as DREAM, fp-RFDR and BR2₂¹, are applicable at MAS speeds faster than 40 kHz.^[18,24,25] As the coherence transfer in these methods relies on the homo-nuclear dipolar interaction in the first term of the Magnus expansion, these benefit from transfer efficiencies that are independent of the MAS frequency. Another advantage is the

possibility to apply these methods to perdeuterated proteins to observe ^{13}C - ^{13}C ^[55,56] or ^1H - ^1H proximities.^[11-15] The first-order recoupling sequences are prone to dipolar truncation and they allow mainly the observation of proximities between closest neighbors for short recoupling times.^[25,30,43,44,51,55] In uniformly ^{13}C -labeled proteins, these close contacts correspond to one-bond restraints, which are useful for spectral assignment. At longer recoupling times, cross-peaks corresponding to two or three-bonds transfers can be observed for uniformly ^{13}C -labeled proteins.^[25,45,51,57] Conversely, for isotopically diluted samples, such as perdeuterated proteins,^[11-15] position-specific ^{13}C -labeled proteins^[51,58,59] or selectively fluorinated^[60] or tritiated^[61] molecules, longer range distances can be measured using longer recoupling times, provided the recoupling sequence is robust to inferences of hetero-nuclear dipolar coupling, CSA, spread in resonance frequencies and rf inhomogeneity or maladjustments.

In this chapter, we introduce a new super-cycle for the first-order recoupling sequence, fp-RFDR. It is shown by numerical simulations that this super-cycle improves the robustness to offset, CSA and rf-inhomogeneity. Furthermore, ^{13}C - ^{13}C 2D dipolar-mediated homo-nuclear correlation (*D*-HOMCOR) experiments are performed on uniformly ^{13}C -labeled L-histidine.HCl test sample and a tetra-peptide in which 3 residues were uniformly ^{13}C and ^{15}N labeled. On these samples, we evidence intra- and inter-residue remote correlations. ^{31}P - ^{31}P 2D *D*-HOMCOR for $\text{Al}(\text{PO}_3)_3$ also demonstrates the higher efficiency at long recoupling times for the new super-cycle compared to the existing ones, especially in case of very large CSAs.

2.1 Pulse sequence

The fp-RFDR sequence is one of the most popular first-order homo-nuclear dipolar recoupling scheme, in particular at high spinning speeds. This sequence is depicted in Fig.1a for the observation of ^{13}C - ^{13}C proximities. In the present article, except in Fig.9, the fp-RFDR sequence is applied to the ^{13}C channel. It corresponds to a train of π -pulses of finite duration, τ_p , applied every rotor period, T_R . The pulse fraction is defined as $f = \tau_p/T_R$. The basic phase cycle of fp-RFDR is XY-4,^[62] which corresponds to the symmetry $[\text{R}4_4^{-1}]_{45}$, i.e. the $\text{R}4_4^{-1}$ symmetry with an overall phase shift of 45° .^[63] This symmetry

achieves zero-quantum homo-nuclear dipolar recoupling with suppression of CSA, hetero-nuclear J and dipolar couplings and isotropic chemical shift in the first-order Average Hamiltonian (AH).^[51] The fp-RFDR sequence, which employs a windowed basic inversion element $R = \tau\text{-}180_0\text{-}\tau$, is not γ -encoded and recouples the space components $m = \pm 1$ and ± 2 of the homo-nuclear dipolar interaction.^[63-65] Here, 180_0 indicates a rectangular, resonant π -pulse of length τ_p and phase x , and τ a delay. The magnitude of the recoupled homo-nuclear dipolar interaction tends to zero when there is no chemical shielding and when the length τ_p of the π -pulses becomes negligible with respect to the rotor period, T_R , as in the RFDR sequence, i.e. when the rf-field is much larger than the spinning speed ($\nu_{1\pi} \gg \nu_R$).^[51,66] However, at high MAS speeds (e.g. $\nu_R \approx 60$ kHz), even the strongest available carbon rf-fields (e.g. $\nu_{1\pi} \approx 170$ kHz) result in a significant duration of the π -pulses ($\tau_p \approx 3$ μ s) with respect to the rotor period ($T_R \approx 17$ μ s), thus leading to non-negligible pulse fraction, $f \approx 0.2$, and hence to significant recoupled homo-nuclear dipolar interactions. Furthermore, for broadband recoupling experiments, the rf-field must exceed the spread in resonance frequency, $\nu_{1\pi} > \Delta\nu_{\text{iso}}^{\text{max}}$. For instance, at $B_0 = 21.1$ T, the difference, $\Delta\nu_{\text{iso}}$, between carbonyl and aliphatic ^{13}C signals can reach 39 kHz (170 ppm) and $\nu_{1\pi}$ must thus be larger than 40 kHz. In addition, the average rf-field must not match the undesirable rotary resonance recoupling (R^3) conditions for hetero-nuclear dipolar coupling.^[52,67]

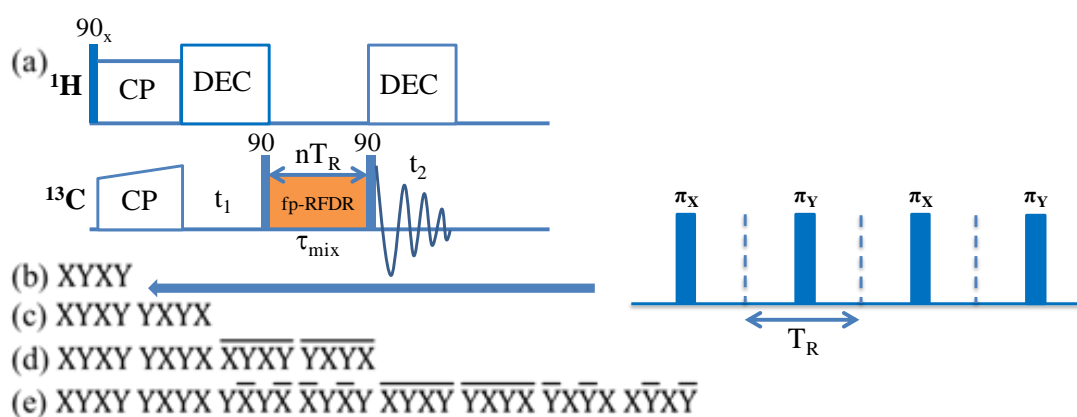


Fig.1. (a) General scheme for ^{13}C - ^{13}C 1Q-1Q D -HOMCOR experiments using fp-RFDR as zero-quantum homo-nuclear dipolar recoupling with (b) XY4, (c) XY8, (d) XY16, and (e) $(\text{XY}8)_4^1$ phase cyclings. All pulses of the fp-RFDR recoupling part are π -pulses.

Irradiation on other channels, in particular the ^1H one, can be applied to compensate

the contribution of hetero-nuclear dipolar coupling to the second and higher order terms of the Magnus expansion.^[52] In fact, it has been shown that the interference of ^1H - ^{13}C dipolar couplings with ^{13}C - ^{13}C dipolar recoupling via fp-RFDR can be avoided in two regimes employing either high-power or no ^1H decoupling fields.^[52] In the first regime, the hetero-nuclear decoupling interferences can only be avoided when the ^1H decoupling rf-field during the mixing time exceeds the ^{13}C nutation frequency by a factor of 3 or more ($\nu_{1\text{dec}}(^1\text{H}) > 3\nu_{1\pi}$). Therefore, in this regime, broadband ^{13}C - ^{13}C fp-RFDR experiments then require very strong decoupling rf-fields, which can cause significant sample heating and can denature temperature-sensitive biological systems. In the regime *sans* ^1H decoupling, the second order terms involving ^1H - ^{13}C hetero-nuclear dipolar couplings can be minimized by employing high carbon rf-fields and fast or ultra-fast spinning speeds. This regime, which reduces sample heating, will be the one analyzed in the following.

In the absence of ^1H decoupling, there are only three parameters to optimize with the fp-RFDR scheme: the carrier frequency, the rf-field amplitude and the length of the recoupling period, τ_{mix} . For broadband fp-RFDR, the carrier frequency should be placed in the middle of the spectrum and the rf-field must be close to the highest nutation frequency compatible with the probe specification (see section 3.2). Therefore, only the recoupling time, τ_{mix} , must be optimized experimentally.

The robustness of fp-RFDR to interferences of hetero-nuclear dipolar coupling, and chemical shielding can be improved by using a super-cycle. The XY-8 phase cycle (Fig.1c)^[50,62] corresponds to the symmetry $[\text{R}4_4^{-1}\text{R}4_4^1]_{45}$ (a 45° phase shift of $[\text{R}4_4^{-1}\text{R}4_4^1]$) and belongs to the class of phase inversion super-cycles.^[63,68,69] This phase cycle suppresses the second order cross-terms proportional to zero-quantum spin operators (i.e. the cross terms between interactions with spin components μ_1 and μ_2 , such as $\mu_1 + \mu_2 = 0$),^[68,69] which are primarily responsible for the depolarization in zero-quantum homo-nuclear dipolar recoupling, such as fp-RFDR.^[52] The additional second-order terms can be suppressed by combining this phase inversion cycle with the M-quantum super-cycle, M^χ , i.e. by repeating $[\text{R}4_4^{-1}\text{R}4_4^1]_{45}$ M times with an overall phase shift of $360p\chi/M$ for p th elements of the series. For instance, the XY-16 phase cycle (Fig.1d)^[62,70] corresponds to a nested super-cycle formed by combining a phase inversion super-cycle

and a 2^1 global super-cycle: $\{[R4_4^{-1}R4_4^1]_{45}\}2^1 = [R4_4^{-1}R4_4^1]_{45}[R4_4^{-1}R4_4^1]_{225}$.^[63,68,69] It has been shown that nested 3^1 super-cycle improves the robustness of zero-quantum homo-nuclear dipolar recoupling, which differs from fp-RFDR.^[68] The improved robustness resulted from the suppression of second-order cross-terms, proportional to single- and double-quantum operators.^[68,69] In this article, we introduce a nested 4^1 global super-cycle for fp-RFDR, which corresponds to the symmetry $\{[R4_4^{-1}R4_4^1]_{45}\}4^1 = [R4_4^{-1}R4_4^1]_{45}[R4_4^{-1}R4_4^1]_{135}[R4_4^{-1}R4_4^1]_{225}[R4_4^{-1}R4_4^1]_{315}$ (denoted fp-RFDR-(XY8) 4^1 in the following). It must be noted that this super-cycling is easy to implement at fast or ultra-fast MAS, where the rotor period becomes short enough with respect to the mixing time. Indeed, the 32 rotor periods required for the basic cycle only last 960 μs at $\nu_R = 33$ kHz, and 480 μs at $\nu_R = 66$ kHz, which is much less than the required mixing time, even for a one-bond ^{13}C - ^{13}C coupling, which requires at least $\tau_{\text{mix}} \geq 2$ ms.

Here, the fp-RFDR-(XY8) 4^1 is implemented into the usual single-quantum single-quantum (1Q-1Q) *D*-HOMCOR 2D experiments using zero-quantum homo-nuclear dipolar recoupling. The pulse scheme used for 1Q-1Q ^{13}C - ^{13}C *D*-HOMCOR experiment is shown in Fig.1a. First, the ^{13}C transverse magnetization is created by cross-polarization (CP) from ^1H nuclei in order to increase the sensitivity. The ^{13}C isotropic chemical shifts are then encoded by allowing the 1Q coherences to evolve during the indirect evolution period, t_1 . At the end of the t_1 period, the 1Q coherences are converted into longitudinal ^{13}C magnetization using 90° pulses. During τ_{mix} , the fp-RFDR sequence promotes the exchange of longitudinal magnetizations between the ^{13}C nuclei, which are coupled by dipolar interactions. At the end of τ_{mix} , the longitudinal ^{13}C magnetization is converted back into 1Q coherences, which are detected during the t_2 period. ^1H hetero-nuclear decoupling is applied during the t_1 and t_2 periods, but not during τ_{mix} when using fast or ultra-fast MAS.

For the ^{31}P - ^{31}P *D*-HOMCOR experiments, owing to the absence of protons in the sample, the CP step is replaced by a single 90° pulse on the ^{31}P channel and no ^1H hetero-nuclear decoupling is applied during the t_1 and t_2 periods.

It must be mentioned that the fp-RFDR recoupling can also be employed in 2Q-1Q *D*-HOMCOR experiments by bracketing it with a pair of 90° pulses,^[71,72] but such implementation was not tested in this work for fp-RFDR-(XY8) 4^1 .

2.2 Numerical simulations

The simulations were performed using SPINEVOLUTION software.^[73] The powder averaging was accomplished using 1680 orientations (168 $\{\alpha_{MR}, \beta_{MR}\}$ -pairs*10 γ_{MR} -angles). The 168 $\{\alpha_{MR}, \beta_{MR}\}$ -pairs, which relate the molecular and rotor frames, were selected according to the REPULSION algorithm.^[74] The magnetic field was $B_0 = 18.8$ T, the spinning speed $\nu_R = 64$ kHz, and the rf-field of fp-RFDR π -pulses, had either a changing value (Fig.3,S2) or a fixed value of $\nu_{1\pi} = 160$ (Fig.2,4-6,S1) then leading to a filling factor of $f = 0.2$.

Simulations were first performed for a simple $^{13}\text{C}1$ - $^{13}\text{C}2$ spin-system with a short one-bond inter-nuclear vector of $d_{\text{C}1\text{-C}2} = 156$ pm ($|b_{\text{C}1\text{-C}2}|/2\pi = 2$ kHz), and then extended to a more realistic $^{13}\text{C}1$ - $^{13}\text{C}2$ - $^{13}\text{C}3$ spin-system with two short and one long distances of $d_{\text{C}1\text{-C}2} = d_{\text{C}2\text{-C}3} = 156$ pm and $d_{\text{C}1\text{-C}3} = 312$ pm ($|b_{\text{C}1\text{-C}2}|/2\pi = |b_{\text{C}2\text{-C}3}|/2\pi = 2$ kHz and $|b_{\text{C}1\text{-C}3}|/2\pi = 250$ Hz). The anisotropic chemical de-shielding constants, δ_{aniso} , were either equal to zero (Figs.2-4,S2), 21 ppm (Fig.6), 120 ppm (Fig.S1), or a variable parameter (Fig.5).

Figs.2-6,S1 (resp 4,S2) plot the build-up of the transfer efficiency from C1 to C2 (C1 \rightarrow C2) (resp C1 \rightarrow C3) as function of the mixing time. For each τ_{mix} value, this efficiency is defined as the amplitude of the cross-peak transferred from C1 to C2 divided by the amplitude of the diagonal peak of C1 for $\tau_{\text{mix}} = 0$. The C1 \rightarrow C2 efficiency is calculated with the sequence described in Fig.1a without the proton and CP parts. One first creates a $I_{x\text{-C}1}$ magnetization and one detects the $I_{x\text{-C}2}$ magnetization for $t_1 = t_2 = 0$. This magnetization corresponds to the cross-peak intensity, $A_{\text{C}1\rightarrow\text{C}2}(\tau_{\text{mix}})$, with C1 frequency along F1 and C2 frequency along F2. The efficiency is normalized to the amplitude of the diagonal peak, $A_{\text{C}1\rightarrow\text{C}1}(\tau_{\text{mix}} = 0)$, which is calculated starting from $I_{x\text{-C}1}$ magnetization and detecting $I_{x\text{-C}1}$ magnetization after $t_1 = t_2 = \tau_{\text{mix}} = 0$. The efficiency is then equal to the $A_{\text{C}1\rightarrow\text{C}2}(\tau_{\text{mix}})/A_{\text{C}1\rightarrow\text{C}1}(\tau_{\text{mix}} = 0)$ ratio.

In Figs.S1,S2 and 2-6, the difference in isotropic chemical shifts between the two analyzed carbons was varied from $\Delta\nu_{\text{iso}} = 0$ to 50 kHz, and the carrier frequency was always placed in the middle of the two resonances.

To test the effect of ^1H - ^1H dipolar interactions, similar simulations were performed for the aliphatic sites of L-histidine.HCl, $\text{C1}^\alpha\text{H}^\alpha\text{-C2}^\beta\text{H}_2^\beta\text{-H}_2^\gamma$ (Fig.6). All protons had identical isotropic chemical shifts, without CSA, and on-resonance irradiation was applied to the ^1H channel.

2.2.1 Two spin-system

In Fig.2, the build-up curves are represented for the rf-field of $\nu_{1\pi} = 160$ kHz ($f = 0.2$) and a C1-C2 spin-system of two carbon atoms separated with a short one-bond distance of 156 pm, but not submitted to any CSA. It is clear that the $(\text{XY8})_4^1$ super-cycle achieves the best transfer efficiency for large $\Delta\nu_{\text{iso}}$ and τ_{mix} values. In particular, transfer efficiencies of ca. 0.5 are obtained even for large frequency differences, such as $\Delta\nu_{\text{iso}} = 50$ kHz, which exceed those observed at the highest present magnetic field of 23.5 T. In contrast, there is a drop in transfer efficiency for XY8 and XY16 super-cycles for large frequency differences (e.g. $\Delta\nu_{\text{iso}} = 50$ kHz) and for long mixing times required to observe two or three bond carbon-carbon cross-peaks ($\tau_{\text{mix}} > 5$ ms).

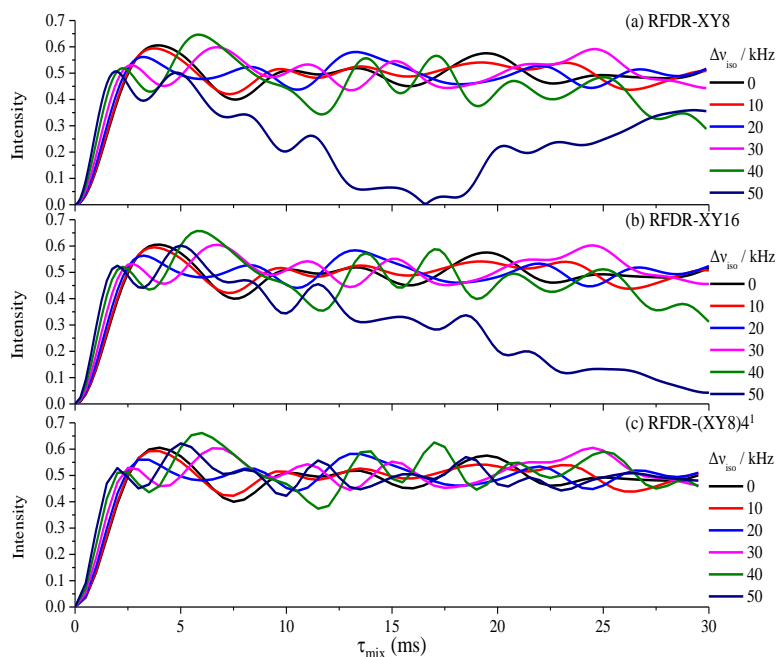


Fig.2. Transfer efficiency for a C1-C2 spin-system versus τ_{mix} for six frequency differences: $\Delta\nu_{\text{iso}} = 0, 10, 20, 30, 40, 50$ kHz. The labels of $\Delta\nu_{\text{iso}}$ values are indicated on the right-hand side of the figures. $\delta_{\text{aniso}}(\text{C1}, \text{C2}) = 0$, $\nu_{\text{R}} = 64$ kHz, $B_0 = 18.8$ T, $\nu_{1\pi} = 160$ kHz, $\tau_{\text{p}} = 3.125$ μs , $f = 0.2$, (a) fp-RFDR-XY8, (b) fp-RFDR-XY16, and (c) fp-RFDR-(XY8) $_4^1$.

However, isolated two-spin systems are rarely encountered in solids, especially in bio-molecules, except when the sample is selectively labeled, and to obtain more detailed insight, we have then introduced larger spin-systems in the simulations.

2.2.2 Three spin-system: choice of rf-field

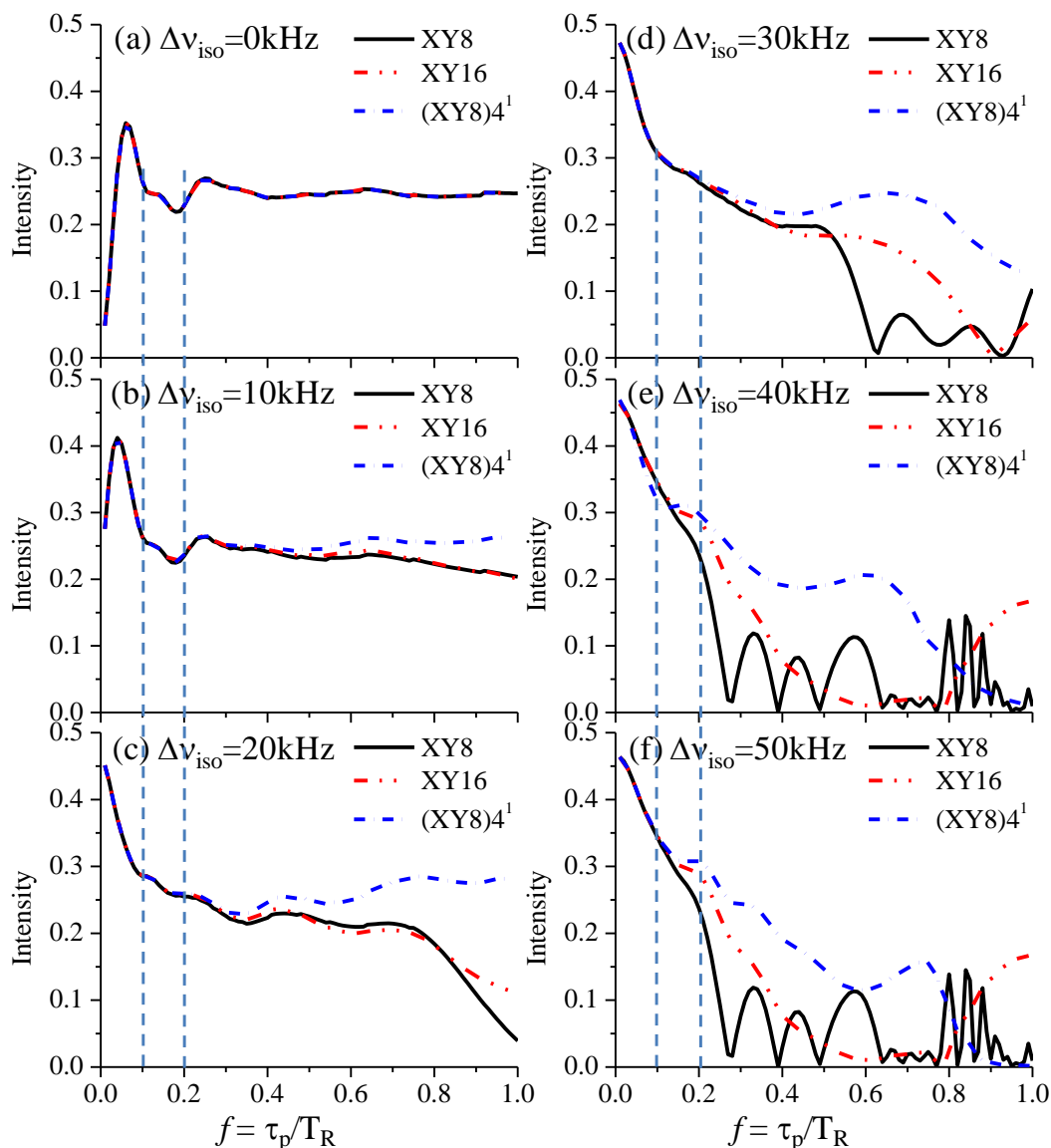


Fig.3. C1 \rightarrow C2 transfer efficiency for the C1-C2-C3 spin-system, versus pulse fraction f , with six frequency differences: $\Delta\nu_{\text{iso}} = 0$ (a), 10 (b) 20 (c), 30 (d) 40 (e), and 50 (f) kHz. $\delta_{\text{aniso}}(\text{C1,C2,C3}) = 0$, $\nu_{\text{R}} = 64$ kHz, $B_0 = 18.8$ T, $\tau_{\text{mix}} = 8$ ms. The vertical lines define: either $\nu_{1\pi} = 320$ kHz ($f = 0.1$), or $f = 2$ for comparison with Fig.2.

Before starting the experiment, it is important to choose first the rf-field, and hence the pulse fraction. The effects of this f parameter are demonstrated in Fig.3, for six

chemical shift differences, on the short $C1 \rightarrow C2$ one-bond transfer in the three spin-system not submitted to any CSA, for the mixing time of $\tau_{\text{mix}} = 8$ ms.

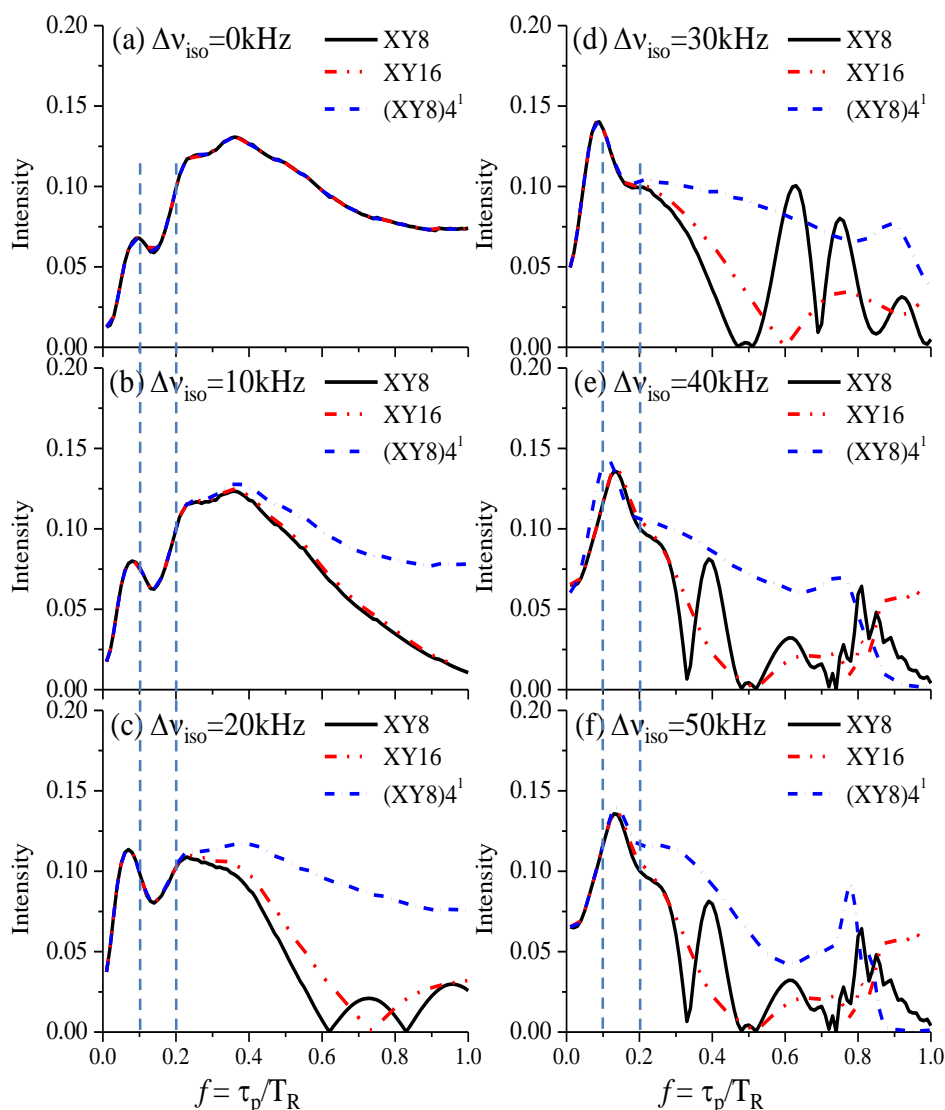


Fig.S2. Plot of the $C1 \rightarrow C3$ transfer efficiency for the $C1$ - $C2$ - $C3$ spin-system, versus pulse fraction f , with six frequency differences: $\Delta v_{\text{iso}} = 0$ (a), 10 (b), 20 (c), 30 (d), 40 (e), 50 (f) kHz. $\delta_{\text{aniso}}(C1,C2,C3) = 0$, $\nu_R = 64$ kHz, $B_0 = 18.8$ T, $\tau_{\text{mix}} = 8$ ms.

It should be pointed out that in this figure, the rf-field varies with the pulse fraction according to $\nu_{1\pi} = \nu_R/2f$. It must be first noted that, for the same inter-nuclear distance of 156 pm and same mixing time of $\tau_{\text{mix}} = 8$ ms, the $C1 \rightarrow C2$ transfer efficiency for $f = 0.2$ of this three spin-system (ca. 0.25) is twice smaller than that observed for an isolated two spin-system (ca. 0.5) (Fig.2). This is due to the fact the $C1$ magnetization has been transferred to $C2$ first *and* then $C3$, through a relayed transfer with $C2$.^[25,45,52,57] Indeed,

the mixing time of 8 ms is ca. four times larger than that required for a one-bond $C1 \rightarrow C2$ or $C2 \rightarrow C3$ transfer. The $\tau_{\text{mix}} = 8$ ms was chosen due to the fact that at this mixing time, the transfer efficiency for two-bond transfer $C1 \rightarrow C3$ for different Δv_{iso} values also reaches a plateau (Fig. S3b). A direct $C1 \rightarrow C3$ transfer should have required a longer mixing time of $\tau_{\text{mix}} \approx 15$ -30 ms (Fig. S3a), due the small involved dipolar interaction of $|b_{C1-C3}|/2\pi = 250$ Hz. Thus our simulation results confirm the “relayed” transfer mechanism.

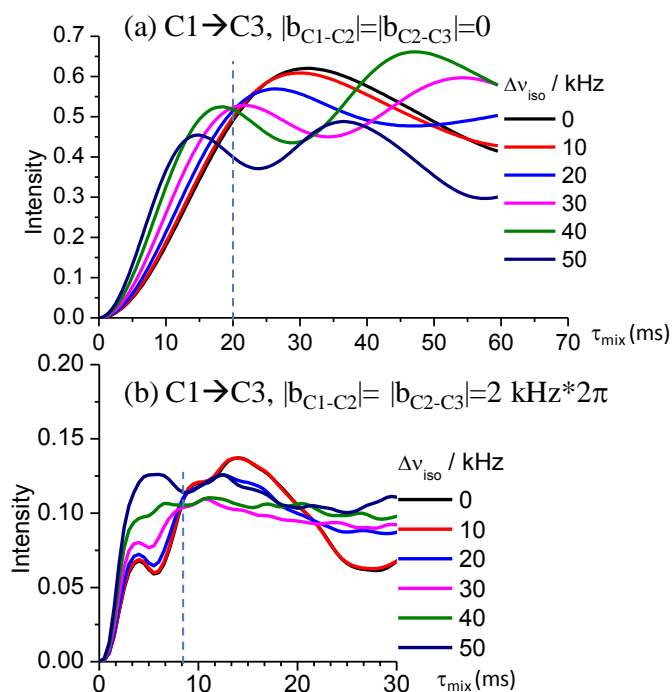


Fig.S3. Plot of the $C1 \rightarrow C3$ transfer efficiency with fp-RFDR-(XY8) 4 for the C1-C2-C3 spin-system with two conditions (a) $|b_{C1-C2}|/2\pi = |b_{C2-C3}|/2\pi = 0$ kHz (b) $|b_{C1-C2}|/2\pi = |b_{C2-C3}|/2\pi = 2$ kHz versus τ_{mix} . δ_{aniso} (C1,C2,C3) = 0, $\nu_R = 64$ kHz, $B_0 = 18.8$ T.

For identical on-resonance chemical shifts, $\Delta v_{\text{iso}} = 0$, the three phase cyclings lead to identical efficiencies. It must be noted that this common efficiency tends to zero for ideal π -pulses ($f \approx 0$), as this regime corresponds to the RFDR sequence.^[50,66] This is not the case for real pulse lengths and/or for nonidentical on-resonance chemical shifts. As a general rule, the efficiency increases with decreasing f factor, except for small to moderate chemical shift differences ($\Delta v_{\text{iso}} \leq 15$ kHz) and very short pulses, $f \leq 0.05$. However, such short pulses correspond to very strong rf-fields ($\nu_{1\pi} \geq 640$ kHz) that are impossible to obtain with commercial MAS probes, and in the following we will only

consider f factors larger than 0.1, corresponding to actual rf-fields, $\nu_{1\pi} \leq 320$ kHz. For small to moderate chemical shift differences ($\Delta\nu_{\text{iso}} \leq 15\text{-}20$ kHz), the efficiency is little dependent on the f factor and thus on the rf-field. This is not the case for larger chemical shift differences, for which shortest π -pulses and thus largest possible rf-fields should be used. In any case, the (XY8)⁴ super-cycling gives the best efficiency, especially for very large chemical shift differences which are available at very large fields.

The f factor must also be optimized for two-bond transfers, which are more difficult to observe than one-bond transfers. The effects of the f parameter for the C1 \rightarrow C3 transfer of the three-spin system are shown in Fig.S2, for the same recoupling time of $\tau_{\text{mix}} = 8$ ms.

However, the f dependence on the relayed two-bond C1 \rightarrow C3 transfer is almost the same as that on the one-bond C1 \rightarrow C2 transfer, except that $f < 0.1$ does not favor the C1 \rightarrow C3 transfer. Thus our results suggest to choose the highest possible rf-field with the (XY8)⁴ super-cycling but with $f > 0.1$. For heat-sensitive proteins, (XY8)⁴ with moderate rf-fields (e.g. $\nu_{1\pi} \approx 107$ kHz, $f \approx 0.3$) may be recommended, while for other case, high rf-fields (e.g. $\nu_{1\pi} \approx 160$ kHz, $f \approx 0.2$) can be used.

As a conclusion, except in the case of heat-sensitive proteins, the rf-field should be maximized in order to observe the best S/N ratio, especially that of cross-peaks related to large frequency differences and/or long inter-nuclear distances. In addition, the (XY8)⁴ super-cycling should always be used.

2.2.3 Three spin-system: rf-inhomogeneity

Experimentally, the rf-field is not constant into the coil, which may largely decrease the experimental S/N ratio. Indeed, RFDR schemes are based on the application of π -pulses, which cannot be perfect π -pulses over the full sample when the rf-field is not constant. To quantify this drawback, we have calculated for $\tau_{\text{mix}} = 8$ ms the efficiency of the one-bond (C1 \rightarrow C2) and two-bond (C1 \rightarrow C3) transfers in the three spin-system, versus the change of the rf-field occurring into the sample with respect to the nominal value of $\nu_{1\pi, \text{nom}} = 160$ kHz (Fig.4). The π -pulse length was fixed to its nominal value of $\tau_p = 3.125$ μs ($f = 0.2$). It must be first noted that the two-bond C1 \rightarrow C3 transfer efficiency

is ca. three times smaller than that observed for the one-bond $C1 \rightarrow C2$ transfer. One also observes that the dependences of $C1 \rightarrow C3$ and $C1 \rightarrow C2$ transfer efficiencies on the rf-inhomogeneity are almost the same. Globally, one observes in Fig.4 an efficiency decrease of 20 % with an rf-field change of ca. ± 9 % for XY8, ± 18 % for XY16, and ± 35 % for $(XY8)_4^1$ (not fully shown) super-cyclings. This means that most of the time full rotor samples can be used with complete efficiency with $(XY8)_4^1$ super-cycling, whereas the sensitivity of XY16 and especially XY8 super-cyclings will be largely decreased due to rf-inhomogeneity.

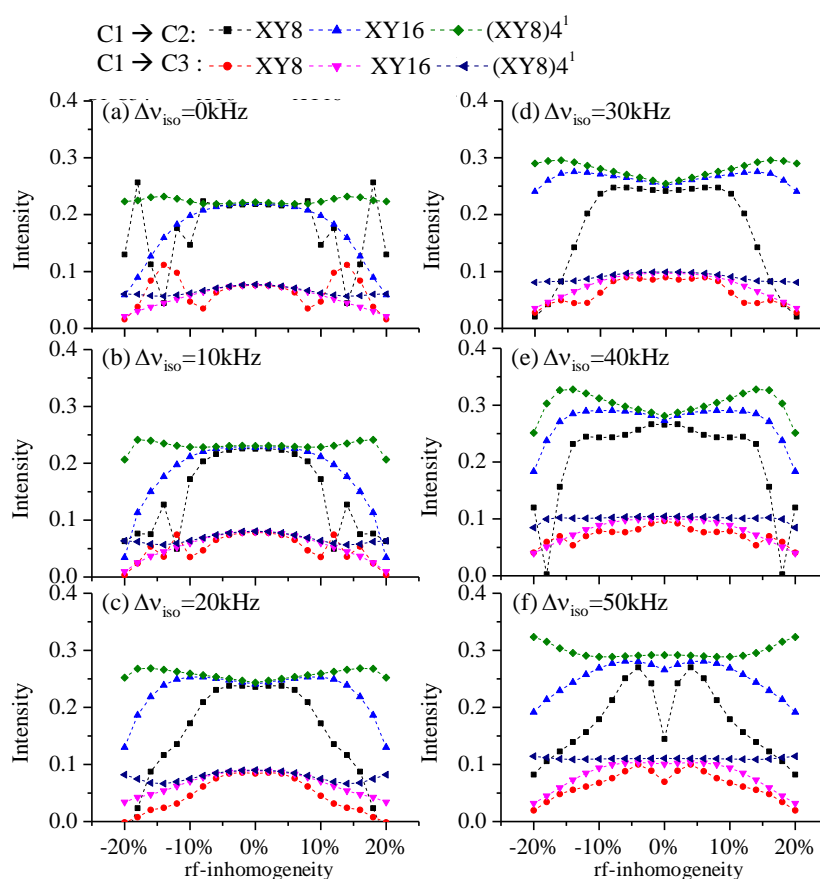


Fig.4. $C1 \rightarrow C2$ and $C1 \rightarrow C3$ transfer efficiencies for the C1-C2-C3 spin-system, versus rf-field variation with respect to the nominal value of $\nu_{1\pi, \text{nom}} = 160$ kHz ($\tau_p = 3.125$ μs , $f = 0.2$), with six frequency differences: $\Delta v_{iso} = 0$ (a), 10 (b), 20 (c), 30 (d), 40 (e), and 50 (f) kHz. $\delta_{\text{aniso}}(C1, C2, C3) = 0$, $\nu_R = 64$ kHz, $B_0 = 18.8$ T, $\tau_{\text{mix}} = 8$ ms. Phase cyclings and transfers are indicated on the top of the figures.

2.2.4 Three spin-system: CSA effect

The CSA of ^{13}C is quite large at the high magnetic fields employed for the NMR study of bio-molecules, since the CSA in Hz is proportional to the B_0 field. As example, it

can extend up to 120 ppm, which corresponds to 30 kHz at 23.5 T. We have analyzed its effects on RFDR experiments by representing in Fig.5 the one-bond C1 \rightarrow C2 transfer efficiency observed in the three spin-system with $\nu_{1\pi} = 160$ kHz ($f = 0.2$), versus the frequency difference, $\Delta\nu_{\text{iso}}$, and the CSA, δ_{aniso} . For small to moderate chemical shielding, $\Delta\nu_{\text{iso}} \leq 25$ kHz and $\delta_{\text{aniso}} \leq 15$ kHz, the three super-cyclings offer similar efficiencies. However, their robustness to larger chemical shielding, which is observed at very high magnetic fields, is not identical, and again the (XY8)⁴¹ super-cycle gives the best efficiency (Fig.5d). It must be noted that its efficiency can even slightly increase for very large frequency differences (Fig.5c).

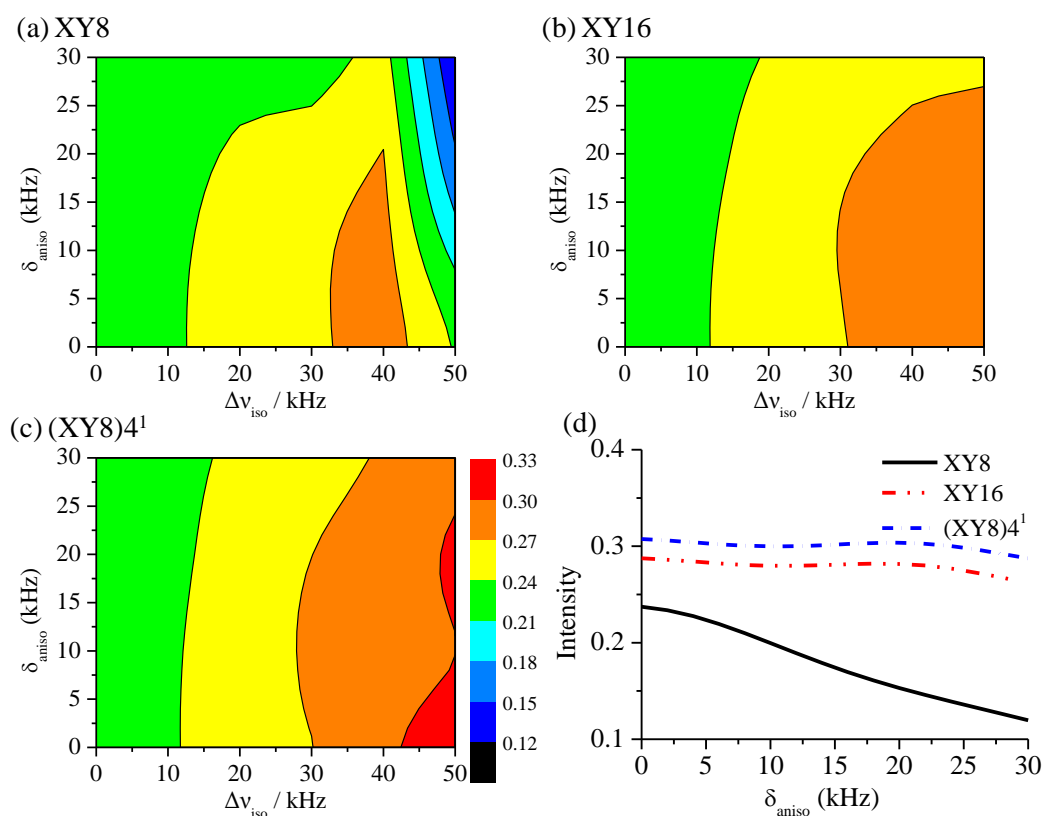


Fig.5. C1 \rightarrow C2 transfer efficiency for the C1-C2-C3 spin-system, versus frequency differences, $\Delta\nu_{\text{iso}}$, and CSA: $\delta_{\text{aniso}}(\text{C1}) = \delta_{\text{aniso}}(\text{C2}) = \delta_{\text{aniso}}(\text{C3})$ with $\eta_{\text{CSA}} = 0$, $(\alpha_{\text{CSA}}, \beta_{\text{CSA}}, \gamma_{\text{CSA}}) = (0, 60, 0)$ (C1), $(30, 90, 0)$ (C2) and $(40, 30, 120)$ (C3). $B_0 = 18.8$ T, $\nu_R = 64$ kHz, $\nu_{1\pi} = 160$ kHz ($f = 0.2$). (a) fp-RFDR-XY8, (b) fp-RFDR-XY16, and (c) fp-RFDR-(XY8)⁴¹. (d) Slices from $\Delta\nu_{\text{iso}} = 50$ kHz.

2.2.5 C1H-C2H₂-H₂ spin-system

Previous simulations have been performed for isolated ¹³C1-¹³C2 or ¹³C1-¹³C2-¹³C3 spin-systems, and ¹H-¹³C and ¹H-¹H couplings were not considered, whereas in

bio-molecules, carbon atoms are most of the time surrounded by numerous protons. The effects of ^1H - ^{13}C and ^1H - ^1H dipolar interactions were thus investigated by simulating the efficiency of magnetization transfer from C1^α to C2^β in the case of a $\text{C1}^\alpha\text{H}^\alpha\text{-C2}^\beta\text{H}_2^\beta\text{-H}_2^\gamma$ spin system. Fig.6 demonstrates again that the $(\text{XY8})_4^1$ super-cycle benefits from the highest transfer efficiency and robustness to isotropic chemical shift, compared to XY8 and XY16. Indeed, in the presence of ^1H - ^{13}C and ^1H - ^1H dipolar interactions, XY8 and XY16 transfer efficiencies decay for $\Delta\nu_{\text{iso}} \geq 40$ kHz and long τ_{mix} time, even with large carbon rf-field of $\nu_{1\pi} = 160$ kHz. Conversely, in the presence or the absence of ^1H - ^{13}C and ^1H - ^1H dipolar interactions, $(\text{XY8})_4^1$ yields stable transfer efficiencies of about 0.5 in this two carbons spin-system, even for $\Delta\nu_{\text{iso}} = 50$ kHz.

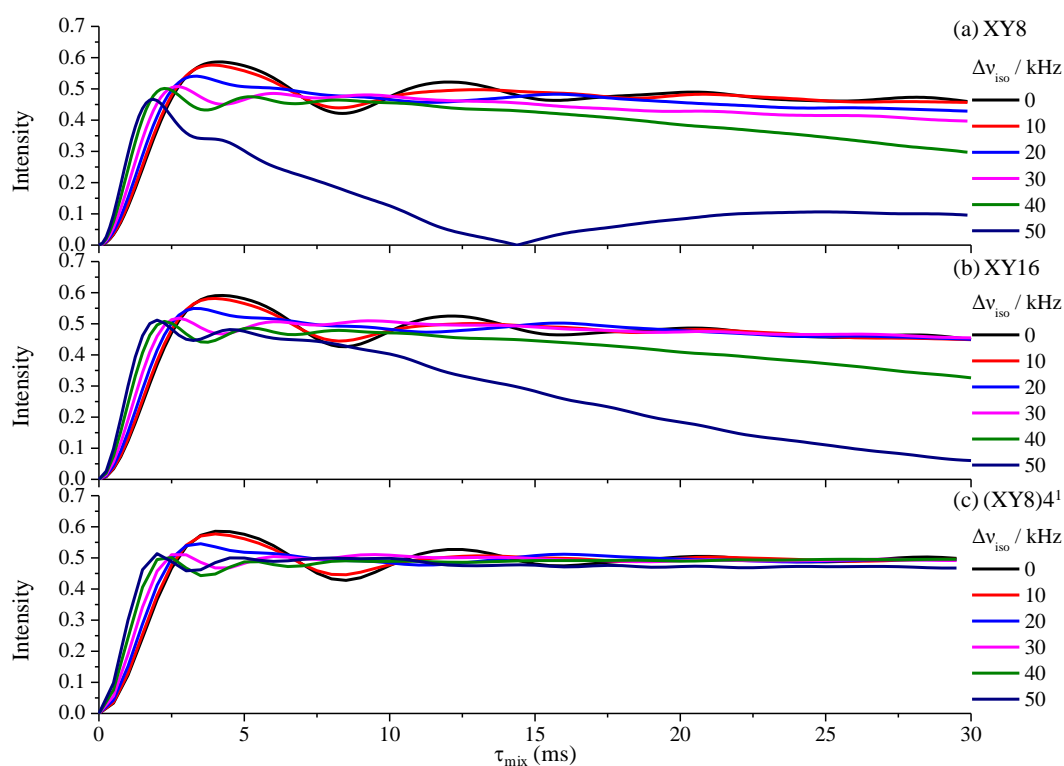


Fig.6. $\text{C1}^\alpha \rightarrow \text{C2}^\beta$ transfer efficiency for the model spin-system of L-histidine. $\text{HCl}\cdot\text{H}_2\text{O}(\text{C1}^\alpha\text{H}^\alpha\text{-C2}^\beta\text{H}_2^\beta\text{-H}_2^\gamma)$, versus τ_{mix} , for six frequency differences between the C1^α and C2^β resonances: $\Delta\nu_{\text{iso}} = 0, 10, 20, 30, 40, 50$ kHz. $\delta_{\text{aniso}}(\text{C1}^\alpha) = \delta_{\text{aniso}}(\text{C2}^\beta) = 21$ ppm, $\nu_{1\pi} = 160$ kHz ($f = 0.2$), $\nu_{\text{R}} = 64$ kHz, $B_0 = 18.8$ T, (a) fp-RFDR-XY8, (b) fp-RFDR-XY16, and (c) fp-RFDR- $(\text{XY8})_4^1$.

2.3 Experimental section

Experimental verifications were performed on a Bruker AVANCE-III 900 spectrometer with $B_0 = 21.1$ T. ^{13}C - ^{13}C 1Q-1Q *D*-HOMCOR 2D spectra using fp-RFDR

recoupling were recorded for two uniformly ^{13}C labeled samples: L-histidine·HCl·H₂O, purchased from CortecNet and used without purification, and one Val-Ala-Phe-Gly tetra-peptide uniformly labeled on Val-Ala-Phe and synthesized by Dr P. Bertani. The ^{13}C spectra of both samples display a large spread in ^{13}C isotropic chemical shift up to $\Delta\delta_{\text{iso}} \approx 160$ ppm. A Bruker double-resonance $\varnothing = 1.3$ mm MAS probe was used with $\nu_{\text{R}} = 60$ kHz. The fp-RFDR sequences used to record ^{13}C 1Q-1Q *D*-HOMCOR spectra are displayed in Fig.1, and they used ^{13}C π -pulse lengths of typically ca. $3\ \mu\text{s}$ (i.e. $\nu_{1\pi} = 167$ kHz, $f = 0.18$). The contact time for cross-polarization was 3 ms, and SPINAL-64 proton dipolar decoupling^[75] was applied during evolution and detection periods, t_1 and t_2 (see Fig.1). The 2D spectra acquired with and without ^1H decoupling during fp-RFDR recoupling time were identical, and hence spectra shown in Figs.7 and 8 were acquired *without decoupling during τ_{mix}* . Recycle delays were 3 s for all experiments.

^{31}P 1Q-1Q *D*-HOMCOR 2D spectra using fp-RFDR recoupling were acquired on $\text{Al}(\text{PO}_3)_3$ in the monoclinic form.^[76,77] The phosphorous recycle delay was long, 30 s, and thus to increase the sensitivity, we used a bigger rotor with 2.5 mm diameter, and the spinning speed was thus limited to $\nu_{\text{R}} = 31.5$ kHz. The rf field nutation frequency for fp-RFDR π -pulses was $\nu_{1\pi} = 50$ kHz. Additional experimental details are given in the figure captions.

2.4 Results and Discussion

2.4.1 ^{13}C - ^{13}C correlation

Fig.7 compares the three ^{13}C - ^{13}C 1Q-1Q *D*-HOMCOR 2D spectra of [^{13}C]-L-histidine.HCl used as test sample with fp-RFDR recoupling during $\tau_{\text{mix}} = 8$ ms and three different super-cycles: XY8, XY16 and (XY8) 4 with $f = 0.18$. Clearly, using XY8 (Fig.7a) the cross-peaks are much smaller than those observed using XY16 (Fig.7b) or (XY8) 4 (Fig.7c). The C^2 - C^α and C^2 - C' cross-peaks (surrounded by circles in Fig.7c) are hardly detectable with XY8, whereas they are observed with XY16 and (XY8) 4 . The corresponding shortest distances are inter-molecular and of 440 and 410 pm for C^2 - C^α and C^2 - C' , respectively. To more easily compare the three phase cyclings, the horizontal

slices along C^2 are shown in Fig.7e. It's clear that the intensities of C^2-C' and C^2-C^α cross-peaks with $(XY8)^4$ are ca. 1.2 times higher than that with XY16, and ca. 3 times higher than that of XY8. The same enhancement factors are observed for C^2-C^4 , C^2-C^5 , and C^2-C^β cross-peaks. The long-range inter-molecule correlations observed for L-histidine.HCl using fp-RFDR may involve relayed transfers.^[25,45,52,57]

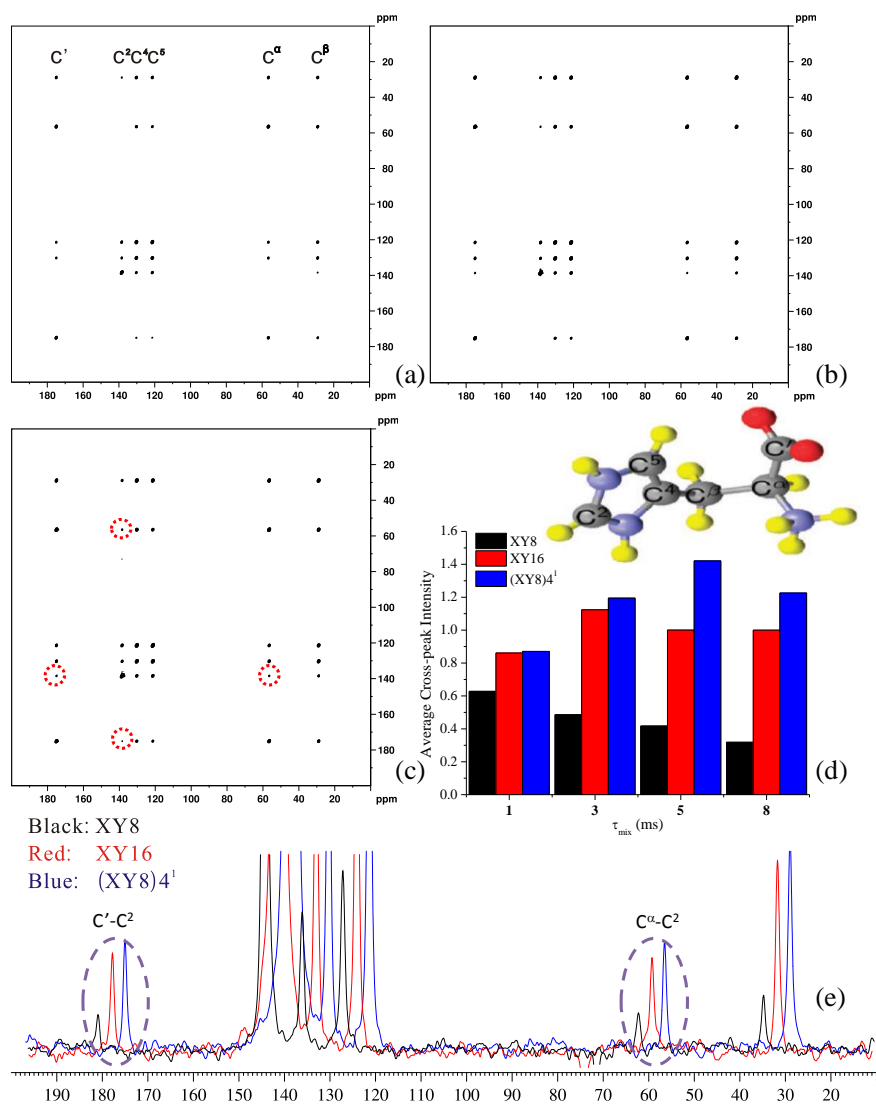


Fig.7. Experimental ^{13}C - ^{13}C 1Q-1Q D-HOMCOR 2D spectra of L-histidine.HCl using fp-RFDR at $B_0 = 21.1$ T with $\nu_R = 60$ kHz and $\nu_{1\pi} = 167$ kHz ($f = 0.18$). 2D spectra have been recorded at $\tau_{\text{mix}} = 8$ ms with super-cycling: (a) XY8, (b) XY16, and (c) $(XY8)^4$. Two cross-peaks, hardly-observable in (a) are circled in (c) for $(XY8)^4$. (d) Comparison of the averaged one-bond efficiencies, observed for $\tau_{\text{mix}} = 1, 3, 5, 8$ ms. The maximum variation for individual peaks are in the range of ± 0.1 . (e) Horizontal slices taken through C^2 atom at 138 ppm. The 2D spectra result from averaging 16 transients for each of 512 increments. The recycle delay was 3 s.

To compare more precisely the experimental results with the simulations, we plotted

in Fig.7d the evolution of the averaged intensity of the one-bond cross-peaks ($C'-C^\alpha$, $C^\alpha-C^\beta$, $C^\beta-C^4$, C^4-C^5) versus τ_{mix} recoupling time. Experimental averaged intensities are consistent with those of simulations concerning one-bond correlations shown in Fig.2-6 and S1. Indeed, they show a decrease of XY8 signal intensities after the first maximum at about $\tau_{\text{mix}} \approx 2$ ms. They also show that at $\tau_{\text{mix}} = 5$ ms, (XY8) 4^1 yields about 30% higher correlation intensities than XY16, and roughly 3-fold higher intensities than XY8. At longer mixing times, e.g. $\tau_{\text{mix}} = 8$ ms, the signal slightly decreases for the three sequences, due to losses from imperfect hetero-nuclear decoupling and spin-spin relaxation-time (T_2') decay. However, in spite of the lack of ^1H decoupling during the mixing time, these losses are not very important owing to high ν_R and $\nu_{1\pi}$ frequencies. More generally, one observes that (XY8) 4^1 phase cycling achieves relatively large improvement with a long-mixing time, and small improvement with a short mixing time for one or two-bond correlations. In addition to (XY8) 4^1 , other long super-cycles were tested for fp-RFDR, including two versions of XY32 and one of XY64.^[78] However, these phase cycles exhibit slightly lower performances than fp-RFDR-XY16 (results not shown).

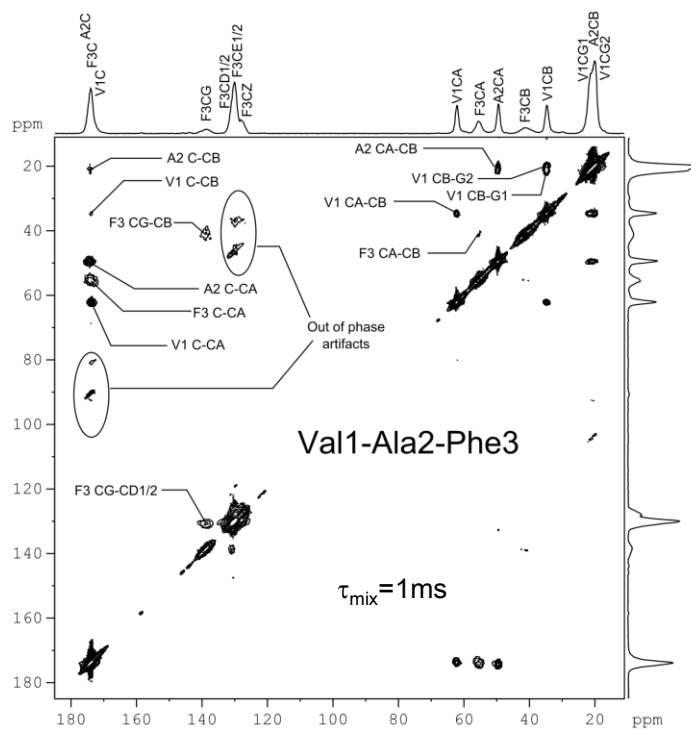


Fig.S4. ^{13}C SQ-SQ fp-RFDR (XY8) 4^1 spectrum of Val-Ala-Phe ^{13}C -enriched tetra-peptide recorded in 1.5h, with 16 transients on a 1.3 mm probe spinning at $\nu_R = 60$ kHz. $B_0 = 21.1$ T, recycle delay 3 s, $\tau_{\text{mix}} = 1$ ms, $\nu_{1\pi} = 167$ kHz, $\tau_p = 3$ μs , $f = 0.18$. CP for ^{13}C excitation: contact time 1.5 ms, $\nu_{1\text{H}} = 100$ kHz with ramp

90%. ^1H decoupling during t_1 and t_2 with only 15 kHz. F1 spectral width is 40 kHz with 160 hyper-complex points using States-TPPI.

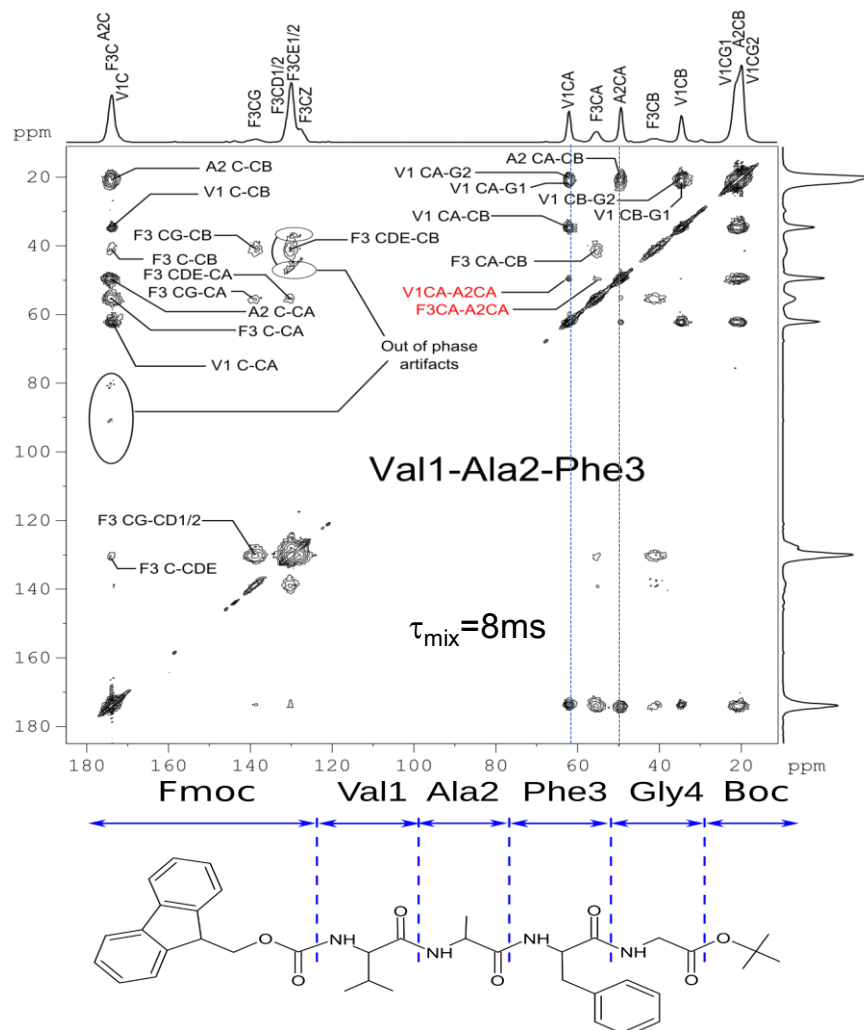


Fig.S5. Bottom: Fmoc-[U- ^{13}C , ^{15}N]-Val-[U- ^{13}C , ^{15}N]-Ala-[U- ^{13}C , ^{15}N]-Phe-Gly-*t*-Boc tetra-peptide molecule. Top: its ^{13}C SQ-SQ fp-RFDR (XY8) 4 spectrum on Val1-Ala2-Phe3 ^{13}C -enriched, recorded in 1.5h, with 16 transients on a 1.3 mm probe spinning at $\nu_R = 60$ kHz. $B_0 = 21.1$ T, recycle delay 3 s, $\tau_{\text{mix}} = 8$ ms, $\nu_{1\pi} = 167$ kHz, $\tau_p = 3$ μs , $f = 0.18$. CP for ^{13}C excitation: contact time 1.5 ms, $\nu_{\text{IH}} = 100$ kHz with ramp 90%. ^1H decoupling during t_1 and t_2 with only 15 kHz. F1 spectral width is 40 kHz with 160 hyper-complex points using States-TPPI. The assignment follows the MRDB convention. The two vertical lines at 50 and 62 ppm, correspond to Fig.8e and c, respectively.

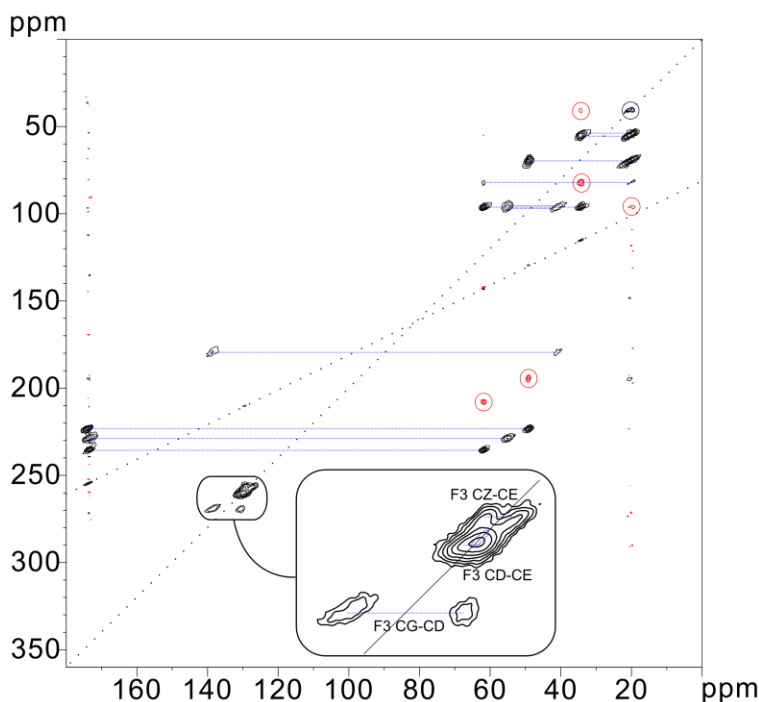


Fig.S6. ^{13}C - ^{13}C DQ-SQ $\text{BR}2^{1/2}$ spectrum of Val-Ala-Phe ^{13}C -enriched tetra-peptide recorded in 9h, with 32 transients on a 1.3 mm probe spinning at $\nu_R = 60$ Hz. $B_0 = 21.1$ T, recycle delay 3 s, $\tau = 544$ μs , with an rf-field of 30 kHz. CP for ^{13}C excitation: contact time 1.5 ms, $\nu_{1\text{H}} = 100$ kHz with ramp 90%. ^1H decoupling during t_1 and t_2 with only 15 kHz. F1 spectral width is rotor synchronized with 512 hyper-complex points using States-TPPI.

To further demonstrate the advantage of $(\text{XY}8)^4$, the three super-cycles were tested to observe the ^{13}C - ^{13}C through-space proximities in Val-Ala-Phe-Gly tetra-peptide uniformly labeled on Val-Ala-Phe. The three corresponding 2D spectra at $\tau_{\text{mix}} = 8$ ms are shown in Fig.8a-c, whereas the horizontal slices taken at 50 (A2CA, Fig.8e) and 62 (V1CA, Fig.8d) ppm show that the transfer efficiency of fp-RFDR- $(\text{XY}8)^4$ is roughly 20 % larger than that of fp-RFDR-XY16, and again much more efficient than XY8. Super-cyclings XY16 and especially $(\text{XY}8)^4$ allow the observation of very small cross-peaks related to inter-residue correlations, such as A2CA-V1CA and A2CA-F3CA (Fig.8e), which are very difficult to detect with XY8 cycling. These observations are consistent with previous results with L-histidine. fp-RFDR spectra with $\tau_{\text{mix}} = 1$ was also recorded and are shown in Fig.S4. Although the resolution remains poor, especially for the Phe residue, these spectra allowed the assignment of most peaks (Fig.S5). The backbone sequence can be followed at 8 ms, where the C^α - C^α inter-residue cross-peaks V1CA-A2CA and F3CA-A2CA corresponding to CA-CO-N-CA remote correlations are observed (Fig.8e), with inter-nuclear distances of ca. 380 pm. Inter-residue correlations

CO-N-CA are not observed separately, since they overlap with CA-CO intra-residue correlation. Indeed, the three CO peaks are not properly resolved. It should be noted that the aromatic region of Phe is particularly crowded and close to the uninformative diagonal. In order to fully assign this region, a DQ-SQ ^{13}C correlation using BR2₂¹ was performed (Fig.S6).^[25,53,54] It is to be noted that DQ-SQ and SQ-SQ experiments perfectly complement each other. DQ-SQ spectra only show one-bond cross-peaks, and these can have very close or even same resonance frequencies; therefore, these spectra are very simple to analyze. In a second step, SQ-SQ spectra show cross-peaks corresponding to one, two and even three bonds. However, analyzes of their cross-peaks close to the diagonal is difficult to perform. When analyzing long-range distances for protein folding, second-order SQ-SQ methods should then be used.^[26-28,34-36] It must be reminded that in the solid-state, the experiment time of all HOMCOR 2D spectra can be largely decreased and the resolution enhanced, by using covariance acquisition and data treatment,^[79,80] even for DQ-SQ methods.^[81]

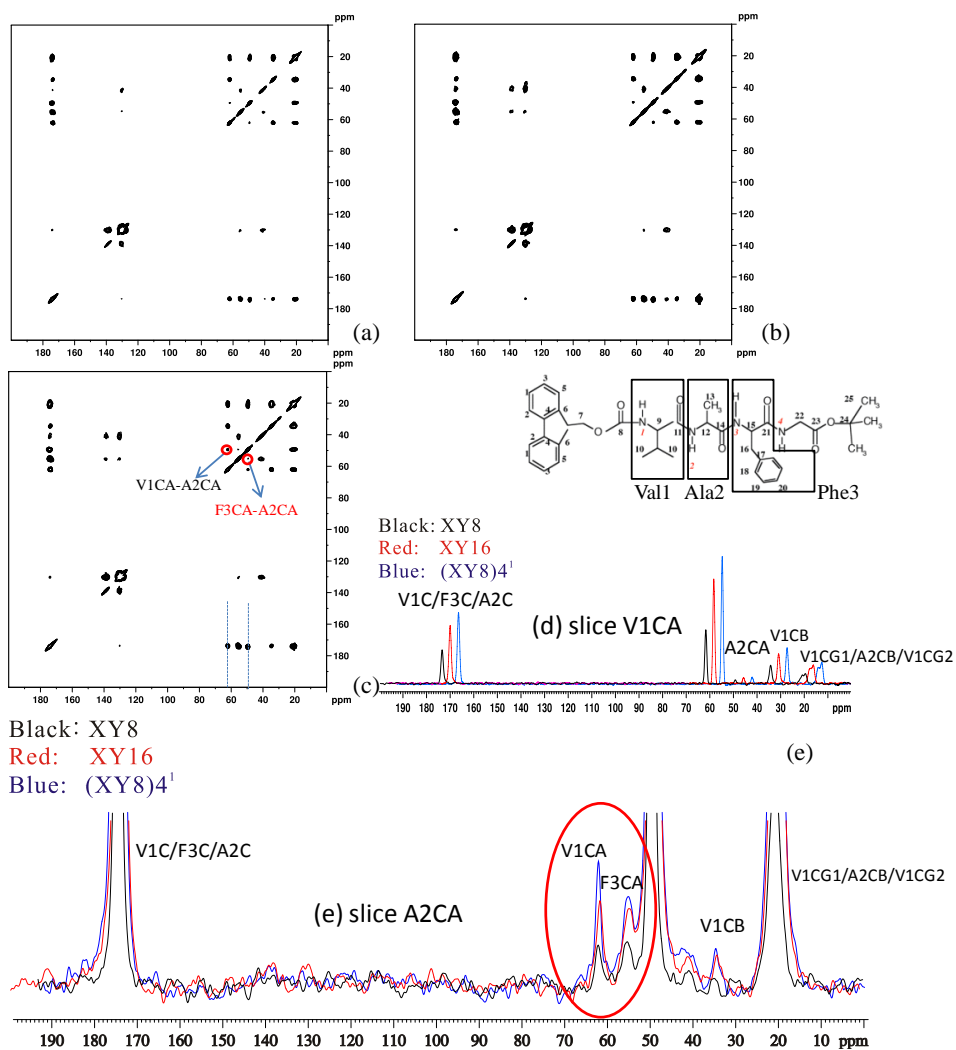


Fig.8. Experimental ^{13}C - ^{13}C 1Q-1Q fp-RFDR spectra of Val-Ala-Phe-Gly tetra-peptide ($[\text{U-}^{13}\text{C}]$ on Val-Ala-Phe), with $B_0 = 21.1$ T, $\nu_R = 60$ kHz, $\nu_{1\pi} = 167$ kHz ($f = 0.18$) and $\tau_{\text{mix}} = 8$ ms. Super-cycling: (a) XY8, (b) XY16, (c) $(\text{XY8})_4^1$. F3CA-A2CA cross-peaks, hardly observable in (a) are circled in (c). (d,e) Horizontal slices taken at 62 and 50 ppm, corresponding to V1CA and A2CA resonances, respectively. The two inter-residue V1CA-A2CA (62 ppm) and F3CA-A2CA (55 ppm) cross-peaks are surrounded in (e). The 2D spectra result from averaging 16 transients for each of 320 increments. The recycle delay was 3 s. No ^1H decoupling was applied during τ_{mix} , whereas SPINAL-64 decoupling was applied during t_1 and t_2 with 13 kHz rf. For colors, reader is referred to the electronic version of the paper. In (e), the surrounded peaks correspond to inter-residues in between C^α

2.4.2 ^{31}P - ^{31}P correlations

To demonstrate the tolerance of fp-RFDR- $(\text{XY8})_4^1$ to very large CSAs, we have chosen to analyze the ^{31}P 1Q-1Q *D*-HOMCOR spectra of $\text{Al}(\text{PO}_3)_3$ in its monoclinic form.^[76,77] At $B_0 = 21.1$ T, the three phosphorous atoms are submitted to the very large CSA of ca. 80 kHz, but they present a small isotropic chemical shift spread of 2.4 kHz (6.6 ppm), and thus we have used a moderate rf-field of $\nu_{1\pi} = 50$ kHz ($f = 0.315$). In this

case, at $\tau_{\text{mix}} = 10$ ms, fp-RFDR-(XY8) 4^1 (fig.9c) displays a signal ca. two times larger than fp-RFDR-XY16 (Fig.9b), and ca. three times larger than fp-RFDR-XY8 (Fig.9a).

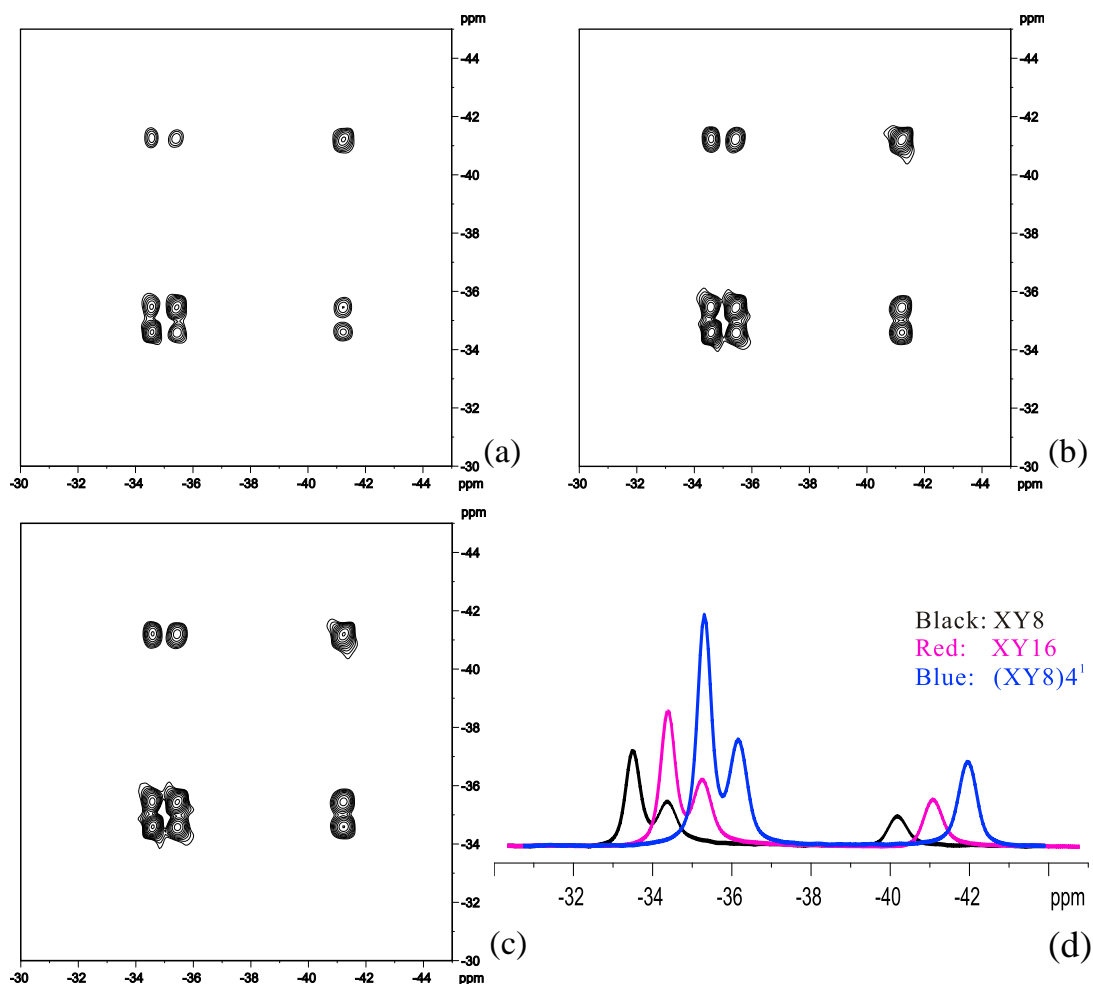


Fig.9. Experimental ^{31}P - ^{31}P 1Q-1Q *D*-HOMCOR 2D spectra of $\text{Al}(\text{PO}_3)_3$ in its monoclinic form using fp-RFDR at $B_0 = 21.1$ T with $\nu_R = 31.5$ kHz and $\nu_{1\pi} = 50$ kHz ($f = 0.315$). 2D spectra have been recorded at $\tau_{\text{mix}} = 10$ ms with super-cycle: (a) XY8, (b) XY16, and (c) (XY8) 4^1 . (d) Slices taken at -34.5 ppm. The 2D spectra result from averaging 8 transients for each of 148 increments. The recycle delay was 30 s.

2.5 Conclusions

In this chapter, we have shown that the super-cycled fp-RFDR-(XY8) 4^1 scheme leads to a zero-quantum homo-nuclear recoupling method which is efficient at very high magnetic-fields and high MAS frequencies. This super-cycle exhibits high robustness to (i) CSAs, (ii) differences in isotropic chemical shifts, (iii) rf-inhomogeneity and (iv) ^1H - ^{13}C and ^1H - ^1H dipolar interactions, thus avoiding any ^1H decoupling during the mixing time. The performances of fp-RFDR-XY8, fp-RFDR-XY16 and

fp-RFDR-(XY8)⁴ have been compared using simulations and experiments with very large offsets and/or CSAs. In all cases, fp-RFDR-(XY8)⁴ is superior to the two other types of sequences, especially in case of very large CSAs and long recoupling times. Its performances should allow its use for ¹³C 1Q-1Q *D*-HOMCOR at high MAS frequencies and magnetic fields up to at least 28 T. At magnetic fields larger than 28 T, composite π -pulses might be useful.^[82] Owing to its high transfer efficiency and high robustness for long recoupling times, fp-RFDR-(XY8)⁴ has been proven to be useful for the enhancement of ¹³C-¹³C long-range inter-residue correlations in uniformly labeled samples. fp-RFDR-(XY8)⁴ may be used for the observation of ¹⁵N-¹⁵N proximities or long-range contacts in isotopically diluted spin system, such as perdeuterated proteins^[7-11] or specifically ¹³C-labeled biomolecules.^[52,58,59] Such investigations are currently in progress in our laboratory.

References:

- [1] F. Castellani, B.V. Rossum, A. Diehl, M. Schubert, K. Rehbein, H. Oschkinat, Structure of a protein determined by solid-state magic-angle-spinning NMR spectroscopy, *Nature*, 420 (2002) 98-102.
- [2] A. Lange, S. Becker, K. Seidel, K. Giller, O. Pongs, M. Baldus, A concept for rapid protein-structure determination by solid-state NMR spectroscopy, *Angew. Chem., Int. Ed.*, 44 (2005) 2089-2092.
- [3] C. Wasmer, A. Lange, H.V. Melckebeke, A.B. Siemer, R. Riek, B.H. Meier, Amyloid fibrils of the HET-s (218-289) Prion form a β solenoid with a triangular hydrophobic core, *Science*, 319 (2008) 1523-1526.
- [4] A. Lange, K. Giller, S. Hornig, M.F. Martin-Eauclaire, O. Pongs, M.S. Becker, M. Baldus, Toxin-induced conformational changes in a potassium channel revealed by solid-state NMR, *Nature*, 440 (2006) 959-962.
- [5] C. Wasmer, A. Lange, H.V. Melckebeke, A.B. Siemer, R. Riek, B.H. Meier, Amyloid fibrils of the HET-s (218-289) Prion form a β solenoid with a triangular hydrophobic core, *Science*, 319 (2008) 1523-1526.
- [6] R. Tycko, Solid-state NMR studies of amyloid fibril structure, *Annu. Rep. Phys. Chem.*, 62 (2011) 279-299.
- [7] A. Lange, K. Giller, S. Hornig, M.F. Martin-Eauclaire, O. Pongs, M.S. Becker, M. Baldus,

Toxin-induced conformational changes in a potassium channel revealed by solid-state NMR, *Nature*, 440 (2006) 959-962.

[8] M. Hong, Y. Zhang, F. Hu, Membrane protein structure and dynamics from NMR spectroscopy, *Annu. Rev. Phys. Chem.*, 63 (2012) 1-24.

[9] Y. Ishii, N.P. Wickramasinghe, S. Chimon, A new approach in 1D and 2D ^{13}C high-resolution solid-state NMR spectroscopy of paramagnetic organometallic complexes by very fast magic-angle spinning, *J. Am. Chem. Soc.*, 125 (2003) 3438-3439.

[10] I. Bertini, L. Emsley, M. Lelli, C. Luchinat, J. Mao, G. Pintacuda, Ultra-fast MAS solid-state NMR permits extensive ^{13}C and ^1H detection in paramagnetic metallo-proteins, *J. Am. Chem. Soc.*, 132 (2010) 5558-5559.

[11] D.H. Zhou, J.J. Shea, A.J. Nieuwkoop, W.T. Franks, B.J. Wylie, C. Mullen, D. Sandoz, C.M. Rienstra, *Angew. Chem. Int. Ed.*, 46 (2007) 8380-8383.

[12] S. Asami, P. Schmieder, B. Reif, *J. Am. Chem. Soc.*, 132 (2010) 15133-15135.

[13] R. Linser, B. Bardiaux, V. Higman, U. Fink, B. Reif, *J. Am. Chem. Soc.*, 133 (2011) 5905-5912.

[14] M. Huber, S. Hiller, P. Schanda, M. Ernst, A. Böckmann, R. Verel, B.H. Meier, *Chem. Phys. Chem.*, 12 (2011) 915-918.

[15] M.J. Knight, A.L. Webber, A.J. Pell, P. Guerry, E. Barbet-Massin, I. Bertini, I.C. Felli, L. Gonnelli, R. Pieratelli, L. Emsley, A. Lesage, T. Hermann, G. Pintacuda, *Angew. Chem. Int. Ed.*, 50 (2011) 11697-11701.

[16] M. Ernst, A. Samoson, B.H. Meier, Low-power decoupling in fast magic-angle spinning NMR, *Chem. Phys. Lett.*, 348 (2001) 293-302.

[17] M. Ernst, A. Samoson, B.H. Meier, Low-power XiX decoupling in MAS NMR experiments, *J. Magn. Reson.*, 163 (2003) 332-339.

[18] S. Laage, J.R. Sachleben, S. Steuernagel, R. Pieratelli, G. Pintacuda, L. Emsley, Fast acquisition of multi-dimensional spectra in solid-state NMR enabled by ultra-fast MAS, *J. Magn. Reson.*, 196 (2009) 133-141.

[19] J.P. Demers, V. Chevelkov, A. Lange, *Solid-state Nucl. Magn. Reson.*, 40 (2011) 101-113.

[20] Y. Ishii, R. Tycko, Sensitivity enhancement in solid-state ^{15}N NMR by indirect detection with high-speed magic angle spinning, *J. Magn. Reson.*, 142 (2000) 199-204.

[21] M. Weingarth, J. Tröbosc, J.P. Amoureux, G. Bodenhausen, P. Tekely, *Solid-state Nucl. Magn. Reson.*, 40 (2011) 21-26.

[22] A.G. Webb, *Prog. Nucl. Magn. Reson. Spectrosc.*, 31 (1997) 1-42.

[23] D. Sakellariou, G. Le Goff, J.F. Jacquinet, *Nature*, 447 (2007) 694-698.

- [24] M. Ernst, M.A. Meier, T. Tuherm, A. Samoson, B.H. Meier, Low-power high-resolution solid-state NMR of peptides and proteins, *J. Am. Chem. Soc.*, 126 (2004) 4764-4765.
- [25] O. Lafon, J. Trebosc, B. Hu, G. de Paepe, J.P. Amoureux, Observing ^{13}C - ^{13}C connectivities at high magnetic fields and very high spinning frequencies, *Chem. Commun.*, 47 (2011) 6930-6932.
- [26] M. Weingarth, G. Bodenhausen, P. Tekely, Broadband magnetization transfer using moderate radio-frequency fields for NMR with very high static fields and spinning speeds, *Chem. Phys. Lett.*, 488 (2010) 10-16.
- [27] B. Hu, O. Lafon, J. Trebosc, Q. Chen, J.P. Amoureux, Broad-band homo-nuclear correlations assisted by ^1H irradiation for bio-molecules in very high magnetic field at fast and ultra-fast MAS frequencies, *J. Magn. Reson.*, 212 (2011) 320-329.
- [28] M. Weingarth, Y. Masuda, K. Takegoshi, G. Bodenhausen, P. Tekely, Sensitive ^{13}C - ^{13}C correlation spectra of amyloid fibrils at very high spinning frequencies and magnetic fields, *J. Biomol. NMR.*, 50 (2011) 129-136.
- [29] I. Scholz, M. Huber, T. Manolikas, B.H. Meier, M. Ernst, MIRROR recoupling and its application to spin diffusion under fast magic-angle spinning, *Chem. Phys. Lett.*, 460 (2008) 278-283.
- [30] J.R. Lewandowski, G. De Paepe, M.T. Eddy, J. Struppe, W. Maas, R.G. Griffin, Proton assisted recoupling at high spinning frequencies, *J. Phys. Chem. B* 113 (2009) 9062-9069.
- [31] N.M. Szeverenyi, M.J. Sullivan, G.E. Maciel, Observation of spin exchange by two-dimensional Fourier transform ^{13}C cross polarization-magic-angle spinning, *J. Magn. Reson.*, 47 (1982) 462-475.
- [32] A. Grommek, B.H. Meier, M. Ernst, Distance information from proton-driven spin diffusion under MAS, *Chem. Phys. Lett.*, 427 (2006) 404-409.
- [33] B.H. Meier, Polarization transfer and spin diffusion in solid state NMR, in: W.S. Warren (Ed.), *Advances in Magnetic and Optical Resonance*, vol. 18, Academic Press, New York, 1994, p. 1.
- [34] D. Marulanda, M.L. Tasayco, A. McDermott, M. Cataldi, V. Arriaran, T. Polenova, *J. Am. Chem. Soc.* 126 (2004) 16608-16620.
- [35] K. Takegoshi, S. Nakamura, T. Terao, ^{13}C - ^1H dipolar-assisted rotational resonance in magic-angle spinning NMR, *Chem. Phys. Lett.*, 344 (2001) 631-637.
- [36] K. Takegoshi, S. Nakamura, T. Terao, ^{13}C - ^1H dipolar-driven ^{13}C - ^{13}C recoupling without ^{13}C rf irradiation in nuclear magnetic resonance of rotating solids, *J. Chem. Phys.*, 118 (2003) 2325-2341.
- [37] C.R. Morcombe, V. Gaponenko, R.A. Byrd, K.W. Zilm, Diluting abundant spins by isotope

- edited radio-frequency field assisted diffusion, *J. Am. Chem. Soc.*, 126 (2004) 7196-7197.
- [38] L. Duma, D. Abergel, F. Ferrage, P. Pelupessy, P. Tekely, G. Bodenhausen, Broadband dipolar recoupling for magnetization transfer in solid-state NMR correlation spectroscopy, *Chem. Phys. Chem.*, 9 (2008) 1104-1106.
- [39] M. Weingarth, D.E. Demco, G. Bodenhausen, P. Tekely, Improved magnetization transfer in solid-state NMR with fast magic angle spinning, *Chem. Phys. Lett.*, 469 (2009) 342-348.
- [40] M. Weingarth, G. Bodenhausen, P. Tekely, Broadband carbon-13 correlation spectra of micro crystalline proteins in very high-magnetic fields, *J. Am. Chem. Soc.*, 131 (2009) 13937-13939.
- [41] A. Lange, K. Seidel, L. Verdier, S. Luca, M. Baldus *J. Am. Chem. Soc.*, 125 (2003) 12640-12648.
- [42] X. Peng, D. Libich, R. Janik, G. Harauz, V. Ladizhansky *J. Am. Chem. Soc.*, 130 (2008) 359-369.
- [43] G. de Paepe, J.R. Lewandowski, R.G. Griffin, Spin dynamics in the modulation frame: application to homo-nuclear recoupling in magic angle spinning solid state NMR, *J. Chem. Phys.*, 129 (2008) 245101.
- [44] M.J. Bayro, M. Huber, R. Ramachandran, T.C. Davenport, B.H. Meier, M. Ernst, R.G. Griffin, Dipolar truncation in magic-angle spinning NMR recoupling experiments, *J. Chem. Phys.*, 130 (2009) 114506.
- [45] G. de Paepe, *Annu. Rev. Phys. Chem.*, 63 (2012) 661-684.
- [46] G. De Paepe, J.R. Lewandowski, R.G. Griffin, Spin dynamics in the modulation frame: application to homo-nuclear recoupling in magic angle spinning solid-state NMR, *J. Chem. Phys.*, 129 (2008) 245101.
- [47] M. Hohwy, C.M. Rienste, C.P. Jaroniec, R.G. Griffin, Fivefold symmetric homonuclear dipolar recoupling in rotating solids: application to double-quantum spectroscopy, *J. Chem. Phys.*, 110 (1999) 7983-7992.
- [48] R. Schneider, K. Seidel, M. Etkorn, A. Lange, S. Becker, M. Baldus, Probing molecular motion by double-quantum (^{13}C - ^{13}C) solid-state NMR spectroscopy: application to ubiquitin, *J. Am. Chem. Soc.*, 132 (2010) 223-233.
- [49] R. Verel, M. Ernst, B.H. Meier, Adiabatic dipolar recoupling in Solid-State NMR: the DREAM scheme, *J. Magn. Reson.*, 150 (2001) 81-99.
- [50] A.E. Bennett, J.H. Ok, R.G. Griffin, S. Vega, Chemical shift correlation spectroscopy in rotating solids: radio-frequency driven dipolar recoupling and longitudinal exchange, *J. Chem. Phys.*, 96 (1992) 8624-8627.
- [51] Y. Ishii, ^{13}C - ^{13}C dipolar recoupling under very fast magic angle spinning in solid-state

nuclear magnetic resonance: applications to distance measurements, spectral assignments, and high-throughput secondary-structure determination, *J. Chem. Phys.*, 114 (2001) 8473-8483.

[52] M.J. Bayro, R. Ramachandran, M.A. Caporini, M.T. Eddy, R.G. Griffin, Radio frequency-driven recoupling at high magic-angle spinning frequencies: homo-nuclear recoupling sans hetero-nuclear decoupling, *J. Chem. Phys.*, 128 (2008) 052321.

[53] B. Hu, Q. Wang, O. Lafon, J. Trebosc, F. Deng, J.P. Amoureux, Robust and efficient spin-locked symmetry-based double-quantum homonuclear dipolar recoupling for probing ^1H - ^1H proximity in the solid-state, *J. Magn. Reson.*, 198 (2009) 41-48.

[54] Q. Wang, B. Hu, O. Lafon, J. Trebosc, F. Deng, J.P. Amoureux, Double-quantum homo-nuclear NMR correlation spectroscopy of quadrupolar nuclei subjected to magic-angle spinning and high magnetic field, *J. Magn. Reson.*, 200 (2009) 251-260.

[55] C.R. Morcombe, V. Gaponenko, R.A. Byrd, K.W. Zilm *J. Am. Chem. Soc.* 127 (2005) 397-404.

[56] K.Y. Huang, A.B. Siemer, A.E. McDermott, Homo-nuclear mixing sequences for perdeuterated proteins, *J. Magn. Reson.*, 208 (2011) 122-127.

[57] A. Brinkmann, M. Edén, M.H. Levitt, *J. Chem. Phys.*, 112 (2000) 8539.

[58] M.J. Bayro, T. Maly, N.R. Birkett, C.M. Dobson, R.G. Griffin, *Angew. Chem. Int., Ed.* 48 (2009) 5708-5710.

[59] M.J. Bayro, G.T. Debelouchina, M.T. Eddy, N.R. Birkett, C.E. MacPhee, M. Rosay, W.E. Maas, C. M. Dobson, R.G. Griffin, *J. Am. Chem. Soc.*, 133 (2011) 13967-13974.

[60] M.L. Gilchrist, K. Monde, Y. Tomita, T. Iwashita, K. Nakanishi, A.E. McDermott *J. Magn. Reson.*, 152 (2001) 1-6.

[61] A.K.L. Yuen, O. Lafon, T. Charpentier, M. Roy, F. Brunet, P. Berthault, D. Sakellariou, B. Robert, S. Rimski, F. Pilon, J.C. Cintrat, B. Rousseau, *J. Am. Chem. Soc.*, 132 (2010) 1734-1735.

[62] T. Gullion, D.B. Baker, M.S. Conradi, New compensated Carr-Purcell sequences, *J. Magn. Reson.*, 89 (1990) 479-484.

[63] M.H. Levitt, Symmetry-based pulse sequences in magic-angle spinning solid-state NMR, in *Encyclopedia of Magnetic Resonance*, eds-in-chief R.K. Harris and R.E. Wasylichen, John Wiley: Chichester. Published online 15th of March 2007.

[64] N.C. Nielsen, H. Bildsoe, H.J. Jakobsen, M.H. Levitt, *J. Chem. Phys.*, 101 (1994) 1805.

[65] C. Martineau, J. Trebosc, B. Bouchevreau, F. Taulelle, O. Lafon, J.P. Amoureux, *Phys. Chem. Chem. Phys.*, 14 (2012), 7112-7119.

[66] R. Tycko, Dipolar recoupling: homonuclear experiments, in *Encyclopedia of Magnetic Resonance*, eds-in-chief R.K. Harris and R.E. Wasylichen, John Wiley: Chichester. Published

online 15th of September 2009.

- [67] T.G. Oas, R. G. Griffin, M. H. Levitt, *J. Chem. Phys.*, 89 (1998) 692.
- [68] A. Brinkmann, J. Schmedt auf der G ünne, M.H. Levitt, *J. Magn. Reson.*, 156 (2002) 79-96.
- [69] A. Brinkmann, M. Eden, *J. Chem. Phys.*, 120 (2004) 11726-11745.
- [70] A.E. Bennett, C.M. Rienstra, J.M. Griffiths, W. Zhen, J.P.T. Lansbury, R.G. Griffin, *J. Chem. Phys.*, 108 (1998) 9463-9479.
- [71] F.J. Blanco, R. Tycko, *J. Magn. Reson.*, 149 (2001) 131-138.
- [72] B. Hu, L. Delevoye, O. Lafon, J. Tr ¢bosc, J.P. Amoureux, *J. Magn. Reson.* 200 (2009) 178-188.
- [73] M. Veshtort, R.G. Griffin, SPINEVOLUTION: a powerful tool for the simulation of solid and liquid state NMR experiments, *J. Magn. Reson.*, 178 (2006) 248-282.
- [74] M. Bak, N.C. Nielsen, REPULSION: a novel approach to efficient powder averaging in solid-state NMR, *J. Magn. Reson.*, 125 (1997) 132-139.
- [75] B.M. Fung, A.K. Khitrin, K. Ermolaev, An improved broadband decoupling sequence for liquid crystals and solids, *J. Magn. Reson.*, 142 (2000) 97-101.
- [76] Z. Kanene, Z.A. Konstant, V. Krasnikov, *Neorg Mat.*, 21 9 (1985) 1552.
- [77] D. Coillot, G. Tricot, E. Creton, L. Montagne, *J. Eur. Ceram. Soc.*, 28, 6 (2008) 1135-1141.
- [78] K. Pervushin, V. Galliusa, C. Ritterb, Improved TROSY-HNCA experiment with suppression of conformational exchange induced relaxation, *J. Biomol. NMR.*, 21 (2001) 161-166. XY32 is implemented as $XYXY\ YXYX\ \overline{XYXY}\ \overline{YXYX}\ \overline{XYXY}\ \overline{YXYX}\ XYXY\ YXYX$; T. Gullion, Introduction to rotational-echo double-resonance NMR. *Concepts Magn. Reson.*, 10 (1998) 277-289. XY32 is implemented as $XYXY\ YXYX\ \overline{XYXY}\ \overline{YXYX}\ \overline{XYXY}\ \overline{YXYX}\ XYXY\ YXYX$.
- [79] R. Bruschiweiler, F. Zhang, Covariance nuclear magnetic resonance spectroscopy, *Journal of Chemical Physics*, 120 (2004) 5253-5260 ; B.W. Hu, P. Zhou, I. Noda, G.Z. Zhao, An NMR approach applicable to biomolecular structure characterization, *Analytical Chemistry*, 77 (2005) 7534;
- [80] B. Hu, J.P. Amoureux, J. Tr ¢bosc, M. Deschamps, G. Tricot, Solid-state NMR covariance of homonuclear correlation spectra, *Journal of Chemical Physics*, 128 (2008) 134502; Y. Li, Q. Wang, Z. Zhang, J. Yang, B. Hu, Q. Chen, I. Noda, F. Deng, Covariance spectroscopy with a non-uniform and consecutive acquisition scheme for signal enhancement of the NMR experiments, *J. Magn. Reson.*, 10.1016/j.jmr.2012.02.016 (2012).
- [81] O. Lafon, B. Hu, J.-P. Amoureux, P. Lesot, Fast and High-Resolution Stereochemical Analysis by Nonuniform Sampling and Covariance Processing of Anisotropic Natural Abundance 2D 2H NMR Datasets, *Chem. Eur. J.*, 17 (2011) 6716 – 6724.

[82] M.H. Levitt, R. Freeman, Compensation for pulse imperfections in NMR Spin Echo experiments, *J. Magn. Reson.*, 43 (1981), 65-80.

Chapter 3: Through-space Homo-nuclear Correlation Spectroscopy: SHANGHAI+

The Solid-State Nuclear Magnetic Resonance (SS-NMR) spectroscopy, with atomic-resolution, permits probing the structure and the dynamics of complex biological systems,^[1-7] such as amyloid fibrils^[3, 7] or membrane proteins.^[4, 6] However, the lack of sensitivity and resolution are often the two major limitations for the investigation of complex biological systems. These two limitations are decreased by using high static magnetic fields, B_0 , which consequently require using high magic-angle spinning (MAS) frequencies, ν_R , to remove the spinning sidebands that obscure the spectra. As an example, at $B_0 = 21.1$ T, a minimum MAS speed of ca. $\nu_R \geq 27$ kHz is required to suppress the spinning sidebands for aromatic ^{13}C nuclei experiencing chemical shift anisotropy (CSA) of 120 ppm.

However, in the presence of MAS for resolution purpose, the ^{13}C - ^{13}C dipolar couplings have to be restored with recoupling techniques. Very recently, we have proposed a new pulse sequence, called SHA+ (Second-order Hamiltonian among Analogous nuclei plus) (Fig.1d)^[8], based on SHANGHAI (Fig.1c)^[9] and PARIS_{xy,2} (Fig.1b)^[10-12], which allows an efficient ^{13}C - ^{13}C proton-driven recoupling at high-magnetic fields and high MAS frequencies. This method is little sensitive to dipolar truncation, thus allowing direct or relayed polarization transfers in amyloid fibrils between ^{13}C atoms, distant by up to ca. 10 Å. It has also been shown that long-distance restraints can be obtained with PDS (proton-driven spin-diffusion),^[1] DARR (dipolar-assisted rotational resonance),^[13, 14] and PAR (proton-assisted recoupling)^[15] methods, but only up to 7 Å, whereas NHC and CHHC methods can probe the short-range H^α - H^{N} and H^α - H^α contacts up to 3 Å.^[16, 17]

In selectively labeled amyloid fibril A β 42 sample, the long A21^{C β} -F20^{C α} distances of 7.8-9.6 Å were revealed at 21.1 T with SHA+ used with a long mixing time of $\tau_{\text{mix}} = 700$ ms. To avoid any rotational resonance (R^2) broadening, a *broad-band* excitation was chosen, and the spinning speed was thus larger than the carbon frequency range, $\nu_R > \Delta\nu_{\text{iso}}^{\text{max}}$. However, the recoupling parameters were not optimized for this pair of carbon atoms,

but for the $A21^{C\beta}$ - $F20^{CO}$ pair. This choice was related to the fact the F20 residue is uniformly ^{13}C -labeled, whereas A21 is selectively labeled at C^β . Therefore, the $A21^{C\beta}$ - $F20^{Car}$ transfer was mainly relayed through $F20^{CO}$, which is the closest carbon in F20 residue with $A21^{C\beta}$ - $F20^{CO} = 3.55 \text{ \AA}$. Practically, this optimized recoupling was achieved by matching the frequency difference of these two carbons, with $\Delta\nu_{iso}$ ($A21^{C\beta}$ - $F20^{CO}$) = 34.8 kHz at 21.1 T, to one of the basic recoupling resonances, that we will call modulation sidebands (MSs) in the following, and which are proportional to the spinning frequency, i.e. $\Delta\nu_{iso} = \chi\nu_R$. In this *broad-band* experiment, the MS with $\chi = 0.825$ was chosen, which led for this $A21^{C\beta}$ - $F20^{CO}$ spin-pair to an optimized spinning speed of $\nu_R = 42.3 \text{ kHz}$ at 21.1 T. Furthermore, a proton radio-frequency (rf) field of ca. $\nu_{1H} \approx 26 \text{ kHz} \approx 0.6\nu_R$ was employed for dipolar recoupling, because: (i) in this rf-region the MS values are little rf-field dependent, hence leading to a good robustness with respect to rf-inhomogeneity, and (ii) strong 1H - 1H interactions are reintroduced due to the close homo-nuclear $n = 1/2$ rotary resonance recoupling (R^3) HORROR condition,^[18] which facilitates the signal transfer at high spinning speed where the 3D 1H - 1H network is partly disentangled.

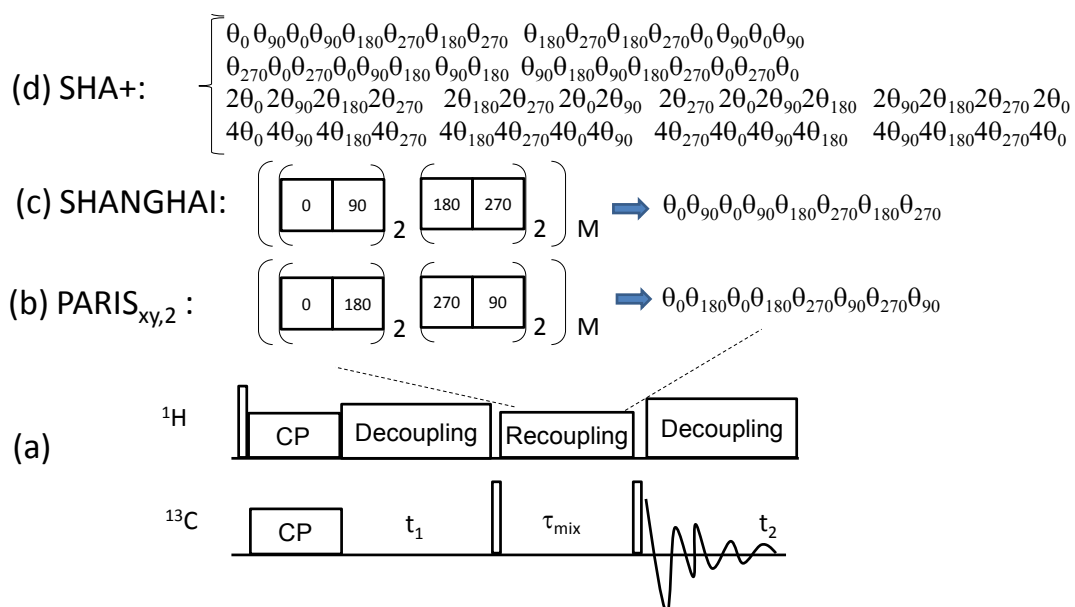


Fig.1. (a) General scheme of the 2D 2nd-order ^{13}C - ^{13}C spin diffusion experiments assisted by 1H irradiation, without ^{13}C irradiation during the mixing period. (b-d) Schemes of the recoupling sequences that are applied on the 1H channel during the mixing time, τ_{mix} , (b) PARIS_{xy,2}, (c) SHANGHAI, (d) SHA+. Each pulse length θ is equal to $T_R/2$.

However, long mixing times, to observe long distances, might potentially cause overheating and damage the protein samples. Therefore, it is desirable to lower the rf-power, while keeping the ability to detect long-distance constraints. One simple way is to decrease the spinning speed, which leads to reducing the ν_{1H} rf-field fulfilling the HORROR condition. With this goal in mind, we re-examined the SHA+ pulse sequence, and found out that several other recoupling conditions, with $\chi > 1$, can be used for *selective* optimized transfer, such as $\chi = 1.175$, which leads for the A21^{C β} -F20^{CO} distance to $\nu_R = 29.8$ kHz and $\nu_{1H} \approx 18$ kHz at $B_0 = 21.1$ T ($\Delta\nu_{iso} = 34.8$ kHz), or $\nu_R = 19.74$ kHz and $\nu_{1H} \approx 10$ -12 kHz at $B_0 = 14.1$ T ($\Delta\nu_{iso} = 23.2$ kHz). Indeed, the spinning speed, and hence the proton rf-field for HORROR recoupling, are proportional to $1/\chi$, and therefore, only 49% of rf-power ($\propto 1/\chi^2$) is needed compared with the condition of $\chi = 0.825$. Moreover, using a lower spinning speed (i) increases the transfer efficiency owing to the fact SHA+ is a second-order method, with ¹H rf-irradiation only, whose efficiency is thus ca. inverse proportional to the spinning speed, and (ii) may allow using bigger rotors to increase the S/N ratio. However, it must be noted that the use of $\chi > 1$ for one particular carbon pair leads to a R² broadening for pairs with frequency differences close to ν_R , thus decreasing the resolution along ridges parallel to the diagonal of the 2D spectra.

We also demonstrate that the best *broad-band* efficiency, with lowest ¹H rf-field and best resolution, can be achieved when the spinning speed is only slightly larger than the carbon frequency range: $\nu_R \geq \Delta\nu_{iso}^{max}$. In the case of A β 42 fibril, this optimized *broad-band* condition also maximizes the *selective* A21^{C β} -F20^{CO} long distance transfer owing to the fact: $\Delta\nu_{iso}(A21^{C\beta}-F20^{CO}) = \Delta\nu_{iso}^{max}$.

3.1 Numerical simulations

The simulations were performed using SPINEVOLUTION software.^[19] The powder averaging was accomplished using 1680 orientations with 168 (α_{MR}, β_{MR})-pairs and 10 γ_{MR} angles. The 168 (α_{MR}, β_{MR})-pairs, which relate the Molecular and Rotor frames, were selected according to the REPULSION algorithm.^[20] In the following, for each τ_{mix} time, the polarization transfer efficiency is defined as the amplitude of *one* of the two

cross-peaks divided by the amplitude of the diagonal peak for $\tau_{\text{mix}} = 0$. To compare more easily the present results with those previously published for SHANGHAI and PARIS_{xy,2},^[9] the simulations were performed at the same magnetic field of $B_0 = 21.1$ T, with the MAS frequency of $\nu_R = 32$ kHz and a mixing time of $\tau_{\text{mix}} = 250$ ms.

Simulations presented in Figs.2a,b and 3a were performed on a C1H-C2 spin-system, with the inter-nuclear distances of $r_{\text{C1-C2}} = 1.532$ Å ($|b_{\text{C1-C2}}/(2\pi)| \approx 2.1$ kHz), $r_{\text{C1-H}} = 1.079$ Å ($|b_{\text{C1-H}}/(2\pi)| \approx 23.9$ kHz), and $r_{\text{C2-H}} = 2.152$ Å ($|b_{\text{C2-H}}/(2\pi)| \approx 3.0$ kHz). The influence of ^1H - ^1H dipolar interactions was investigated by performing simulations for a C1H-C2H₂-H₂ spin-system in Figs.2c,d and 3b. For this spin-system, the inter-nuclear distances are those between the aliphatic sites in a crystal of L-glutamine with C1H = C $^\alpha$ H $^\alpha$, C2H₂ = C $^\beta$ H₂ $^\beta$ and H₂ = H₂ $^\gamma$. In all the simulations, the ^1H chemical shifts are identical and the irradiation on ^1H channel is applied on resonance.

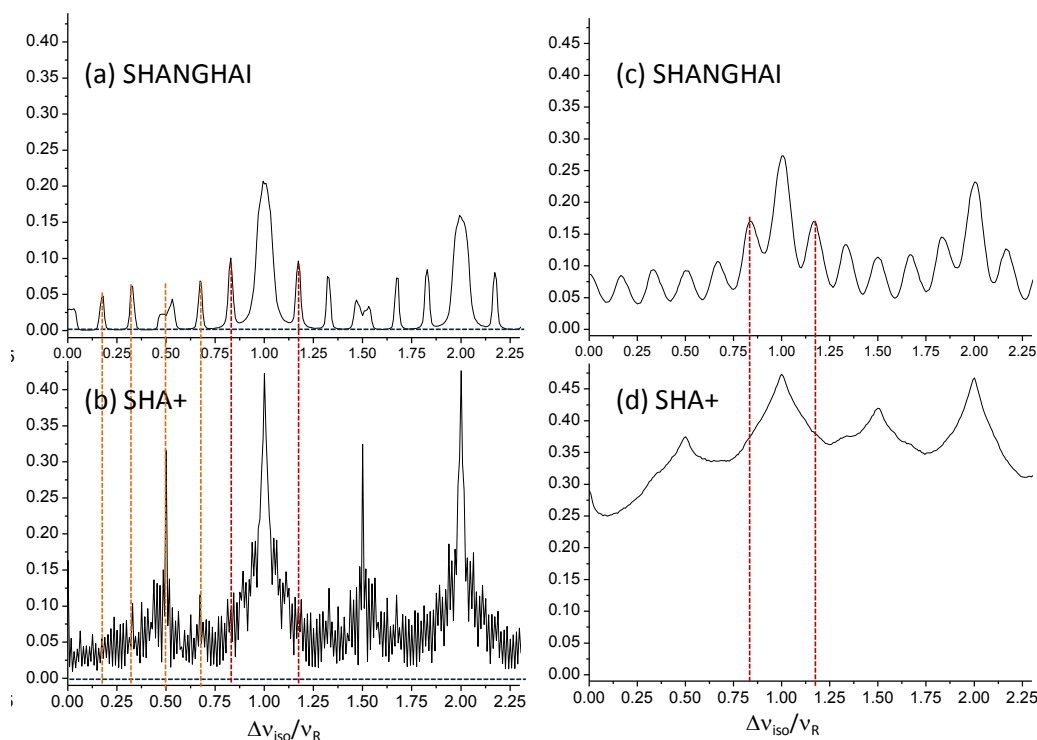


Fig.2. Simulated recoupling efficiency of SHANGHAI (a,c) and SHA+ (b,d), observed with $\tau_{\text{mix}} = 250$ ms, $\nu_R = 32$ kHz and $\nu_{1\text{H}} = \nu_R/2 = 16$ kHz, versus the reduced carbon frequency difference, $\Delta\nu_{\text{iso}}/\nu_R$. The spin-system is C1H-C2 in (a,b) and C1H-C2H₂-H₂ in (c,d). The other simulation parameters are given in the text.

First, we will concentrate on the HORROR condition with $\nu_{1\text{H}} = \nu_R/2 = 16$ kHz, which corresponds theoretically to the optimal rf-field for ^1H - ^1H HORROR recoupling as

mentioned before.^[18] Figs.2a,b show the efficiency for the C1H-C2 spin-system. One observes that the dipolar recoupling of SHA+ (Fig.2b) is always more efficient and less sensitive to Δv_{iso} than that of SHANGHAI (Fig.2a). Indeed, the minimum value of SHA+ is 0.025, with many sharp lines due to the concatenation of all pulse lengths, compared with SHANGHAI where many holes with zero transfer are observable. In SHANGHAI, the MSs can be easily identified (Table.1), and their two most efficient values occur for $\chi = 0.825$ and 1.175 (Fig.2a). Due to the sharp resonances, the fundamental MSs cannot be easily identified with SHA+, but we can assume that their positions are approximately those in SHANGHAI, as indicated with vertical dashed lines in Figs.2a,b. Figs.2c,d show that for the C1H-C2H₂-H₂ spin system, (i) all the main MS positions are kept in SHANGHAI, but are broadened by the introduction of the strongly-coupled proton system, (ii) SHA+ is little sensitive to Δv_{iso} , and (iii) ca. twice more efficient than SHANGHAI. At last we should point out that the closer we approach the R² condition, $\Delta v_{\text{iso}} = v_{\text{R}}$, the better the efficiency.

Table.1. Main MS positions, $\chi = \Delta v_{\text{iso}}/v_{\text{R}}$. They are easily observed by simulating the recoupling efficiency of a simple C1H-C2 spin-system at ultra-fast MAS. The χ values are symmetrical with respect to 0.5 and 1. Those of PARIS_{xy,m=1 or 2} are also given for completeness.

Sequence	$\chi < 1$	$1 < \chi < 2$
PARIS _{xy,1}	0.5	1.5
PARIS _{xy,2}	0.25, 0.75	1.25, 1.75
SHANGHAI	0.175, 0.325, 0.5, 0.675, 0.825	1.175, 1.325, 1.5, 1.675, 1.825
SHA+	$0 \leftrightarrow 1$ (0.175, 0.325, 0.5, 0.675, 0.825) ^[a]	$1 \leftrightarrow 2$ (1.175, 1.325, 1.5, 1.675, 1.825) ^[a]

[a]. In principle all MS conditions can be used for protonated systems; however, for non-protonated systems, the values in the parenthesis should be preferred.

In order to compare with previous results in ref ^[9], we also demonstrate in Fig.3 the full 2D simulations with $v_{\text{R}} = 32$ kHz, versus Δv_{iso} and v_{1H} . For the C1H-C2 spin-system, there exist two most efficient recoupling conditions with a quasi continuous distribution of Δv_{iso} (green dashed lines in Fig.3a): a broad one for $v_{\text{1H}} \approx v_{\text{R}}/4 = 8$ kHz and a narrow one for $v_{\text{1H}} \approx v_{\text{R}}/2 = 16$ kHz. The first condition at $v_{\text{1H}} \approx v_{\text{R}}/4$ can be useful for broad-band recoupling using very weak rf-field, which has been proved experimentally.^[8] As shown in Fig.3b, calculated for the C1H-C2H₂-H₂ spin-system, the presence of ¹H-¹H dipolar couplings: (i) increases the transfer efficiency, which becomes ca. twice that of

SHANGHAI for the same spin-system, and (ii) broadens the recoupling conditions, which become almost uniform. Fig.3b also show a higher transfer efficiency for SHA+ along the MIRROR recoupling conditions (MIXed Rotational and ROTary Resonance, also called Resonance Interference Recoupling, RIR), $\nu_{1H} \approx \Delta\nu_{iso}$ and $\nu_{1H} \approx \nu_R - \Delta\nu_{iso}$ (red dotted-dashed lines).^[21] In Fig.3b, it can also be observed that in protonated systems, the rf-condition $\nu_{1H} \approx \nu_R/4$ is less efficient than that with $\nu_{1H} \approx \nu_R/2$. This is the reason why it is recommended using the second condition in protonated systems, except for very fragile bio-molecules. Furthermore, one observes that the region corresponding to the two symmetrical conditions of $\Delta\nu_{iso}/\nu_R = 0.825$ and 1.175 ($\Delta\nu_{iso} = 26.4$ and 37.6 kHz) are indeed independent of proton rf-field if the setup of $\nu_{1H}/\nu_R \approx 0.5$ - 0.6 is used (blue bars in Fig.3b).

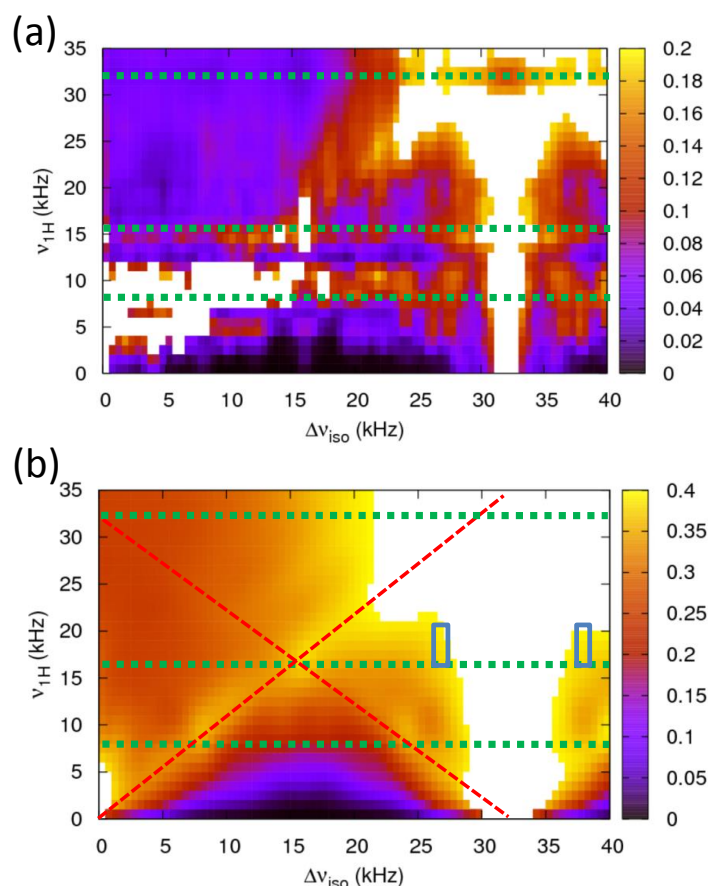


Fig.3. Simulated recoupling efficiency of the SHA+ sequence versus the rf-field amplitude, ν_{1H} , and the carbon frequency difference, $\Delta\nu_{iso}$, with $\tau_{mix} = 250$ ms and $\nu_R = 32$ kHz. The spin-systems are: (a) C1H-C2, and (b) C1H-C2H₂-H₂. When the efficiency is larger than 0.2 (a) or 0.4 (b), the zone is indicated in white. The conditions $\nu_{1H}/\nu_R = 0.25$, 0.5 and 1 are indicated as horizontal green dashed lines, and those corresponding to MIRROR, $\nu_{1H} = \Delta\nu_{iso}$ or $\nu_R - \Delta\nu_{iso}$, as oblique red dashed lines.

3.2 Experimental verifications

The A β 42 fibril is identical to that previously investigated.^[8] In this sample, two polymorphs co-exist with a ratio of ca. 9/1. However, we will only investigate the major polymorph in this article. The F20 residue is uniformly ¹³C- and ¹⁵N-labeled, whereas the A21 is selectively ¹³C-labeled at C $^{\beta}$. The formation of fibrils was confirmed by electron microscopy.^[8]

Experimental verifications have been performed on a Bruker 600 spectrometer ($B_0 = 14.1$ T), equipped with an AVANCE-III console. A commercial Bruker double-resonance MAS probe with rotor of 2.5 mm outer diameter, which permits spinning frequencies up to $\nu_R = 35$ kHz, was used for all experiments. In this case, using the same probe, the same sample volume and the same mixing time, allow an easy quantitative comparison of the transfer efficiencies. Typical 90° pulse lengths were 3 μ s on both channels. The contact time for cross-polarization was 3 ms, and SPINAL-64 proton dipolar decoupling sequence was used during evolution and detection periods.^[22] Recycle delays were of 3 s for all experiments. Additional experimental details are given in the figure captions.

Here, we demonstrate that SHA+ can be used to analyze *selectively* inter-residue connectivities between A21 C^{β} and F20 carbons with a spinning speed smaller than the chemical shift difference, i.e. with the condition $\chi = \Delta\nu_{\text{iso}}/\nu_R > 1$. We have chosen a long mixing time of $\tau_{\text{mix}} = 700$ ms to observe long distance constraints, and the main MS resonance with $\chi = 1.175$ with highest efficiency (Fig.2a) to match the chemical shift difference of $\Delta\nu_{\text{iso}}$ (A21 C^{β} -F20 C^{O}) = 23.2 kHz, which leads to $\nu_R = 19.7$ kHz, in order to optimize this transfer. We have also chosen a recoupling rf-field of $\nu_{\text{IH}} \approx 11.8$ kHz $\approx 0.6\nu_R$, to be close to the HORROR condition. These values have been selected since they lead to an efficient SHA+ recoupling (MS: $\chi = 1.175$) with a spinning rate of $\nu_R = 19.7$ kHz that is larger than the largest possible CSA of 18 kHz (120 ppm at $B_0 = 14.1$ T). Other MS *selective* conditions with lower spinning speed; e.g. $\nu_R = 17.5$ kHz with $\chi = 1.325$, would have led to smaller efficiency (Fig.2d) and to spinning sidebands at that field. It must be noted that such a spinning speed of $\nu_R = 19.7$ kHz allows using rotors

with diameters larger than 2.5 mm (e.g. 3.2 mm rotor) to increase the S/N ratio. We have used a 2.5 mm rotor to allow an easy comparison with the $\chi = 0.825$ condition, which requires faster spinning speed (see below).

As mentioned before, the best *broad-band* efficiency, avoiding any R^2 broadening, can be achieved when ν_R is only slightly larger than $\Delta\nu_{\text{iso}}^{\text{max}}$, which also corresponds in A β 42 fibril to an optimized *selective* A21^{CB}-F20^{CO} transfer. It is well-known that R^2 broadening only occurs when ν_R is nearly equal to $\Delta\nu_{\text{iso}}$. Therefore, we have chosen $\nu_R = 24.2$ kHz, which is only 1 kHz larger than the carbon frequency range of $\Delta\nu_{\text{iso}}^{\text{max}} = 23.2$ kHz, and which corresponds to $\chi = 0.958$ for the A21^{CB}-F20^{CO} transfer.

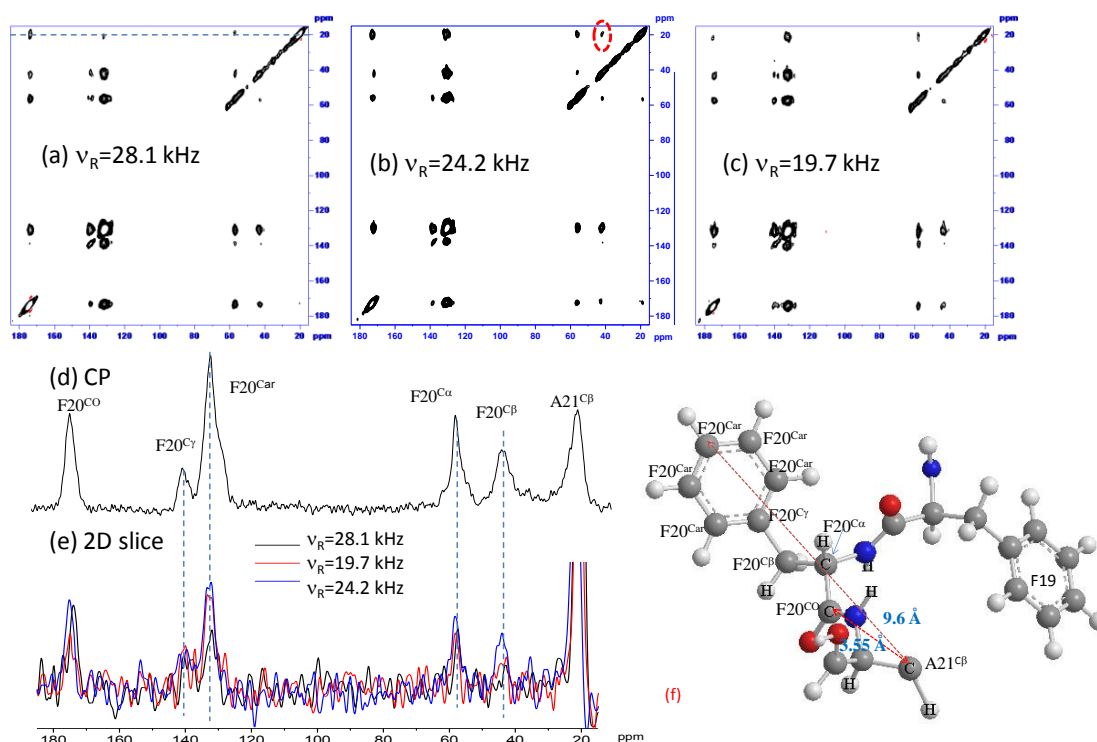


Fig.4. Experimental ^{13}C - ^{13}C SHA+ 2D spectra on a selectively labeled A β 42 fibril recorded at 14.1 T with $\nu_R = 28.1$ (a), 24.2 (b) and 19.7 kHz (c), corresponding to $\chi = 0.875$, 0.958 and 1.125, respectively, for the A21^{CB}-F20^{CO} transfer. The mixing time is $\tau_{\text{mix}} = 700$ ms, NS = 512, the number of t_1 increments is 80 ($t_{1,\text{max}} = 2.70$ ms), and $\nu_{\text{IH}} \approx 0.6\nu_R$. The experimental time for each experiment is 52h. (d) CP-MAS spectrum at $\nu_R = 19.7$ kHz for reference, and (e) comparison of the selected 1D slices along 20 ppm, corresponding to the correlation with A21^{CB} signal. (f) Model spin system of A β 42 extracted from a structure model.

To compare experimentally these MS conditions with the one previously used in ref [8], we have recorded the 2D ^{13}C - ^{13}C SHA+ spectra of labeled A β 42 fibril, with $\nu_R = 28.1$ (*broad-band*), 24.2 (*broad-band*) and 19.7 kHz (*selective*), corresponding for the

A21^{C β} -F20^{CO} transfer to $\chi = 0.825$ (Fig.4a), 0.958 (Fig.4b), and 1.175 (Fig.4c), respectively.

In Fig.4d and 4e, we show respectively the MAS spectrum and the three horizontal slices at 20 ppm corresponding to A21^{C β} . The A21^{C β} -F20^{CO}, A21^{C β} -F20^{C α} and A21^{C β} -F20^{C γ} inter-nuclear distances are equal to 3.55, 4.74 and 7.20 Å, respectively. The A21^{C β} -F20^{Car} distances range between 7.8 and 9.6 Å, corresponding to dipolar values of $|b_{CH}/(2\pi)| = 9-16$ Hz. Here, it should be pointed out that the *inter-molecular* distances between A21^{C β} in one molecular strip and F20^{Car} in nearby strips are also in the range of 7.8-9.6 Å (Fig.S1c in ref ^[8]). It should be mentioned that PDS and PARIS_{xy,2} pulse sequence could not reveal the A21^{C β} -F20^{Car} correlation (results not shown here).

Interestingly, as compared to $\nu_R = 28.1$ kHz, we observe that at $\nu_R = 19.7$ kHz, the three peaks of A21^{C β} -F20^{C γ} , A21^{C β} -F20^{Car}, and A21^{C β} -F20^{C β} are enhanced, while that of A21^{C β} -F20^{CO} is attenuated. However, with the condition of $\nu_R = 24.2$ kHz, all the cross-peaks are enhanced. It should be reminded that only the A21^{C β} -F20^{CO} short transfer of 3.55 Å is direct, while the longer transfers between A21^{C β} and the other F20 carbon species can be considered as mostly mediated through F20^{CO}. Thus the attenuation of the peak A21^{C β} -F20^{CO} at $\nu_R = 19.7$ kHz compared with that observed at $\nu_R = 28.1$ kHz, is certainly due to the dissipation at long mixing time of the signal from F20^{CO} to other carbons in F20 residue, with the premise that the efficiencies for $\chi = 0.825$ and 1.175 are the same. However, with the condition of $\chi = 0.958$, the transfer efficiency between A21^{C β} -F20^{CO} is enhanced, resulting in the enhancement of all the other indirect transfers. It should be pointed out that this explanation has been confirmed with results (not shown) observed at $\nu_R = 25.2$ kHz ($\chi = 0.92$). Indeed, the efficiency was then lower than that of $\chi = 0.958$, but higher than those of $\chi = 0.825$ and 1.175, which is consistent with our simulations in Fig.2d.

Most importantly, in the SHA+ spectra observed at $B_0 = 14.1$ T with $\nu_R = 19.7, 24.2,$ and 28.1 kHz, the peak A21^{C β} -F20^{C β} can be clearly observed, while this peak was lost at $B_0 = 21.1$ T with $\nu_R = 42.3$ kHz.^[8] This difference is due to the fact that the polarization transfer is mediated by second-order terms, which are inversely proportional to ν_R . Therefore, the decrease of the spinning speed leads to better efficiency of signal transfer.

3.3 Conclusion

We have explored the MS recoupling conditions of SHA+, and found that this sequence can be used in two different recoupling regimes, depending on the ratio between the spinning speed and the carbon frequency range, $\Delta\nu_{\text{iso}}^{\text{max}}$.

The first regime, $\nu_{\text{R}} > \Delta\nu_{\text{iso}}^{\text{max}}$, is recommended for *broad-band* recoupling to avoid any rotational resonance (R^2) broadening. In this regime, the spinning speed should be only slightly larger than $\Delta\nu_{\text{iso}}^{\text{max}}$, to obtain the best transfer efficiency. This condition could be used in most cases.

The second regime, $\nu_{\text{R}} < \Delta\nu_{\text{iso}}^{\text{max}}$, benefits from higher transfer efficiency and S/N ratio owing to the use of slower spinning speed. It should be used *selectively* to observe long-range constraints. Moreover, using lower spinning speed may allow using bigger rotors which should again increase the S/N ratio. It also leads to lower proton rf-power, which facilitates the use of longer mixing time, and avoids the denaturation of temperature-sensitive proteins. However, it must be reminded that using a spinning speed smaller than the chemical shift difference, $\chi > 1$, may deteriorate the resolution for cross-peaks with chemical shift difference close to the spinning speed. It should also be noted that decreasing the spinning speed may in some cases lead to a change of ^1H decoupling regime from low- to high-power. However, when working at very high magnetic fields, such as the forthcoming 1.2 GHz spectrometers, selective SHA+ recoupling with $\chi = 1.175$ can even lead to spinning rates of ca. $\nu_{\text{R}} \geq 40$ kHz, under which low-power ^1H decoupling is efficient. A theoretical justification for this SHA+ sequence is under progress.

References:

- [1] F. Castellani, B.v. Rossum, A. Diehl, M. Schubert, K. Rehbein, H. Oschkinat, Structure of a protein determined by solid-state magic-angle-spinning NMR Naturespectroscopy, *Nature*, 420 (2002) 98–102.
- [2] A. Lange, S. Becker, K. Seidel, K. Giller, O. Pongs, M. Baldus, A concept for rapid protein-structure determination by solid-state NMR spectroscopy, *Angew. Chem., Int. Ed.*, 44 (2005) 2089–2092.

- [3] C. Wasmer, A. Lange, H.V. Melckebeke, A.B. Siemer, R. Riek, B.H. Meier, Amyloid fibrils of the HET-s (218–289) Prion form a β solenoid with a triangular hydrophobic core, *Science*, 319 (2008) 1523–1526.
- [4] A. Lange, K. Giller, S. Hornig, M.F. Martin-Eauclaire, O. Pongs, M. S. Becker, M. Baldus, Toxin-induced conformational changes in a potassium channel revealed by solid-state NMR, *Nature*, 440 (2006) 959–962.
- [5] M. Renault, A. Cukkemane, M. Baldus, Solid-State NMR Spectroscopy on Complex Biomolecules, *Angew. Chem. Int. Ed.*, 210 (2010) 8346–8357.
- [6] M. Hong, Y. Zhang, F. Hu, Membrane protein structure and dynamics from NMR spectroscopy, *Annu. Rev. Phys. Chem.*, 63 (2012) 1–24.
- [7] R. Tycko, Solid-state NMR studies of amyloid fibril structure, *Annu. Rep. Phys. Chem.*, 62 (2011) 279–299.
- [8] B. Hu, J. Trebosc, O. Lafon, Q. Chen, Y. Masuda, K. Takegoshi, J.-P. Amoureux, Very-Long-Distance Correlations in Proteins Revealed by Solid-State NMR Spectroscopy, *ChemPhysChem*, 13 (2012) 3585–3588.
- [9] B. Hu, O. Lafon, J. Trebosc, Q. Chen, J.-P. Amoureux, Broad-band homo-nuclear correlations assisted by ^1H irradiation for bio-molecules in very high magnetic field at fast and ultra-fast MAS frequencies, *J. Magn. Reson.*, 212 (2011) 320–329.
- [10] M. Weingarth, Y. Masuda, K. Takegoshi, G. Bodenhausen, P. Tekely, Sensitive ^{13}C – ^{13}C correlation spectra of amyloid fibrils at very high spinning frequencies and magnetic fields, *J. Biomol. NMR*, 50 (2011) 129–136.
- [11] M. Weingarth, G. Bodenhausen, P. Tekely, Broadband carbon-13 correlation spectra of micro crystalline proteins in very high-magnetic fields, *J. Am. Chem. Soc.*, 131 (2009) 13937–13939.
- [12] M. Weingarth, D.E. Demco, G. Bodenhausen, P. Tekely, Improved magnetization transfer in solid-state NMR with fast magic angle spinning, *Chem. Phys. Lett.*, 469 (2009) 342–348.
- [13] K. Takegoshi, S. Nakamura, T. Terao, ^{13}C – ^1H dipolar-assisted rotational resonance in magic-angle spinning NMR, *Chem. Phys. Lett.*, 344 (2001) 631–637.
- [14] K. Takegoshi, S. Nakamura, T. Terao, ^{13}C – ^1H dipolar-driven ^{13}C – ^{13}C recoupling without ^{13}C rf irradiation in nuclear magnetic resonance of rotating solids, *J. Chem. Phys.*, 118 (2003) 2325–2341.
- [15] G. De Paepe, J.R. Lewandowski, A. Loquet, A. Bockmann, R.G. Griffin, Proton Assisted Recoupling and Protein Structure Determination, *J. Chem. Phys.*, 129 (2008) 245101.
- [16] A. Lange, K. Seidel, L. Verdier, S. Luca, M. Baldus, Analysis of Proton-Proton Transfer Dynamics in Rotating Solids and Their Use for 3D Structure Determination, *J. Am. Chem. Soc.*,

125 (2003) 12640-12648.

[17] M. Aluas, C. Tripon, J.M. Griffin, X. Filip, V. Ladizhansky, R.G. Griffin, S.P. Brown, C. Filip, CHHC and 1H–1H magnetization exchange: Analysis by experimental solid-state NMR and 11-spin density-matrix simulations, *J. Magn. Reson.*, 199 (2009) 173–187.

[18] N.C. Nielsen, H. Bildsoe, H.J. Jakobsen, M.H. Levitt, Double-quantum homonuclear rotary resonance: efficient dipolar recovery in magic-angle spinning nuclear magnetic resonance, *J. Chem. Phys.*, 101 (1994) 1805-1812.

[19] M. Veshtort, R.G. Griffin, SPINEVOLUTION: a powerful tool for the simulation of solid and liquid state NMR experiments, *J. Magn. Reson.*, 178 (2006) 248–282.

[20] M. Bak, N.C. Nielsen, REPULSION: a novel approach to efficient powder averaging in solid-state NMR, *J. Magn. Reson.*, 125 (1997) 132-139.

[21] I. Scholz, M. Huber, T. Manolikas, B.H. Meier, M. Ernst, MIRROR recoupling and its application to spin diffusion under fast magic-angle spinning, *Chem. Phys. Lett.*, 460 (2008) 278-283.

[22] B.M. Fung, A.K. Khitrin, K. Ermolaev, An Improved Broadband Decoupling Sequence for Liquid Crystals and Solids, *J. Magn. Reson.*, 142 (2000) 97–101.

Chapter 4: Through-space Hetero-nuclear Correlation Spectroscopy: improving the resolution

Two-dimensional (2D) hetero-nuclear correlation (HETCOR) experiments are key tools of solid-state NMR spectroscopy to probe through-bond connectivities or through-space proximities between distinct isotopes.^[1-4] The connectivities and the proximities are revealed through coherence transfers via *J*- or dipolar couplings, respectively. When the one-dimensional (1D) NMR spectra of both correlated isotopes contain several signals, the 2D HETCOR experiments are especially efficient since they allow unambiguous observation of connectivities or proximities between specific sites.

We focus here on 2D HETCOR experiments between protons and another isotope. In solution, the sensitivity of HETCOR experiments can be dramatically enhanced by indirect detection through ¹H signals using Heteronuclear Single-Quantum Coherence (HSQC) and Heteronuclear Multiple-Quantum Coherence (HMQC) sequences.^[5-7] These methods have been routinely employed for the last three decades in solutions. In solids, it is well-established that effectiveness of indirect ¹H detection requires low ¹H concentration and/or high MAS frequencies, $\nu_R \geq 30$ kHz, since broad ¹H signal can negate sensitivity enhancement.^[8-40] One method to correlate ¹H and another spin-1/2 nuclei, such as ¹³C or ¹⁵N, is the double cross-polarization (CP) transfer.^[8,9] This method has notably permitted the acquisition of ¹H-¹³C and ¹H-¹⁵N 2D HETCOR spectra, with ¹³C and ¹⁵N natural abundance respectively, of numerous compounds including proteins and surface-bound organic molecules in functionalized mesoporous silica.^[14,19,20] However, CP transfers between ¹H and quadrupolar nuclei lack efficiency and robustness owing to the complex spin dynamics of quadrupolar nuclei during spin locking.^[41,42] Consequently, a more efficient and robust technique for HETCOR between ¹H and quadrupolar nuclei has been developed that is based on the dipolar-mediated HMQC (*D*-HMQC) sequence.^[26,38] In particular, the *D*-HMQC method has been exploited to observe ¹H-¹⁴N proximities in amino-acids,^[21-28] pharmaceuticals,^[30-32] and hybrid materials.^[33,34] Innovative variants of *D*-HMQC incorporating DANTE or overtone pulses at twice the ¹⁴N Larmor frequency have also been introduced recently to correlate

^1H and ^{14}N nuclei.^[35–37] The indirect observation of half-integer spin quadrupolar nuclei, notably ^{43}Ca , with a low gyromagnetic ratio can also be performed by *D*-HMQC pulse sequence.^[38–40]

Unfortunately, proton-detected HMQC spectra often exhibit large line-broadening along the indirect dimension compared to 1D experiment. This broadening stems from the decay of heteronuclear multiple-quantum (MQ) coherences under ^1H - ^1H dipolar couplings. It has been shown that rotor-synchronized ^1H - ^1H dipolar decoupling based on symmetry $\text{C}6_2^3$, $\text{C}8_1^4$ and $\text{R}6_1^3$, can be applied during the indirect evolution period, t_1 , to reduce the ^1H - ^1H dipolar couplings and hence to achieve resolution enhancement along the indirect dimension of proton-detected HMQC spectra.^[27,38]

This chapter aims at analyzing the performances of various decoupling schemes during t_1 period, including continuous wave (CW), symmetry-based sequences,^[43–46] phase-modulated Lee-Goldburg (PMLG),^[47–53] and decoupling using mind-boggling optimization (DUMBO).^[54–57] We will compare the different properties of the decoupling schemes, including spectral resolution, t_1 -noise, number of parameters to optimize, and radio-frequency (rf) field requirement. In particular, we will show that specific ^1H - ^1H dipolar decoupling yields better resolution along the indirect dimension of proton-detected HMQC sequences than CW irradiation. When observing indirectly broad spectra presenting numerous spinning sidebands, the *D*-HMQC sequence must be fully rotor-synchronized owing to the particular use of rotor-synchronized indirect sampling and dipolar recoupling sequence. In this case, we will also propose an innovative solution to reduce spurious spinning sidebands resulting from the modulation of window delays before and after the decoupling sequence.

This chapter is organized as follows. Section 1 will describe the pulse sequences and the recoupling schemes used and their properties using first-order average Hamiltonian (AH) theory. In section 2, the decoupling efficiencies of CW and symmetry-based sequences will be investigated with numerical simulations of the spin dynamics. In section 3, the performances of the decoupling sequences are compared experimentally. This comparison is performed for 2D ^1H - $\{^{13}\text{C}\}$ *D*-HMQC spectra of $[\text{U-}^{13}\text{C}]\text{-L-histidine.HCl.H}_2\text{O}$ (histidine in the following) at 9.4 T and $\nu_{\text{R}} = 32.3$ kHz as well as 18.8 and 21.1 T and $\nu_{\text{R}} \approx 62$ kHz. The reason to test decoupling performances on

a spin 1/2 nucleus, like ^{13}C , is that its line-widths are easy to measure. The sensitivity and resolution enhancement produced by t_1 decoupling are then used to observe correlation between aliphatic protons and ^{14}N nuclei in 2D $^1\text{H}\{-^{14}\text{N}\}$ DANTE- D -HMQC spectrum of histidine at 21.1 T and $\nu_R = 62.1$ kHz.

4.1 Pulse sequence and theory

4.1.1 The D -HMQC sequence

The proton-detected HMQC sequence using coherence transfers via heteronuclear dipolar coupling, denoted D -HMQC hereafter, is depicted in Fig.1. The indirectly detected isotope is denoted I in the following. We refer to proton-detected D -HMQC experiment with $I = ^{13}\text{C}$ or ^{14}N as $^1\text{H}\{-^{13}\text{C}\}$ or $^1\text{H}\{-^{14}\text{N}\}$. The D -HMQC sequence derives from the HMQC scheme that exploits coherence transfers via J -coupling (denoted J -HMQC) by the insertion of heteronuclear dipolar recoupling on the ^1H channel during the defocusing and refocusing delays, τ_{rec} . Here, $\text{SR}4_1^2$ scheme has been chosen as heteronuclear dipolar recoupling.^[38,58–60] This sequence consists of two consecutive $\text{R}4_1^2$ and $\text{R}4_1^{-2}$ blocks, each lasting one rotor period, T_R , and its robustness is improved by a three-step super-cycling: $\text{SR}4_1^2 = [\text{R}4_1^2 \text{R}4_1^{-2}]_0 [\text{R}4_1^2 \text{R}4_1^{-2}]_{120} [\text{R}4_1^2 \text{R}4_1^{-2}]_{240}$. Consequently, the super-cycle of $\text{SR}4_1^2$ lasts $6T_R$. However, this recoupling sequence works well even if the super-cycle is not completed. Here, the τ_{rec} interval was adjusted in steps of T_R , i.e. $\tau_{\text{rec}} = pT_R$ where p denotes an integer number. This finer time resolution makes it easier to maximize the build-up of heteronuclear MQ coherences.^[60] The $\text{SR}4_1^2$ recoupling reintroduces the space component $|m| = 2$ of $^1\text{H}\text{-}I$ heteronuclear dipolar coupling and ^1H chemical shift anisotropy (CSA). Nevertheless, these two interactions do not interfere with each other since their contributions to the first-order AH commute. $\text{SR}4_1^2$ recoupling offers several advantages for proton-detected D -HMQC: (i) it suppresses the $^1\text{H}\text{-}^1\text{H}$ dipolar interactions in the first-order AH, hence limiting the signal decay during τ_{rec} , (ii) it is robust to isotropic and anisotropic chemical shifts as well as rf maladjustment, (iii) it is not affected by dipolar truncation since it accomplishes longitudinal two-spin order recoupling ($H_z I_z$) of the $^1\text{H}\text{-}I$ dipolar interaction, (iv) it

benefits from low rf field requirement since the rf field amplitude must only be twice the MAS frequency, $\nu_{1,\text{rec}} = 2\nu_R$, and (v) the only adjustable parameter is the τ_{rec} delay, which simplifies the recoupling optimization.

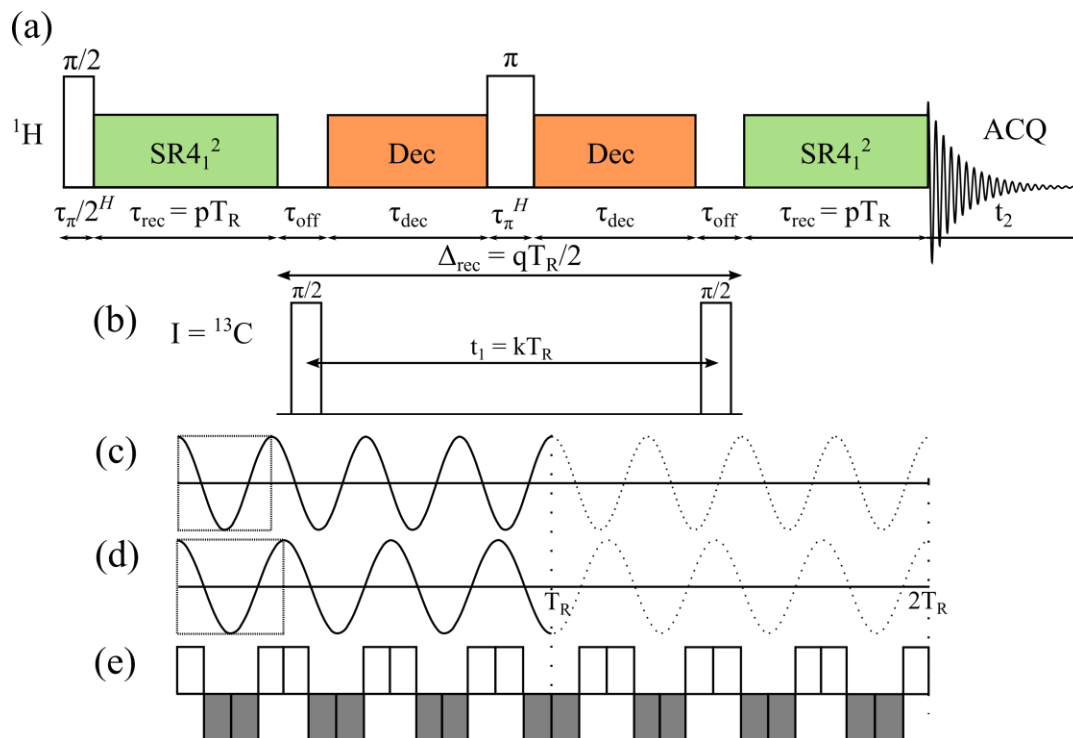


Fig.1. (a) ^1H - $\{I\}$ D -HMQC sequence using SR4_1^2 recoupling and ^1H - ^1H dipolar decoupling during t_1 period. In the I channel, the excitation/reconversion process is performed using two square pulses (^{13}C or ^{14}N). See Fig.S1 for a sequence using two D^3_4 DANTE pulses for ^{14}N indirect detection. The phase cycling is given in ref. [60]. The pulse lengths on ^1H channel are denoted $\tau_{\pi/2}^H$ and τ_{π}^H , whereas those on ^{13}C channel are denoted $\tau_{\pi/2}^C$. Drawings are representing: (c) the SAM_4 , (d) the $\text{SAM}_{3,5}$ and (e) the C14_7^2 ($\alpha_0\alpha_{180}$) decoupling schemes. When using a shape-pulse length of $\Delta\tau_{\text{dec}} = T_R$ (full thick curves in (c,d)), a change of sign of this shape-pulse is required every rotor period to keep the symmetry based properties and the smoothness for $\text{SAM}_{3,5}$, whereas this is not the case for SAM_4 . When using SAM_n schemes with a shape-pulse length of $\Delta\tau_{\text{dec}} = T_R/n$ (dashed squares), no change of sign is required.

SR4_1^2 is non- γ -encoded, and as it reintroduces the space component $|m| = 2$, the starts of the two SR4_1^2 sequences must be separated by a multiple of half-rotor period. As $\tau_{\text{rec}} = pT_R$, the delay between the two SR4_1^2 recoupling parts must be a multiple of half-rotor period as well: $\Delta_{\text{rec}} = qT_R/2$ with q an integer number.

The excitation and the reconversion of MQ coherences are achieved by two rectangular $\pi/2$ pulses for ^1H - $\{^{13}\text{C}\}$ experiments (Fig.1b). For ^1H - $\{^{14}\text{N}\}$ HMQC, these processes can either be done with two rectangular pulses (Fig.1b), or with two trains of rotor-synchronized short rectangular pulses in the manner of Delays Alternating with

Nutation for Tailored Excitation, DANTE (Fig.S1). This DANTE scheme has been recently proposed as an efficient excitation method for ^{14}N nuclei subject to large quadrupole interactions.^[35,61,62] Here, we employed interleaved DANTE pulse trains, denoted D_4^3 , which consist of a comb of 4 equally spaced short pulses per rotor period applied during 3 rotor periods.

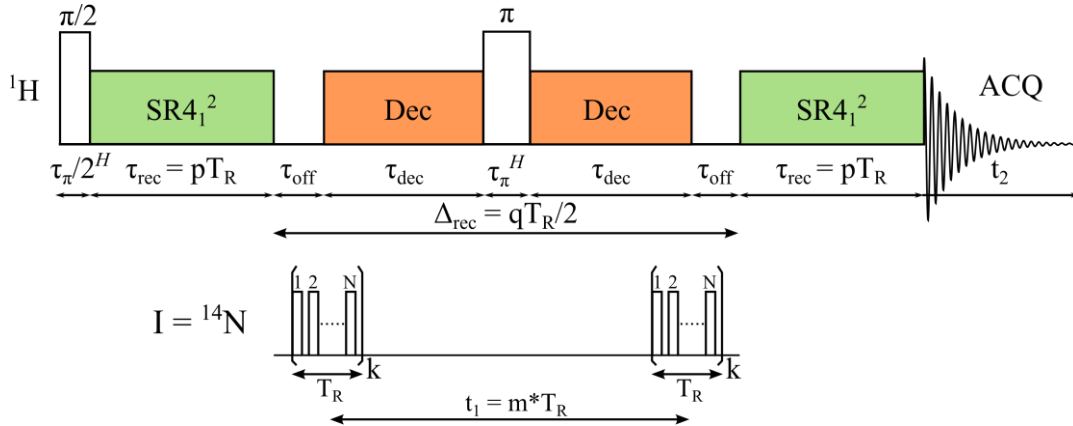


Fig.S1. $^1\text{H}\{-^{14}\text{N}\}$ D -HMQC sequence using $\text{SR}4_1^2$ recoupling and $^1\text{H}\text{-}^1\text{H}$ dipolar decoupling during t_1 period. In the I channel (^{14}N), the excitation/reconversion process is performed using two D_4^3 DANTE pulses.

In the case of $^1\text{H}\{-^{13}\text{C}\}$ D -HMQC experiments, the indirect evolution period, t_1 , is defined as the delay between the centers of the two pulses on the ^{13}C channel. Obviously, the condition $\Delta_{\text{rec}} = qT_R/2 \geq t_1 + \tau_{\pi/2}^{\text{C}}$ is required, and hence, this delay is calculated as

$$\Delta_{\text{rec}} = \begin{cases} \left\lceil 2 \frac{t_1 + \tau_{\pi/2}^{\text{C}}}{T_R} \right\rceil \frac{T_R}{2} & \text{for } D - \text{HMQC} \\ \left\lceil 2 \frac{t_1 + KT_R}{T_R} \right\rceil \frac{T_R}{2} & \text{for DANTE - } D - \text{HMQC} \end{cases} \quad (1)$$

Where $\lceil x \rceil$ is the smallest integer not less than x , and K the number of rotor periods each DANTE train lasts ($K = 3$ with D_4^3). For $^1\text{H}\{-^{13}\text{C}\}$ D -HMQC experiment, the t_1 period was rotor-synchronized, $t_1 = kT_R$, to eliminate spinning sidebands, thus simplifying the 2D spectrum and improving its signal-to-noise (S/N) ratio. Interleaved DANTE excitation produces rotor-synchronized echoes. The consecutive echoes are shifted by T_R/N , which allows oversampling in the indirect dimension by using smaller increments of $\Delta t_1 = T_R/N$.

4.1.2 The decoupling sequences

As explained in introduction, the improvement of spectral resolution in the indirect dimension of proton-detected HMQC experiments requires the suppression of ^1H - ^1H dipolar interactions during t_1 .^[27,38] Furthermore, the employed decoupling scheme must preserve the ^1H - I heteronuclear MQ coherences created by the first $\pi/2$ pulse on the I channel. Here, several decoupling schemes were tested, including CW ^1H irradiation, and ^1H - ^1H dipolar decoupling, which are either rotor-synchronized ($CN_n^{N/2}$ [43-46]) or non-rotor-synchronized (PMLG^[47-53] and DUMBO^[54-57]).

(a) CW decoupling

CW decoupling is considered in this paper because when $\nu_{1,\text{dec}}$ and ν_R values are commensurable, the CW decoupling corresponds to rotor-synchronized sequences with symmetry CN_n^0 and RN_n^0 . However rotary resonance recoupling (R^3) conditions corresponding to $\nu_{1,\text{dec}} = j\nu_R$ with $j = 1/2, 1, 2$ as well as 3 and 4 when considering higher order effects must be avoided because of the reintroduction of anisotropic component.^[63] For example, ^1H - ^1H dipolar interactions are recoupled at $j = 1/2$ or 1, while recoupling of ^1H - I heteronuclear dipolar interactions occurs at $j = 1$ or 2. These recoupled anisotropic interactions can broaden the NMR signals along the indirect dimension of HMQC spectra. Furthermore, the CW irradiation must not disperse the ^1H - I MQ coherences. These can be preserved if the ^1H coherences are spin-locked by the CW irradiation, which thus must have the same phase as the first $\pi/2$ pulse on the ^1H channel, or if the phase of CW irradiation is shifted by $\pi/2$ with respect to the phase of the central π pulse since

$$\exp(-i\varphi I_x)\exp(-i\pi I_y)\exp(-i\varphi I_x) = \exp(-i\pi I_y) \quad (2)$$

where φ is the nutation angle during each CW irradiation. In Eq.2, we assume that the phase of CW irradiation is x , whereas that of the central π pulse is y . However, the compensation in Eq.2 is prone to offset effects or rf maladjustments. Therefore, the spin-lock first solution should be preferred in practice (see section IV).

(b) $CN_n^{N/2}$ decoupling

The $CN_n^{N/2}$ decoupling involves phase shifts of 180° between subsequent cycles. These cycles derive from a basic element C . We employed as C element either two rectangular pulses with opposite phases, $\alpha_0\alpha_{180}$ (see Fig.1e), or a half-cosine pulse (see

Fig.1c and d). Here, $\alpha_0\alpha_{180}$ denotes two consecutive rectangular and resonant rf pulses with identical flip angle, α , identical length, $nT_R/(2N)$ but with phases shifted by 180° . The $CN_n^{N/2}$ sequence built from $\alpha_0\alpha_{180}$ basic element is denoted $CN_n^{N/2}(\alpha_0\alpha_{180})$ hereafter. The α angle in radians is given by [46]

$$\alpha = \pi \frac{n}{N} \times \frac{v_{1,dec}}{v_R} \quad (3)$$

The half-cosine pulse is used for the smooth amplitude-modulated (SAM) version.^[44–46] It has been well-established that smooth amplitude modulation can reduce the pulse transients, the size of which scales with the amplitude and phase changes.^[64] The $CN_n^{N/2}$ (half-cos) sequences are denoted $SAM_{N/(2n)}$ hereafter.

The sequences with $CN_n^{N/2}$ symmetry suppress all terms in first-order AH arising from ^1H - ^1H and ^1H - I dipolar couplings, as well as ^1H CSA, while ^1H isotropic chemical shift terms are preserved and can be described by an effective field along the z -axis.^[43,46] In the case of one ^1H - I spin pair irradiated by decoupling with $CN_n^{N/2}$ symmetry, the first-order AH is: [46]

$$\overline{H} = \kappa_{\text{isoCS}} \left(\Omega_H H_z + \pi J_{HI} H_z I_z \right) + \Omega_I I_z \quad (4)$$

where Ω_H and Ω_I denote the resonance offset frequency of ^1H and I nuclei respectively, I_z and H_z are the operators for the angular momentum z -component of the ^1H and I nuclei, respectively, J_{HI} is the heteronuclear J -coupling between ^1H and I nuclei. Eq.4 indicates that the effective field resulting from isotropic chemical shifts terms is along the z -axis.

The scaling factor of the isotropic chemical shift κ_{isoCS} is:^[46]

$$\kappa_{\text{isoCS}} = \begin{cases} \text{sinc}(\alpha) & C = \alpha_0\alpha_{180} \\ J_0\left(2\frac{\alpha}{\pi}\right) & C = \text{half-cos} \end{cases} \quad (5)$$

where $\text{sinc}(\alpha) = \sin(\alpha)/\alpha$, and J_0 is the zero-order Bessel function of the first kind. For both $C = \alpha_0\alpha_{180}$ and $C = \text{half-cos}$, α angle is defined according to Eq.3, where $v_{1,dec}$ denotes the maximal value of the rf field amplitude. In Fig.2a, the κ_{isoCS} factor is plotted as function of α angle. For both basic elements, κ_{isoCS} decreases for increasing α angle, i.e. increasing $v_{1,dec}$ value.

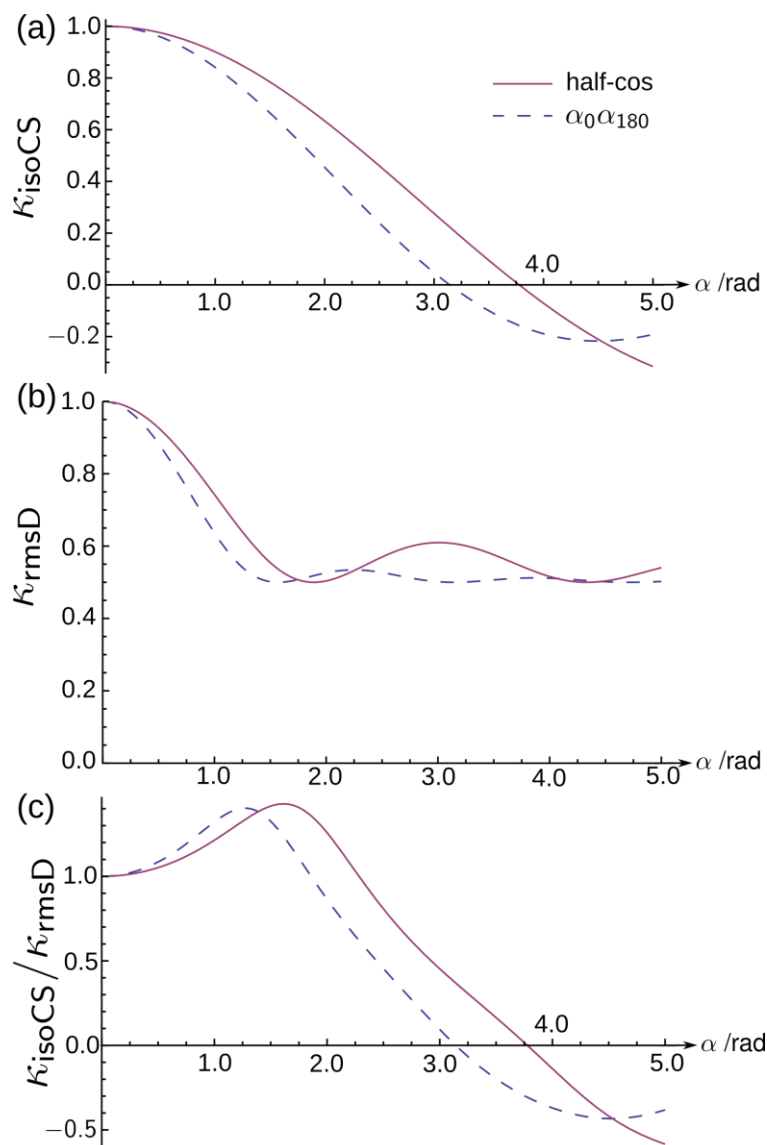


Fig.2. Plots of (a) κ_{isoCS} and (b) κ_{rmsD} scaling factors as well as (c) the $\kappa_{\text{isoCS}}/\kappa_{\text{rmsD}}$ ratio as function of the pulse angle α for sequences $CN_n^{N/2}$ with basic element $C = \alpha_0 \alpha_{180}$ (dashed line) and half-cos (continuous line).

The $CN_n^{N/2}$ symmetry eliminates the ^1H - ^1H and ^1H - I dipolar couplings in the first-order AH. Hence, the observed line-width stems from the contribution of the dipolar couplings to higher-order AH terms. The calculation of these higher-order terms is often complex. However, in the absence of interferences between MAS and rf irradiation, i.e. away from R^3 conditions, no difference should be noticed between MAS and static conditions regarding the dependence of the magnitude of the residual dipolar couplings on $v_{1,\text{dec}}$.^[65,66] Therefore, we simply calculate ^1H - ^1H dipolar couplings contribution to the second-order AH under static conditions for two subsequent cycles of $CN_n^{N/2}$ sequences,

i.e. $\alpha_0\alpha_{180}\alpha_{180}\alpha_0$ for $CN_n^{N/2}(\alpha_0\alpha_{180})$ and cosine pulse for SAM. For an H_1 - H_2 spin pair, this contribution is equal to:

$$\overline{H_D} = \kappa_{D0} \frac{1}{2\sqrt{6}} \left(4H_{1z}H_{2z} - H_1^+H_2^- - H_1^-H_2^+ \right) + \frac{\kappa_{D2}}{2} H_1^+H_2^+ + \frac{\kappa_{D-2}}{2} H_1^-H_2^- \quad (6)$$

where $\kappa_{D\mu}$ with $\mu = 2, 0, -2$ denotes the scaling factor of the term proportional to the μ -quantum operator and H_k^\pm are the ladder operators of H_k protons. The expression of $\overline{H_D}$ given in Eq.6 only contains zero- and double-quantum operators. Terms proportional to single-quantum operators are eliminated by the shift of 180° between subsequent cycles. The norm of $\overline{H_D}$ is scaled by the root-mean square (rms) of the scaling factors:

$$\kappa_{\text{rmsD}} = \sqrt{\kappa_{D0}^2 + \kappa_{D2}^2 + \kappa_{D-2}^2} = \begin{cases} \frac{1}{2} \sqrt{1 + 3\text{sinc}^2(2\alpha)} & C = \alpha_0\alpha_{180} \\ \frac{1}{2} \sqrt{1 + 3J_0^2\left(\frac{4\alpha}{\pi}\right)} & C = \text{half} - \cos \end{cases} \quad (7)$$

Fig.2b shows that κ_{rmsD} factor decreases down to ca. 0.5 for $\alpha \approx 3.5$ and oscillates in the range [0.5-0.6] for $\alpha \geq 3.5$. This figure proves that $CN_n^{N/2}(\alpha_0\alpha_{180})$ and SAM irradiations are not able to fully suppress the ^1H - ^1H dipolar coupling terms in the AH under static condition. Happily, a large part of the remaining dipolar interaction is averaged by fast MAS, then leading to the observation of highly resolved ^1H spectra. This is especially true with ultra-fast MAS, as the spinning speed ($\nu_R \geq 60$ kHz) is then much larger than ^1H - ^1H dipolar interactions in most samples.

The ratio $\kappa_{\text{isoCS}}/\kappa_{\text{rmsD}}$ allows an estimation of the best rf conditions to enhance the resolution of ^1H spectra acquired with $CN_n^{N/2}$ decoupling. In Fig.2c, $\kappa_{\text{isoCS}}/\kappa_{\text{rmsD}}$ ratio is plotted as function of α angle. This ratio is maximal at $\alpha = 1.25$ and 1.6 rad for $CN_n^{N/2}(\alpha_0\alpha_{180})$ and SAM decoupling, respectively. According to Eq.3, these optimal angles correspond to an optimal rf field amplitude of

$$\nu_{1,\text{dec}}^{\text{opt}} = A \frac{N}{2n} \nu_R \quad (8)$$

with $A = 0.8$ and 1.0 for $CN_n^{N/2}(\alpha_0\alpha_{180})$ and SAM decoupling, respectively. For SAM, $\nu_{1,\text{dec}}^{\text{opt}}$ in Eq.8 is the maximal value of the rf field amplitude. However, the rf power is

related to the *rms* amplitude, $v_{1,dec}^{rms} = v_{1,dec} / \sqrt{2}$. Therefore, SAM achieves optimal spectral resolution using slightly lower rf power than $CN_n^{N/2}(\alpha_0\alpha_{180})$. The optimal rf field amplitudes given by Eq.8 are in good agreement (within 20 %) with those previously determined using numerical simulations.^[46]

An interesting point is the role of chemical shift recoupling during decoupling. Indeed resolution, a priori, does not affect the experiment as proton chemical shifts are refocused by the π pulse. We will see that it is not so obvious and chemical shift difference seems to play a role in homonuclear decoupling efficiency.

(c) PMLG and DUMBO decoupling schemes

The PMLG and DUMBO families of homonuclear decoupling schemes use constant-amplitude and phase-modulated rf irradiation. These techniques are applied in a non-synchronous way with the rotor period to avoid recoupling of the dipolar interaction. These sequences achieve efficient suppression of the ^1H - ^1H dipolar couplings, while preserving the ^1H isotropic chemical shifts. The basic PMLG sequence consists of two linear phase ramps: one with a positive slope and the other with a negative slope. Furthermore, these two phase ramps programmed in discrete steps are shifted by 180° .^[47] For instance, the PMLG- N_p^x basic cycle is composed of $2N$ pulses, the first ramp has a positive slope and the phase of its first pulse is close to x . Each phase ramp generates a 2π rotation in spin space about an effective field tilted from the z -axis. Super-cycled versions of PMLG have also been proposed.^[50,52] For instance, PMLG- $N_p^{x\bar{x}}$ consists of two successive PMLG- N_p^x and PMLG- $N_p^{\bar{x}}$ sequences. During this super-cycled version, the effective field related to isotropic chemical shifts is aligned with the z -axis. Here, we employed PMLG-5 $N_p^{x\bar{x}}$ decoupling.

The DUMBO sequences consist of periodic phase modulations, which differ from linear ramps and are described using Fourier series. The phase modulation of the original DUMBO-1 sequence was developed using numerical simulations.^[54] Subsequently, the phase modulation was experimentally optimized, leading to the sequences eDUMBO-1₂₂,^[56] and eDUMBO-1₊.^[57] Using a Legendre polynomial basis,^[57] it has been shown that the dominant feature of the DUMBO phase modulations is a linear phase ramp similar to that employed in PMLG.^[67] However, in DUMBO sequences, small

oscillations are superimposed on the linear ramp and the DUMBO phase modulation consists of four steps, instead of two phase ramps for PMLG- N_p^x . For the basic DUMBO-1 sequence, the effective field resulting from isotropic chemical shifts is tilted from the z -axis. Similarly to PMLG- $N_p^{x\bar{x}}$, super-cycled versions of DUMBO scheme, denoted DUMBO $^{\phi\bar{\phi}}$, have also been introduced.^[51] They consist of two successive DUMBO sequences shifted by 180°, which produce an effective field related to isotropic chemical shifts aligned with the z -axis. Here, we tested DUMBO-1 $^{\phi\bar{\phi}}$ and eDUMBO-1 $^{\phi\bar{\phi}}_{22}$ sequences.

The evolution under isotropic chemical shift during $CN_n^{N/2}$, PMLG- $N_p^{x\bar{x}}$ or DUMBO $^{\phi\bar{\phi}}$ sequences corresponds to a rotation about the z -axis. Hence, this evolution is refocused by the central π pulse and the coherences of protons with distinct isotropic chemical shifts keep identical phases during the decoupling.

4.1.3 Time increment optimization

For all decoupling sequences presented above, except the CW, there is a minimal cycle time, $\Delta\tau_{\text{dec}}$, which depends on the decoupling sequence and that determines the minimum t_1 increment. For $CN_n^{N/2}$ sequence, we compared in this article the implementation with $\Delta\tau_{\text{dec}} = T_R$ and nT_R/N . For PMLG- $N_p^{x\bar{x}}$ or DUMBO $^{\phi\bar{\phi}}$, $\Delta\tau_{\text{dec}}$ increment was equal to the length of basic cycle of PMLG and DUMBO sequences, respectively.

However, the sum $2\tau_{\text{dec}} + \tau_{\pi^H}$ is not necessarily equal to a multiple of the half rotor period and can be shorter than $\Delta_{\text{rec}} = qT_R/2$. Therefore, window delays, τ_{off} , during which the decoupling on the ^1H channel is turned off, must be inserted on both sides of the central π pulse to fulfill the required condition of half rotor period. Since the ^1H coherences decay rapidly during these window delays under the effect of ^1H - ^1H dipolar couplings, the lengths of these delays must be minimized to reduce signal losses by choosing

$$\tau_{d e \bar{c}} = \left\lceil \frac{\Delta_{r e \bar{c}} - \tau_{\pi^H}}{2\Delta\tau_{d e c}} \right\rceil \Delta\tau_{d e c} \quad (9)$$

where $\lfloor x \rfloor$ is the largest integer not greater than x . The τ_{off} delay is equal to

$$\tau_{\text{off}} = (\Delta_{\text{rec}} - 2\tau_{\text{dec}} - \tau_{\pi}^{\text{H}})/2 \quad (10)$$

Long τ_{off} delays decrease the signal intensity. The above equation shows that τ_{off} value depends on Δ_{rec} and τ_{dec} delays, and then can change with t_1 value. For instance, Table 1 shows that for $\nu_{\text{R}} = 62.5$ kHz and $\Delta\tau_{\text{dec}} = T_{\text{R}}$, τ_{off} delay varies by $0.5T_{\text{R}}$ between t_1 periods equal to an integer numbers of rotor periods. Then, when $\Delta t_1 = T_{\text{R}}$, i.e. an indirect spectral of $\text{SW}_1 = \nu_{\text{R}}$, a signal intensity modulation with a period of $2T_{\text{R}}$ is superimposed to the signal evolution as function of t_1 . This modulation leads to spinning sidebands at $0.5\nu_{\text{R}}$ from the centerband. These unwanted spinning sidebands can be eliminated by using $\Delta t_1 = 2T_{\text{R}}$, i.e. $\text{SW}_1 = 0.5\nu_{\text{R}}$. However, this solution reduces the spectral width along the indirect dimension. Another solution consists in using smaller increment for the decoupling sequence. For instance, for $\Delta\tau_{\text{dec}} = T_{\text{R}}/4$, τ_{off} delay does not depend on the t_1 value (see Table 1), and thus there is no spurious signal modulation.

Table 1. Ratios $\Delta_{\text{rec}}/T_{\text{R}}$, $\tau_{\text{dec}}/\Delta\tau_{\text{dec}}$ and $\tau_{\text{off}}/T_{\text{R}}$ for $^1\text{H}\{-^{13}\text{C}\}$ *D*-HMQC experiment as function of the t_1 value for two different $\Delta\tau_{\text{dec}}$ increments. These ratios were calculated at $\nu_{\text{R}} = 62.5$ kHz using $\tau_{\pi}^{\text{H}} = 2.2$ μs and $\tau_{\pi/2}^{\text{C}} = 2.0$ μs .

t_1/T_{R}	$\Delta_{\text{rec}}/T_{\text{R}}$	$\Delta\tau_{\text{dec}} = T_{\text{R}}$		$\Delta\tau_{\text{dec}} = T_{\text{R}}/4$	
		$\tau_{\text{dec}}/\Delta\tau_{\text{dec}}$	$\tau_{\text{off}}/T_{\text{R}}$	$\tau_{\text{dec}}/\Delta\tau_{\text{dec}}$	$\tau_{\text{off}}/T_{\text{R}}$
1	1.5	0	0.69	2	0.19
2	2.5	1	0.19	4	0.19
3	3.5	1	0.69	6	0.19
4	4.5	2	0.19	8	0.19

4.2 Numerical simulations

4.2.1 Simulation parameters

The simulations were performed using SPINEVOLUTION software.^[68] The powder averaging was accomplished using 2184 orientations (168 $\{\alpha_{\text{CR}}, \beta_{\text{CR}}\}$ -pairs \times 13 γ_{CR} -angles). The $\{\alpha_{\text{CR}}, \beta_{\text{CR}}, \gamma_{\text{CR}}\}$ Euler angles relate the crystallite and rotor frames. The

$\{\alpha_{CR}, \beta_{CR}\}$ -pairs were selected according to the REPULSION algorithm,^[69] whereas the γ_{CR} angle was regularly stepped from 0 to 360°. The magnetic field and spinning speed were $B_0 = 9.4$ T and $\nu_R = 32$ kHz (Figs.3 and S3) or 18.8 T and $\nu_R = 64$ kHz (Fig.4). Numerical simulations were performed for $^1\text{H}\{-^{13}\text{C}\}$ *D*-HMQC experiments. The SR4₁² dipolar recoupling sequence was applied on the ^1H channel with an rf-amplitude of $\nu_{1,\text{rec}} = 2\nu_R$, during $\tau_{\text{rec}} = 0.5$ ms. The $\pi/2$ pulses on ^1H and ^{13}C channel as well as the central ^1H π pulse were assumed ideal. Simulations were performed without decoupling on the ^1H channel during t_1 or with various decoupling schemes, including CW, C14₂⁷ ($\alpha_0\alpha_{180}$) and SAM_{*N*(2*n*)} with $N/(2n) = 2.5, 3, 3.5, 4, 4.5$ and 5. The rf field amplitudes of the decoupling sequences are indicated in the figures.

Simulations were performed for the CH-CH₂ spin system corresponding to the C ^{α} H ^{α} and C ^{β} H ^{β} ₂ groups of L-histidine HCl. The ^{13}C isotropic chemical shifts of CH and CH₂ groups were equal to 54 and 26 ppm, respectively, whereas the ^1H ones of CH and CH₂ groups were equal to 4 and 3.4 ppm. No chemical shift anisotropy (CSA) was taken into account. The initial and detected operators were H_z^α and $\text{H}^{\alpha+}$ for the C ^{α} H ^{α} cross peak and $\text{H}_{1z}^\beta + \text{H}_{2z}^\beta$ and $\text{H}_{1+}^\beta + \text{H}_{2+}^\beta$ for C ^{β} H ^{β} ₂ cross peak. The heteronuclear MQ coherences during t_1 period were selected using a two-step phase cycling of the second $\pi/2$ pulse on the ^{13}C channel. The intensities of the C ^{α} H ^{α} and C ^{β} H ^{β} ₂ cross peaks were extracted from the F₁ slices at frequency $F_2 = 4$ and 3.4 ppm, respectively, in the direct spectral dimension. The F₁ slice was obtained by Fourier Transform of the time-domain signal using 600 t_1 increments with $\Delta t_1 = 2T_R$.

4.2.2 Decoupling efficiency

Application of a decoupling sequence during t_1 period aims at improving the spectral resolution along the indirect dimension by suppressing $^1\text{H}\text{-}^1\text{H}$ and $^1\text{H}\text{-I}$ dipolar couplings. The suppression of these interactions enhances the intensity of cross peaks. In numerical simulations, the efficiency of the decoupling was estimated with the resolution enhancement factor, which corresponds to the ratio between the cross peak intensities observed with and without decoupling. Fig.3 shows this enhancement factor for CH and CH₂ peaks in $^1\text{H}\{-^{13}\text{C}\}$ *D*-HMQC spectra simulated at 9.4 T and $\nu_R = 32$ kHz. The $V_{1,\text{dec}}^{\text{rms}}$

value was equal to 100 kHz for sequences using constant rf field amplitude (CW and $C14^7_2$ ($\alpha_0\alpha_{180}$)), or $0.8N\nu_R/(2n)$ for $SAM_{N/(2n)}$ decoupling. The employed $\nu_{1,dec}^{rms}$ value for $SAM_{N/(2n)}$ corresponds to the optimal rf field amplitude for the acquisition of high-resolution 1H spectra and is also close to the optimal value determined from Fig. 2c.^[45] All decoupling methods enhance the cross peak amplitude, but the highest amplitudes are obtained using decoupling sequences $C14^7_2$ ($\alpha_0\alpha_{180}$), $SAM_{3.5}$, SAM_4 , $SAM_{4.5}$ and SAM_5 . Among these sequences, $SAM_{3.5}$ benefits from the lowest rf field requirement.

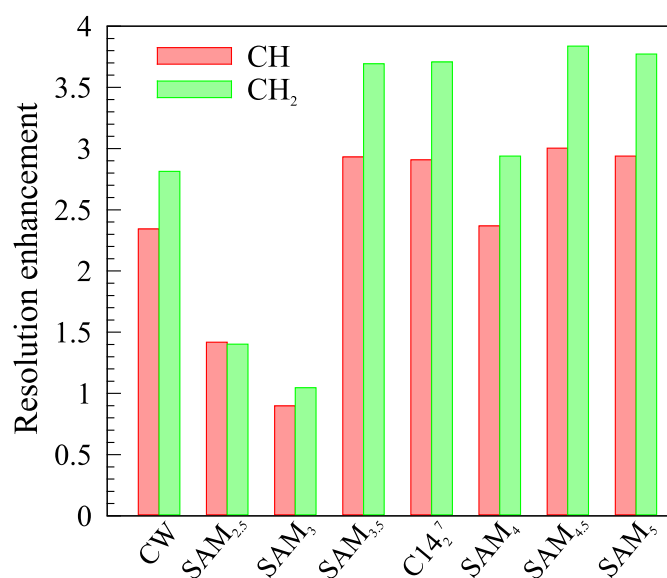


Fig.3. Resolution enhancement due to t_1 decoupling of $C^\alpha H^\alpha$ (left bar) and $C^\beta H^\beta_2$ (right bar) cross peaks in 1H - $\{^{13}C\}$ D -HMQC spectra for CH-CH₂ spin system at $B_0 = 9.4$ T, with $\nu_R = 32$ kHz and $SR4^2_1$ recoupling with $\tau_{rec} = 0.5$ ms. For CW, $SAM_{2.5}$, SAM_3 , $SAM_{3.5}$, $C14^7_2$ ($\alpha_0\alpha_{180}$), SAM_4 , $SAM_{4.5}$, and SAM_5 decoupling, $\nu_{1,dec}^{rms}$ values are equal to 100, 64, 78, 90, 100, 102, 115, and 128 kHz, respectively. $C14^7_2$ ($\alpha_0\alpha_{180}$) is shortened to $C14^7_2$ in the axis label. Additional parameters used in the simulations are indicated in the section III.1.

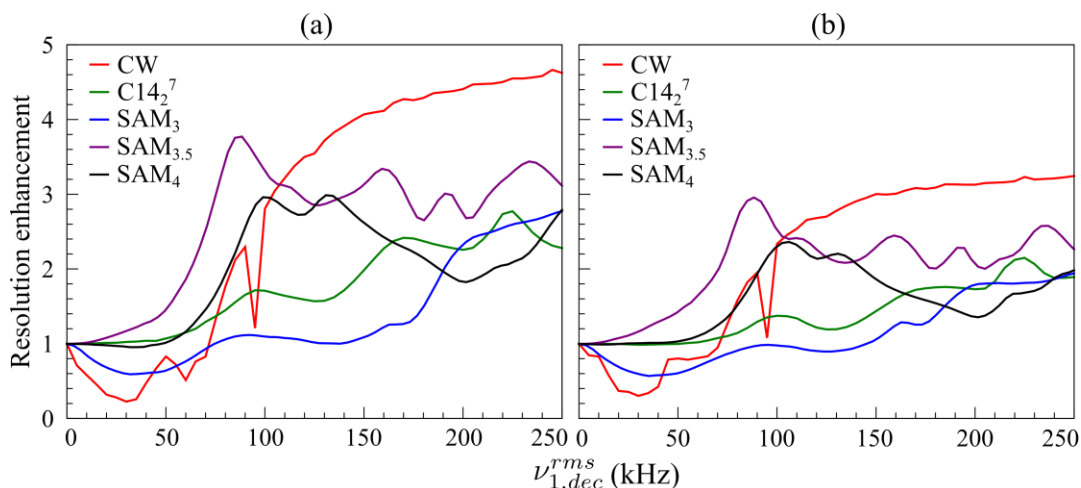


Fig.S2. Simulations of resolution enhancement due to t_1 decoupling of $C^\alpha H^\alpha$ (left) and $C^\beta H^\beta_2$ (right) cross peaks in $^1H\{-^{13}C\}$ D -HMQC spectra for $^{13}C^1H\text{-}^{13}C^1H_2$ spin system as function of $\nu_{1,dec}^{rms}$ values for various decoupling schemes at $B_0 = 9.4$ T, with $\nu_R = 32$ kHz and $SR4_1^2$ recoupling with $\tau_{rec} = 0.5$ ms

We also calculated the resolution enhancement factor in $^1H\{-^{13}C\}$ D -HMQC spectra as function of the rf field amplitude of the decoupling at 9.4 T and $\nu_R = 32$ kHz (Fig.S2), as well as 18.8 T and $\nu_R = 64$ kHz (Fig.4). These simulations confirm that R^3 conditions ($j = \frac{1}{2}, 1, 2$ and $3\dots$) have deleterious effects on CW decoupling effectiveness, which requires $\nu_{1,dec}$ values greater than $3\nu_R$ to be efficient. Furthermore, the efficiency of CW decoupling decreases for increasing MAS frequency, as already observed when CW is used as conventional heteronuclear decoupling during the acquisition.^[70,71]

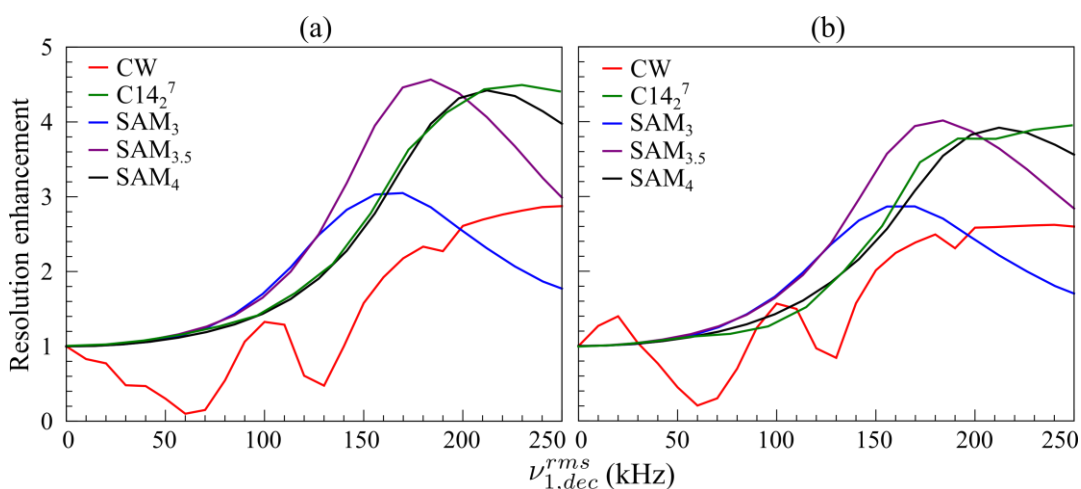


Fig.4. Resolution enhancement due to t_1 decoupling of $C^\alpha H^\alpha$ (left) and $C^\beta H^\beta_2$ (right) cross peaks in $^1H\{-^{13}C\}$ D -HMQC spectra for $CH\text{-}CH_2$ spin system as function of $\nu_{1,dec}^{rms}$ values for various decoupling schemes at $B_0 = 18.8$ T, with $\nu_R = 64$ kHz and $SR4_1^2$ recoupling with $\tau_{rec} = 0.5$ ms.

As seen in Fig.4, $SAM_{3,5}$, SAM_4 and $C14_2^7$ ($\alpha_0\alpha_{180}$) decoupling schemes result in the

highest cross peak intensities at $\nu_R = 64$ kHz. Among these sequences, SAM_{3.5} sequence requires the lowest *rms* rf field amplitude. Furthermore, the efficiencies of these symmetry-based decouplings are not depleted near R³ conditions. The maximal cross peak intensity is achieved at $V_{1,dec}^{rms} \approx 0.8N\nu_R/(2n)$ for SAM_{N/(2n)} decoupling and $V_{1,dec}^{rms} \approx 3.5\nu_R$ for C14⁷₂ ($\alpha_0\alpha_{180}$). These optimal values are similar to those determined for the acquisition of high-resolution ¹H spectra (Eq.8).^[45] Such optimal values result from a competition between the simultaneous decrease in the isotropic chemical shifts and residual ¹H-¹H dipolar coupling for increasing $V_{1,dec}^{rms}$ value (see Fig.2). The existence of these optima proves that the terms related to isotropic chemical shifts in the first-order AH of CN_n^{N/2}($\alpha_0\alpha_{180}$) and SAM sequences contribute to the elimination of ¹H-¹H dipolar couplings and the improvement of the spectral resolution along the indirect dimension.

At 9.4T and $\nu_R = 32$ kHz, maximal cross peak intensity is obtained when $V_{1,dec}^{rms} \approx 0.8N\nu_R/(2n)$ for SAM_{3.5} and SAM₄ (Fig.S2). It is noted that such optima are not observed for SAM₃ and C14⁷₂ ($\alpha_0\alpha_{180}$), which do not provide efficient decoupling at such MAS frequency.

4.3 Experimental demonstrations

4.3.1 Sample and experimental conditions

All NMR experiments were acquired on [U-¹³C]-L-histidine.HCl.H₂O (histidine hereafter) purchased from CortecNet and used without purification. 2D ¹H-¹³C *D*-HMQC spectra of histidine were acquired with and without decoupling during the t_1 period using either (i) a wide-bore Bruker Avance II 400 MHz NMR spectrometer operating at 9.4 T equipped with a triple-resonance 2.5 mm MAS probe used in double-resonance mode, or (ii) two narrow-bore Bruker Avance III 800 and 900 MHz spectrometers, operating at 18.8 and 21.1 T, equipped with a double-resonance 1.3 mm MAS probe. The ¹H and ¹³C chemical shifts are referenced to tetramethylsilane (TMS). The sample was spun at $\nu_R = 32.3, 62.5$ and 62.1 kHz at 9.4, 18.8 and 21.1 T, respectively.

^1H - ^{13}C dipolar couplings were reintroduced during defocusing and refocusing delays by applying SR4_1^2 recoupling on ^1H channel.

On Bruker Avance II spectrometer, CW, SAM_3 and SAM_4 decoupling schemes were implemented during t_1 period of D -HMQC sequence. However, for this console, the commands are executed by a single processor for all channels and hence, the pulse programs on different channels cannot be executed independently. This imposes restriction on the programming of D -HMQC sequence with decoupling during t_1 . In particular, the decoupling must start after the first $\pi/2$ ^{13}C pulse and stop before the second $\pi/2$ ^{13}C pulse, which increases the τ_{off} delay. Furthermore, the indirect spectral width (SW_1) value depends on the decoupling sequence since $\Delta t_1 = 2\Delta\tau_{\text{dec}}$. Here, $^1\text{H}\{-^{13}\text{C}\}$ D -HMQC 2D spectra of histidine were acquired at $\nu_{\text{R}} = 32.3$ kHz and 9.4 T using $\text{SW}_1 = \nu_{\text{R}}/2$, i.e. $\Delta t_1 = 2\Delta\tau_{\text{dec}} = 2T_{\text{R}}$. This $\Delta\tau_{\text{dec}}$ value is fully compatible with SAM_3 and SAM_4 sequences but not suitable for $\text{SAM}_{3.5}$ and C14_2^7 ($\alpha_0\alpha_{180}$) decoupling or for non-rotor synchronized decoupling, such as PMLG and DUMBO. Such limitation was probably the reason for the failure of PMLG decoupling with D -HMQC in reference [27].

For Bruker Avance III spectrometers (equipped with IPSO controller and topspin 3), the pulse sequence programming language allows parallel and independent instructions on each channel. This enables a versatile implementation of the decoupling during t_1 period. In particular, Δt_1 increment can be chosen independently of $\Delta\tau_{\text{dec}}$ delay. Furthermore, arbitrary back to back shaped pulse with amplitude and/or phase modulation can be defined with a time resolution of 50 ns, instead of 350 ns on Bruker Avance II console. This improved time resolution decreases phase transients for shaped decoupling, such as SAM, especially at high MAS frequency. For these spectrometers, CW, SAM_3 , $\text{SAM}_{3.5}$, SAM_4 , C14_2^7 ($\alpha_0\alpha_{180}$), PMLG-5 $\frac{x\bar{x}}{p}$, DUMBO-1 $\phi\bar{\phi}$ and eDUMBO-1 $\frac{\phi\bar{\phi}}{22}$ decouplings were applied during the t_1 period of $^1\text{H}\{-^{13}\text{C}\}$ D -HMQC experiments. The PMLG and DUMBO sequences were optimized by monitoring the intensity of a spin-echo under the decoupling conditions.[72] For these non-rotor-synchronized sequences, offset, pulse length and rf field have to be optimized.

2D $^1\text{H}\{-^{14}\text{N}\}$ DANTE- D -HMQC spectra of histidine were acquired with and without $\text{SAM}_{3.5}$ decoupling during the t_1 period using a narrow-bore Bruker Avance III 900 MHz

spectrometer operating at 21.1 T equipped with 1.3 mm MAS probe. The ^{14}N chemical shifts are referenced to the resonance of solid-state NH_4Cl compound at 0 ppm. The sample was spun at $\nu_R = 62.1$ kHz.

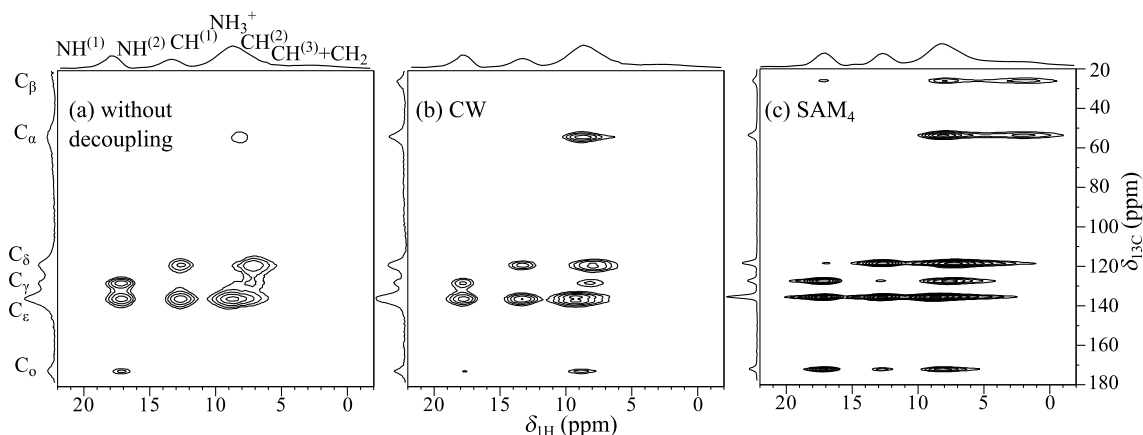


Fig.5. Experimental 2D $^1\text{H}\{-^{13}\text{C}\}$ D -HMQC spectra of histidine at 9.4 T and $\nu_R = 32.3$ kHz: (a) without decoupling, (b) with CW decoupling ($\nu_{1,dec}^{rms} = 150$ kHz), and (c) with SAM₄ decoupling ($\nu_{1,dec}^{rms} = 113$ kHz, $\Delta\tau_{dec} = T_R$). The three spectra are displayed with identical contour levels. $^1\text{H}\text{-}^{13}\text{C}$ dipolar couplings were restored using SR4₁² recoupling with $\nu_{1,rec} = 64.6$ kHz and $\tau_{rec} = 434$ μs . The rf nutation frequency of the $\pi/2$ and central π pulses on ^1H channel was equal to 108 kHz, whereas that of the $\pi/2$ ^{13}C pulses was equal to 70 kHz. The 2D spectra recorded in States-TPPI mode result from the averaging of $NS = 16$ transients for each of $N_1 = 256$ t_1 increment, with $\Delta t_1 = 2T_R$, i.e. $SW_1 = \nu_R/2$. The recycle delay was equal to 1 s, which corresponds to a total acquisition time 2h for each 2D spectrum. The ^1H and ^{13}C projections are shown in ‘skyline’ mode.

4.3.2 $^1\text{H}\{-^{13}\text{C}\}$ D -HMQC 2D experiments at 9.4 T and $\nu_R = 32.3$ kHz

Fig.5 shows the 2D $^1\text{H}\{-^{13}\text{C}\}$ D -HMQC spectra of histidine acquired without decoupling or with CW and SAM₄ decoupling during t_1 period at 9.4 T and $\nu_R = 32.3$ kHz. As expected, CW and SAM₄ decouplings improve the spectral resolution along the indirect dimension. Moreover, SAM₄ scheme achieves higher resolution than CW. In particular, the resolution improvement offered by SAM₄ decoupling facilitates the detection of $C^\beta\text{H}^\beta$ cross peaks, which are hardly visible without decoupling. More quantitatively, SAM₄ decoupling produces 6- to 23-fold increase in the signal intensity (Fig.6) with respect to spectra acquired without decoupling during t_1 period. Furthermore, the $\nu_{1,dec}^{rms}$ value of SAM₄ is lower than that of CW, which is close to the maximal rf field delivered by the ^1H channel of the probe. The $\nu_{1,dec}^{rms}$ value of SAM₄ was optimized and

its optimum value is in agreement with the predicted value (Eq.8) and with numerical simulations.

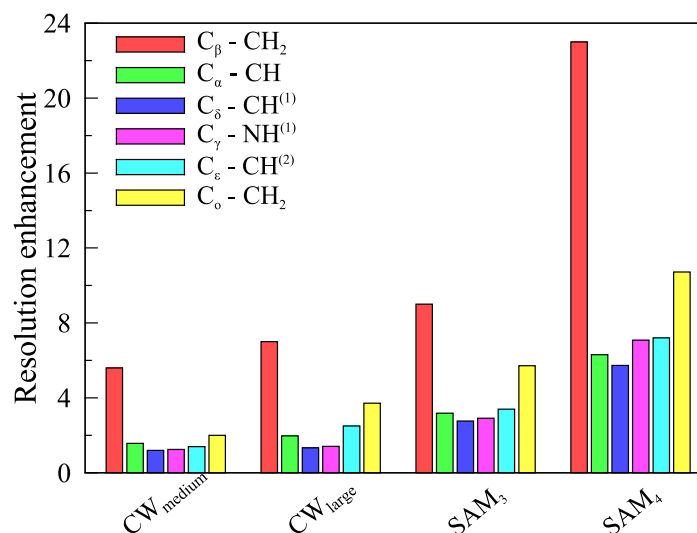


Fig.6. Resolution enhancement of the six one-bond cross-peaks in $^1H\text{-}\{^{13}C\}$ D -HMQC spectra of histidine observed at 9.4 T, with $\nu_R = 32.3$ kHz, $SW1 = \nu_R/2$, and $\Delta\tau_{dec} = T_R$ (SAM_n). The $\nu_{1,dec}^{rms}$ value is equal to 123 kHz for CW_{medium} , 175 kHz for CW_{large} , 123 kHz for SAM_3 and 113 kHz for SAM_4 . The peak intensities for SAM_4 are those of the cross peaks in the 2D spectrum of Fig.5c. Other experimental parameters are given in the caption of Fig.5.

The D -HMQC signal intensity is plotted as function of rf field amplitude of CW decoupling in Fig.S3b. As expected, CW requires $\nu_{1,dec}^{rms}$ value larger than $3\nu_R$ to avoid R^3 conditions. We also verified that the phase of the CW decoupling affects the signal D -HMQC intensity in agreement with the above explanation (see II-2-1 part and Fig.S3c). Conversely, the higher spectral resolution for SAM_4 compared to CW was not predicted by numerical simulations (see Fig.S2). This discrepancy must stem from the limited number of protons in the numerical simulations.

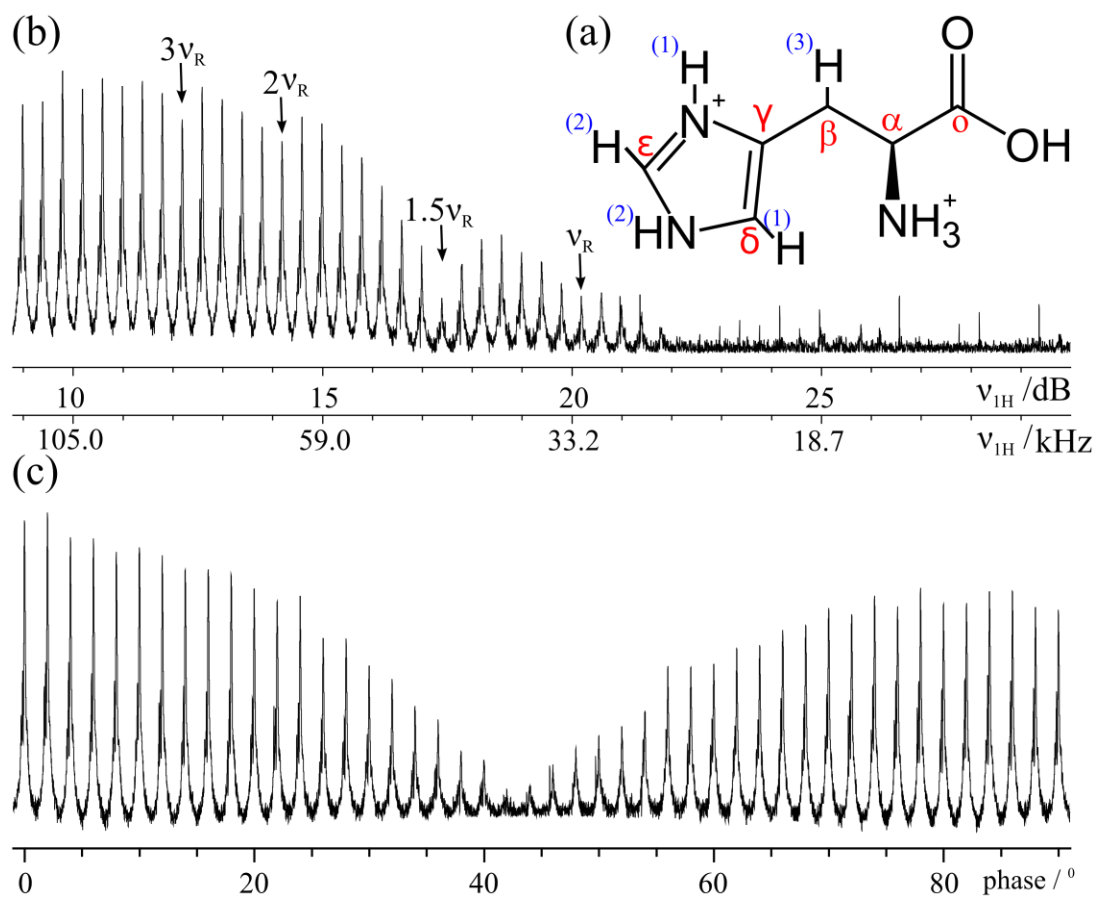


Fig.S3. (a) Histidine molecule. (b,c) Stack of experimental ^1H 1D $^1\text{H}\{-^{13}\text{C}\}$ *D*-HMQC spectra of histidine, recorded at 9.4 T, with $\nu_R = 32.3$ kHz, SR4_1^2 recoupling ($\nu_{\text{rec}} = 64.6$ kHz, $\tau_{\text{rec}} = 375$ μs), and CW decoupling applied during $t_1 = 4$ ms: (b) versus the rf-field, ν_{IH} (dB), with $\varphi = 0$, (c) versus the CW phase, φ , with $\nu_{\text{IH}} = 150$ kHz.

4.3.3 $^1\text{H}\{-^{13}\text{C}\}$ *D*-HMQC 2D experiments at 18.8 T and 21.1 T using $\nu_R \approx 62$ kHz

(a) Line narrowing

$^1\text{H}\{-^{13}\text{C}\}$ *D*-HMQC 2D experiments were also performed at high magnetic fields, 18.8 and 21.1 T, and $\nu_R \approx 62$ kHz. The range of ^{13}C isotropic chemical shifts of histidine is equal to 31 kHz at 18.8 T and 35 kHz at 21.1 T. Therefore, $\text{SW}_1 = \nu_R$ condition i.e. $\Delta t_1 = T_R$, was employed to avoid resonance folding in the ^{13}C dimension. The 18.8 and 21.1 T magnets are equipped with Bruker Avance III spectrometers, which permitted the implementation of decoupling with arbitrary $\Delta\tau_{\text{dec}}$ increment.

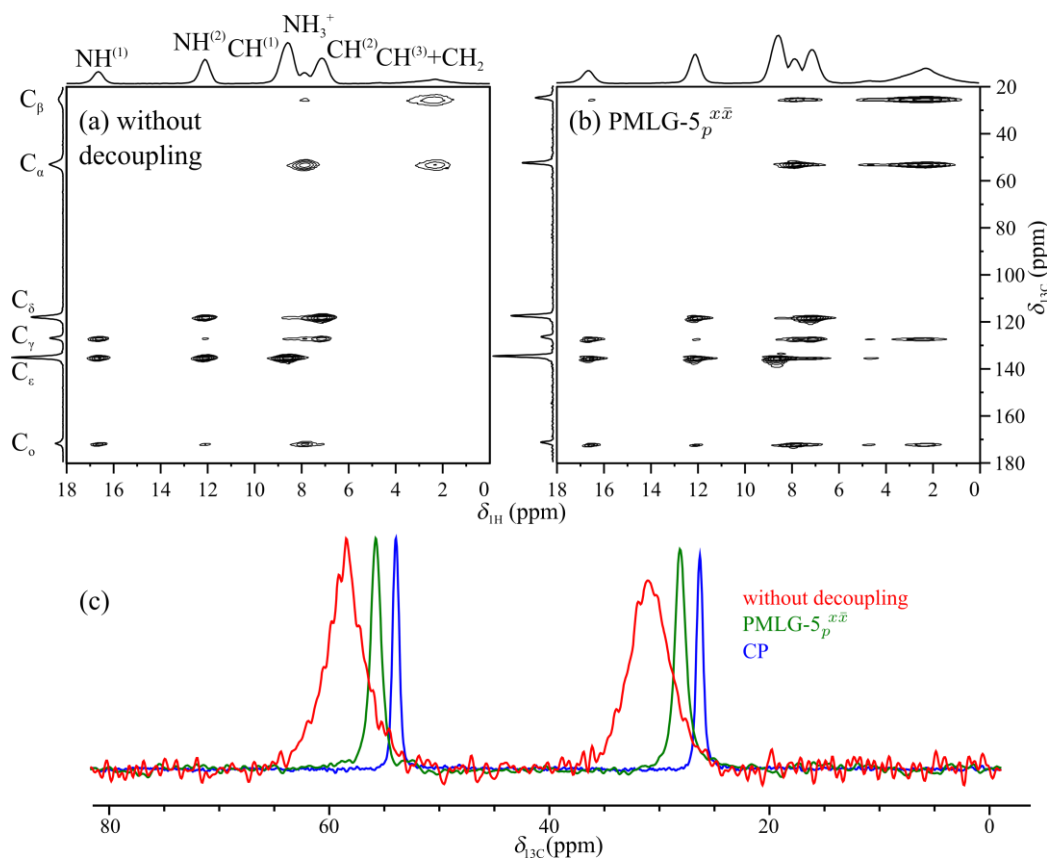


Fig.7. Experimental 2D $^1\text{H}\{-^{13}\text{C}\}$ D -HMQC spectra of histidine at 18.8 T and $\nu_R = 62.5$ kHz: (a) without decoupling and (b) with PMLG-5 $_p^{x\bar{x}}$ decoupling. The cycle time of PMLG-5 $_p^{x\bar{x}}$ is $\Delta\tau_{\text{dec}} = 13$ μs and $\nu_{1,\text{dec}}^{\text{rms}} = 227$ kHz. The two spectra are displayed with identical contour levels. $^1\text{H}\text{-}^{13}\text{C}$ dipolar couplings were restored using SR4_1^2 recoupling with $\nu_{1,\text{rec}} = 125$ kHz and $\tau_{\text{rec}} = 400$ μs . The rf nutation frequency of the $\pi/2$ and central π pulses on ^1H channel was equal to 227 kHz, whereas that of the $\pi/2$ ^{13}C pulses was equal to 220 kHz. The 2D spectra result from the averaging of $NS = 4$ transients for each of $N_1 = 1024$ t_1 increment, with $\Delta t_1 = T_R$, i.e. $\text{SW}_1 = \nu_R$. The recycle delay was equal to 1.5 s, which corresponds to a total acquisition time of 1.7 h for each 2D spectrum. Only the positive signal is shown on the spectra. The ^1H and ^{13}C projections are shown in ‘skyline’ mode. (c) Comparison of slices along the F_1 dimension at $\delta_{1\text{H}} = 2.3$ ppm of spectra shown in a) and b) with a directly observed ^{13}C CPMAS experiment recorded with SPINAL-64 heteronuclear decoupling at 300 kHz rf field and $\nu_R = 62.5$ kHz. The two spectra observed without decoupling and with PMLG-5 $_p^{x\bar{x}}$ decoupling have been shifted to the left to more easily compare their resolution with respect to that observed with CPMAS.

Fig.7 shows the 2D $^1\text{H}\{-^{13}\text{C}\}$ D -HMQC spectra of histidine acquired without decoupling or with PMLG-5 $_p^{x\bar{x}}$ decoupling during t_1 period at 18.8 T and $\nu_R = 62.5$ kHz. Fig.7c proves that one can almost achieve the same resolution in D -HMQC as in directly observed ^{13}C spectrum thanks to PMLG decoupling. Other decoupling schemes have been applied during t_1 period and the columns of the obtained spectra corresponding to H^a and H^b protons are displayed in Fig.8. In that figure, the intensities of C^b resonance have been normalized to that in the slice acquired with PMLG-5 $_p^{x\bar{x}}$ decoupling (Fig.8d).

The scaling factors are indicated on each figure since they reflect the line width along F1. Note that the spectra were made using a t_1 evolution of 8 ms which is too short in some cases to prevent truncation.

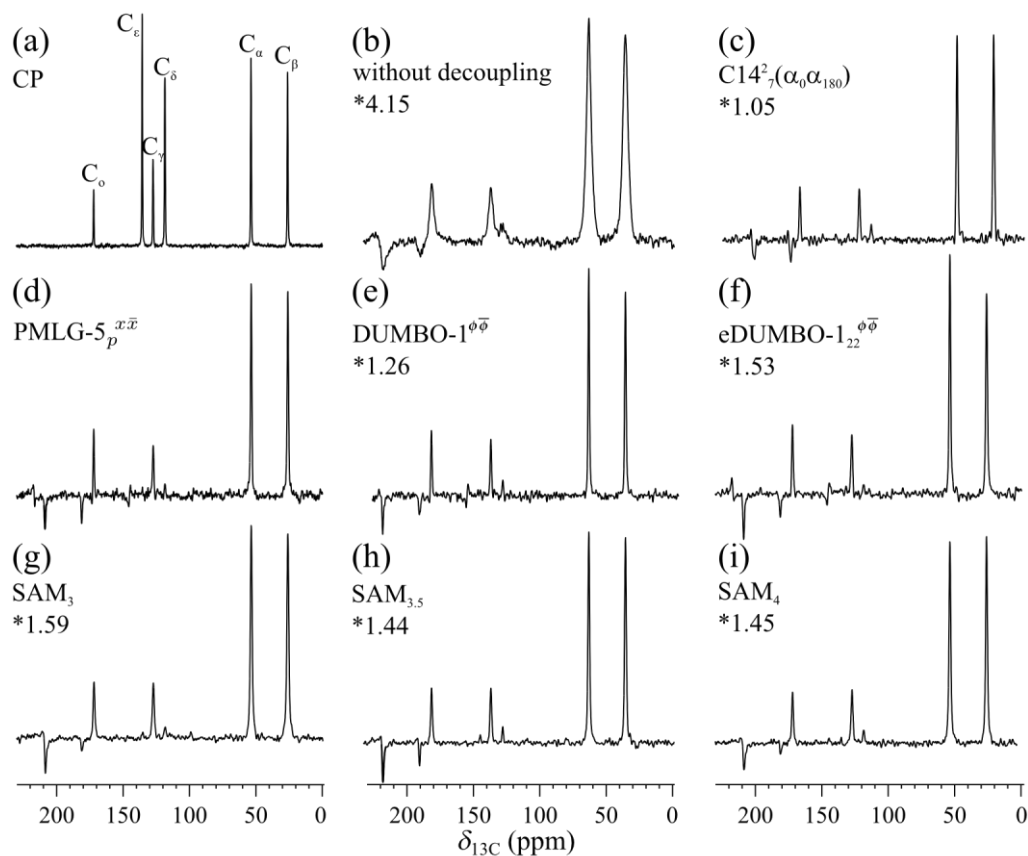


Fig.8. Comparison of the slices along the F1 dimension at $\delta_{1H} = 2.3$ ppm of experimental 2D 1H - $\{^{13}C\}$ D -HMQC spectra of histidine at 18.8 T and $\nu_R = 62.5$ kHz acquired without (b), or with (c-i) t_1 -decoupling using: (c) $C14^2_7(\alpha_0\alpha_{180})$, (d) PMLG-5 $p^{x\bar{x}}$, (e) eDUMBO-1 $_{22}^{\phi\bar{\phi}}$, (f) DUMBO-1 $^{\phi\bar{\phi}}$, (g) SAM₃, (h) SAM_{3,5}, and (i) SAM₄ scheme. The $^1H \rightarrow ^{13}C$ CP-MAS 1D spectrum using SPINAL-64 decoupling at 10 kHz rf field is shown in (a) for comparison of the resolution. The cycle time of PMLG-5 $p^{x\bar{x}}$, eDUMBO-1 $_{22}^{\phi\bar{\phi}}$ and DUMBO-1 $^{\phi\bar{\phi}}$ is $\Delta\tau_{dec} = 13$ μs and the $\nu_{1,dec}^{rms}$ value of this decoupling scheme is 227 kHz. The $\Delta\tau_{dec}$ increment is equal to T_R for SAM₃, SAM_{3,5} and SAM₄ sequences. The spectrum without decoupling during t_1 period was acquired using the pulse sequence with SAM₃ decoupling but with $\nu_{1,dec}^{rms} = 0$. The $\nu_{1,dec}^{rms}$ value for SAM₃, SAM_{3,5} and SAM₄ schemes is $227/\sqrt{2} = 160$ kHz. Other experimental parameters are given in the caption of Fig.7.

For all decoupling sequences, the same rf field peak value of 227 kHz was used, which corresponds to the maximal rf field amplitude delivered by the 1.3 mm probe. This value is close to the optimal rf field amplitude for $C14^2_7(\alpha_0\alpha_{180})$, which is about 220 kHz according to numerical simulations. A peak value of 227 kHz corresponds to $\nu_{1,dec}^{rms} = 160$

kHz for SAM decoupling, whereas according to the numerical simulations, the optimal $V_{1,dec}^{rms}$ values of SAM₃, SAM_{3.5} and SAM₄ are equal to 150, 175 and 200 kHz, respectively.

All decoupling sequences drastically improve the resolution along the F_1 dimension. The reduction in FWHM by applying decoupling ranges from 4.15 for PMLG-5 $\frac{x\bar{x}}{p}$ and C14⁷₂ ($\alpha_0\alpha_{180}$) to 2.6 for SAM₃. The decoupling efficiency can be probed from the peak intensity and decreases in the following order: PMLG-5 $\frac{x\bar{x}}{p}$, C14⁷₂ ($\alpha_0\alpha_{180}$), eDUMBO-1 $\frac{\phi\bar{\phi}}{22}$, SAM_{3.5} \approx SAM₄, DUMBO-1 $\phi\bar{\phi}$ and SAM₃. The enhancements of cross peak intensity for rotor-synchronized decoupling are in good agreement with those predicted from the numerical simulations of Fig.4. The $V_{1,dec}^{rms}$ amplitudes used for SAM_{3.5} and SAM₄ decoupling are less than the optimal values and hence higher rf-fields should achieve better line-narrowing. However, these optimal rf fields are not compatible with the specifications of the probe.

(b) t_1 noise analysis

Noise observed in indirect dimension of D -HMQC is not homogeneous over the 2D spectrum, and it is larger on columns where peaks are present (Fig.S5). This extra signal, called t_1 noise, comes from an imperfect phase cycling mostly generated by spinning speed fluctuations and rf field instabilities. Precise evaluation of this noise is difficult as it is changing with the long recycling delay time scale. In the D -HMQC case, the high sensitivity to fluctuations originates from the SR4₁² recoupling sequence. The second τ_{rec} period must refocus the dephasings related to dipolar coupling and CSA that were recoupled during the first τ_{rec} period. As SR4₁² is non- γ -encoded,^[58] very small spinning speed fluctuations, as small as 1 Hz, can modulate significantly the intensity of unwanted signals. Instabilities of rf field should be a bit less critical since SR4₁² is rather robust with this respect.^[60] Such fluctuations between two scans will prevent a clean phase cycling. Hence t_1 noise is proportional to the unfiltered proton signal. When increasing transverse relaxation through homonuclear decoupling one increases this unfiltered signal at large t_1 values and hence the noise it produces. Such behavior can be observed in Fig.S4 for SAM_{3.5} decoupling, where one observes that the noise level increases with the rf-field. Fortunately, the overall S/N ratio also increases with better decoupling. However,

for very large rf field, at the limit of probe handling, noise increases faster. This may be due to heating produced by decoupling that could perturb the rotation or to rf field instabilities. All decoupling sequences are not equal with respect to rf field instabilities. For example, DUMBO generally requires higher power than PMLG or SAM. Moreover, phase transients produce voltage overshoots that can trigger rf instabilities. SAM is free of such transients and its rms rf field amplitude is lower. This can explain why we generally observed less t_1 noise in SAM experiments.

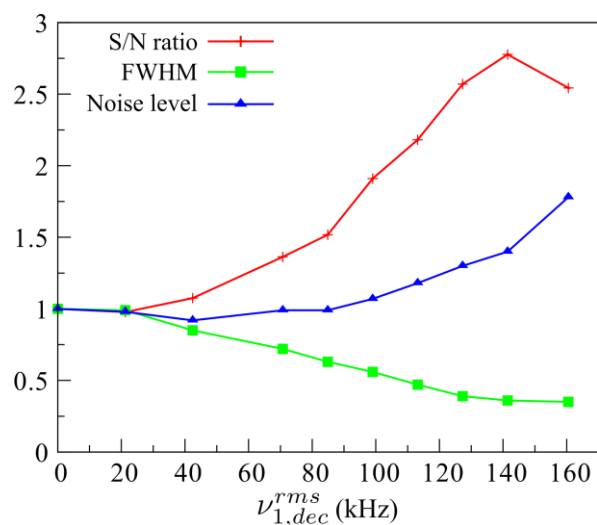


Fig.S4. Experimental line-width (FWHM), rms amplitude of the noise (Noise level), and S/N ratio of the $C^\beta H_2^\beta$ cross-peak versus $\nu_{1,dec}^{rms}$ value for 2D 1H - ^{13}C D -HMQC spectra of histidine at 18.8 T and $\nu_R = 62.5$ kHz acquired with SAM_{3,5} decoupling during t_1 period. FWHM, Noise level, and S/N ratio are normalized with respect to those observed without decoupling. $\Delta t_1 = T_R = 16 \mu s$ ($SW1 = \nu_R$), $\Delta \tau_{dec} = T_R$, $N_{t1} = 1024$, $NS = 4$, and $\tau_{rd} = 1.5$ s.

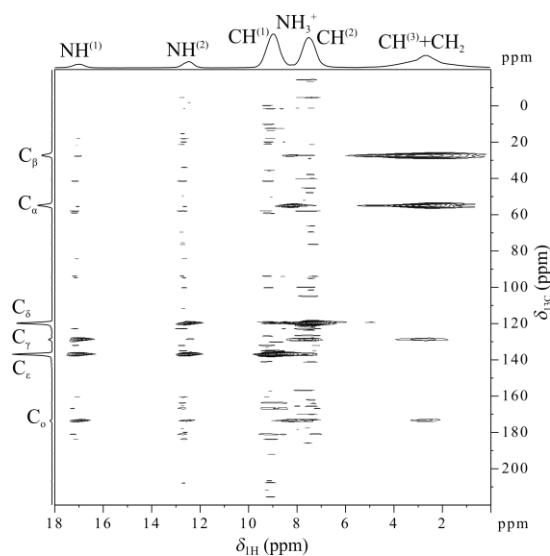


Fig.S5. Experimental 1H - ^{13}C D -HMQC spectrum of histidine recorded at 21.1 T with $\nu_R = 62.1$ kHz,

$SW_1 = \nu_R$, $SR4_1^2$ recoupling ($\tau_{rec} = 12T_R = 193 \mu s$, and $\nu_{1rec} = 2\nu_R = 124.2 \text{ kHz}$), $SAM_{3,5}$ decoupling with $\Delta\tau_{dec} = T_R/3.5 = 4.57 \mu s$, and $\nu_{1,dec}^{rms} = 130 \text{ kHz}$. The rf nutation frequency of the $\pi/2$ and central π pulses on 1H channel was equal to 178 kHz, whereas that of the $\pi/2$ ^{13}C pulses was equal to 109 kHz. The 2D spectrum results from the averaging of $NS = 4$ transients for each of $N_1 = 744$ t_1 increment, with $\Delta t_1 = T_R$, i.e. $SW_1 = \nu_R$. The recycle delay was equal to 2 s, which corresponds to a total acquisition time of 1.7 h for each 2D spectrum. The 1H and ^{13}C projections are shown in 'skyline' mode.

Finally, one must say that in fully ^{13}C enriched histidine, t_1 noise is limited because most protons are involved in the filtered signal. On the contrary, in the case of natural abundance samples, a large number of protons are not close to ^{13}C nuclei. They are thus only producing t_1 noise, but not signal. In a general way, t_1 noise becomes critical when the ratio phase cycled filtered/unfiltered signal is low. Probes with gradients may overcome this limitation but they do not exist yet for solids with gradient strength compatible with short timings. Since gradient filtered HMQC requires extra π -pulses it would not be a solution when used for integer spins, e.g. ^{14}N , as their magnetizations cannot be efficiently inverted.

(c) Artfactual spinning sidebands

The slices, shown in Fig.8, also exhibit negative sidebands separated by $0.5\nu_R$ from the center-bands of C^α and C^β peaks. These sidebands come from an extra delay before and after the recoupling parts that is modulated to keep rotor synchronized the proton echo pulses [60].

For rotor-synchronized decoupling sequences, we used an increment of $\Delta\tau_{dec} = T_R$. For $\Delta t_1 = T_R$, this increment results in a modulation of the signal intensity with a period of $2T_R$ (Table.1), which produces sidebands separated by $0.5\nu_R$ from the centerbands. Similar sidebands are also obvious in the slice without decoupling (see Fig.8b) since it was acquired with the sequence incorporating SAM_3 decoupling, but using $\nu_{1,dec}^{rms} = 0$.

For non-rotor-synchronized decoupling sequences, the $\Delta\tau_{dec}$ increment and hence the τ_{off} value, are not commensurable with T_R . In addition to the negative sidebands every $0.5\nu_R$, this leads to folded modulation sidebands spread across SW_1 , which translate into additional t_1 -noise.

Sidebands separated by $0.5\nu_R$ are particularly undesired since they can overlap with real signals, and consequently, a solution to reduce them is required. They can be

minimized by using a shorter $\Delta\tau_{\text{dec}}$ increment, which reduces the length of τ_{off} delay and its modulation (Table 1). This solution was tested by acquiring 2D $^1\text{H}\{-^{13}\text{C}\}$ D -HMQC spectrum of histidine at 21.1 T and $\nu_{\text{R}} = 62.1$ kHz using $\text{SAM}_{3.5}$ decoupling with $\Delta\tau_{\text{dec}} = T_{\text{R}}/3.5$, the length of a full cosine pulse, and $\Delta t_1 = T_{\text{R}}$. The 2D spectrum is displayed in Fig.S5, and Fig.S6 shows that the application of $\text{SAM}_{3.5}$ reduces FWHM by a factor of 3, 2.6 and 1.8 for C^β , C^α and C' resonances, respectively, even if the $\nu_{1,\text{dec}}^{\text{rms}}$ value of 130 kHz is much lower than its optimal value of 174 kHz. As expected, the resolution enhancement is higher for the $\text{C}^\beta\text{H}_2^\beta$ cross peak since the methylene protons experience larger dipolar couplings. Furthermore, the spectrum acquired with $\Delta\tau_{\text{dec}} = T_{\text{R}}/3.5$ exhibits very weak spinning sidebands separated by $0.5\nu_{\text{R}}$ from the centerband (Fig.9c). Short decoupling increment $\Delta\tau_{\text{dec}} = nT_{\text{R}}/(2N)$ can be easily implemented for $\text{CN}_n^{N/2}$ symmetries, including SAM, using parallel programming available on Bruker Avance III spectrometer.

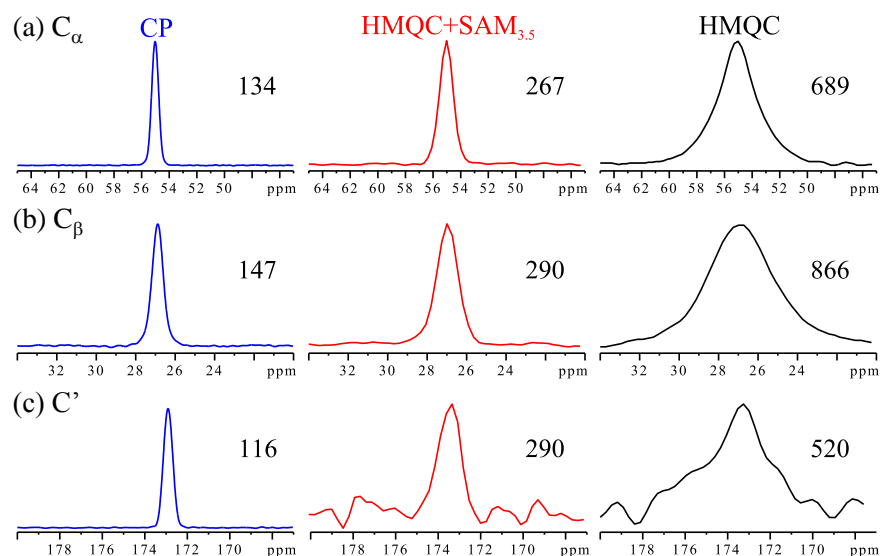


Fig.S6. Spectral regions centered on (a) C^α , (b) C^β , and (c) C' resonances in the experimental 1D $^1\text{H}\rightarrow^{13}\text{C}$ CP-MAS spectrum (left column) and in the F_1 slices at $\delta_{1\text{H}} = 2.3$ ppm extracted from experimental 2D $^1\text{H}\{-^{13}\text{C}\}$ D -HMQC spectra (middle and right columns) of histidine at 21.1 T and $\nu_{\text{R}} = 62.1$ kHz. The regions displayed in the middle and right columns are extracted from D -HMQC spectra with $\text{SAM}_{3.5}$ decoupling or without decoupling during t_1 period. $\text{SAM}_{3.5}$ decoupling was achieved using $\nu_{1,\text{dec}}^{\text{rms}} = 130$ kHz and $\Delta\tau_{\text{dec}} = T_{\text{R}}/3.5 = 4.57$ μs . The 2D $^1\text{H}\{-^{13}\text{C}\}$ D -HMQC spectrum with $\text{SAM}_{3.5}$ decoupling is shown in Fig.S5. FWHM of the resonance are indicated in the figure. $^1\text{H}\rightarrow^{13}\text{C}$ CP-MAS transfer was achieved using rf nutation frequencies of 178 and 89 for $\pi/2$ pulse and spin lock on the ^1H channel and 27 for the spin lock on the ^{13}C channels, the CP contact time was 3 ms and SPINAL-64 decoupling with $\nu_{1,\text{dec}}^{\text{rms}} = 11$

kHz was applied to the ^1H channel during the acquisition. Other experimental parameters are given in the caption of Fig.S5.

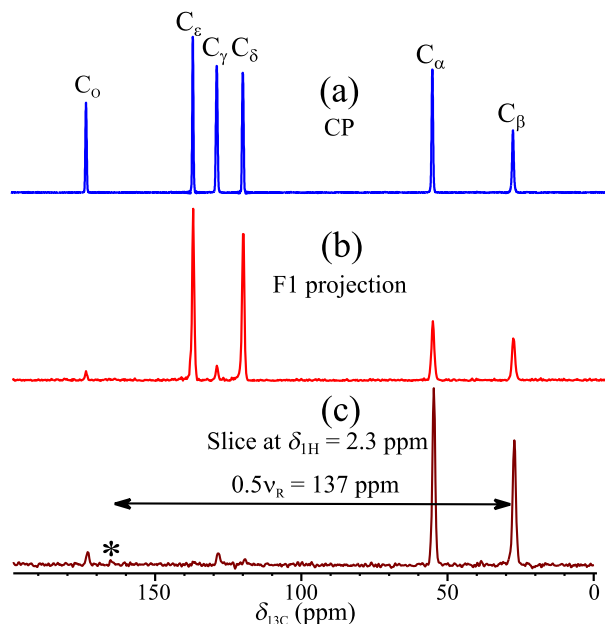


Fig.9. Comparison for histidine sample of (a) the experimental 1D $^1\text{H} \rightarrow ^{13}\text{C}$ CP-MAS spectrum with SPINAL-64 ^1H decoupling, (b) the ^{13}C projection and (c) the F_1 slice at $\delta_{1\text{H}} = 2.3$ ppm of $^1\text{H}\{-^{13}\text{C}\}$ D-HMQC spectrum (Fig.S6) using SAM_{3,5} decoupling during t_1 period. The spectra are acquired at 21.1 T and $\nu_R = 62.1$ kHz. In (c), the peak labeled with * corresponds to a spurious sideband of C^β resonance. Other experimental parameters are given in the caption of Fig.S7.

4.3.4 Application to $^1\text{H}\{-^{14}\text{N}\}$ DANTE-D-HMQC at 21.1 T and $\nu_R = 62.1$ kHz

It has been shown during the last few years the possibility to probe the local environment of nitrogen atoms by NMR taking advantage of its 99.6 % natural abundance.^{[21–37],[73–76]} This method avoids time consuming and expensive ^{15}N enrichments. However, the direct detection of ^{14}N nuclei is still challenging since ^{14}N isotope has a nuclear spin equal to 1, a small gyromagnetic ratio ($\gamma(^{14}\text{N})/\gamma(^1\text{H}) = 0.07$) and is submitted to a quadrupole interaction that is often of several MHz, yielding broad powder pattern. The indirect detection of ^{14}N nuclei via ^1H is usually preferred because it benefits from higher sensitivity.^{[21–37],[74,75]} In particular, $^1\text{H}\{-^{14}\text{N}\}$ D-HMQC sequence is generally the most sensitive technique to detect ^{14}N nuclei. The rotor-synchronization of Δt_1 increment leads to the folding of all spinning sidebands onto the centerbands in F_1 dimension. High magnetic field is recommended as: (i) it decreases the second-order ^{14}N line-widths along F_1 , (ii) it increases the chemical shift differences, and (iii) consequently decreases the ^1H line-widths along F_2 . High MAS frequency is also advantageous since it

(i) decreases signal losses due to ^1H - ^1H dipolar couplings, (ii) enhances the resolution along F2, and (iii) enlarges SW_1 . The use of probes with small diameter coil also increases the maximal accessible rf field amplitude. Unfortunately, owing to the low $\gamma(^{14}\text{N})$ ratio, the maximal ν_1 value on ^{14}N channel lies usually around 80 kHz for 1.3 mm double-resonance probe. This rf field is relatively small compared to the magnitude of the first-order quadrupolar interaction and short rectangular pulses using such rf field excite ^{14}N SQ coherences with a modest efficiency. Recently, it has been proved that these coherences can be excited with a higher efficiency by replacing the rectangular pulses by D_N^K schemes.^[35] The D_N^K excitation profile is composed of a comb shape which excites spectral regions separated by $N\nu_R$ from the carrier frequency over a few MHz.^[61,77,78] Hence, these schemes provide a uniform excitation of families of sidebands spread over a few MHz. Furthermore, decoupling during the t_1 period of the 2D ^1H - $\{^{14}\text{N}\}$ D -HMQC experiments has been demonstrated to enhance the resolution of the ^{14}N dimension for solid-state amino-acids.^[27]

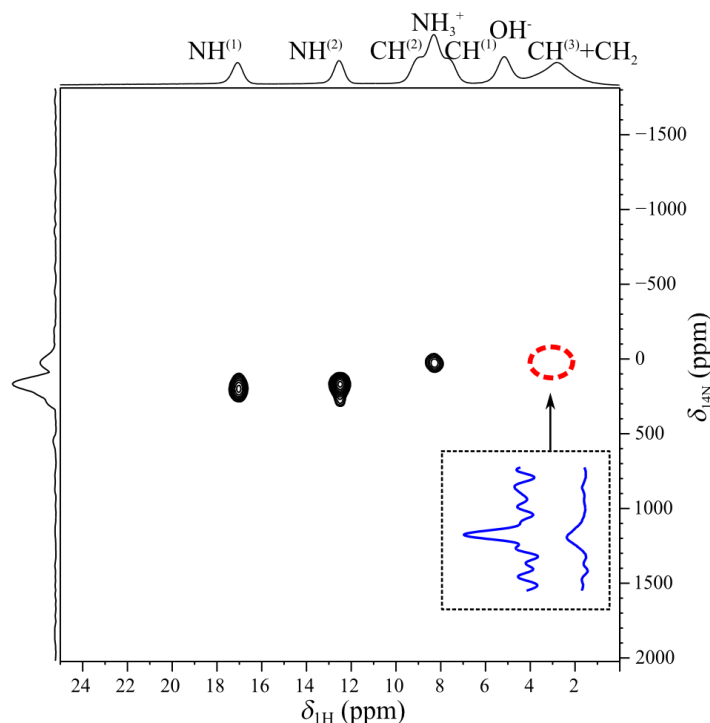


Fig. 10. Experimental 2D ^1H - $\{^{14}\text{N}\}$ DANTE- D -HMQC spectra of histidine at 21.1 T and $\nu_R = 62.1$ kHz with SAM_{3.5} decoupling using $\nu_{1,dec}^{rms} = 167$ kHz and $\Delta\tau_{dec} = T_R/3.5 = 4.57$ μs . The cross-peak between ammonium ^{14}N nucleus and the H^α and H^β protons is only visible at lower contour level in the red dotted circle. This correlation is only apparent with long recoupling times, and is more intense with (left) than without (right) t_1 -decoupling as shown in the expansion below. ^1H - ^{13}C dipolar couplings were restored

using SR4_1^2 recoupling with $\nu_{1,\text{rec}} = 2\nu_{\text{R}} = 124.2$ kHz and $\tau_{\text{rec}} = 24T_{\text{R}} = 386$ μs . The rf nutation frequency of the $\pi/2$ and central π pulses on ^1H channel was equal to 208 kHz. ^{14}N coherences were excited and reconverted using D^3_4 scheme using rf field nutation frequency of 58 kHz and pulse length of 1 μs . A four-fold over-sampling of the ^1H signal has been used, $\Delta t_1 = T_{\text{R}}/4$, leading to the very large spectral width of $\text{SW}_1 = 4\nu_{\text{R}} = 248.4$ kHz. The 2D spectra result from the averaging of $NS = 32$ transients for each of $N_1 = 100$ t_1 increments, with $\Delta t_1 = T_{\text{R}}/2$, i.e. $\text{SW}_1 = 4\nu_{\text{R}}$. The recycle delay was equal to 2 s, which corresponds to a total acquisition time of 2 h for each 2D spectrum. The ^1H and ^{14}N projections are shown in ‘skyline’ mode.

We have recorded such $^1\text{H}\{-^{14}\text{N}\}$ 2D spectra of histidine at 21.1 T, with $\nu_{\text{R}} = 62.1$ kHz, two D^3_4 Dante pulses on the ^{14}N channel, and a four-fold over-sampling of ^1H signal. In Fig.10, we show the 2D $^1\text{H}\{-^{14}\text{N}\}$ DANTE-*D*-HMQC spectrum recorded with $\text{SAM}_{3.5}$ t_1 -decoupling and $\tau_{\text{rec}} = 24T_{\text{R}} = 386$ μs .

Three one-bond $^1\text{H}\text{-}^{14}\text{N}$ cross-peaks are noticeable in Fig.10, which correspond to N-H distance of 104 pm, i.e. a dipolar coupling constant $|\text{b}_{1\text{H}\text{-}14\text{N}}/(2\pi)| = 7.7$ kHz. At lower contour level, a cross peak between ammonium ^{14}N nucleus and H^α and H^β protons can also be observed within the red dotted circle. The lower intensity of this cross peak arises from the longer N-H distances. For instance, H^α proton is distant by 209 pm from ammonium NH_3^+ nucleus and the dipolar coupling constant between these nuclei is only $|\text{b}_{1\text{H}\text{-}14\text{N}}/(2\pi)| = 950$ Hz.

This cross-peak is also related to $^1\text{H}\text{-}^1\text{H}$ homogeneous dipolar interactions that are more difficult to decouple with the ultra-fast spinning speed alone. The amplitude of this cross-peak increases with the recoupling time, and as example it was not observed with $\tau_{\text{rec}} = 12T_{\text{R}} = 193$ μs . It also increases by performing a t_1 -decoupling which decreases the line-width by a factor of ca. two, as shown in the expansion below the red circle. For ammonium protons, the resolution improvement is limited to 10%, since the tumbling of NH_3 group already diminishes the magnitude of $^1\text{H}\text{-}^1\text{H}$ dipolar coupling. $\text{SAM}_{3.5}$ was employed since it minimizes the t_1 -noise (see Fig.8), because high S/N is required to detect such small correlation between ammonium ^{14}N nucleus and $\text{H}^{\alpha,\beta}$ protons

4.4 Conclusions

We showed that the spectral resolution along the indirect dimension of proton-detected HMQC spectra can be enhanced by applying decoupling schemes during the t_1 period to a level close to best directly observed decoupled CP spectra. The

performances of various decoupling schemes were compared. We demonstrated that ^1H - ^1H dipolar decoupling sequences, such as SAM, $\text{C14}^{7_2}(\alpha_0\alpha_{180})$, PMLG or DUMBO, yield better spectral resolution than CW. Furthermore, the preservation of ^1H isotropic chemical shifts during the decoupling scheme improves the elimination of ^1H - ^1H dipolar couplings. At $\nu_{\text{R}} = 62$ kHz, we recorded a *D*-HMQC spectrum using PMLG sequence, the resolution of which matches the resolution of directly observed ^{13}C . Resolution improvement for SAM sequences was limited by the specifications of the 1.3 mm probe, since the optimal peak rf field amplitude for $\text{SAM}_{3.5}$ and SAM_4 exceeds the maximal rf field the probe can deliver. At $\nu_{\text{R}} \approx 32$ kHz, similar spectral resolutions were obtained using $\text{C14}^{7_2}(\alpha_0\alpha_{180})$, $\text{SAM}_{3.5}$ and SAM_4 since all decoupling schemes were applied at optimal rf field value. Hardware limitations of AVII consoles did not allow using non rotor synchronized sequences like PMLG or DUMBO. Thanks to transient free pulses, Smoothed Amplitude Modulation generally produced spectra with reduced t_1 noise levels, which is beneficial for the observation of weak long-range correlations. Furthermore, symmetry-based decoupling schemes, such as SAM and $\text{C14}^{7_2}(\alpha_0\alpha_{180})$, do not require any optimization, whereas rotor-unsynchronized sequences, such as PMLG and DUMBO, require the optimization of three parameters, the pulse length, the rf field and the offset. Moreover, artifactual spinning sidebands due to the modulation of window delays can be strongly reduced for symmetry-based sequences. Experimentally, the independent execution of pulse sequences on each channel using Bruker Avance III spectrometer greatly facilitates the implementation of decoupling schemes, especially the unsynchronized ones.

References:

- [1] D.C. Apperley, R.K. Harris, P. Hodgkinson, *Solid State NMR: Basic Principle & Practice*, Momentum Press, New York, 2012.
- [2] S.E. Ashbrook, D.M. Dawson, J.M. Griffin, *Solid-State Nuclear Magnetic Resonance Spectroscopy*, in: D.W. Bruce, D. O'Hare, R.I. Walton (Eds.), *Local Struct. Charact.*, John Wiley & Sons, Ltd, 2014: pp. 1–88.
- [3] J.-P. Amoureux, J. Trébosc, L. Delevoye, O. Lafon, B. Hu, Q. Wang, *Correlation NMR spectroscopy involving quadrupolar nuclei.*, *Solid State Nucl. Magn. Reson.* 35 (2009) 12–18.

- [4] M. Deschamps, D. Massiot, Correlation Experiments Involving Half-integer Quadrupolar Nuclei, *eMagRes*. (2011).
- [5] A.A. Maudsley, R.R. Ernst, Indirect Detection of Magnetic Resonance by Heteronuclear Two-dimensional Spectroscopy, *Chem. Phys. Lett.* 50 (1977) 368–372.
- [6] L. Müller, Sensitivity enhanced detection of weak nuclei using heteronuclear multiple quantum coherence, *J. Am. Chem. Soc.* 101 (1979) 4481–4484.
- [7] G. Bodenhausen, D.J. Ruben, Natural abundance nitrogen-15 NMR by enhanced heteronuclear spectroscopy, *Chem. Phys. Lett.* 69 (1980) 185–189.
- [8] Y. Ishii, R. Tycko, Sensitivity Enhancement in Solid State ^{15}N NMR by Indirect Detection with High-Speed Magic Angle Spinning, *J. Magn. Reson.* 142 (2000) 199–204.
- [9] Y. Ishii, J.P. Yesinowski, R. Tycko, Sensitivity enhancement in solid-state (^{13}C) NMR of synthetic polymers and biopolymers by (^1H) NMR detection with high-speed magic angle spinning., *J. Am. Chem. Soc.* 123 (2001) 2921–2922.
- [10] I. Schnell, B. Langer, S.H. Söntjens, M.H. van Genderen, R.P. Sijbesma, H.W. Spiess, Inverse detection and heteronuclear editing in ^1H - ^{15}N correlation and ^1H - ^1H double-quantum NMR spectroscopy in the solid state under fast MAS., *J. Magn. Reson.* 150 (2001) 57–70.
- [11] I. Schnell, K. Saalwächter, ^{15}N - ^1H bond length determination in natural abundance by inverse detection in fast-MAS solid-state NMR spectroscopy., *J. Am. Chem. Soc.* 124 (2002) 10938–10939.
- [12] B. Reif, R.G. Griffin, ^1H detected ^1H , ^{15}N correlation spectroscopy in rotating solids., *J. Magn. Reson.* 160 (2003) 78–83.
- [13] V. Chevelkov, B.J. van Rossum, F. Castellani, K. Rehbein, A. Diehl, M. Hohwy, et al., ^1H detection in MAS solid-state NMR spectroscopy of biomacromolecules employing pulsed field gradients for residual solvent suppression., *J. Am. Chem. Soc.* 125 (2003) 7788–7789.
- [14] J.W. Wiench, C.E. Bronnimann, V.S.-Y. Lin, M. Pruski, Chemical shift correlation NMR spectroscopy with indirect detection in fast rotating solids: studies of organically functionalized mesoporous silicas., *J. Am. Chem. Soc.* 129 (2007) 12076–12077.
- [15] D.H. Zhou, J.J. Shea, A.J. Nieuwkoop, W.T. Franks, B.J. Wylie, C. Mullen, et al., Solid-state protein-structure determination with proton-detected triple-resonance 3D magic-angle-spinning NMR spectroscopy., *Angew. Chem. Int. Ed. Engl.* 46 (2007) 8380–8383.
- [16] D.H. Zhou, G. Shah, M. Cormos, C. Mullen, D. Sandoz, C.M. Rienstra, Proton-detected solid-state NMR spectroscopy of fully protonated proteins at 40 kHz magic-angle spinning., *J. Am. Chem. Soc.* 129 (2007) 11791–11801.

- [17] D.H. Zhou, C.M. Rienstra, Rapid analysis of organic compounds by proton-detected heteronuclear correlation NMR spectroscopy with 40 kHz magic-angle spinning., *Angew. Chem. Int. Ed. Engl.* 47 (2008) 7328–7331.
- [18] K. Mao, M. Pruski, Directly and indirectly detected through-bond heteronuclear correlation solid-state NMR spectroscopy under fast MAS., *J. Magn. Reson.* 201 (2009) 165–174.
- [19] D.H. Zhou, G. Shah, C. Mullen, D. Sandoz, C.M. Rienstra, Proton-detected solid-state NMR spectroscopy of natural-abundance peptide and protein pharmaceuticals., *Angew. Chem. Int. Ed. Engl.* 48 (2009) 1253–1256.
- [20] S.M. Althaus, K. Mao, J.A. Stringer, T. Kobayashi, M. Pruski, Indirectly detected heteronuclear correlation solid-state NMR spectroscopy of naturally abundant ^{15}N nuclei, *Solid State Nucl. Magn. Reson.* (2013) 1–5.
- [21] S. Cavadini, S. Antonijevic, A. Lupulescu, G. Bodenhausen, Indirect detection of nitrogen-14 in solids via protons by nuclear magnetic resonance spectroscopy., *J. Magn. Reson.* 182 (2006) 168–72.
- [22] S. Cavadini, A. Abraham, G. Bodenhausen, Proton-detected nitrogen-14 NMR by recoupling of heteronuclear dipolar interactions using symmetry-based sequences, *Chem. Phys. Lett.* 445 (2007) 1–5.
- [23] S. Cavadini, S. Antonijevic, A. Lupulescu, G. Bodenhausen, Indirect detection of nitrogen-14 in solid-state NMR spectroscopy., *Chemphyschem.* 8 (2007) 1363–1374.
- [24] Z. Gan, J.-P. Amoureux, J. Trébosc, Proton-detected ^{14}N MAS NMR using homonuclear decoupled rotary resonance, *Chem. Phys. Lett.* 435 (2007) 163–169.
- [25] S. Antonijevic, N. Halpern-Manners, Probing amide bond nitrogens in solids using ^{14}N NMR spectroscopy., *Solid State Nucl. Magn. Reson.* 33 (2008) 82–87.
- [26] S. Cavadini, A. Abraham, G. Bodenhausen, Coherence transfer between spin nuclei and nitrogen-14 in solids., *J. Magn. Reson.* 190 (2008) 160–164.
- [27] S. Cavadini, V. Vitzthum, S. Ulzega, A. Abraham, G. Bodenhausen, Line-narrowing in proton-detected nitrogen-14 NMR, *J. Magn. Reson.* 202 (2010) 57–63.
- [28] Y. Nishiyama, Y. Endo, T. Nemoto, H. Utsumi, K. Yamauchi, K. Hioka, et al., Very fast magic angle spinning (^1H - ^{14}N) 2D solid-state NMR: sub-micro-liter sample data collection in a few minutes., *J. Magn. Reson.* 208 (2011) 44–48.
- [29] A.L. Webber, S. Masiero, S. Pieraccini, J.C. Burley, A.S. Tatton, D. Iuga, et al., Identifying guanosine self assembly at natural isotopic abundance by high-resolution ^1H and ^{13}C solid-state NMR spectroscopy., *J. Am. Chem. Soc.* 133 (2011) 19777–19795.

- [30] A.S. Tatton, T.N. Pham, F.G. Vogt, D. Iuga, A.J. Edwards, S.P. Brown, Probing intermolecular interactions and nitrogen protonation in pharmaceuticals by novel ^{15}N -edited and 2D ^{14}N - ^1H solid-state NMR, *CrystEngComm*. 14 (2012) 2654–2659.
- [31] K. Maruyoshi, D. Iuga, O.N. Antzutkin, S.P. Velaga, S.P. Brown, Identifying the intermolecular hydrogen-bonding supramolecular synthons in an indomethacin – nicotinamide cocrystal by solid-state NMR, *Chem. Commun.* 48 (2012) 10844–10846.
- [32] A.S. Tatton, T.N. Pham, F.G. Vogt, D. Iuga, A.J. Edwards, S.P. Brown, Probing Hydrogen Bonding in Cocrystals and Amorphous Dispersions Using $^{14}\text{N} - ^1\text{H}$ HMQC Solid-State NMR, *Mol. Pharm.* 10 (2013) 999–1007.
- [33] B. Bouchevreau, C. Martineau, C. Mellot-draznieks, A. Tuel, M.R. Suchomel, J. Trépośc, et al., High-Resolution Structural Characterization of Two Layered Aluminophosphates by Synchrotron Powder Diffraction and NMR Crystallographies, *Chem. Mater.* 25 (2013) 2227–2242.
- [34] J. Wack, T. Ahnfeldt, N. Stock, J. Senker, Identifying Selective Host – Guest Interactions Based on Hydrogen Bond Donor – Acceptor Pattern in Functionalized Al-MIL-53 Metal – Organic Frameworks, *J. Phys. Chem. C*. 117 (2013) 11991–20001.
- [35] V. Vitzthum, M.A. Caporini, S. Ulzega, G. Bodenhausen, Broadband excitation and indirect detection of nitrogen-14 in rotating solids using Delays Alternating with Nutation (DANTE)., *J. Magn. Reson.* 212 (2011) 234–239.
- [36] Y. Nishiyama, M. Malon, Z. Gan, Y. Endo, T. Nemoto, Proton – nitrogen-14 overtone two-dimensional correlation NMR spectroscopy of solid-sample at very fast magic angle sample spinning, *J. Magn. Reson.* 230 (2013) 160–164.
- [37] L.A. O'Dell, R. He, J. Pandohee, Identifying H–N proximities in solid-state NMR using ^{14}N overtone irradiation under fast MAS, *CrystEngComm*. 15 (2013) 8657–8667.
- [38] O. Lafon, Q. Wang, B. Hu, F. Vasconcelos, J. Trépośc, S. Cristol, et al., Indirect detection via spin-1/2 nuclei in solid state NMR spectroscopy: application to the observation of proximities between protons and quadrupolar nuclei., *J. Phys. Chem. A*. 113 (2009) 12864–12878.
- [39] J. Trépośc, O. Lafon, B. Hu, J.-P. Amoureux, Indirect high-resolution detection for quadrupolar spin-3/2 nuclei in dipolar HMQC solid-state NMR experiments, *Chem. Phys. Lett.* 496 (2010) 201–207.
- [40] A. Wong, D. Laurencin, R. Dupree, M.E. Smith, Two-dimensional ^{43}Ca - ^1H correlation solid-state NMR spectroscopy., *Solid State Nucl. Magn. Reson.* 35 (2009) 32–36.
- [41] J.-P. Amoureux, M. Pruski, Theoretical and experimental assessment of single-and multiple-quantum cross-polarization in solid state NMR, *Mol. Phys.* 100 (2002) 1595–1613.

- [42] S.E. Ashbrook, S. Wimperis, Spin-locking of half-integer quadrupolar nuclei in nuclear magnetic resonance of solids: second-order quadrupolar and resonance offset effects., *J. Chem. Phys.* 131 (2009) 194509.
- [43] P.K. Madhu, X. Zhao, M.H. Levitt, High-resolution ^1H NMR in the solid state using symmetry-based pulse sequences, *Chem. Phys. Lett.* 346 (2001) 142–148.
- [44] J.-P. Amoureux, B. Hu, J. Trébosc, Enhanced resolution in proton solid-state NMR with very-fast MAS experiments., *J. Magn. Reson.* 193 (2008) 305–307.
- [45] J.-P. Amoureux, B. Hu, J. Trébosc, Q. Wang, O. Lafon, F. Deng, Homonuclear dipolar decoupling schemes for fast MAS., *Solid State Nucl. Magn. Reson.* 35 (2009) 19–24.
- [46] O. Lafon, Q. Wang, B. Hu, J. Trébosc, F. Deng, J.-P. Amoureux, Proton-proton homonuclear dipolar decoupling in solid-state NMR using rotor-synchronized z-rotation pulse sequences., *J. Chem. Phys.* 130 (2009) 014504.
- [47] E. Vinogradov, P.K. Madhu, S. Vega, High-resolution proton solid-state NMR spectroscopy by phase-modulated Lee – Goldburg experiment, *Chem. Phys. Lett.* 314 (1999) 443–450.
- [48] E. Vinogradov, P.K. Madhu, S. Vega, Phase modulated Lee–Goldburg magic angle spinning proton nuclear magnetic resonance experiments in the solid state: A bimodal Floquet theoretical treatment, *J. Chem. Phys.* 115 (2001) 8983.
- [49] M. Leskes, P.K. Madhu, S. Vega, Proton line narrowing in solid-state nuclear magnetic resonance: new insights from windowed phase-modulated Lee-Goldburg sequence., *J. Chem. Phys.* 125 (2006) 124506.
- [50] M. Leskes, P.K. Madhu, S. Vega, A broad-banded z-rotation windowed phase-modulated Lee–Goldburg pulse sequence for ^1H spectroscopy in solid-state NMR, *Chem. Phys. Lett.* 447 (2007) 370–374.
- [51] M. Leskes, S. Steuernagel, D. Schneider, P.K. Madhu, S. Vega, Homonuclear dipolar decoupling at magic-angle spinning frequencies up to 65kHz in solid-state nuclear magnetic resonance, *Chem. Phys. Lett.* 466 (2008) 95–99.
- [52] M. Leskes, P.K. Madhu, S. Vega, Supercycled homonuclear dipolar decoupling in solid-state NMR: toward cleaner ^1H spectrum and higher spinning rates., *J. Chem. Phys.* 128 (2008) 052309.
- [53] M. Leskes, P.K. Madhu, S. Vega, Why does PMLG proton decoupling work at 65kHz MAS?, *J. Magn. Reson.* 199 (2009) 208–213.
- [54] D. Sakellariou, A. Lesage, P. Hodgkinson, L. Emsley, Homonuclear dipolar decoupling in solid-state NMR using continuous phase modulation, *Chem. Phys. Lett.* 319 (2000) 253–260.

- [55] A. Lesage, D. Sakellariou, S. Hediger, B. El éna, P. Charmont, S. Steuernagel, et al., Experimental aspects of proton NMR spectroscopy in solids using phase-modulated homonuclear dipolar decoupling, *J. Magn. Reson.* 163 (2003) 105–113.
- [56] B. Elena, G. de Pa èpe, L. Emsley, Direct spectral optimisation of proton–proton homonuclear dipolar decoupling in solid-state NMR, *Chem. Phys. Lett.* 398 (2004) 532–538.
- [57] E. Salager, J.-N. Dumez, R.S. Stein, S. Steuernagel, A. Lesage, B. Elena-Herrmann, et al., Homonuclear dipolar decoupling with very large scaling factors for high-resolution ultrafast magic angle spinning ^1H solid-state NMR spectroscopy, *Chem. Phys. Lett.* 498 (2010) 214–220.
- [58] A. Brinkmann, A.P.M. Kentgens, Magic-Angle-Spinning Solid-State NMR Spectroscopy for the Determination of Hydrogen Bond Lengths, *J. Am. Chem. Soc.* 128 (2006) 14758–14759.
- [59] B. Hu, J. Tr ébosc, J.-P. Amoureux, Comparison of several hetero-nuclear dipolar recoupling NMR methods to be used in MAS HMQC/HSQC., *J. Magn. Reson.* 192 (2008) 112–122.
- [60] X. Lu, O. Lafon, J. Tr ébosc, G. Tricot, L. Delevoye, F. M éar, et al., Observation of proximities between spin-1/2 and quadrupolar nuclei: which heteronuclear dipolar recoupling method is preferable?, *J. Chem. Phys.* 137 (2012) 144201.
- [61] V. Vitzthum, M. a Caporini, S. Ulzega, J. Tr ébosc, O. Lafon, J.-P. Amoureux, et al., Uniform broadband excitation of crystallites in rotating solids using interleaved sequences of delays alternating with nutation., *J. Magn. Reson.* 223 (2012) 228–236.
- [62] X. Lu, J. Tr ébosc, O. Lafon, D. Carnevale, S. Ulzega, G. Bodenhausen, et al., Broadband excitation in solid-state NMR using interleaved DANTE pulse trains with N pulses per rotor period., *J. Magn. Reson.* 236 (2013) 105–116.
- [63] M. Ernst, A. Samoson, B.H. Meier, Decoupling and recoupling using continuous-wave irradiation in magic-angle-spinning solid-state NMR: a unified description using bimodal Floquet theory., *J. Chem. Phys.* 123 (2005) 64102.
- [64] A.J. Vega, Controlling the effects of pulse transients and RF inhomogeneity in phase-modulated multiple-pulse sequences for homonuclear decoupling in solid-state proton NMR., *J. Magn. Reson.* 170 (2004) 22–41.
- [65] Z. Gan, P.K. Madhu, J.-P. Amoureux, J. Tr ébosc, O. Lafon, A tunable homonuclear dipolar decoupling scheme for high-resolution proton NMR of solids from slow to fast magic-angle spinning, *Chem. Phys. Lett.* 503 (2011) 167–170.
- [66] X. Lu, O. Lafon, J. Tr ébosc, A.S. Lilly Thankamony, Y. Nishiyama, Z. Gan, et al., Detailed analysis of the TIMES and TIMES0 high-resolution MAS methods for high-resolution proton NMR., *J. Magn. Reson.* 223 (2012) 219–227.

- [67] M.E. Halse, L. Emsley, A common theory for phase-modulated homonuclear decoupling in solid-state NMR., *Phys. Chem. Chem. Phys.* 14 (2012) 9121–30.
- [68] M. Veshtort, R.G. Griffin, SPINEVOLUTION: a powerful tool for the simulation of solid and liquid state NMR experiments., *J. Magn. Reson.* 178 (2006) 248–282.
- [69] M. Bak, N.C. Nielsen, REPULSION, A Novel Approach to Efficient Powder Averaging in Solid-State NMR, *J. Magn. Reson.* 125 (1997) 132–139.
- [70] I.J. Shannon, K.D.M. Harris, S. Arumugam, High-resolution solid state ^{13}C NMR studies of ferrocene as a function of magic angle sample spinning frequency, *Chem. Phys. Lett.* 196 (1992) 588–594.
- [71] M. Ernst, H. Zimmermann, B.H. Meier, A simple model for heteronuclear spin decoupling in solid-state NMR, *Chem. Phys. Lett.* 317 (2000) 581–588.
- [72] K. Mao, M. Pruski, Homonuclear dipolar decoupling under fast MAS: resolution patterns and simple optimization strategy., *J. Magn. Reson.* 203 (2010) 144–149.
- [73] T. Giavani, H. Bildsøe, J. Skibsted, H.J. Jakobsen, A solid-state ^{14}N magic-angle spinning NMR study of some amino acids, *J. Magn. Reson.* 166 (2004) 262–272.
- [74] S. Cavadini, A. Lupulescu, S. Antonijevic, G. Bodenhausen, Nitrogen-14 NMR spectroscopy using residual dipolar splittings in solids., *J. Am. Chem. Soc.* 128 (2006) 7706–7707.
- [75] Z. Gan, Measuring amide nitrogen quadrupolar coupling by high-resolution $^{14}\text{N}/^{13}\text{C}$ NMR correlation under magic-angle spinning., *J. Am. Chem. Soc.* 128 (2006) 6040–6041.
- [76] L.A. O'Dell, R.W. Schurko, Fast and simple acquisition of solid-state ^{14}N NMR spectra with signal enhancement via population transfer., *J. Am. Chem. Soc.* 131 (2009) 6658–6659.
- [77] D. Carnevale, V. Vitzthum, O. Lafon, J. Trébosc, J. Amoureux, G. Bodenhausen, Broadband excitation in solid-state NMR of paramagnetic samples using Delays Alternating with Nutation for Tailored Excitation (“ Para-DANTE ”), *Chem. Phys. Lett.* 553 (2012) 68–76.
- [78] X. Lu, J. Trébosc, O. Lafon, D. Carnevale, S. Ulzega, G. Bodenhausen, et al., Broadband excitation in solid-state NMR using interleaved DANTE pulse trains with N pulses per rotor period., *J. Magn. Reson.* 236 (2013) 105–16.

Chapter 5: Through-space Hetero-nuclear Correlation Spectroscopy: detection of nuclei experiencing large anisotropic interactions using frequency-selective pulses

Nuclear magnetic resonance (NMR) is a powerful spectroscopy that provides precious insights into the structure and the dynamics of solids. Contrary to diffraction methods, NMR is suitable for well crystallized samples, but also for amorphous or glass compounds. In particular, two-dimensional (2D) hetero-nuclear correlation (HETCOR) experiments are key tools of solid-state NMR spectroscopy to probe through-bond connectivities or through-space proximities between distinct isotopes.^[1-4] The connectivities and the proximities are revealed by coherence transfers via *J*- or dipolar couplings, respectively.

However, 2D HETCOR experiments are still challenging for isotopes exhibiting wide spectra that are spread over hundreds or thousands of kHz. This situation is encountered in paramagnetic and conductive samples,^[5,6] in which the NMR spectra are broadened by the interactions between the nuclei and the unpaired or conduction electrons. It is also encountered in diamagnetic samples since: (i) about 75% of all NMR active nuclides have spin $I \geq 1/2$ and can thus be subject to large quadrupolar interactions,^[3,4] and (ii) some spin-1/2 ‘heavy’ isotopes, such as ¹¹⁹Sn, ¹⁹⁵Pt, ¹⁹⁹Hg and ²⁰⁹Pb, experience large chemical shift anisotropies (CSA).^[7] HETCOR experiments for nuclei displaying wide spectra face many challenges. First, the detection bandwidth of the probe can be narrower than the 1D spectrum, which hence requires piecewise acquisition of the 2D HETCOR spectrum. Second, even when the 1D spectrum does lie into the probe detection bandwidth, the radio-frequency (rf) fields delivered by usual solid-state NMR probes are often insufficient to achieve efficient and uniform excitation of wide powder patterns, in particular for nuclei with low gyromagnetic ratio. Third, the uniform excitation of quadrupolar nuclei is difficult due to the intricate spin dynamics in the simultaneous presence of rf fields and sample rotation.

Since a few years, several methods have been proposed for wide-line HETCOR experiments. Very short ($\leq 1 \mu\text{s}$) pulses allow the excitation of wide spectra; however, this is at the expense of a decreased sensitivity. For instance, they have been used in $^1\text{H} \rightarrow ^{13}\text{C}$ dipolar-mediated INEPT (*D*-INEPT) for paramagnetic samples,^[8] and in *D*-HMQC experiments such as $^{13}\text{C}\{-^{14}\text{N}\}$ for peptides,^[9,10] and $^1\text{H}\{-^{23}\text{Na}\}$ or $^{31}\text{P}\{-^{23}\text{Na}\}$ with STMAS quadrupolar filter (*D*-HMQC-ST).^[11] However, longer pulses are also used for the excitation of nuclei experiencing large anisotropic interactions. For instance, HETCOR experiments involving half-integer spin quadrupolar nuclei often employ pulses selective for the central transition, which last about $10 \mu\text{s}$, since this transition is not broadened by the first-order quadrupolar interaction.^[12–18] On solids, the excitation of ^{14}N nuclei in HMQC experiments is typically achieved using rf pulses lasting from 10 to $20 \mu\text{s}$ with amplitude of $\nu_1 \approx 50 \text{ kHz}$.^[19–24] These long ^{14}N pulses, which correspond to flip angles ranging from 180° to 360° , instead of 90° -pulses for HMQC applied to liquid samples, have been found using experimental optimization, but the reason of their efficiency is not known yet, and the influence of their length and strength on the transfer efficiency has not been investigated in details. Note also that $^{13}\text{C}\{-^{14}\text{N}\}$ *J*-HMQC experiments have recently been achieved by applying very long ^{14}N rf pulses of 1–2 ms at rf amplitude of about 40 kHz.^[25]

Adiabatic pulses with modulation of the rf field amplitude and carrier frequency have also been demonstrated to increase the excitation bandwidth of cross-polarization (CP) transfer under both static,^[26,27] and Magic-Angle Spinning (MAS) conditions.^[28–31] However, to the best of our knowledge, adiabatic CP transfer has not yet been used to acquire HETCOR MAS experiments with a wide-line spectral dimension. Trains of rotor-synchronized short pulses in the manner of Delays Alternating with Nutation for Tailored Excitation, DANTE,^[32,33] have been recently employed for broadband excitation of quadrupolar nuclei in 2D HETCOR MAS experiments using HMQC^[34–36] or CP pulse sequences.^[37–41]

In this chapter, we investigate the conditions under which pulses lasting tens of microseconds efficiently excite wide-line spectra in the indirect dimension of HMQC experiments. We focus on HMQC sequence because it is one of the most efficient and robust HETCOR method to correlate spin-1/2 and quadrupolar nuclei. In particular,

HMQC sequences using indirect detection via protons are advantageous in terms of sensitivity at high MAS frequencies, ν_R .^[42] Note that besides HMQC, long rectangular pulses have been used for other NMR experiments, including: (i) the selective saturation of an entire family of spinning sidebands to simplify the spectrum,^[33] (ii) the “FAst Spinning gives Transfer Enhancement at Rotary resonance” (FASTER) method^[43–45] in MQMAS experiment, (iii) the Rotational-Echo Saturation-Pulse Double-Resonance (RESPDOR)^[46–51] and Low-Alpha/Low-Amplitude Rotational-Echo Double-Resonance (LA-REDOR)^[52–54] methods to quantify the dipolar dephasing of one spin-1/2 nucleus coupled to one isotope experiencing large anisotropic NMR interactions, and (iv) techniques for selectively exciting under MAS a subset of crystallites from a powder sample.^[55] In RESPDOR and LA-REDOR experiments, it has been demonstrated that long rf pulses scramble the magnetization of nuclei that are subject to large anisotropic NMR interactions. For powder samples, this scrambling results in an apparent saturation, i.e. the cancellation of all powder-averaged populations and coherences.^[33,49,53]

The present chapter analyzes the performances of rf pulses for the indirect excitation of wide-line spectra in HMQC experiments. We compare the efficiency and the robustness of rectangular pulses applied to the indirectly detected nuclei with or without DANTE rotor-synchronized repetition. In particular, we show that in both cases the indirectly detected nuclei experiencing large anisotropic NMR interactions can be excited efficiently with either a broadband or a frequency-selective regime. The first regime is in principle the most efficient but it requires high rf field strengths that may not be compatible with the specifications of the probe, especially for low-gamma isotopes. In that case, we demonstrate that an efficient alternative is the use of frequency-selective pulses, which require moderate rf field strengths and benefit from good robustness to rf field inhomogeneity, offset and MAS instabilities.

The analysis will be performed with an indirectly detected I nucleus with a spin value of either $\frac{1}{2}$ or 1. In the first case we have chosen ^{195}Pt , which is known to be often subject to a very large CSA, whereas for the second case, we have chosen ^{14}N which is an important nucleus with very large ubiquity that is most of the time subject to a large quadrupole interaction. In order to simplify the discussion, in the following, the detected

nucleus will always be ^1H , but obviously the same results should apply to any spin-1/2 nucleus.

5.1 Pulse sequence

The proton-detected HMQC sequences are depicted in Fig.1. The indirectly detected isotope is denoted I henceforth. We refer to proton-detected HMQC experiments with $I = ^{195}\text{Pt}$ and ^{14}N as $^1\text{H}\{-^{195}\text{Pt}\}$ and $^1\text{H}\{-^{14}\text{N}\}$, respectively. For $^1\text{H}\{-^{195}\text{Pt}\}$ HMQC experiments, only single-quantum (1Q) coherences can process during t_1 period. Conversely, due to the spin-1 value of ^{14}N , both 1Q and double-quantum (2Q) coherences can evolve during the t_1 period of $^1\text{H}\{-^{14}\text{N}\}$ HMQC experiments. These experiments are thus denoted 1Q-HMQC and 2Q-HMQC, in the following. The excitation and the reconversion of $^1\text{H}\text{-}I$ MQ coherences are achieved using either two rectangular single pulses (Fig.1a) or two DANTE schemes (Fig.1b). These, denoted D_N^K , consist of a comb of N equally spaced pulses per rotor period, $T_R = 1/\nu_R$, applied during K rotor periods.^[56] Here, we mainly employed basic DANTE schemes with $N = 1$ but experimental results with interleaved DANTE schemes ($N > 1$) are also displayed in Fig.S15. The rf pulses of the two D_N^K trains have identical lengths, amplitudes and phases. The length and amplitude of the two single pulses and of each individual pulse of the two D_N^K trains are denoted t_p and ν_1 in the following.

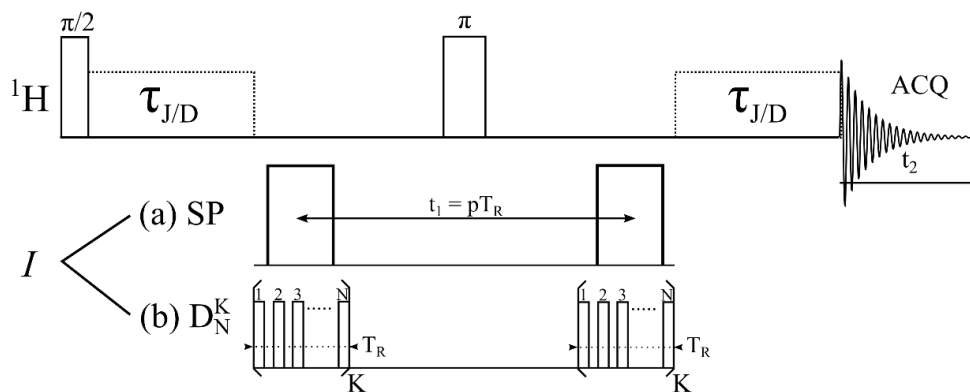


Fig.1. $^1\text{H}\{-I\}$ HMQC pulse sequences using: (a) two rectangular single pulses (SP) or (b) two D_N^K DANTE schemes for the excitation and reconversion of hetero-nuclear MQ coherence. In the case of J -HMQC, no rf irradiation is applied during $\tau_{J/D}$ delays, whereas a dipolar recoupling sequence, such as SR4_1^2 , is applied during $\tau_{J/D}$ in case of D -HMQC sequence.

The coherence transfers from ^1H to I spin and back are achieved via either the ^1H - I J_{HI} -scalar (J -HMQC) or dipolar (D -HMQC) couplings. In D -HMQC, dipolar recoupling sequences, such as $\text{SR4}^2_{1, [57]}$ are applied during the defocusing and refocusing delays, $\tau_{J/D}$, to restore the ^1H - I dipolar interactions.^[14,16,58]

Here, the indirect evolution period, t_1 , defined as the interval between the centers of the two single pulses (Fig.1a) or the two DANTE schemes (Fig.1b) is rotor-synchronized, i.e. is equal to an integer number of rotor periods to ensure the absence of spinning sidebands along the indirect spectral dimension.

5.2 Theory

5.2.1 Coherence transfer

In ^1H - $\{I\}$ J -HMQC experiments, the first 90_y° pulse applied to protons creates ^1H x -magnetization.

For $I = ^{195}\text{Pt}$, this magnetization evolves during $\tau_{J/D}$ under J_{HI} coupling into:

$$S_x \cos(\pi J_{HI} \tau_{J/D}) + 2S_y I_z \sin(\pi J_{HI} \tau_{J/D}) \quad (1)$$

where $2S_y I_z$ is the y -magnetization of proton, in antiphase with respect to the coupling with ^{195}Pt .

For $I = ^{14}\text{N}$, this magnetization evolves into:

$$S_x \left(\frac{1+2\cos(2\pi J_{HI} \tau_{J/D})}{3} \right) + S_x Q_z \left(\frac{\cos(2\pi J_{HI} \tau_{J/D})-1}{3} \right) + S_y I_z \sin(2\pi J_{HI} \tau_{J/D}) \quad (2)$$

where $S_x Q_z$ is the x -magnetization of proton, leading to a triplet with intensities 1:-2:1 for the coupling with ^{14}N nucleus, and $S_y I_z$ is the y -magnetization of proton, leading to a triplet with intensities 1:0:-1.^[59]

In ^1H - $\{^{195}\text{Pt}\}$ J -HMQC experiment, the I_z operator of $S_y I_z$ term in Eq.1 is converted into ^{195}Pt 1Q coherences by applying a 90° pulse on ^{195}Pt channel. In ^1H - $\{^{14}\text{N}\}$ J -HMQC experiment, the I_z operator of $S_y I_z$ term and the Q_z operator of $S_x Q_z$ term in Eq.2 are transformed by a pulse on ^{14}N channel into ^{14}N 1Q coherences in ^1H - $\{^{14}\text{N}\}$ 1Q- J -HMQC experiment and into ^{14}N 2Q coherences in ^1H - $\{^{14}\text{N}\}$ 2Q- J -HMQC experiment.

For D -HMQC experiments, Eq.1 and 2 are still valid for a crystallite containing ^{195}Pt and ^{14}N nuclei, respectively, but the πJ_{HI} frequency must be replaced by the recoupled

dipolar coupling.

We analyze below how the population operators (I_z for spin-1/2 or I_z and Q_z for spin-1) are converted into 1Q and 2Q coherences by rf pulses under MAS. In particular, three limit regimes are discussed: (i) broadband, (ii) selective, and (iii) 2Q coherence excitations.

5.2.2 Broadband excitation

Undistorted MAS spectra can be excited by a rectangular pulse or a DANTE scheme provided the individual pulse length is short enough:^[36]

$$t_p \leq 1/FW \quad (3)$$

In the above equation, FW is the full width of the static spectrum and is equal to $\nu_0 \delta_{\text{aniso}}(3 + \eta_{\text{CSA}})/2$ for CSA and $3C_Q/2$ for quadrupole interaction with $I = 1$, where ν_0 is the Larmor frequency, δ_{aniso} the anisotropic deshielding constant, η_{CSA} the CSA asymmetry parameter and $C_Q = e^2qQ$ the quadrupolar coupling constant. However, optimal 90° excitation by short pulses requires high rf field strength according to

$$\nu_1 = 1/(4t_p) \geq FW/4 \quad (4)$$

for a single pulse and

$$\nu_1 \approx 1/(4KNt_p) \geq FW/(4KN) \quad (5)$$

for a D_N^K train.^[36] The comparison of Eq.4 and 5 shows that DANTE schemes achieve broadband excitation at ν_1 values approximately KN times lower than with single pulses.

In $^1\text{H}\{-^{195}\text{Pt}\}$ J -HMQC experiments, a rectangular single pulse satisfying Eq.3 and 4 or a D_N^K train satisfying Eq.3 and 5 produce a 90° tilt of the magnetization, and thus convert I_z into I_y . Therefore, Eq.1 shows that the optimum delay is $\tau_{J/D} = 1/(2J_{HI})$ for spin-1/2 nuclei. The effect of broadband excitation pulses on spin-1 nucleus has been previously described.^[60] Such strong pulses with phase x and 90° tilt angle convert I_z into I_y and Q_z into $-(3D_x + Q_z)/2$, where D_x is the double quantum coherence with x phase. Therefore, for $^1\text{H}\{-^{14}\text{N}\}$ 1Q- (or 2Q-) J -HMQC experiments using broadband excitations, the coefficient of I_z (or Q_z) operator in Eq.2 must be maximal and the optimal delay is $\tau_{J/D} = 1/(4J_{HI})$ (or $1/(2J_{HI})$).

5.2.3 Sideband selective excitation

An NMR spectrum displays several spinning sidebands (SSB), when

$$FW \gg \nu_R \quad (6)$$

The selective excitation of a single SSB requires the use of a long rectangular pulse with a length

$$t_p \geq T_R \quad (7)$$

The theoretical framework for the description of selective SSB excitation has been introduced in the case of CSA,^[33,61] and it uses the so-called “jolting” frame. In this frame, the rf irradiation profile acquires a SSB pattern that depends on the anisotropic interaction and hence on the crystallite orientation. If the rf field strength is much lower than the MAS frequency,

$$\nu_1 \ll \nu_R \quad (8)$$

for every crystallite, in the jolting frame the rf Hamiltonian takes the form:

$$\bar{H} = \omega_1 A_n R_z(-\phi_n) I_x R_z(\phi_n) \quad (9)$$

where $\omega_1 = 2\pi\nu_1$. ϕ_n is the phase of the n th-SSB, and A_n its relative intensity with respect to the total one observed in a 1D spectrum excited by an ideal 90° pulse. The scaling of the rf field strength by A_n ratio stems from the fact that the instantaneous resonance frequency of the nucleus changes rapidly during the pulse and hence the rf field rotates the magnetization only during a part of the pulse duration. For SSB manifolds produced by CSA, it has been shown that A_n does not depend on γ_{PR} angle, which relates the Principal axis system (PAS) of the CSA tensor of I spin into the Rotor frame.^[61] However, it depends *a priori* on the two other Euler angles $\{\alpha_{PR}, \beta_{PR}\}$ relating these two frames. Eq.9 has been derived for SSB manifold produced by CSA. Nevertheless, the jolting frame can also be used for another anisotropic NMR interaction, such as the quadrupolar one, and a similar scaling of the rf field proportional to SSB intensity must also occur in that case.

Caravatti *et al* have shown that a long rectangular pulse with a carrier frequency equal to the frequency of the n th-SSB and satisfying Eq.6 to 8 selectively excites the irradiated sideband and hence a single-pulse NMR experiment using such excitation produces a 1D spectrum containing exclusively the n th-SSB.^[33]

For a HMQC sequence, which uses SSB-selective pulses on $I = 1/2$ channel, the signal corresponding to $p = \pm 1$ coherence orders of nucleus I during t_1 period, is proportional to

$$\langle (I_z | U_p U_{t_1} I^\pm U_{t_1}^{-1} U_p^{-1}) (I^\pm | U_p I_z U_p^{-1}) \rangle \quad (10)$$

where the angular bracket denotes the powder average and the scalar product in operator space is defined by $(A|B) = \text{Tr}\{A^\dagger B\}$, with A^\dagger the adjoint of A .^[62] U_p denotes the propagator for the excitation and reconversion pulses on I channel, which are equal since the two pulses are rotor-synchronized, and U_{t_1} that for the evolution under isotropic chemical shift (δ_{iso}) of I spin during t_1 period. The rotor-synchronization of t_1 period also ensures the absence of evolution under CSA_I and the ladder operators, $I^\pm = I_x \pm iI_y$, only evolve during t_1 under the δ_{iso} shift as

$$U_{t_1} I^\pm U_{t_1}^{-1} = \exp(-i\Omega_I^0 t_1) I^\pm \quad (11)$$

where Ω_I^0 denotes the angular frequency corresponding to δ_{iso} shift. By substituting Eq.11 into Eq.10 and using the property of complex conjugation of the scalar product and the invariance of the trace under cyclic permutation, Eq.10 simplifies into

$$\exp(-i\Omega_I^0 t_1) |\langle (I^\pm | U_p I_z U_p^{-1}) \rangle|^2 \quad (12)$$

Using Eq.9, the U_p propagator can be expressed in the ordinary rotating frame, revolving at the reference frequency around the z-axis in the laboratory frame, as

$$U_p = R_z[\phi_c(t_p) - \phi_n] \exp(-i\omega_1 A_n I_x t_p) R_z[-\phi_c(t_p) + \phi_n] \quad (13)$$

where $\phi_c(t_p)$ is the phase accumulated during t_p due to the evolution of the δ_{iso} shift and CSA and $R_z[\phi_c(t_p)]$ is the operator representing the transformation from the jolting frame to the ordinary rotating frame.^[33,61] For a powder sample subject to a selective excitation of its n th SSB, the substitution of Eq.13 into Eq.12 leads to a signal proportional to

$$\frac{1}{2} \exp(-i\Omega_I^0 t_1) \langle \sin^2(\omega_1 A_n t_p) \rangle \quad (14)$$

This equation shows that for HMQC sequence, SSB-selective pulses applied to $I = 1/2$ nuclei and satisfying Eq.6 to 8, act as broadband rectangular pulses but with the rf field strength scaled down by A_n . As said before, this A_n ratio depends on $\{\alpha_{\text{PR}}, \beta_{\text{PR}}\}$ Euler angles corresponding to each crystallite.

As discussed above, we assume here that Eq.9, demonstrated analytically for a

spin-1/2 nucleus experiencing CSA, is still valid for the SSB selective excitation in the spectrum of spin-1 nucleus subject to quadrupolar interaction. Under this assumption, Eq.14 is also the analytical expression of the $^1\text{H}\{-^{14}\text{N}\}$ 1Q- J -HMQC signal using SSB selective excitation pulses on ^{14}N channel passing through $S_y I_z$ operator at the end of the first $\tau_{1/D}$ delay and the beginning of the second one. The validity of Eq.14 in that case is demonstrated below using spin-dynamics numerical simulations (Fig.5b). Using Eq.9, we can also show that the $^1\text{H}\{-^{14}\text{N}\}$ 2Q- J -HMQC signal with $p = \pm 2$ during t_1 period, passing through $S_x Q_z$ operator at the end of the first $\tau_{1/D}$ delay and the beginning of the second one and using SSB selective excitation pulses on ^{14}N channel is proportional to

$$\frac{1}{2} \exp(-i2\Omega_I^0 t_1) \langle \sin^4(\omega_1 A_n t_p) \rangle \quad (15)$$

5.2.4 Excitation of 2Q coherences

We have explained above how ^{14}N 2Q coherences can be created from Q_z operator using broadband or SSB selective excitation. It has been demonstrated experimentally and theoretically that 2Q coherences of spin-1 nuclei, such as ^2H and ^{14}N , can be excited in a static sample directly from I_z operator by applying a weak on resonance rf field.^[63–70] This effect can be understood as a second-order perturbation of the first-order quadrupolar interaction by the rf irradiation. The excitation of 2Q coherences requires rf field strength much weaker than the quadrupolar splitting:

$$\nu_1 \ll \Delta\nu_Q \quad (16)$$

given by

$$\Delta\nu_Q = \frac{3}{4} C_Q [3\cos^2(\beta_{PL}^Q) - 1 + \eta_Q \sin^2(\beta_{PL}^Q) \cos(2\gamma_{PL}^Q)] \quad (17)$$

where $\{\beta_{PL}^Q, \gamma_{PL}^Q\}$ Euler angles relate the ^{14}N electric field gradient (efg) quadrupolar PAS and the Laboratory frame. It has been shown that on resonance rf pulse with x phase satisfying Eq.16 transforms the operator I_z of a spin-1 nucleus in a static sample into

$$-D_y \sin(2\pi\nu_{2Q} t_p) \quad (18)$$

where the 2Q nutation frequency, ν_{2Q} , for a given crystallite is given by

$$\nu_{2Q} = 2\nu_1^2 / \Delta\nu_Q \quad (19)$$

Furthermore, it can be shown that a weak on resonance rf field (Eq.16) is not able to

convert Q_z operator into 2Q coherences for a static sample. For a powder, $\Delta\nu_Q$ splitting and ν_{2Q} frequency depend on the crystallite orientation and Eq.16 is not valid for most crystallites.

Under sample rotation, $\Delta\nu_Q$ and ν_{2Q} values become time-dependent and hence MAS can affect the excitation of 2Q coherences. Nevertheless, to the best of our knowledge, no theoretical analysis of 2Q excitation of spin-1 nuclei under MAS has been reported so far.

5.3 Numerical simulations

5.3.1 Simulation parameters

The simulations of spin dynamics were performed using the SIMPSON^[71] and SPINEVOLUTION^[72] software. The powder averaging was accomplished using 2184 orientations: 168 $\{\alpha_{PR}, \beta_{PR}\}$ -pairs \times 13 γ_{PR} -angles. The $\{\alpha_{PR}, \beta_{PR}, \gamma_{PR}\}$ Euler angles relate the Principal axes system of the interaction (CSA or quadrupolar) and the Rotor frame. The $\{\alpha_{PR}, \beta_{PR}\}$ -pairs were selected according to the REPULSION algorithm,^[73] whereas the γ_{PR} angle was regularly stepped from 0 to 360°. The magnetic field was $B_0 = 18.8$ T and the MAS frequency was $\nu_R = 31.25$ or 62.5 kHz.

Both single-pulse and J -HMQC experiments were simulated. The spin system was a single I nucleus in the first case and an isolated ^1H - I pair in the second case, with I nucleus being either ^{195}Pt ($I = 1/2$, $\nu_{0,195\text{Pt}} = 172$ MHz) or ^{14}N ($I = 1$, $\nu_{0,14\text{N}} = 57.8$ MHz).

^{195}Pt nuclei often experience large CSA,^[74] and here we used $\nu_0\delta_{\text{aniso}} = 667$ kHz and $\eta_{\text{CSA}} = 0$, which yield $FW = 1$ MHz, except in Fig.S3 where $\nu_0\delta_{\text{aniso}}$ was varied from 0 to 1 MHz in step of 10 kHz.

^{14}N nucleus experiences quadrupolar interaction. For instance, in γ -glycine, ^{14}N nucleus has $C_Q = 1.18$ MHz, which yields $FW = 1.77$ MHz, and an EFG asymmetry parameter of $\eta_Q = 0.5$.^[19] However, ^{14}N sites with much larger C_Q values are found in other compounds.^[9,75] Hence, ^{14}N results were calculated for $C_Q = 1.18$ and 2.36 MHz using $\eta_Q = 0.5$. For ^{14}N simulations, quadrupolar interaction up to the second order was included, except in Figs.S7 and S14, for which only the first-order term was considered.

According to their usual small values, no dipolar coupling, so that no ^1H and ^{14}N

CSA were included in the simulations. For both ^1H - ^{195}Pt and ^1H - ^{14}N spin pairs, the hetero-nuclear scalar coupling was $J_{HI} = 400$ Hz. All rf pulses were applied on resonance. In case of long pulses this corresponds to a center-band selective excitation, which is thus ruled by the A_0 ratio in Eq.14 and 15. However, in Figs.6 and S12 the ^{14}N carrier frequency was varied to test the robustness to offset.

For simulations of 1D experiments with a single-pulse, the density matrix was analyzed at the end of the pulse by taking its projections onto operator basis. We chose the angular momentum operators basis $\{E, I_x, I_y, I_z\}$ with E the identity operator for ^{195}Pt nucleus, and the Cartesian operators basis $\{E, I_x, I_y, I_z, K_x, K_y, Q_z, D_x, D_y\}$ for ^{14}N nucleus.^[60] In the latter basis, K_x and K_y operators represent the x - and y -magnetizations of ^{14}N nucleus, antiphase with respect to the first-order quadrupolar interaction, Q_z the quadrupolar order and D_x and D_y the double-quantum coherences with x and y phases.

For ^1H - $\{I\}$ J -HMQC 2D experiments, ideal $\pi/2$ and π pulses were applied on the ^1H channel, whereas ^{195}Pt or ^{14}N coherences were excited using either two rectangular single pulses (SP, Fig.1a) or two D^{K_1} DANTE trains (Fig.1b) with $K = 2, 4$, or 8 .^[34-36,56] For ^1H - $\{I\}$ 1Q- J -HMQC experiments, $p = +1$ was selected during t_1 period, whereas it was $p = +2$ for 2Q- J -HMQC experiments.

The ^1H - $\{I\}$ J -HMQC results have been obtained with 1D simulations, for which $t_1 = mT_R$ with $m = 2$ for SP variant and $m = K$ for D^{K_1} trains. For simulations of ^1H - $\{^{195}\text{Pt}\}$ and ^1H - $\{^{14}\text{N}\}$ 1Q- J -HMQC we used $\tau_{J/D} = 1/(2J_{HI}) = 1.25$ ms, since this delay achieves maximal transfer efficiency. For ^1H - $\{^{14}\text{N}\}$ 2Q- J -HMQC simulations of Fig.9, both $\tau_{J/D}$ delays of $1/(2J_{HN}) = 1.25$ ms and $1/(4J_{HN}) = 0.625$ ms were employed.

To compare more easily the results, the J -HMQC transfer efficiency was normalized with respect to that calculated using two ideal $\pi/2$ pulses on the I channel and the same $\tau_{J/D}$ delay. The A_0 value in Fig.3d was calculated as the ratio between the integrated intensities of the center-band after a long pulse and the total one observed after an ideal 90° pulse. Additional details about numerical simulations are given in the figure captions.

5.3.2 Simulations for ^{195}Pt nucleus

(a) Single pulse experiment

As seen in Fig.S1, we first simulated the ^{195}Pt NMR 1D powder spectra after a single rectangular pulse with various t_p lengths. As expected, the excitation band-width of the pulse decreases for increasing t_p value. Nevertheless, for $t_p \leq T_R/2 = 8 \mu\text{s}$, the intensity of the center-band is not significantly larger than that of the two first sidebands resonating at frequency $\nu_{\text{iso}} \pm \nu_R$. Conversely, for pulses with $t_p \geq T_R = 16 \mu\text{s}$, the intensity of the center-band becomes much larger than that of the other sidebands and the pulse achieves selective excitation of the center-band. This result demonstrates the validity of Eq.7.

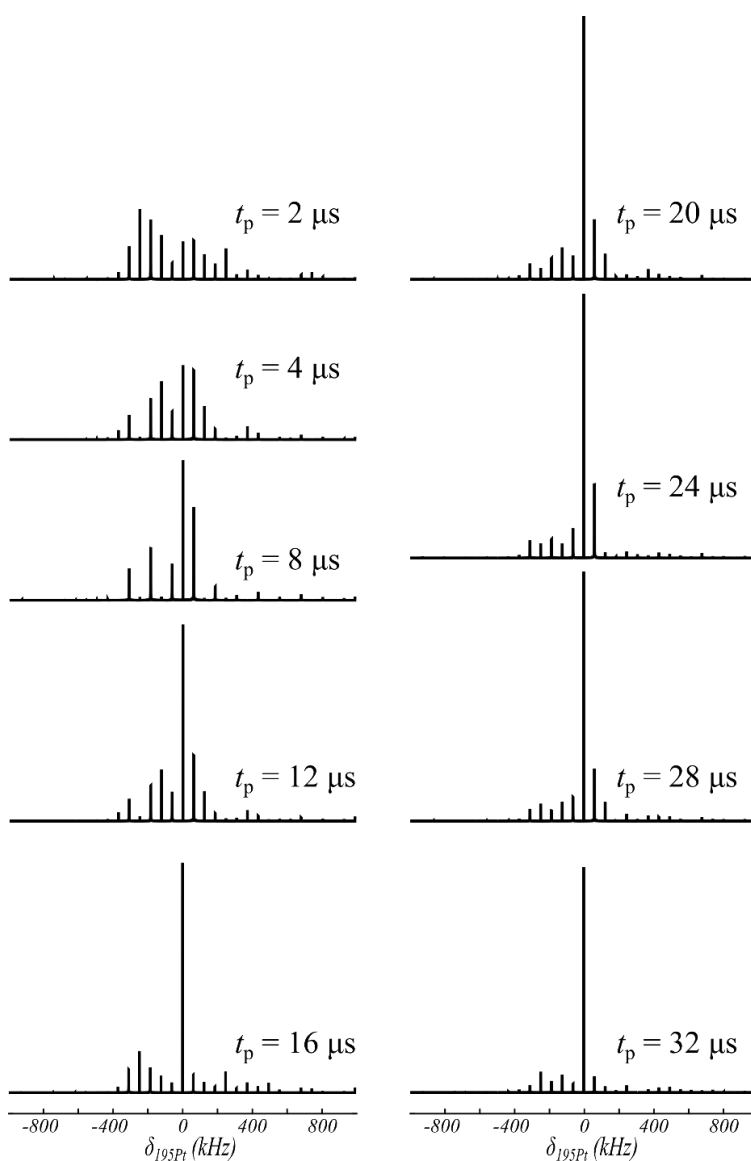


Fig.S1. Simulated ^{195}Pt 1D spectra at $\nu_R = 62.5 \text{ kHz}$ excited by a single rectangular pulse using $\nu_1 = 40 \text{ kHz}$. The spectrum was calculated for various pulse lengths, t_p , varied from 2 to 32 μs . $\nu_0\delta_{\text{aniso}} = 667 \text{ kHz}$ and $\eta_{\text{CSA}} = 0$, the other simulation parameters are given in section IV-1.

The projections of the simulated powder averaged density matrix for an isolated ^{195}Pt nucleus after a single rectangular pulse with phase x were also calculated as function of t_p and ν_1 values (Fig.S2). In agreement with Eq.3 and 4, short pulses with $t_p \approx 1 \mu\text{s}$ and $\nu_1 \approx 250 \text{ kHz}$ achieve broadband excitation and efficiently create magnetization along the y-axis. Conversely, long pulses using large rf field scramble the magnetization of the different crystallites and result in an apparent saturation, as already reported for RESPDOR and LA-REDOR experiments.^[33,49,53] Interestingly, pulses with $t_p \approx 16 \mu\text{s}$ and $\nu_1 \approx 50 \text{ kHz}$ also create y-magnetization. This regime corresponds to the selective excitation of the center-band (Fig.S1).

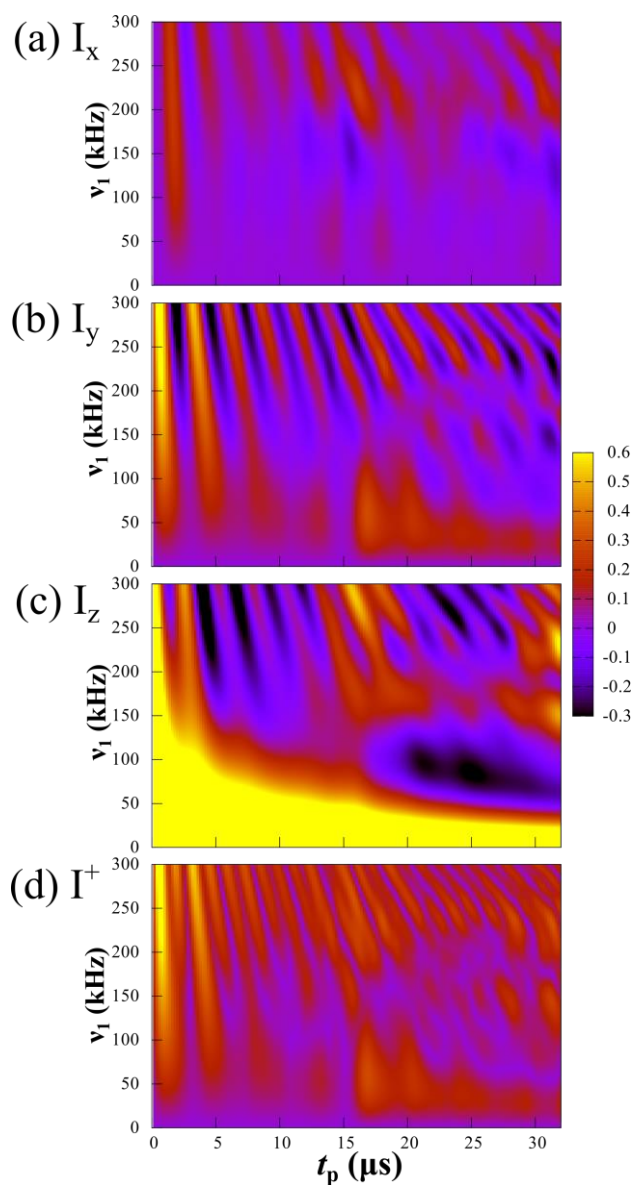


Fig.S2. Projections of the simulated density matrix onto (a) I_x , (b) I_y , (c) I_z and (d) I^+ operator after a single rectangular pulse applied to ^{195}Pt spin. The starting operator was I_z and the projections are normalized with respect to the norm of the starting operator. $\nu_R = 62.5$ kHz, $\nu_0\delta_{\text{aniso}} = 667$ kHz and $\eta_{\text{CSA}} = 0$. The projections were calculated as function of the pulse length, t_p , and the rf field strength, ν_1 .

The evolution of the density matrix during an rf pulse also depends on the CSA value. As seen in Fig.S3e, rf pulse with $\nu_1 = 40$ kHz can rotate the magnetization of spin-1/2 nuclei experiencing CSA up to 100 kHz, i.e. displaying spectra with FW up to 150 kHz. Significant y -magnetization is also produced for $t_p \approx 16$ μs and $\nu_0\delta_{\text{aniso}}$ values ranging from 200 to 400 kHz (i.e. $300 \leq FW \leq 600$ kHz). This local maximum corresponds to SSB-selective excitation since Eq.6 and 7 are valid. For increasing CSA, A_n amplitudes decrease in Eq.9 and hence the SSB-selective pulses become less efficient. Consequently, there is an optimal $\nu_0\delta_{\text{aniso}}$ value for the creation of transverse magnetization by SSB-selective pulses.

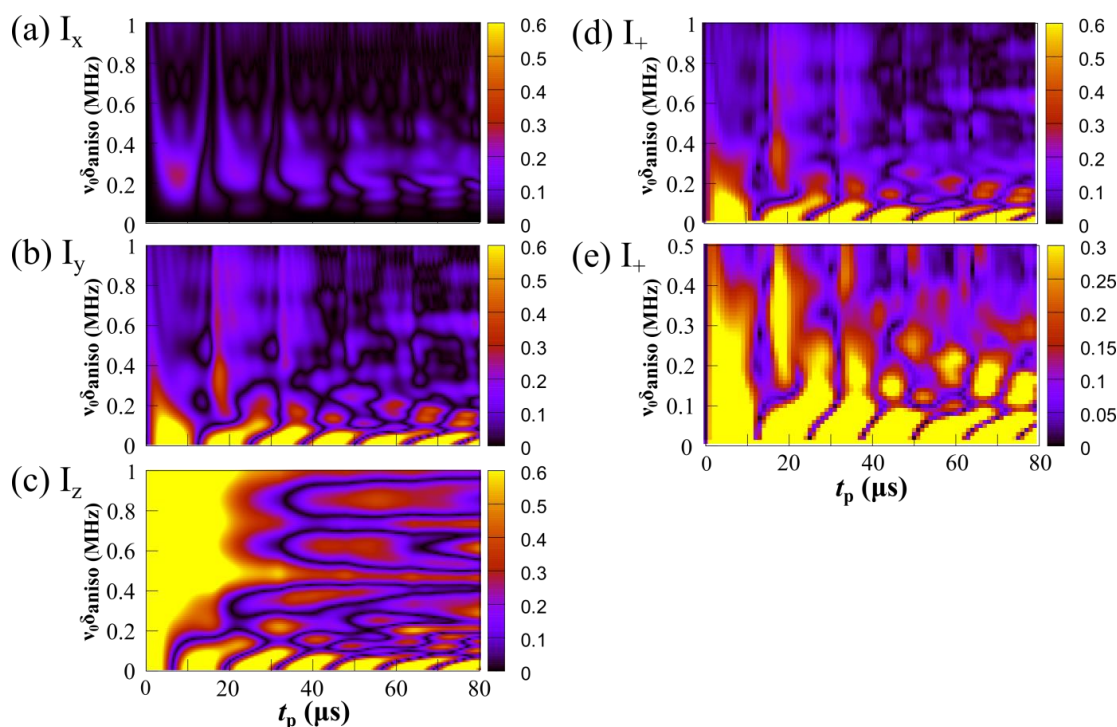


Fig.S3. Projections of the simulated density matrix onto (a) I_x , (b) I_y , (c) I_z and (d) I^+ operators after a single rectangular pulse with $\nu_1 = 40$ kHz applied to ^{195}Pt spin, with $\nu_R = 62.5$ kHz and $\eta_{\text{CSA}} = 0$. The real parts of I_x , I_y , I_z and the modulus of I^+ are shown here. (e) is an expansion of (d) showing more details. The projections were calculated as function of the pulse length, t_p , and the $\nu_0\delta_{\text{aniso}}$ value.

(b) $^1\text{H}\{-^{195}\text{Pt}\}$ J -HMQC experiment

The signal of $^1\text{H}\{-^{195}\text{Pt}\}$ J -HMQC experiment using two rectangular pulses on the ^{195}Pt channel was simulated as function of t_p and ν_1 values (Fig.2a). Here again, short

pulses with $t_p \leq 1 \mu\text{s}$ achieve broadband excitation and the optimal rf field strength is given by Eq.4. Long pulses with $t_p \geq 16 \mu\text{s}$ and $\nu_1 \approx 40 \text{ kHz}$ achieve SSB-selective excitation and yield signal intensity only slightly lower than that achieved by broadband excitation with short pulses. This simulation demonstrates the potential of selective pulses in HMQC-type experiments. As seen in Figs.2a and S4, significant J -HMQC signal is then detected for a broad range of t_p and ν_1 values. The comparison of Figs.2a and S2b shows that selective pulses are more robust and more efficient when used in the indirect channel of J -HMQC 2D experiments than in single-pulse 1D experiment. This higher efficiency of J -HMQC stems from the refocusing of the dephasing occurring during the two pulses and related to ^{195}Pt CSA, owing to the rotor-synchronization of the t_1 period. Conversely, in a single-pulse 1D experiment, the 1Q coherence dephases under CSA only once: during this pulse, and hence no refocusing occurs. This dephasing depends on the crystallite orientation and hence the signal intensity is reduced. Pulses with $t_p \geq 3 \mu\text{s}$ and $\nu_1 \geq 200 \text{ kHz}$ do not produce any significant J -HMQC signal. This lack of signal is consistent with the apparent saturation produced by high-power long pulses in single pulse experiment (Fig.S2).

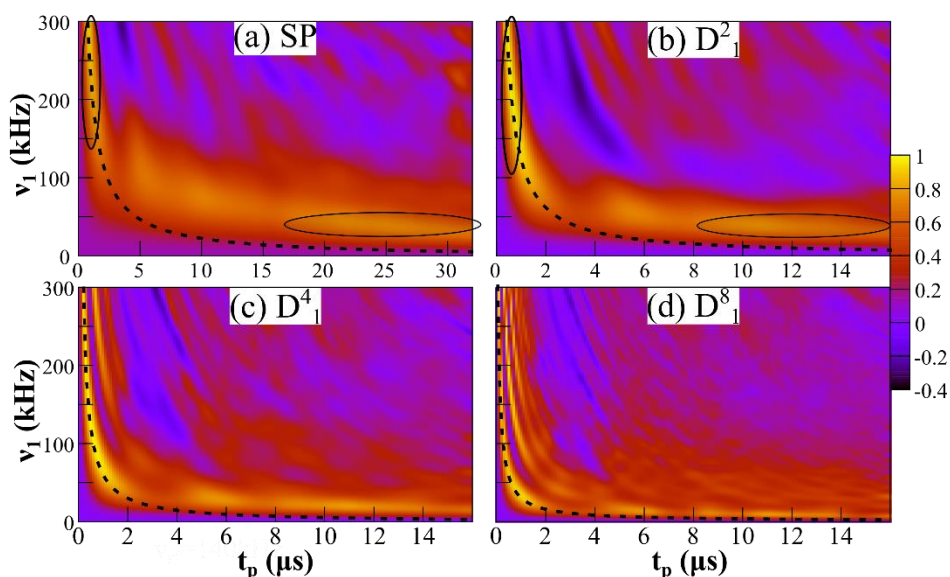


Fig.2. Simulated powder-averaged on-resonance signal of $^1\text{H}\{-^{195}\text{Pt}\}$ J -HMQC experiment at $\nu_R = 62.5 \text{ kHz}$, with $\nu_0\delta_{\text{aniso}} = 667 \text{ kHz}$ and $\eta_{\text{CSA}} = 0$, versus the individual pulse length, t_p , and the rf-field, ν_1 . ^{195}Pt coherences are excited and reconverted using (a) two rectangular single pulses (SP), or two (b) D^2_1 , (c) D^4_1 , and (d) D^8_1 DANTE trains. The regions corresponding to broad-band and SSB-selective excitation are circled in (a) and (b), and the dashed curves correspond to Eq. 4 (a) and 5 (b-d).

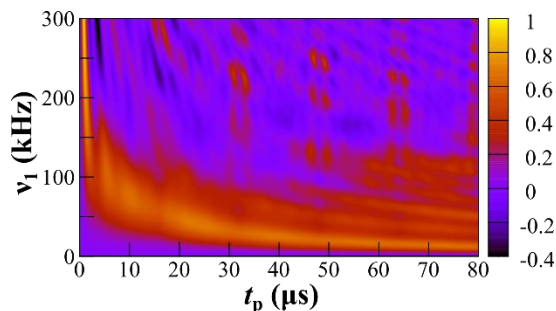


Fig.S4. Simulated powder-averaged signal of $^1\text{H}\{-^{195}\text{Pt}\}$ J -HMQC experiment at $\nu_R = 62.5$ kHz, with $\nu_0\delta_{\text{aniso}} = 667$ kHz and $\eta_{\text{CSA}} = 0$, versus the individual pulse length, t_p , and the rf-field, ν_1 . ^{195}Pt coherences are excited and reconverted using rectangular pulses. The simulation parameters are identical to those of Fig.2a, but the range of t_p values is broader.

Similar simulations were also performed for $^1\text{H}\{-^{195}\text{Pt}\}$ J -HMQC experiment using DANTE trains on the ^{195}Pt channel (Fig.2b-d). For $t_p \leq 1$ μs , these DANTE trains achieve broadband excitation and the optimal ν_1 value is given by Eq.5. As a result, DANTE trains produce efficient broadband excitation at much lower rf field than single rectangular pulses. As already shown, the envelope of the excitation profile of a 90° flip angle obtained with one D^{K_1} train and very short pulses, is a Sinc function with a Full Width at Half Maximum equal to $1.35/t_p$.^[35,36] In the case of frequency selective HMQC experiments, the two D^{K_1} trains mainly only excite the center-band when the total pulse length is ca. $Kt_p \geq T_R = 16$ μs . Therefore, significant signal in J -HMQC experiment is also detected for DANTE trains using long t_p values, since these trains achieve SSB-selective excitation. Conversely, DANTE trains consisting of pulses with $t_p \geq 3$ μs and $\nu_1 \geq 100$ kHz are inefficient in J -HMQC experiment, as already observed for single pulses (Fig.2a).

We then investigated the dependence of J -HMQC transfer efficiency versus the orientation of the CSA tensor. Fig.S5 shows the simulated signal intensity of $^1\text{H}\{-^{195}\text{Pt}\}$ J -HMQC experiment of one crystallite as function of t_p length and the angle, $\beta_{\text{PL}}^0 = \beta_{\text{PR}} + 54.7^\circ$, between the B_0 axis and the Z axis of the PAS of ^{195}Pt CSA tensor, at the *beginning* of the first pulse on ^{195}Pt channel. The instantaneous shift due to CSA at the beginning of the first pulse on ^{195}Pt channel is equal to

$$\nu_{\text{CSA}} = \nu_0\delta_{\text{aniso}} \frac{3\cos^2(\beta_{\text{PL}}^0) - 1}{2} \quad (20)$$

Short 90° pulses with $\nu_1 = 40$ kHz and $t_p \approx 1/(4\nu_1) \approx 6.25$ μs , only excite crystallites with $\beta_{\text{PL}}^0 \approx 54.7^\circ$ and 125.3° , for which ν_{CSA} is close to zero during the pulse (Fig.S5a).

For increasing rf field, 90° pulse length becomes shorter and excites crystallites exhibiting a larger instantaneous shift, i.e. a broader range of β_{PL}^0 values around 54.7° and 125.3° (Figs.S5b to d).

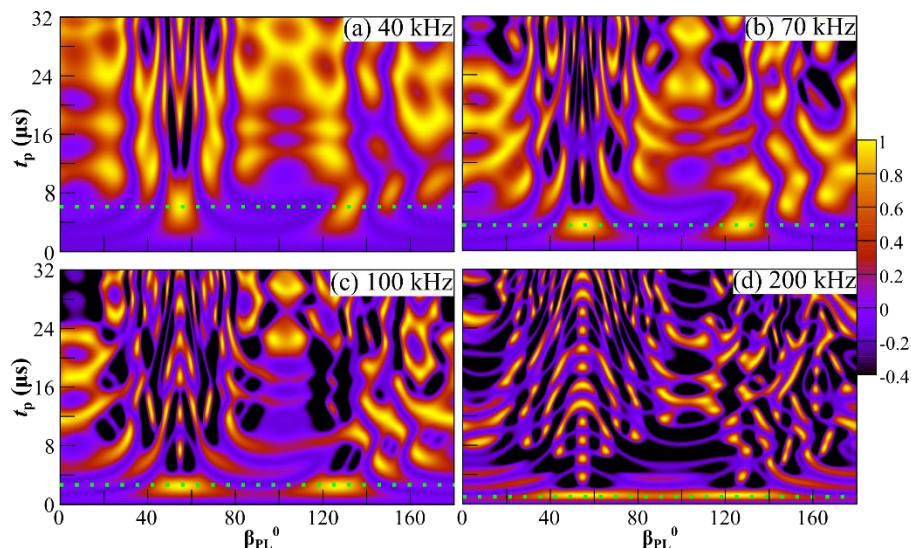


Fig.S5. Simulated $^1\text{H}\{-^{195}\text{Pt}\}$ J -HMQC signal of a crystallite as function of t_p length and the β_{PL}^0 angle for $\nu_1 =$ (a) 40, (b) 70, (c) 100 and (d) 200 kHz. Besides β_{PL}^0 , the orientation of the crystallite is described by the Euler angles α_{PR} and γ_{PR} , which here are both equal to 54.7° . ^{195}Pt coherences are excited and reconverted using two rectangular single pulses. $\nu_{\text{R}} = 62.5$ kHz, $\nu_0\delta_{\text{aniso}} = 667$ kHz and $\eta_{\text{CSA}} = 0$. In each subfigure, the dotted green line indicates the length of conventional 90° pulse.

Pulses with $\nu_1 = 40$ kHz and $t_p \geq 16$ μs satisfy Eqs. 7 and 8 and hence achieve SSB selective excitation. These pulses are able to excite crystallites with many different β_{PL}^0 angles, as shown in Fig.S5a. Only some crystallites with $\beta_{\text{PL}}^0 \approx 32, 46, 62, 77, 133$ or 144° are not well excited by the center-band selective pulses on ^{195}Pt channel. For $\nu_1 \geq \nu_{\text{R}} = 62.5$ kHz and $t_p \geq 16$ μs , there is a shrinkage of the regions of β_{PL}^0 and t_p values leading to high signal intensity because the pulse is not selective for the center-band (Figs.S5b to d). This shrinkage is consistent with the decrease of the $^1\text{H}\{-^{195}\text{Pt}\}$ J -HMQC signal of a powder with increasing rf field strength for $\nu_1 \geq \nu_{\text{R}}$ and $t_p \geq 16$ μs (Fig.2a). For high ν_1 value and long t_p length, the signal intensity becomes highly dependent on the β_{PL}^0 angle, and it can change from -0.4 to 1 , when β_{PL}^0 just changes by a few degrees. Such abrupt variations of the signal intensity with the crystallite orientation have already been reported for other high-power pulse sequences, such as RESPDOR or LA-REDOR,^[53] Double-Frequency Sweep (DFS) and Fast Amplitude Modulation (FAM),^[76,77] which last several rotor periods and result in an apparent saturation of the irradiated transitions for

nuclei experiencing large anisotropic interactions.

Fig.S6 shows the dependence of the simulated signal intensity of $^1\text{H}\{-^{195}\text{Pt}\}$ J -HMQC experiment using center-band selective pulses ($\nu_1 = 40 \text{ kHz} \leq \nu_R$ and $t_p = 24 \mu\text{s}$) as function of $\{\alpha_{\text{PR}}, \beta_{\text{PL}}^0\}$ and $\{\gamma_{\text{PR}}, \beta_{\text{PL}}^0\}$ Euler angles. As $\eta_{\text{CSA}} = 0$, the signal is independent of α_{PR} angle (Fig.S6a). Fig.S6b shows that the signal is also weakly dependent on γ_{PR} angle. This result is consistent with Eq.14 and the independence of A_n ratio with γ_{PR} angle.^[61]

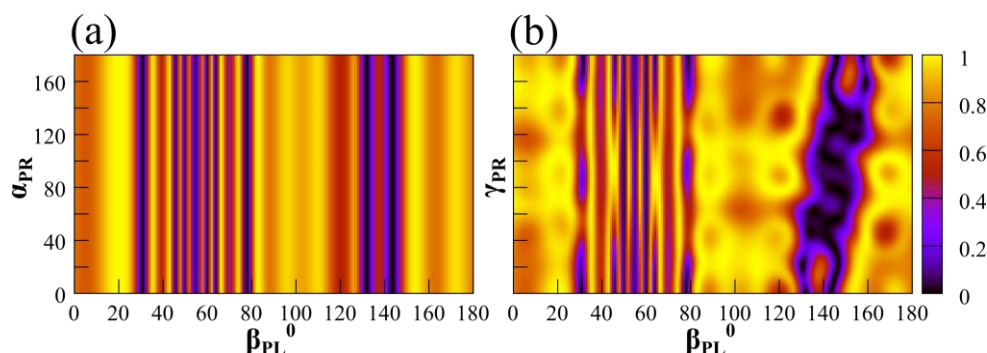


Fig.S6. Simulated $^1\text{H}\{-^{195}\text{Pt}\}$ J -HMQC signal of a crystallite as function of (a) $\{\alpha_{\text{PR}}, \beta_{\text{PL}}^0\}$ with $\gamma_{\text{PR}} = 0$, and (b) $\{\gamma_{\text{PR}}, \beta_{\text{PL}}^0\}$ with $\alpha_{\text{PR}} = 0$ Euler angles. ^{195}Pt coherences are excited and reconverted using single rectangular pulses with $t_p = 24 \mu\text{s}$ and $\nu_1 = 40 \text{ kHz}$. $\nu_R = 62.5 \text{ kHz}$, $\nu_0\delta_{\text{aniso}} = 667 \text{ kHz}$ and $\eta_{\text{CSA}} = 0$.

To evaluate the validity of Eq.14, we simulated the signal intensity of $^1\text{H}\{-^{195}\text{Pt}\}$ J -HMQC experiment as function of β_{PL}^0 angle and ν_1 strength for $t_p = 24$ (Fig.3a) and $80 \mu\text{s}$ (Fig.3b). These two figures show that the build-up of ^{195}Pt 1Q coherences during ^{195}Pt pulses depends on the crystallite orientation. The two columns of Fig.3b, corresponding to $\beta_{\text{PL}}^0 = 54.7$ and 125.3° , are displayed in Fig.3c. When the pulses only selectively excite the center-band ($\nu_1 \leq \nu_R$), Fig.3c shows that the J -HMQC signal intensity of each crystallite is proportional to

$$\sin^2(2\pi\kappa\nu_1 t_p) \quad (21)$$

where the scaling factor κ depends on the β_{PL}^0 angle. The κ factor was determined for different crystallites, i.e. different β_{PL}^0 angles, by fitting the corresponding column of Fig.3b to Eq.21. Fig.3d shows that the best-fit κ factor matches the A_0 amplitude. Furthermore, the crystallites, for which the center-band cancels, i.e. $A_0(\beta_{\text{PL}}^0) \approx 0$, are not excited by the ^{195}Pt pulses and hence do not contribute to the J -HMQC signal. The above results demonstrate the validity of Eq.14.

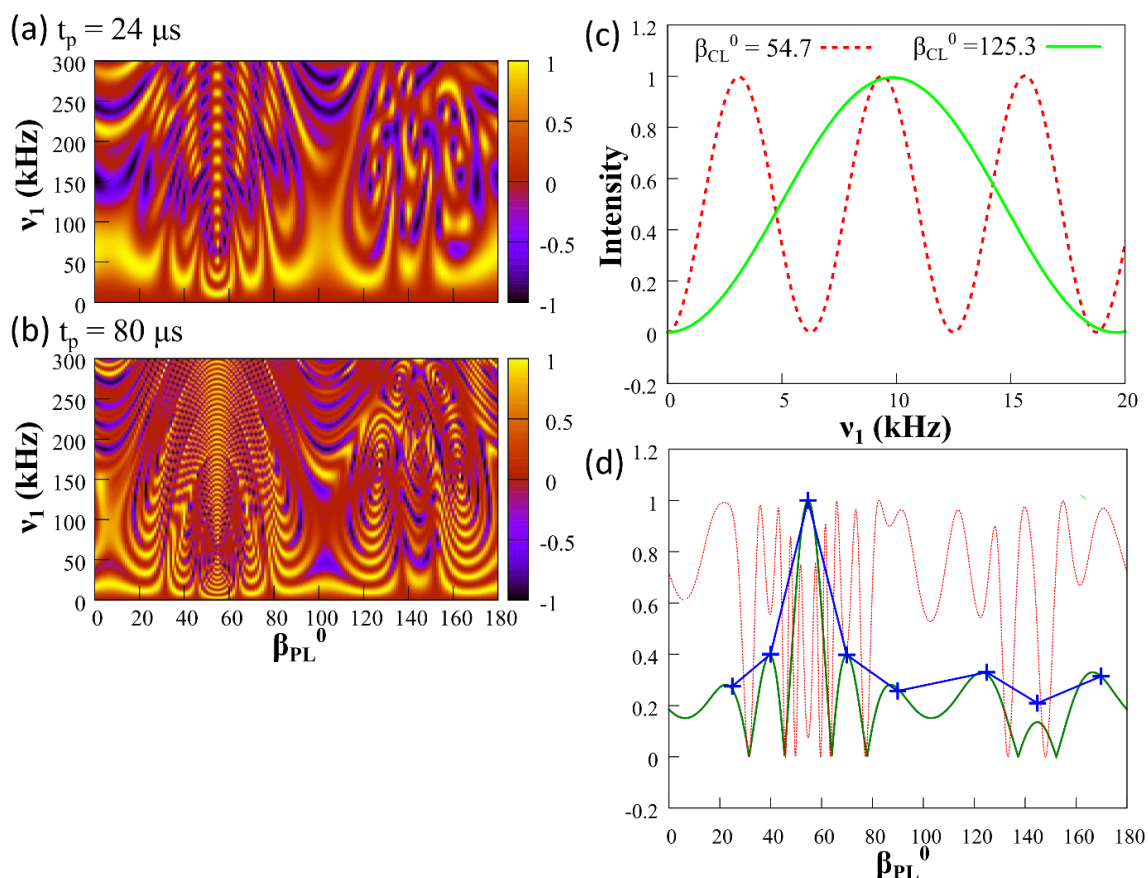


Fig.3. (a,b) Simulated $^1\text{H}\{-^{195}\text{Pt}\}$ J -HMQC signal of one crystallite as function of its β_{PL}^0 angle and ν_1 value for $t_p =$ (a) 24 and (b) 80 μs . (c) Simulated $^1\text{H}\{-^{195}\text{Pt}\}$ J -HMQC signal of one crystallite as function of ν_1 for $t_p = 80 \mu\text{s}$ and $\beta_{\text{PL}}^0 = 54.7$ (red) or 125.3° (blue). (d) The simulated $^1\text{H}\{-^{195}\text{Pt}\}$ J -HMQC signal for $t_p = 80 \mu\text{s}$ and $\nu_1 = 9 \text{ kHz}$ (red line), the A_0 ratio (green line) and the best-fit κ factor (blue cross) are plotted as function of β_{PL}^0 angle. $\alpha_{\text{PR}} = \gamma_{\text{PR}} = 54.7^\circ$, $\nu_{\text{R}} = 62.5 \text{ kHz}$, $\nu_0\delta_{\text{aniso}} = 667 \text{ kHz}$ and $\eta_{\text{CSA}} = 0$

5.3.3 Simulations for ^{14}N nucleus

(a) Single pulse experiment

Fig.S7 shows the projections of the simulated density matrix for an isolated ^{14}N nucleus after a single rectangular pulse with phase x . Short high-power pulses with $\nu_1 \approx 200 \text{ kHz}$ and $t_p \approx 1\text{-}2 \mu\text{s}$ are not sufficient to fully convert z -magnetization into 1Q coherences, since at the end of the pulse the projection of the density matrix does not cancel onto I_z , and is limited to 0.5 onto I_y . Nevertheless, these short strong pulses efficiently create I_y and K_x operators. The presence of K_x operator results from the dephasing under first-order quadrupolar interaction during the pulse.^[60] Pulses with $t_p \geq 16 \mu\text{s}$ and $\nu_1 \approx 40 \text{ kHz}$ achieve selective center-band excitation and create 1Q coherences

(Fig.S7a). Pulses with $t_p \geq 5 \mu\text{s}$ and $75 \leq \nu_1 \leq 150 \text{ kHz}$ excite 2Q transitions (Fig.S7d). However, the simulated coefficient of D_y operator, shown in Fig.S8, significantly differs from that calculated in static as the powder average of Eq.18. This discrepancy indicates that high MAS frequency ($\nu_R = 62.5 \text{ kHz}$) largely affects the creation of 2Q coherences for ^{14}N nucleus. Nevertheless, a detailed theoretical analysis of this effect is beyond the scope of the present article.

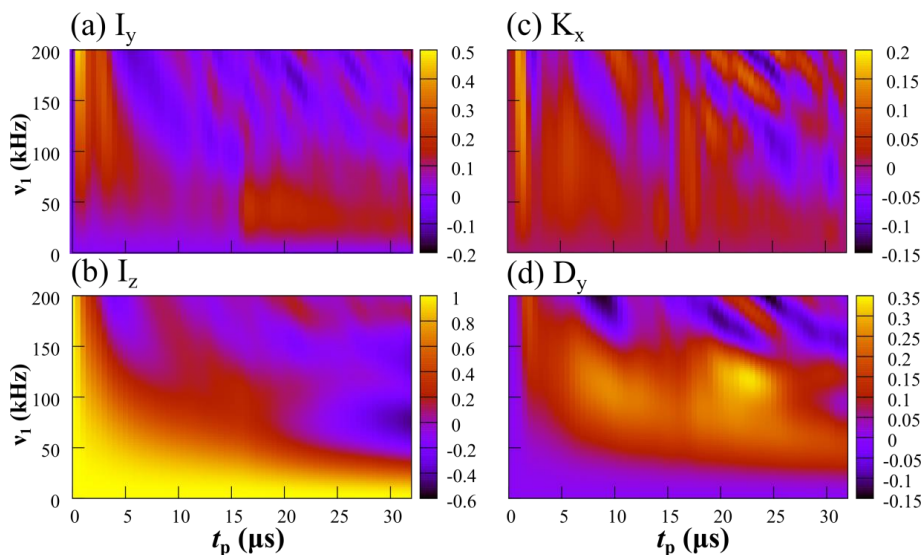


Fig.S7. Projections of the simulated density matrix onto (a) I_y , (b) I_z , (c) K_x , and (d) D_y operators after a single rectangular pulse applied to ^{14}N spin at $\nu_R = 62.5 \text{ kHz}$, with $C_Q = 1.18 \text{ MHz}$ and $\eta_Q = 0.5$. The starting operator was I_z and the projections were normalized with respect to the norm of the starting operator. The quadrupolar interaction was restricted to the first-order term. The projections were calculated as function of the pulse length, t_p , and the rf field strength, ν_1 . The projections onto the other operators (I_x , K_y , Q_z and D_x) are negligible.

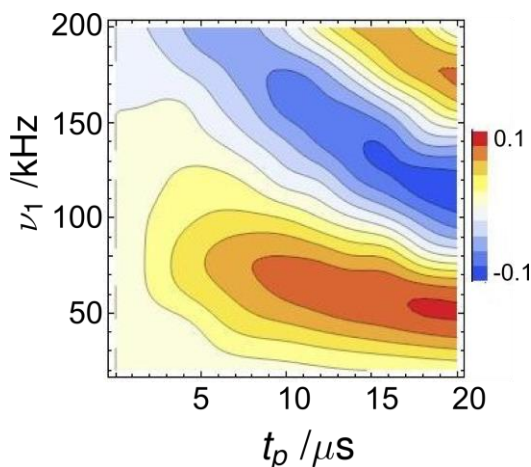


Fig.S8. Coefficient of D_y operator for an isolated ^{14}N nucleus, with $C_Q = 1.18 \text{ MHz}$ and $\eta_Q = 0.5$, in a static sample after a rectangular rf pulse as function of ν_1 strength and t_p length. The coefficient is calculated as the powder average of Eq.15 but only crystallite orientations for which $5\nu_1 \leq \Delta\nu_Q$ (i.e. Eq.16 is valid) are retained in the powder average.

(b) $^1\text{H}\{-^{14}\text{N}\}$ 1Q- J -HMQC experiment

Fig.4 shows the $^1\text{H}\{-^{14}\text{N}\}$ 1Q- J -HMQC signal of a powder as function of t_p length and ν_1 strength. In Fig. 4a, the ^{14}N nucleus has $C_Q = 1.18$ MHz and the ^{14}N 1Q coherences are excited and reconverted using one rectangular single pulse (SP). As already observed for ^{195}Pt , two regimes efficiently excite the 1Q ^{14}N coherences: (i) short pulses with $t_p \leq 1$ μs and $\nu_1 \geq 150$ kHz achieve broadband excitation, whereas (ii) long pulses with $t_p \geq 16$ μs and $\nu_1 \approx 40$ kHz produce selective excitation. Fig.4a demonstrates the efficiency of selective excitation for the indirect detection of ^{14}N nuclei using 1Q- J -HMQC sequence. As already noticed for ^{195}Pt , selective pulses are more efficient in 2D HMQC than in 1D single-pulse experiments (compare Fig.4a and Fig.S7a,c). This higher efficiency of 1Q- J -HMQC experiment stems from the refocusing of the quadrupolar interaction by the rotor-synchronization of the t_1 period. The comparison of Figs.2a and 4a also shows that high-power long rectangular pulses ($t_p \geq 3$ μs and $\nu_1 \geq 200$ kHz) lead to significant signal in $^1\text{H}\{-^{14}\text{N}\}$ 1Q- J -HMQC experiment but not in $^1\text{H}\{-^{195}\text{Pt}\}$ ones. The different regimes can also be distinguished by plotting the 1Q- J -HMQC signal intensity as function of t_p length and the total on resonance flip angle, $\theta_{\text{tot}} = 360\nu_1 t_p$ (Fig.S9). Broadband excitation pulses lead to high signal intensity when the θ_{tot} angle is an odd multiple of 90° , whereas for selective pulses, the highest efficiency is obtained for $\theta_{\text{tot}} \approx 360^\circ$. For $C_Q = 2.36$ MHz, the full-width of the spectrum increases. As expected, the efficiency of broadband excitation pulses with $\nu_1 \leq 300$ kHz decreases. Conversely, the selective excitation pulses using $\nu_1 \approx 40$ kHz are almost as efficient for $C_Q = 1.18$ and 2.36 MHz (Fig.4b).

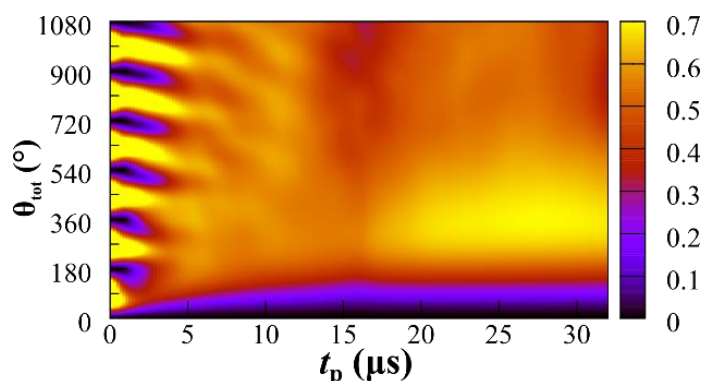


Fig.S9. Simulated powder averaged signal of $^1\text{H}\{-^{14}\text{N}\}$ 1Q- J -HMQC experiment at $\nu_R = 62.5$ kHz versus the t_p length and the total on resonance flip angle, $\theta_{\text{tot}} = 360\nu_1 t_p$, for $C_Q = 1.18$ MHz and $\eta_Q = 0.5$. ^{14}N

coherences are excited and reconverted using two single rectangular pulses.

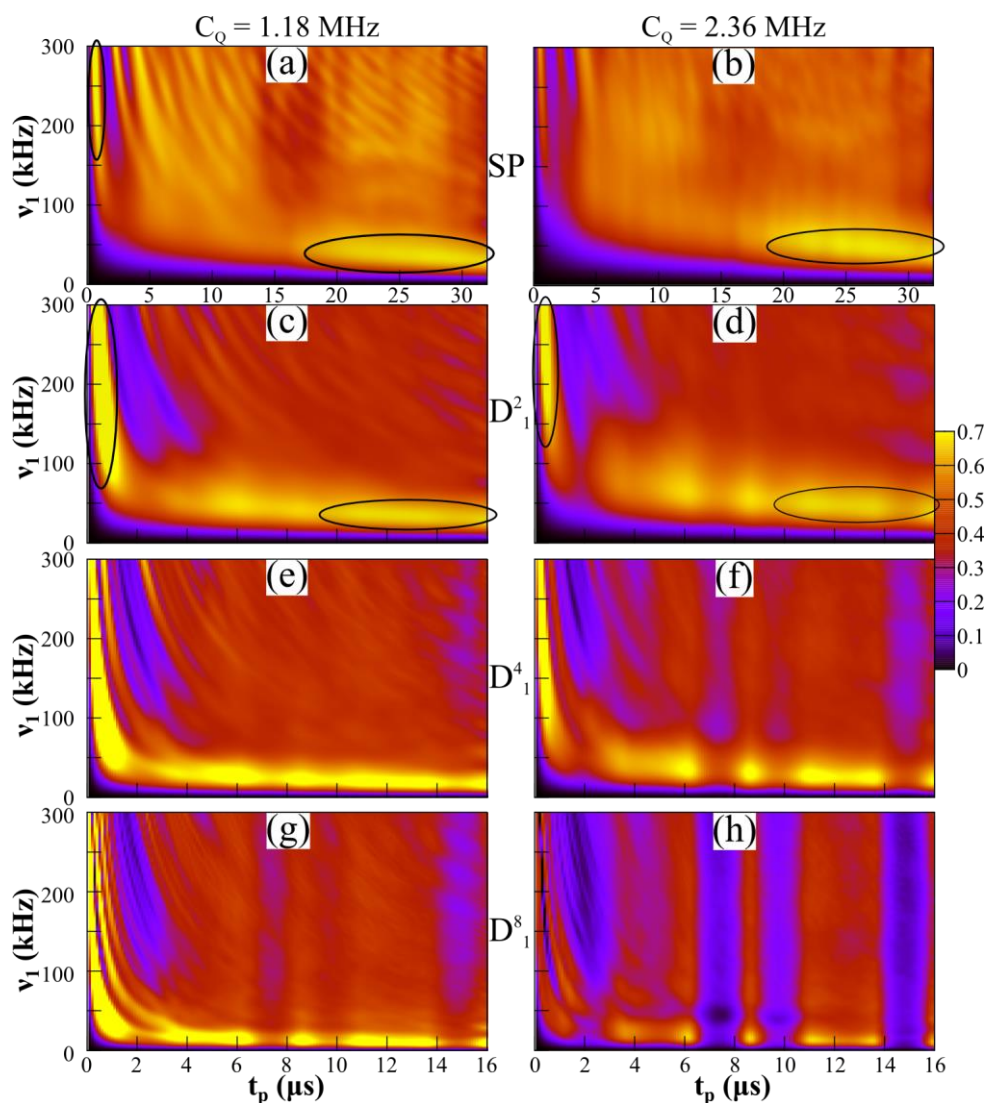


Fig.4. Simulated powder averaged signal of $^1\text{H}\{-^{14}\text{N}\}$ 1Q- J -HMQC experiment at $\nu_R = 62.5$ kHz versus the t_p length and the ν_1 rf-field for $C_Q = 1.18$ (a,c,e,g) and 2.36 (b,d,f,h) MHz, with $\eta_Q = 0.5$. ^{14}N coherences are excited and reconverted using two (a,b) rectangular single pulse (SP), or two (c,d) D^2_1 , (e,f) D^4_1 , and (g,h) D^8_1 DANTE trains. The regions corresponding to broadband and SSB-selective excitation are circled in subfigures (a) to (d).

Similar simulations were also carried out for $^1\text{H}\{-^{14}\text{N}\}$ 1Q- J -HMQC sequence using DANTE schemes (Fig.4c to h). As already observed for $^1\text{H}\{-^{195}\text{Pt}\}$ J -HMQC, DANTE trains are efficient in two distinct regimes: (i) the broadband and (ii) the selective excitations. In both regimes, the optimal ν_1 value for D^K_1 scheme decreases with increasing K value because the sum of the individual pulse lengths, Kt_p , increases. Furthermore, the signal intensity is lower for $C_Q = 2.36$ than 1.18 MHz for long DANTE scheme ($K \geq 4$) because of the coherence loss due to second-order quadrupolar

interaction.^[36] The efficiencies of $^1\text{H}\{-^{14}\text{N}\}$ 1Q- J -HMQC experiments versus ν_1 strength using selective excitations with single pulses and DANTE trains are compared in Fig.S10, and it shows that the optimum selective rf field is approximately inverse proportional to the K value.

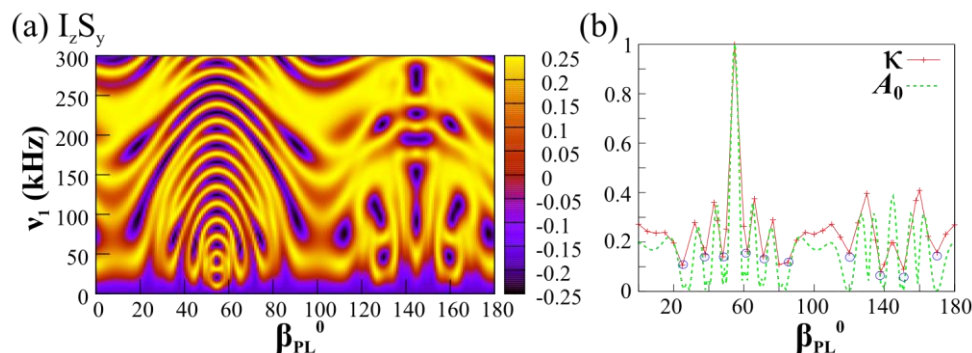


Fig.5. (a) Simulated $^1\text{H}\{-^{14}\text{N}\}$ 1Q- J -HMQC signal of a crystallite as function of β_{PL}^0 angle and ν_1 strength for $t_p = 24 \mu\text{s}$, $\nu_R = 62.5 \text{ kHz}$, $C_Q = 1.18 \text{ MHz}$ and $\eta_Q = 0.5$. (b) The A_0 ratio (green dashed line) and the κ factor (red crosses) are plotted as function of β_{PL}^0 angle. The two other Euler angles are fixed to $\alpha_{\text{PR}} = 0$ and $\gamma_{\text{PR}} = 90^\circ$. The signals in these figures are simulated by selecting the terms in the density matrix proportional to $S_y I_z$ operator at the end of the first $\tau_{J/D}$ period and at the beginning of the second one.

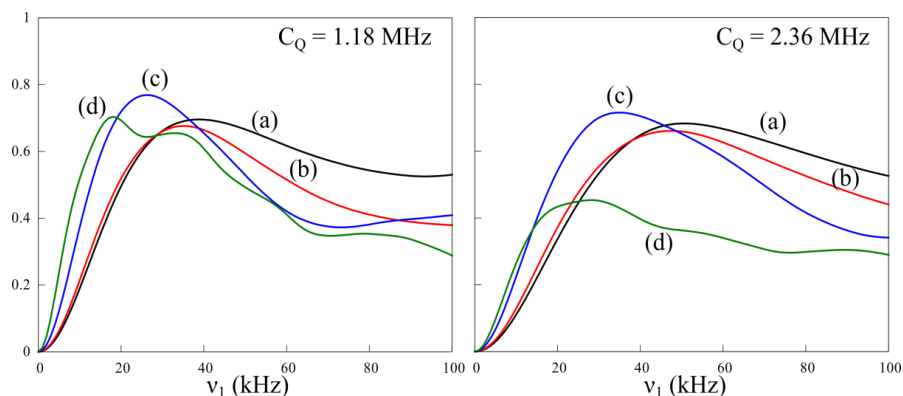


Fig.S10. Simulated powder averaged signal of $^1\text{H}\{-^{14}\text{N}\}$ 1Q- J -HMQC experiment at $\nu_R = 62.5 \text{ kHz}$, versus the rf-field, ν_1 , for $t_p = 25$ (SP) and 11 (top Figs) or 25/K (bottom Figs) (D^K_1) μs with $C_Q = 1.18$ (left) and 2.36 MHz (right), $\eta_Q = 0.5$. ^{14}N coherences are excited and reconverted using two (a) single pulses, or two (b) D^2_1 , (c) D^4_1 and (d) D^8_1 trains.

We then checked the validity of Eq.14 for $^1\text{H}\{-^{14}\text{N}\}$ 1Q- J -HMQC signal passing through $S_y I_z$ terms at the end of the first $\tau_{J/D}$ period and the beginning of the second one in the case of ^{14}N selective pulses. The terms proportional to $S_x Q_z$, were filtered out. Fig.5 shows the simulated signal intensity of $^1\text{H}\{-^{14}\text{N}\}$ 1Q- J -HMQC experiment resulting from $S_y I_z$ terms as function of β_{PL}^0 and ν_1 for $t_p = 24 \mu\text{s}$. As already observed for $^1\text{H}\{-^{195}\text{Pt}\}$ J -HMQC (Fig.3), the optimal ν_1 value highly depends on the crystallite orientation.

According to Eq.8, selective excitation is achieved by pulses with $\nu_1 \leq \nu_R$. Under this condition, the ${}^1\text{H}\{-{}^{14}\text{N}\}$ 1Q- J -HMQC signal is given by Eq.21. As $t_p = 24 \mu\text{s}$, the frequency $1/(\kappa t_p) = 42/\kappa \text{ kHz}$ exceeds the MAS frequency for most crystallite orientations and hence periodic oscillations versus ν_1 of the signal in the selective excitation regime are not observed in Fig.5a. Therefore, the κ factor was calculated as $1/(4\nu_1^{\text{max1}} t_p)$, where ν_1^{max1} is the first smallest rf field producing maximal ${}^1\text{H}\{-{}^{14}\text{N}\}$ 1Q- J -HMQC signal for a given crystallite. As seen in Fig.5a, ν_1^{max1} frequency is smaller than ν_R for most crystallites and hence Eq.21 is valid. Fig.5b demonstrates that there is a good agreement between the κ factor and A_0 ratio, which proves the validity of Eq.14 for ${}^1\text{H}\{-{}^{14}\text{N}\}$ 1Q- J -HMQC experiment using selective excitation.

We also simulated the dependence of the signal intensity of ${}^1\text{H}\{-{}^{14}\text{N}\}$ 1Q- J -HMQC experiment using selective pulses as function of $\{\alpha_{PR}, \beta_{PL}^0\}$ and $\{\gamma_{PR}, \beta_{PL}^0\}$ Euler angles (Fig.S11). The dependence of the signal intensity with γ_{PR} angle (Fig.S11b) is higher than that observed for ${}^{195}\text{Pt}$ nucleus (Fig.S6). This was expected since A_n ratios are only independent of γ_{PR} angles for SSB manifold produced by CSA.^[61]

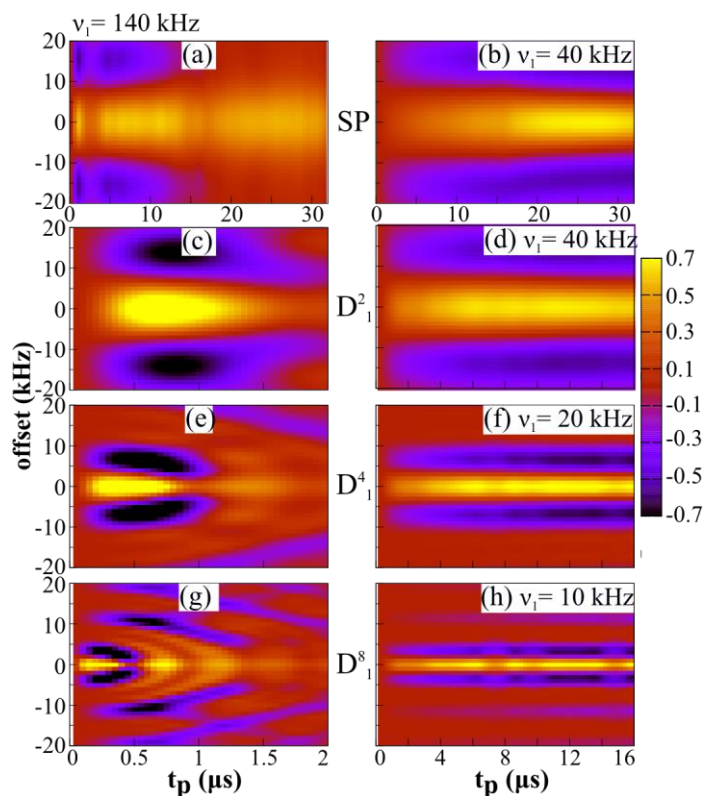


Fig.6. Simulated powder averaged signal of ${}^1\text{H}\{-{}^{14}\text{N}\}$ 1Q- J -HMQC experiments versus the individual pulse length, t_p , and the ${}^{14}\text{N}$ off-resonance carrier frequency for $\nu_R = 62.5 \text{ kHz}$, $C_Q = 1.18 \text{ MHz}$ and η_Q

$= 0.5$. ^{14}N coherences are excited and reconverted using either two rectangular single pulses (SP) (a,b), or two D^2_1 (c,d), D^4_1 (e,f), and D^8_1 (g,h) DANTE trains, which achieve either broadband excitation (first column) using $\nu_1 = 140$ kHz or selective excitation using indicated ν_1 values (second column).

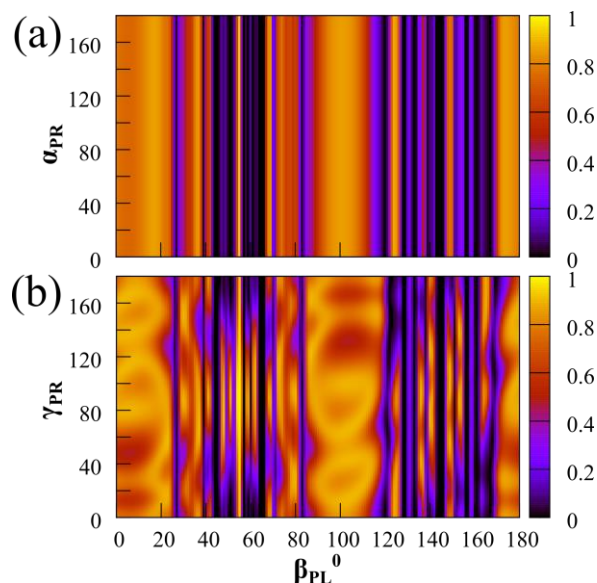


Fig.S11. Simulated $^1\text{H}\{-^{14}\text{N}\}$ 1Q- J -HMQC signal of a crystallite as function of: (a) $(\alpha_{\text{PR}}, \beta_{\text{PL}}^0)$ ($\gamma_{\text{PR}} = 0$), and (b) $(\gamma_{\text{PR}}, \beta_{\text{PL}}^0)$ ($\alpha_{\text{PR}} = 0$) angles. ^{14}N coherences are excited and reconverted using two single rectangular pulses with $t_p = 32 \mu\text{s}$ and $\nu_1 = 40$ kHz. $\nu_R = 62.5$ kHz, $C_Q = 1.18$ MHz and $\eta_Q = 0$.

The sensitivity of $^1\text{H}\{-^{14}\text{N}\}$ 1Q- J -HMQC signal versus ^{14}N offset and pulse length, t_p , has been calculated for $C_Q = 1.18$ (Fig.6) and 2.36 MHz (Fig.S12). Simulations were performed using either broadband or selective excitations with $\nu_1 = 140$ or ≤ 40 kHz, respectively. For two single pulses (Fig.6a,b and S12a,b), the best signal is observed with the moderate rf-field ($\nu_1 = 40$ kHz) and a long selective pulse ($t_p > 20\mu\text{s}$). Under these optimal conditions, the offset band-width, defined as the Full-Width at Half Maximum (FWHM) of the excitation profile is equal to ≈ 10 kHz and this value is the same as that achieved by a large rf-field of $\nu_1 = 140$ kHz. This offset range is most of the time sufficient, as it corresponds to $\text{FWHM} \approx 180$ ppm at 18.8 T, which allows exciting the chemical shift range of ^{14}N nuclei in peptides. For D^2_1 trains, the best efficiency is observed either with the broadband excitation ($t_p \approx 0.8 \mu\text{s}$ and $\nu_1 = 140$ kHz) for $C_Q = 1.18$ MHz (Fig.6c,d) or with the selective regime ($t_p > 8\text{-}10 \mu\text{s}$ and $\nu_1 = 40$ kHz) for $C_Q = 2.36$ MHz (Fig.S12c,d). In both cases, the offset band-widths are similar to those achieved by single pulses, $\text{FWHM} \approx 10$ kHz. This is expected because the total lengths of single pulse with $t_p > 20 \mu\text{s}$ and D^2_1 scheme are similar. The simulations for D^2_1 , D^4_1 and

D^8_1 schemes show that the offset band-width decreases ca. inversely proportional to the K value for both broadband and selective excitations (Fig.S13). It must be noted that this sensitivity to offset is little dependent on t_p length (Fig.6) and C_Q value (compare Figs.6 and S12); actually it only mainly depends on the K and ν_R values (Fig.S13).

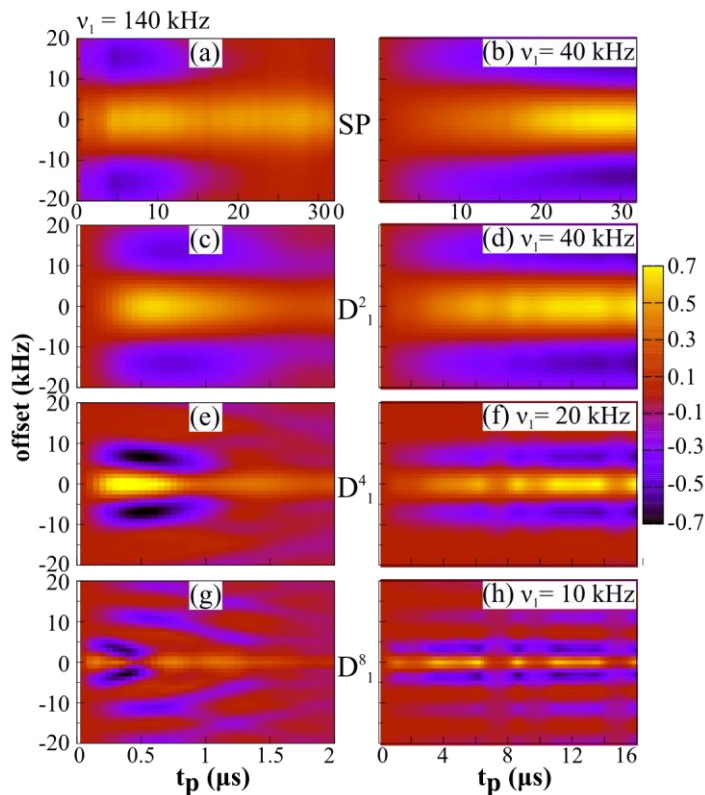


Fig.S12. Simulated powder averaged signal of $^1\text{H}\{-^{14}\text{N}\}$ 1Q- J -HMQC experiments versus the individual pulse length, t_p , and the ^{14}N off-resonance carrier frequency for $\nu_R = 62.5$ kHz, $C_Q = 2.36$ MHz and $\eta_Q = 0.5$. ^{14}N coherences are excited and reconverted using either two rectangular single pulses (SP) (a,b), or two D^2_1 (c,d), D^4_1 (e,f), and D^8_1 (g,h) DANTE trains, which achieve either broadband excitation (first column) using $\nu_1 = 140$ kHz or selective excitation using indicated ν_1 values (second column).

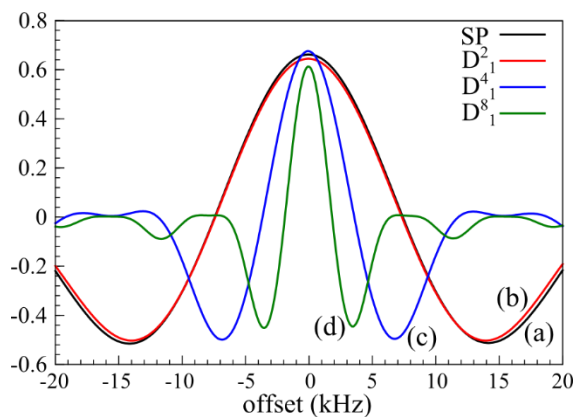


Fig.S13. Simulated powder averaged signal versus ^{14}N off-resonance carrier frequency observed with $^1\text{H}\{-^{14}\text{N}\}$ 1Q- J -HMQC experiments for $C_Q = 2.36$ MHz. ^{14}N coherences are excited and reconverted using

two (a) single pulses (SP) or two (b) D^2_1 , (c) D^4_1 , and (d) D^8_1 trains with $(t_p (\mu\text{s}), v_1 (\text{kHz})) = (25,40)$ (a, SP), $(11,40)$ (b, D^2_1), $(11,20)$ (c, D^4_1), and $(11, 10)$ (d, D^8_1).

Fig.7 displays the signal of $^1\text{H}\{-^{14}\text{N}\}$ 1Q- J -HMQC experiment using two single rectangular pulses as function of t_p length and v_1 field strength for five quadrupolar coupling constants ranging from $C_Q = 0.1$ to 2.36 MHz. These simulations show that selective excitation can only be achieved when Eq.6 is valid, i.e. for spectra much broader than the MAS frequency. More quantitatively, selective excitation is still efficient for $FW/v_R = 12$ ($C_Q = 0.5$ MHz) but not for $FW/v_R \leq 6$ ($C_Q \leq 0.25$ MHz).

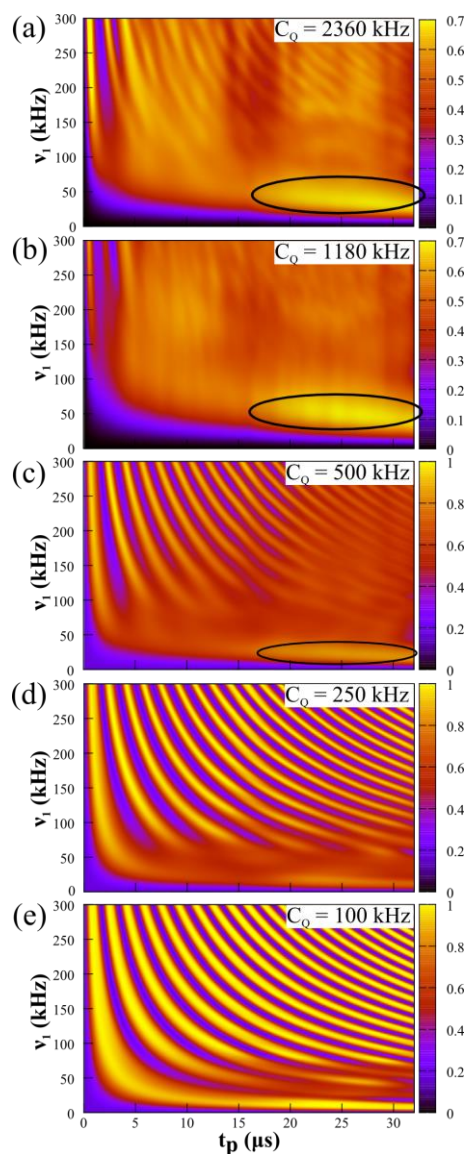


Fig.7. Simulated powder averaged signal at $v_R = 62.5$ KHz of $^1\text{H}\{-^{14}\text{N}\}$ 1Q- J -HMQC experiment versus the individual pulse length, t_p , and the rf-field, v_1 , for $C_Q =$ (a) 2360, (b) 1180, (c) 500, (d) 250, (e) 100 kHz, with $\eta_Q = 0.5$. ^{14}N coherences are excited and reconverted using two single rectangular pulses. The region corresponding to selective excitation is circled in subfigures (a-c).

The signal of $^1\text{H}\{-^{14}\text{N}\}$ 1Q- J -HMQC experiments was also simulated at $\nu_R = 31.25$ kHz as function of t_p length and ν_1 strength (Fig.8). As already observed at $\nu_R = 62.5$ kHz, these simulations show the existence of the two different regimes: (i) broadband and (ii) selective excitations. As expected, center-band selective excitation using single pulses or DANTE trains requires twice longer t_p length at $\nu_R = 31.25$ than at 62.5 kHz. For instance, selective excitation using single pulses requires $t_p \geq 32 \mu\text{s}$, which demonstrates the validity of Eq.7. Similarly, the optimal rf field value for selective excitation is about $\nu_1 \approx 25$ kHz at $\nu_R = 31.25$ kHz and 40 kHz at $\nu_R = 62.5$ kHz in agreement with Eq.8. The signal of $^1\text{H}\{-^{14}\text{N}\}$ 1Q- J -HMQC experiments for $C_Q = 2.36$ MHz is lower at $\nu_R = 31.25$ than at 62.5 kHz because of the longer rotor period, which leads to larger losses due to second-order quadrupolar interaction for DANTE trains and long single pulses achieving selective excitation.

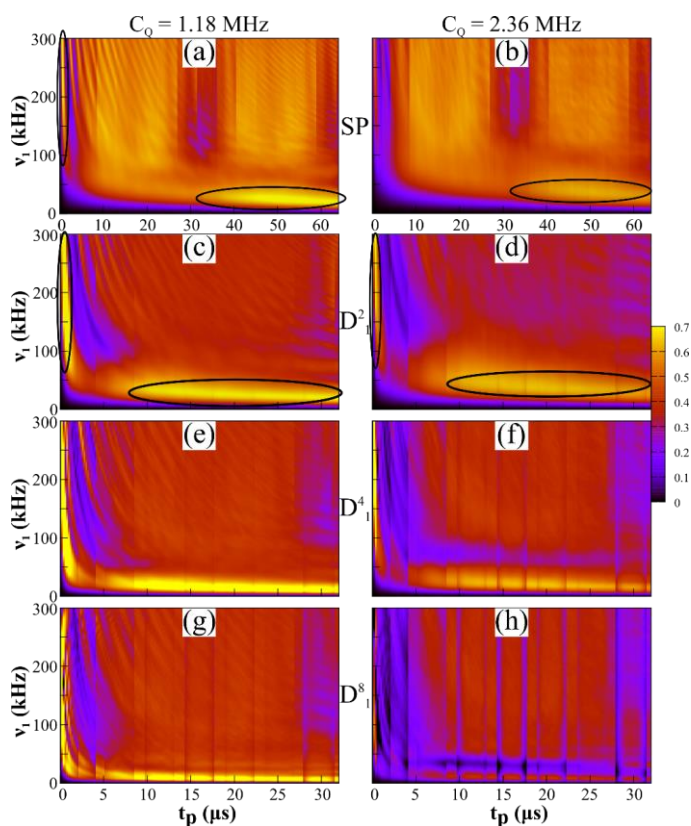


Fig.8. Simulated powder averaged signal of $^1\text{H}\{-^{14}\text{N}\}$ 1Q- J -HMQC experiments at $\nu_R = 31.25$ kHz versus the individual pulse length, t_p , and the rf-field, ν_1 , for $C_Q = 1.18$ (left) or 2.36 MHz (right column), with $\eta_Q = 0.5$. ^{14}N coherences are excited and reconverted using either (a,b) two single rectangular pulses (SP), or two (c,d) D^2_1 , (e,f) D^4_1 , and (g,h) D^8_1 DANTE trains.

(c) $^1\text{H}\{-^{14}\text{N}\}$ 2Q- J -HMQC experiment

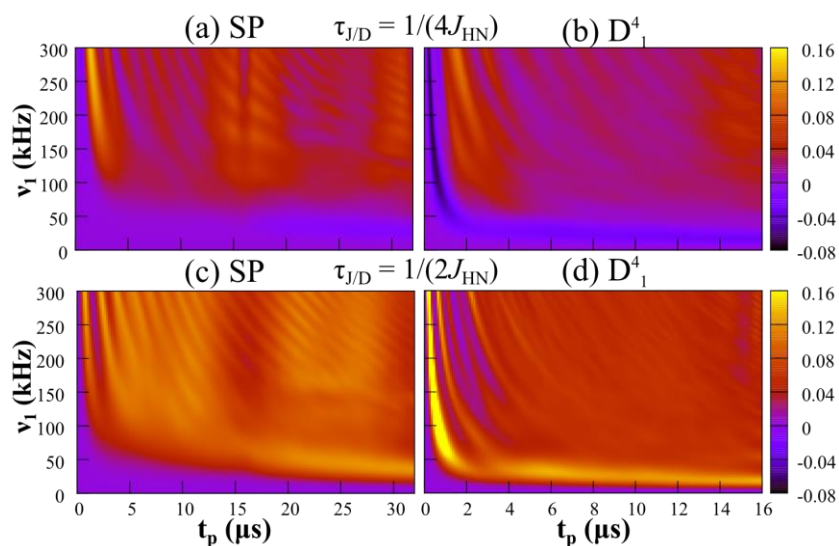


Fig.9. Simulated powder averaged signal of $^1\text{H}\{-^{14}\text{N}\}$ 2Q- J -HMQC experiment at $\nu_{\text{R}} = 62.5$ kHz versus the t_{p} length and the rf-field, ν_1 for $C_{\text{Q}} = 1.18$ MHz and $\eta_{\text{Q}} = 0.5$; $\tau_{\text{J/D}} =$ (a,c) $1/(4J_{\text{HN}})$ or (b,d) $1/(2J_{\text{HN}})$. ^{14}N coherences are excited and reconverted using either (a,c) two single rectangular pulse or (b,d) two D^4_1 DANTE trains.

Fig.9 shows the $^1\text{H}\{-^{14}\text{N}\}$ 2Q- J -HMQC signal of a powder as function of t_{p} length and ν_1 strength. In Figs.9c and d, $\tau_{\text{J/D}}$ delay was equal to $1/(2J_{\text{HN}})$ and according to Eq.2, only the terms proportional to $S_x Q_z$ operator at the end of the first $\tau_{\text{J/D}}$ period and the beginning of the second one contribute to the signal. Figs.9c and d are similar to Figs.4a and e, which indicate again the existence of two regimes to convert Q_z operator into ^{14}N 2Q coherences: (i) broadband and (ii) center-band selective excitations. To better understand Fig.9c, we simulated the evolution of Q_z operator during a rectangular pulse with phase x (Fig.S14). As already reported,^[60] broadband excitation pulses leading to flip angles of 45° and 135° convert Q_z into K_y operator. This y -magnetization, antiphase with respect to first-order quadrupolar interaction, evolves into I_x operator under first-order quadrupolar interaction. Nevertheless, I_x and K_y operators correspond to ^{14}N 1Q coherences and hence do not contribute to the signal of $^1\text{H}\{-^{14}\text{N}\}$ 2Q- J -HMQC experiment. Broadband excitation pulses leading to flip angles of 90° transform Q_z into D_x operator (Fig.S14d) in agreement with the predicted evolution rule for such type of pulse.^[60] Fig.14d also shows that long pulses and especially those achieving center-band selective excitation efficiently convert Q_z operator into D_x one, corresponding to ^{14}N 2Q coherences. During long pulses, D_x operator evolves into D_y operator under isotropic shift. Long pulses also convert Q_z operator into K_y and I_y ones. However, the projections onto

K_y and I_y operators are smaller than those onto D_x one because the former dephase under first-order quadrupolar interaction, whereas the 2Q coherences do not. Furthermore, as noted above, these K_y and I_y operators do not contribute to the signal of $^1\text{H}\{-^{14}\text{N}\}$ 2Q- J -HMQC experiment. In summary, Fig.S14 shows that the $^1\text{H}\{-^{14}\text{N}\}$ 2Q- J -HMQC signal for $\tau_{J/D} = 1/(2J_{HN})$ results from the inter-conversion between Q_z and D_x operators. This inter-conversion is produced by broadband as well as long pulses.

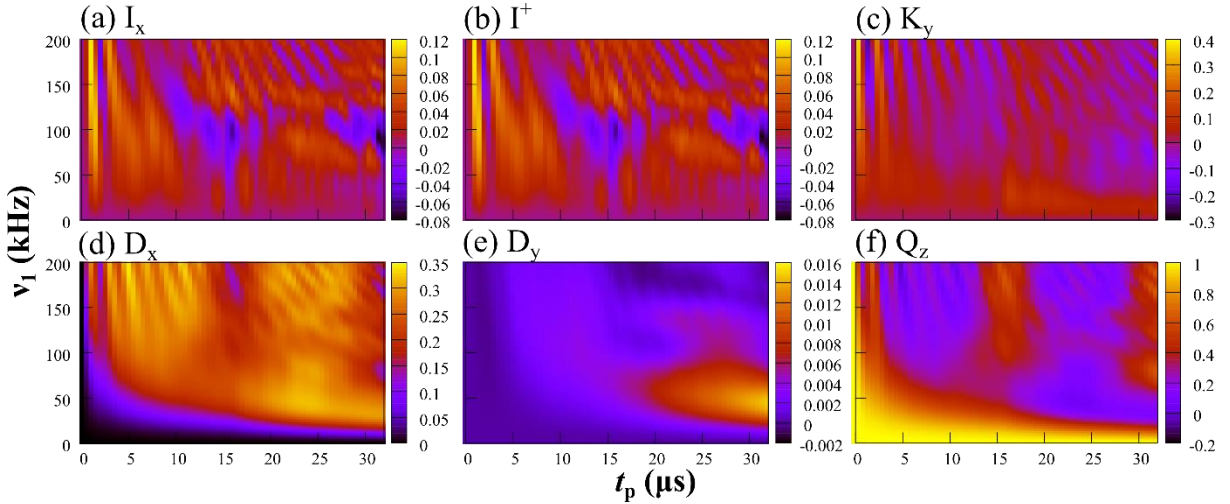


Fig.S14. Projections of the simulated density matrix onto (a) I_y , (b) K_x , (c) I_z and (d) D_y operators after a single rectangular pulse applied to ^{14}N spin at $\nu_R = 62.5$ kHz, with $C_Q = 1.18$ MHz and $\eta_Q = 0.5$. The starting operator was Q_z and the projections were normalized with respect to the norm of the starting operator. The quadrupolar interaction was restricted to the first-order term. The projections were calculated as function of the pulse length, t_p , and the rf field strength, ν_1 . The projections onto the other operators (I_x , K_x) are negligible.

For $\tau_{J/D} = 1/(4J_{HN})$, according to Eq.2 the density operator at the end of the first $\tau_{J/D}$ delay is proportional to

$$\frac{S_x}{3} - \frac{S_x Q_z}{3} + S_y I_z \quad (22)$$

Hence, 2Q coherences can be created by both the transformation of Q_z operator into D_x by the long ^{14}N pulses (Fig.S14d) or by that of I_z operator into D_y (Fig.S9d). Nevertheless, as seen in Figs. 9a and b, the $^1\text{H}\{-^{14}\text{N}\}$ 2Q- J -HMQC signal for long ^{14}N pulses and $\tau_{J/D} = 1/(4J_{HN})$ is weak and the contribution of $S_x Q_z$ and $S_y I_z$ operators must cancel out.

Globally, the best 2Q- J -HMQC efficiency is observed with $\tau_{J/D} \approx 1/(2J_{HN})$, but this efficiency is much lower than that observed with 1Q- J -HMQC experiment (compare Figs.6 and 9).

5.4 Experimental demonstration for $^1\text{H}\{-^{14}\text{N}\}$ 1Q-HMQC

5.4.1 Samples and experimental conditions

All the NMR experiments were performed on isotopically unmodified α -glycine, which contains a single ^{14}N site with $C_Q = 1.18$ MHz and $\eta_Q = 0.54$. A narrow-bore Bruker Avance III 900 MHz spectrometer operating at 21.1 T was used for all NMR experiments ($\nu_0(^{14}\text{N}) = 65$ MHz). The sample was spun at $\nu_R = 60$ kHz in a double-resonance $^1\text{H}/\text{X}$ 1.3 mm MAS probe that can deliver ^{14}N rf-field up to $\nu_1 = 80$ kHz. Most of these experiments were also carried out at 18.8 T (800 MHz for ^1H) but the results are similar to those at 21.1 T and hence they are not presented here.

$^1\text{H}\{-^{14}\text{N}\}$ 1Q-*D*-HMQC experiments were performed using the sequence depicted in Fig.1. $\text{SR}4^2_1$ recoupling sequence was applied during the $\tau_{J/D}$ delay to reintroduce the $^1\text{H}\text{-}^{14}\text{N}$ dipolar couplings. The $^1\text{H}\{-^{14}\text{N}\}$ *D*-HMQC sequence was employed here since it is usually more sensitive than its *J*-HMQC cousin for solids. Actually the J_{HN} scalar and residual dipolar couplings, which are employed for coherence transfer in *J*-HMQC experiments, are smaller than the rate, $1/T_2'$, where T_2' is the homogeneous transverse dephasing time constant of ^1H 1Q coherences.^[23] Furthermore, the transfer efficiency of $^1\text{H}\{-^{14}\text{N}\}$ *J*-HMQC experiment decreases at higher B_0 field since the residual dipolar couplings are inversely proportional to B_0 field.

The $\text{SR}4^2_1$ recoupling sequence employed is a super-cycled version of the symmetry-based $\text{R}4^2_1$ sequence,^[57] and it offers several advantages for $^1\text{H}\{-^{14}\text{N}\}$ *D*-HMQC experiments,^[58,78] including: (i) the suppression of the $^1\text{H}\text{-}^1\text{H}$ dipolar interactions in the first-order Average Hamiltonian, which limits the signal losses during $\tau_{J/D}$ delays, (ii) the high robustness to isotropic and anisotropic chemical shifts as well as rf inhomogeneities, (iii) the reintroduction of $^1\text{H}\text{-}^{14}\text{N}$ dipolar couplings in the form of longitudinal two-spin order Hamiltonian, which is not affected by dipolar truncation, (iv) the low rf field requirement, $\nu_{1\text{H}} = 2\nu_R$, which permits its use at high MAS frequency, and (v) a single adjustable parameter, $\tau_{J/D}$, which simplifies the sequence optimization.

The rf nutation frequency of the $\pi/2$ and π hard pulses on ^1H channel was 200 kHz. The $\tau_{J/D}$ delay was of 100 μs , and the $\text{SR}4^2_1$ sequence was applied to the ^1H channel with

an rf nutation frequency of $\nu_{1H} = 2\nu_{1R} = 120$ kHz. Both single and D^K_1 train of rectangular pulses were employed to excite 1Q coherences of ^{14}N nuclei. Except for Fig.11, the t_1 delay in the 1D version of 1Q-*D*-HMQC sequences was fixed to its minimum rotor-synchronized value equal either to T_R (SP) or KT_R (D^K_1 train). The rf field on ^{14}N channel was applied on resonance, except for Fig.12. The other experimental parameters are indicated in the figure captions.

5.4.2 Effect of rf-field and pulse length

Fig.10a displays the experimental signal of $^1\text{H}\{-^{14}\text{N}\}$ 1Q-*D*-HMQC experiments using single rectangular pulses on α -glycine as function of t_p length and ν_1 strength. The comparison of Figs.4a and 10a shows that there is a good agreement between the simulated and experimental signals. Nevertheless, owing to the probe specifications, $^1\text{H}\{-^{14}\text{N}\}$ 1Q-*D*-HMQC experiments can only be performed with rf strength up to $\nu_1 = 80$ kHz. Hence, short pulses are not able to excite efficiently the ^{14}N signal of α -glycine, even if its C_Q value is only of 1.18 MHz. In other words, the maximal rf field on ^{14}N channel is insufficient so that single rectangular pulses achieve efficient broadband excitation. Higher signal intensity is achieved by long single pulses with $t_p \geq 20$ μs using moderate rf field of $\nu_1 \approx 30\text{-}40$ kHz. These conditions correspond to the regime of center-band selective excitation. Fig.10d permits an easy comparison of $^1\text{H}\{-^{14}\text{N}\}$ 1Q-*D*-HMQC signal intensity between the different regimes. For $\nu_1 = 30$ kHz, the signal intensity for center-band selective single pulses with $t_p = 32$ μs is about fivefold larger than for conventional 90° pulse with $t_p = 1/(4\nu_1) = 8.3$ μs and about 1.8 times larger than that observed for short pulses with $\nu_1 = 80$ kHz and $t_p = 1/(4\nu_1) = 3.1$ μs . In agreement with simulations, high-power long pulses are not optimal for the excitation of 1Q ^{14}N coherences.

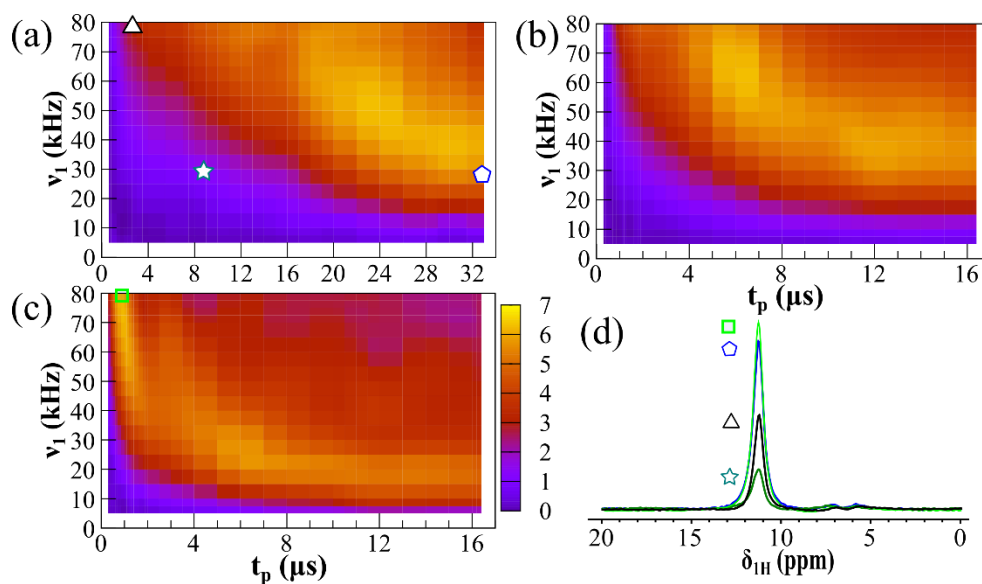


Fig.10. (a-c) Experimental $^1\text{H}\{-^{14}\text{N}\}$ 1Q-D-HMQC signal of α -glycine powder at $B_0 = 21.1$ T and $\nu_R = 60$ kHz versus the t_p length and the ν_1 amplitude. The rf field was incremented from 5 to 80 kHz by step of 10 kHz and the t_p length was incremented from 0.3 to 32 (a) or to 16 (b) μs by step of 1 μs . ^{14}N coherences are excited and reconverted using either two (a) single rectangular pulses (SP), or two (b) D^2_1 , and (c) D^5_1 DANTE trains. (d) Comparison of $^1\text{H}\{-^{14}\text{N}\}$ 1Q-D-HMQC 1D spectra acquired using either SP with (t_p, ν_1) ($\mu\text{s}, \text{kHz}$) = (8.2, 30) (open green star), (3.1, 80) (open black triangle), (32, 30) (open blue pentagon), or D^5_1 with (1, 80) (open light green square).

Similar experiments were performed for D^2_1 and D^5_1 trains (Figs.10b and c). For D^2_1 train, there is again a good agreement with the numerical simulations (compare Figs.4c and 10b) but as for the single pulse, an rf field amplitude limited to $\nu_1 \leq 80$ kHz is not sufficient to observe the broadband excitation regime. Here again, high signal intensity is measured for center-band selective excitation pulses with $t_p \geq 8$ μs and $\nu_1 \approx 30$ -40 kHz. Broadband excitation using D^5_1 trains requires rf field fivefold lower than those employed for single rectangular pulses (Eq.5) and hence such DANTE trains achieves broadband on-resonance excitation for short pulses, $t_p \leq 1.5$ μs , and $\nu_1 \geq 50$ kHz. For these broadband pulses, a total flip angle of about 90° degrees is obtained with $t_p \approx 1/4K\nu_1$ (Eq.5). Such DANTE broadband irradiation leads to the same efficiency as that observed with SP using a selective excitation (Fig.10d), but with a much smaller robustness with respect to offset (Fig.12). The center-band selective excitation regime is detected for pulse lengths, $t_p \geq 4$ μs , and rf-fields $\nu_1 \approx 10$ -20 kHz, which are much smaller than those required for single rectangular pulses and D^2_1 train (compare Figs. 10a, b and c).

5.4.3 Sensitivity to rotor-synchronization

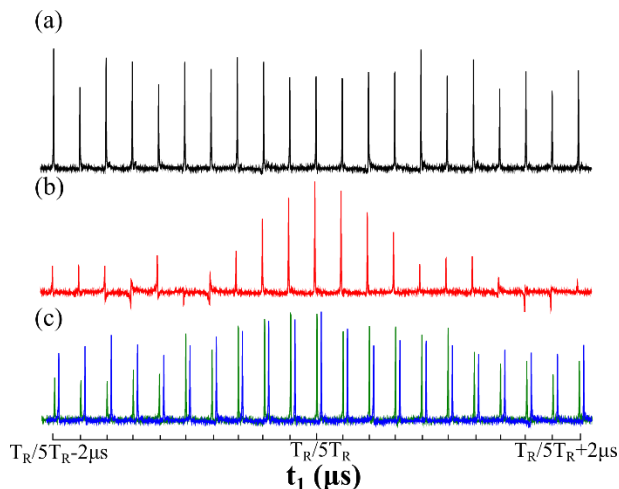


Fig.11. Experimental $^1\text{H}\{-^{14}\text{N}\}$ 1Q- D -HMQC signal of α -glycine powder at $B_0 = 21.1$ T and $\nu_R = 60$ kHz versus the t_1 delay. ^{14}N coherences are excited and reconverted using (a) two single rectangular pulses, with $\nu_1 = 40$ kHz and $t_p = 33$ μs or (b-c) two D^5_1 DANTE trains with (b) $\nu_1 = 80$ kHz and $t_p = 0.8$ μs or (c) $\nu_1 = 20$ kHz and $t_p = 6$ (left) or 15 (right) μs . The t_1 delay is varied between $T_R \pm 2$ μs for single pulses or $5T_R \pm 2$ μs for D^5_1 trains by 0.2 μs step.

Fig.11 shows the variation of $^1\text{H}\{-^{14}\text{N}\}$ 1Q- D -HMQC signal as function of the t_1 delay when using different excitation schemes on ^{14}N channel. Center-band selective excitation is achieved using long pulses of low power used as single pulses (Fig.11a) or incorporated in a D^5_1 train (Fig.11c), whereas broadband excitation is achieved by a D^5_1 train made of high-power short pulses (Fig.11b). The experimental results displayed in Fig.11 demonstrate that selective excitations are efficient, even if the t_1 delay is not an integer multiple of T_R period, i.e. is not perfectly rotor-synchronized. Conversely broadband excitation with DANTE schemes requires a perfectly rotor-synchronized t_1 period. In practice, these results indicate that selective excitation is more robust to fluctuations in MAS frequency. The higher robustness in the selective regime must stem from the fact that the initial time point of the pulse only affects the phase of Hamiltonian of Eq.9, but not its norm. Conversely a time shift of DANTE trains induces distinct phase shift for the different rf spikelets,^[35] and hence the signal amplitude strongly depends on the t_1 period.

5.4.4 Robustness to ^{14}N offset

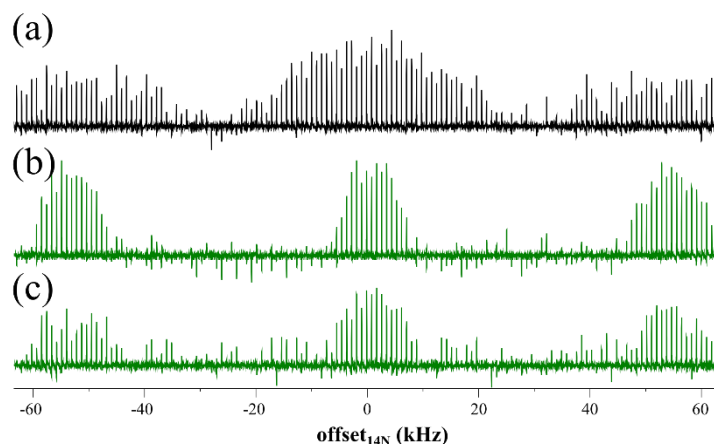


Fig.12. Experimental $^1\text{H}\{-^{14}\text{N}\}$ 1Q-*D*-HMQC signal of α -glycine powder at $B_0 = 21.1$ T and $\nu_R = 60$ kHz versus the offset of ^{14}N carrier frequency. ^{14}N coherences are excited and reconverted using (a) two single rectangular pulses (SP) with $\nu_1 = 40$ kHz and $t_p = 33$ μs , or two D^5_1 trains with (b) $\nu_1 = 80$ kHz and $t_p = 0.8$ μs , or (c) $\nu_1 = 20$ kHz and $t_p = 15$ μs . The ^{14}N offset is varied between ± 63 kHz by step of 1 kHz.

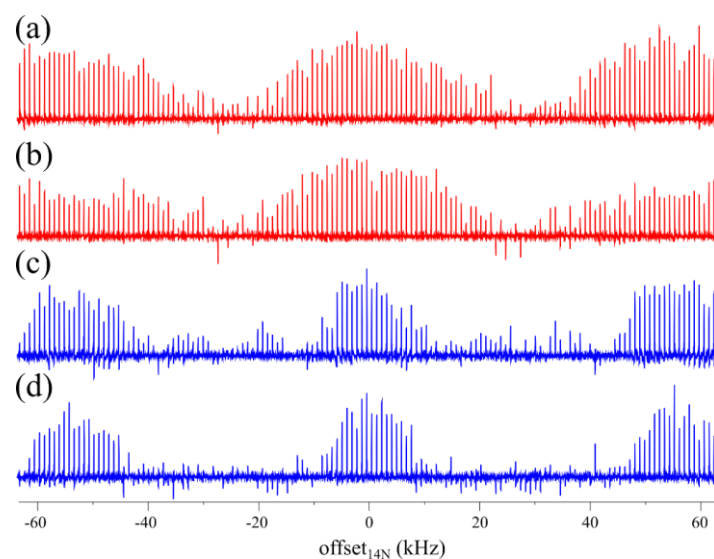


Fig.S15. Experimental $^1\text{H}\{-^{14}\text{N}\}$ 1Q-*D*-HMQC signal of α -glycine powder at $B_0 = 21.1$ T and $\nu_R = 60$ kHz versus the offset of ^{14}N carrier frequency. ^{14}N coherences are excited and reconverted using either a D^2_2 train with $(\nu_1$ (kHz), t_p (μs)) = (80,2) (a), (40, 8) (b), or a D^4_2 train with (70, 1) (c), or (20, 4) (d).

Fig.12 shows the dependence of the signal of $^1\text{H}\{-^{14}\text{N}\}$ 1Q-*D*-HMQC experiments using single selective pulses or DANTE trains (selective or broadband) as function of the ^{14}N offset at $\nu_R = 60$ kHz. As already observed in numerical simulations (Fig.6 and S12), long single pulses with $\nu_1 = 40$ kHz and $t_p = 33$ μs (Fig.12a), which achieve selective excitation, are more robust to offset than D^K_1 train with $K > 2$ either in the regime of broadband (Fig.12b) or selective (Fig.12c) excitation. The single selective pulses can excite the very broad ^{14}N range of FWHM ≈ 20 kHz, but nevertheless, the D^5_1 trains are still able to excite the range of FWHM ≈ 10 kHz (150 ppm at 21.1 T), which is

sufficient for most peptide samples. Interestingly, this value is the same for D^5_1 trains achieving selective or broadband excitation, since it only depends on the total length of the DANTE scheme but not on the t_p length and the ν_1 strength. The FWHM value of interleaved D^2_2 trains, achieving selective or broadband excitation is similar to that of single selective pulses with $t_p = 33 \mu\text{s}$ and twice that of D^4_2 trains (compare Figs.12 and S15). Again, the sensitivity to offset is inverse proportional to the total pulse length. However, all these values are approximately twice larger than those predicted by numerical simulations (Fig.6), but we do not have yet a definitive explanation for such discrepancy between numerical simulations and experiments. The robustness to offset of broadband excitation single pulse does not depend on the MAS frequency. Conversely, Eq.7 indicates that it increases at higher MAS frequency with selective single pulses and DANTE schemes. Furthermore, high MAS frequency also decreases the signal losses due to ^1H - ^1H dipolar coupling and ^{14}N second-order quadrupolar interaction during ^1H - $\{^{14}\text{N}\}$ 1Q- J -HMQC sequence.

5.5 Conclusions

We have explained here for the first time how nuclei experiencing large anisotropic NMR interactions can be indirectly observed by HMQC scheme using selective excitation on the indirect channel with single pulses (SP) or DANTE trains. Numerical simulations have shown that these selective excitations can be employed to efficiently detect spin-1/2 nuclei experiencing large CSA, as well spin-1 nuclei subject to large quadrupolar interaction, such as ^{14}N . They have confirmed that the rf field amplitude is scaled down by the intensity of the center-band in the selective excitation regime. The potential of selective excitations has been demonstrated with ^1H - $\{^{14}\text{N}\}$ 1Q- D -HMQC experiments. These long pulses result in transfer efficiency at least comparable to those achieved by broadband excitation with single strong pulses using maximum rf fields delivered by common MAS probes. Center-band selective pulses use moderate rf fields: slightly lower than the MAS frequency for single pulses or even lower for DANTE schemes made of long pulses. Furthermore, they benefit from high robustness to rf inhomogeneity, MAS fluctuations and offset. Finally, selective SPs require almost no

optimization since this regime displays a broad optimum with respect to the pulse length, $t_p \approx 1.5T_R$, and strength, $v_1 \approx 0.65v_R$, to achieve almost optimal transfer efficiency.

The choice in between the selective excitation with two SPs or two DANTE trains depends on a compromise in between the sensitivity to offsets and the required rf field strength. However, it must be noted that even with SP selective excitations the required rf field strength is weak and smaller than the spinning speed. More globally, the selective excitation with two SPs looks to be the most appropriate way to perform $^1\text{H}\{-^{14}\text{N}\}$ 1Q-HMQC experiments, except when the ^{14}N frequency range is small or moderate where DANTE trains provide a slightly larger efficiency than selective SPs.

These HMQC sequences employing center-band selective pulses, demonstrated here for $^1\text{H}\text{-}^{14}\text{N}$ correlation, could be applied to correlate spin-1/2 nuclei with other spin-1/2 nuclei experiencing large anisotropic shifts in diamagnetic or paramagnetic samples. This approach must also be useful for hetero-nuclear correlation between spin-1/2 and the satellite transition of half-integer spin quadrupolar nuclei. Such type of correlation can lead to improvement in resolution and sensitivity compared to the correlation with the central transition of the half-integer spin quadrupolar nuclei.^[79,80] Nevertheless, filtering methods will be required to disentangle the central and the satellite transitions. These methods are currently under investigation.

Besides, the analysis of the spin dynamics in the center-band selective excitation regime can improve our understanding of other solid-state NMR methods, including RESPDOR/LA-REDOR, DANTE or FASTER-3QMAS experiments.

References:

- [1] D.C. Apperley, R.K. Harris, P. Hodgkinson, *Solid State NMR: Basic principle & practice*, Momentum Press, New York, 2012.
- [2] S.E. Ashbrook, D.M. Dawson, J.M. Griffin, *Solid-State Nuclear Magnetic Resonance Spectroscopy*, in: D.W. Bruce, D. O'Hare, R.I. Walton (Eds.), *Local Struct. Charact.*, John Wiley & Sons, Ltd (2014) 1–88.
- [3] J.P. Amoureux, J. Trébosc, L. Delevoye, O. Lafon, B. Hu, Q. Wang, *Correlation NMR spectroscopy involving quadrupolar nuclei.*, *Solid State Nucl. Magn. Reson.* 35 (2009) 12–8.

- [4] M. Deschamps, D. Massiot, Correlation experiments involving half-integer quadrupolar nuclei, *eMagRes*. (2011).
- [5] S. Parthasarathy, Y. Nishiyama, Y. Ishii, Sensitivity and resolution Enhanced Solid-State NMR for paramagnetic systems and biomolecules under Very Fast Magic Angle Spinning, *Acc. Chem. Res.* 46 (2013) 2127–2135.
- [6] M.J. Knight, I.C. Felli, R. Pierattelli, L. Emsley, G. Pintacuda, Magic Angle Spinning NMR of paramagnetic proteins, *Acc. Chem. Res.* 46 (2013) 2108–16.
- [7] R.W. Schurko, Ultra-wideline solid-state NMR spectroscopy., *Acc. Chem. Res.* 46 (2013) 1985–1995.
- [8] N.P. Wickramasinghe, Y. Ishii, Sensitivity enhancement, assignment, and distance measurement in ^{13}C solid-state NMR spectroscopy for paramagnetic systems under fast magic angle spinning., *J. Magn. Reson.* 181 (2006) 233–43.
- [9] Z. Gan, Measuring amide nitrogen quadrupolar coupling by high-resolution $^{14}\text{N}/^{13}\text{C}$ NMR correlation under magic-angle spinning., *J. Am. Chem. Soc.* 128 (2006) 6040–6041.
- [10] Z. Gan, $^{13}\text{C}/^{14}\text{N}$ heteronuclear multiple-quantum correlation with rotary resonance and REDOR dipolar recoupling., *J. Magn. Reson.* 184 (2007) 39–43.
- [11] J. Trébosc, O. Lafon, B. Hu, J.-P. Amoureux, Indirect high-resolution detection for quadrupolar spin-3/2 nuclei in dipolar HMQC solid-state NMR experiments, *Chem. Phys. Lett.* 496 (2010) 201–207.
- [12] C. A. Fyfe, K.T. Mueller, H. Grondy, K.C. Wong-Moon, Dipolar dephasing between quadrupolar and spin- nuclei. REDOR and TEDOR NMR experiments on VPI-5, *Chem. Phys. Lett.* 199 (1992) 198–204.
- [13] J. Trébosc, B. Hu, J.P. Amoureux, Z. Gan, Through-space R^3 -HETCOR experiments between spin-1/2 and half-integer quadrupolar nuclei in solid-state NMR., *J. Magn. Reson.* 186 (2007) 220–7.
- [14] O. Lafon, Q. Wang, B. Hu, F. Vasconcelos, J. Trébosc, S. Cristol, et al., Indirect detection via spin-1/2 nuclei in solid state NMR spectroscopy: application to the observation of proximities between protons and quadrupolar nuclei., *J. Phys. Chem. A.* 113 (2009) 12864–12878.
- [15] G. Tricot, O. Lafon, J. Trébosc, L. Delevoye, F. M \acute{e} ar, L. Montagne, et al., Structural characterisation of phosphate materials: new insights into the spatial proximities between phosphorus and quadrupolar nuclei using the D-HMQC MAS NMR technique., *Phys. Chem. Chem. Phys.* 13 (2011) 16786–16794.

- [16] X. Lu, O. Lafon, J. Trébosc, G. Tricot, L. Delevoye, F. M é ar, et al., Observation of proximities between spin-1/2 and quadrupolar nuclei: which heteronuclear dipolar recoupling method is preferable?, *J. Chem. Phys.* 137 (2012) 144201.
- [17] G. Tricot, J. Trébosc, F. Pourpoint, R. Gauvin, L. Delevoye, The D-HMQC MAS-NMR technique: an efficient tool for the editing of through-space correlation spectra between quadrupolar and spin-1/2, *Annu. Reports NMR Spectrosc.* 81 (2014) 145–184.
- [18] C. Martineau, B. Bouchevreau, F. Taulelle, J. Trébosc, O. Lafon, J. Paul Amoureux, High-resolution through-space correlations between spin-1/2 and half-integer quadrupolar nuclei using the MQ-D-R-INEPT NMR experiment., *Phys. Chem. Chem. Phys.* (2012) 1–17.
- [19] S. Cavadini, A. Lupulescu, S. Antonijevic, G. Bodenhausen, Nitrogen-14 NMR spectroscopy using residual dipolar splittings in solids., *J. Am. Chem. Soc.* 128 (2006) 7706–7707.
- [20] S. Cavadini, S. Antonijevic, A. Lupulescu, G. Bodenhausen, Indirect detection of nitrogen-14 in solids via protons by nuclear magnetic resonance spectroscopy., *J. Magn. Reson.* 182 (2006) 168–72.
- [21] S. Cavadini, S. Antonijevic, A. Lupulescu, G. Bodenhausen, Indirect detection of nitrogen-14 in solid-state NMR spectroscopy., *Chemphyschem.* 8 (2007) 1363–1374.
- [22] S. Cavadini, A. Abraham, G. Bodenhausen, Proton-detected nitrogen-14 NMR by recoupling of heteronuclear dipolar interactions using symmetry-based sequences, *Chem. Phys. Lett.* 445 (2007) 1–5.
- [23] Z. Gan, J.-P. Amoureux, J. Trébosc, Proton-detected ^{14}N MAS NMR using homonuclear decoupled rotary resonance, *Chem. Phys. Lett.* 435 (2007) 163–169.
- [24] S. Cavadini, V. Vitzthum, S. Ulzega, A. Abraham, G. Bodenhausen, Line-narrowing in proton-detected nitrogen-14 NMR, *J. Magn. Reson.* 202 (2010) 57–63.
- [25] J. A. Jarvis, I.M. Haies, P.T.F. Williamson, M. Carravetta, An efficient NMR method for the characterisation of ^{14}N sites through indirect ^{13}C detection., *Phys. Chem. Chem. Phys.* 15 (2013) 7613–20.
- [26] K.J. Harris, A. Lupulescu, B.E.G. Lucier, L. Frydman, R.W. Schurko, Broadband adiabatic inversion pulses for cross polarization in wideline solid-state NMR spectroscopy., *J. Magn. Reson.* 224 (2012) 38–47.
- [27] K.J. Harris, S.L. Veinberg, C.R. Mireault, A. Lupulescu, L. Frydman, R.W. Schurko, Rapid acquisition of ^{14}N solid-state NMR spectra with broadband cross polarization., *Chemistry.* 19 (2013) 16469–75.
- [28] A.C. Kolbert, A. Bielecki, Broadband Hartmann-Hahn matching in Magic-Angle Spinning NMR via an adiabatic frequency sweep, *J. Magn. Reson. Ser. A.* 116 (1995) 29–35.

- [29] R. Fu, P. Pelupessy, G. Bodenhausen, Frequency-modulated cross-polarization for fast magic angle spinning NMR at high fields: relaxing the Hartmann-Hahn condition, *Chem. Phys. Lett.* 264 (1997) 63–69.
- [30] W.K. Peng, K. Takeda, M. Kitagawa, A new technique for cross polarization in solid-state NMR compatible with high spinning frequencies and high magnetic fields, *Chem. Phys. Lett.* 417 (2006) 58–62.
- [31] W.K. Peng, A. Samoson, M. Kitagawa, Simultaneous adiabatic spin-locking cross polarization in solid-state NMR of paramagnetic complexes, *Chem. Phys. Lett.* 460 (2008) 531–535.
- [32] G. Bodenhausen, R. Freeman, G.A. Morris, A simple pulse sequence for selective excitation in Fourier transform, *J. Magn. Reson.* 23 (1976) 171–175.
- [33] P. Caravatti, G. Bodenhausen, R.R. Ernst, Selective pulse experiments in high-resolution Solid State NMR, *J. Magn. Reson.* 103 (1983) 88–103.
- [34] V. Vitzthum, M.A. Caporini, S. Ulzega, G. Bodenhausen, Broadband excitation and indirect detection of nitrogen-14 in rotating solids using Delays Alternating with Nutation (DANTE), *J. Magn. Reson.* 212 (2011) 234–239.
- [35] V. Vitzthum, M. A. Caporini, S. Ulzega, J. Trébosc, O. Lafon, J.-P. Amoureux, et al., Uniform broadband excitation of crystallites in rotating solids using interleaved sequences of delays alternating with nutation., *J. Magn. Reson.* 223 (2012) 228–236.
- [36] X. Lu, J. Trébosc, O. Lafon, D. Carnevale, S. Ulzega, G. Bodenhausen, et al., Broadband excitation in solid-state NMR using interleaved DANTE pulse trains with N pulses per rotor period., *J. Magn. Reson.* 236 (2013) 105–116.
- [37] B. Hu, J.-P. Amoureux, J. Trébosc, S. Hafner, Through-space MP-CPMAS experiments between spin-1/2 and half-integer quadrupolar nuclei in solid-state NMR., *J. Magn. Reson.* 192 (2008) 8–16.
- [38] D. Wei, U. Akbey, B. Paaske, H. Oschkinat, B. Reif, M. Bjerring, et al., Optimal 2 H rf pulses and ^2H - ^{13}C Cross-Polarization methods for solid-state ^2H MAS NMR of perdeuterated proteins, (2011) 1289–1294.
- [39] X. Lu, A.S.L. Tankamony, J. Trébosc, O. Lafon, J.-P. Amoureux, Probing proximities between different quadrupolar isotopes using multi-pulse cross-polarization., *J. Magn. Reson.* 228 (2013) 148–58.
- [40] S.K. Jain, A.B. Nielsen, M. Hiller, L. Handel, M. Ernst, H. Oschkinat, et al., Low-power polarization transfer between deuterons and spin-1/2 nuclei using adiabatic (RESPIRATION)CP in solid-state NMR., *Phys. Chem. Chem. Phys.* 16 (2014) 2827–30.

- [41] K. Basse, S.K. Jain, O. Bakharev, N.C. Nielsen, Efficient polarization transfer between spin-1/2 and ^{14}N nuclei in solid-state MAS NMR spectroscopy., *J. Magn. Reson.* 244C (2014) 85–89.
- [42] Y. Ishii, R. Tycko, Sensitivity enhancement in solid state ^{15}N NMR by indirect detection with high-speed Magic Angle Spinning, *J. Magn. Reson.* 142 (2000) 199–204.
- [43] T. Vosegaard, P. Florian, D. Massiot, P.J. Grandinetti, Multiple quantum magic-angle spinning using rotary resonance excitation, *J. Chem. Phys.* 114 (2001) 4618.
- [44] Z. Gan, P. Grandinetti, Rotary resonance in multiple-quantum magic-angle spinning, *Chem. Phys. Lett.* 352 (2002) 252–261.
- [45] J.D. Walls, K.H. Lim, A. Pines, Theoretical studies of the spin dynamics of quadrupolar nuclei at rotational resonance conditions, *J. Chem. Phys.* 116 (2002) 79.
- [46] Z. Gan, Measuring multiple carbon-nitrogen distances in natural abundant solids using R-RESPDOR NMR., *Chem. Commun. (Camb).* (2006) 4712–4714.
- [47] L. Chen, Q. Wang, B. Hu, O. Lafon, J. Trébosc, F. Deng, et al., Measurement of hetero-nuclear distances using a symmetry-based pulse sequence in solid-state NMR., *Phys. Chem. Chem. Phys.* 12 (2010) 9395–9405.
- [48] L. Chen, X. Lu, Q. Wang, O. Lafon, J. Trébosc, F. Deng, et al., Distance measurement between a spin-1/2 and a half-integer quadrupolar nuclei by solid-state NMR using exact analytical expressions., *J. Magn. Reson.* 206 (2010) 269–273.
- [49] X. Lu, O. Lafon, J. Trébosc, J.-P. Amoureux, Detailed analysis of the S-RESPDOR solid-state NMR method for inter-nuclear distance measurement between spin-1/2 and quadrupolar nuclei., *J. Magn. Reson.* 215 (2012) 34–49.
- [50] F. Pourpoint, J. Trébosc, R.M. Gauvin, Q. Wang, O. Lafon, F. Deng, et al., Measurement of aluminum-carbon distances using S-RESPDOR NMR experiments., *Chemphyschem.* 13 (2012) 3605–3615.
- [51] F. Pourpoint, A.S. Lilly Thankamony, C. Volkringer, T. Loiseau, J. Trébosc, F. Aussenac, et al., Probing ^{27}Al - ^{13}C proximities in metal-organic frameworks using dynamic nuclear polarization enhanced NMR spectroscopy., *Chem. Commun.* 50 (2014) 933–935.
- [52] E. Nimerovsky, A. Goldbourt, Efficient rotational echo double resonance recoupling of a spin-1/2 and a quadrupolar spin at high spinning rates and weak irradiation fields., *J. Magn. Reson.* 206 (2010) 52–8.
- [53] E. Nimerovsky, A. Goldbourt, Insights into the spin dynamics of a large anisotropy spin subjected to long-pulse irradiation under a modified REDOR experiment., *J. Magn. Reson.* 225 (2012) 130–41.

- [54] A. Goldbourt, Distance measurements to metal ions and other quadrupolar spins by Magic Angle Spinning Solid State NMR, *Isr. J. Chem.* 54 (2014) 125–135.
- [55] A.J. Pell, G. Pintacuda, L. Emsley, Single crystal nuclear magnetic resonance in spinning powders., *J. Chem. Phys.* 135 (2011) 144201.
- [56] D. Carnevale, V. Vitzthum, O. Lafon, J. Trébosc, J. Amoureux, G. Bodenhausen, Broadband excitation in solid-state NMR of paramagnetic samples using Delays Alternating with Nutation for Tailored Excitation (“ Para-DANTE ”), *Chem. Phys. Lett.* 553 (2012) 68–76.
- [57] A. Brinkmann, A.P.M. Kentgens, Magic-Angle-Spinning solid-state NMR spectroscopy for the determination of hydrogen bond lengths, *J. Am. Chem. Soc.* 128 (2006) 14758–14759.
- [58] B. Hu, J. Trébosc, J.-P. Amoureux, Comparison of several hetero-nuclear dipolar recoupling NMR methods to be used in MAS HMQC/HSQC., *J. Magn. Reson.* 192 (2008) 112–122.
- [59] O. Lafon, P. Lesot, Theoretical and experimental investigation of ^{13}C relayed ^2H - ^2H -COSY 2D experiments: application to the analysis of weakly aligned solutes., *J. Magn. Reson.* 174 (2005) 254–64.
- [60] D. Merlet, M. Sarfati, B. Ancian, J. Courtieu, P. Lesot, Description of natural abundance deuterium 2D-NMR experiments in weakly ordered liquid-crystalline solvents using a tailored cartesian spin-operator formalism, *Phys. Chem. Chem. Phys.* 2 (2000) 2283–2290.
- [61] A.J. Pell, G. Kervern, L. Emsley, M. Deschamps, D. Massiot, P.J. Grandinetti, et al., Broadband inversion for MAS NMR with single-sideband-selective adiabatic pulses., *J. Chem. Phys.* 134 (2011) 024117.
- [62] G. Pileio, M. Concistrè, N. McLean, A. Gansmüller, R.C.D. Brown, M.H. Levitt, Analytical theory of gamma-encoded double-quantum recoupling sequences in solid-state nuclear magnetic resonance., *J. Magn. Reson.* 186 (2007) 65–74.
- [63] A. Pines, D.J. Ruben, S. Vega, M. Mehring, New Approach to High-Resolution Proton NMR in Solids: Deuterium Spin Decoupling by Multiple-Quantum Transitions, *Phys. Rev. Lett.* 36 (1976) 110–113.
- [64] S. Vega, W. Shattuck, A. Pines, Fourier-transform double-quantum NMR in solids, *Phys. Rev. Lett.* 37 (1976) 43–46.
- [65] S. Vega, A. Pines, Operator formalism for double quantum NMR, *J. Chem. Phys.* 66 (1977) 5624–5644.
- [66] A. Wokaun, R.R. Ernst, Selective excitation and detection in multilevel spin systems: application of single transition operators, *J. Chem. Phys.* 4 (1977) 1752–1758.

- [67] P. Brunner, M. Reinhold, R.R. Ernst, Double quantum cross polarization. Heteronuclear excitation and detection of NMR double quantum transitions in solids, *J. Chem. Phys.* 73 (1980) 1086–1094.
- [68] M. Reinhold, P. Brunner, R.R. Ernst, Double quantum cross polarization via dipolar order, *J. Chem. Phys.* 74 (1981) 184–188.
- [69] T.K. Pratum, M.P. Klein, Heteronuclear Cross Polarization of solid-state ^{14}N NMR powder patterns, *J. Magn. Reson.* 55 (1983) 421–437.
- [70] A.J. Vega, Quadrupolar nuclei in solids, in: R.K. Harris, R.E. Wasylshen (Eds.), *eMagRes*, John Wiley & Sons, Inc., Chichester, UK, 2010: p. 15th March.
- [71] M. Bak, J.T. Rasmussen, N.C. Nielsen, SIMPSON: a general simulation program for solid-state NMR spectroscopy., *J. Magn. Reson.* 147 (2000) 296–330.
- [72] M. Veshtort, R.G. Griffin, SPIN-EVOLUTION: a powerful tool for the simulation of solid and liquid state NMR experiments., *J. Magn. Reson.* 178 (2006) 248–282.
- [73] M. Bak, N.C. Nielsen, REPULSION, A novel approach to efficient powder averaging in solid-state NMR, *J. Magn. Reson.* 125 (1997) 132–139.
- [74] B.E.G. Lucier, K.E. Johnston, W. Xu, J.C. Hanson, S.D. Senanayake, S. Yao, et al., Unravelling the structure of 'Magnus' pink salt, *J. Am. Chem. Soc.* 136 (2014) 1333–1351.
- [75] L.A. O'Dell, R.W. Schurko, K.J. Harris, J. Autschbach, C.I. Ratcliffe, Interaction tensors and local dynamics in common structural motifs of nitrogen: a solid-state ^{14}N NMR and DFT study., *J. Am. Chem. Soc.* (2010) 527–546.
- [76] D. Iuga, NMR studies of half-integer quadrupolar nuclei sensitivity enhancements using DFS, Radboud University (The Netherlands), 2003.
- [77] Mithun Goswami, Development of methodologies in solid-state NMR and their applications in material chemistry, TIFR (India), 2010.
- [78] M. Shen, J. Trébosc, O. Lafon, F. Pourpoint, B. Hu, Q. Chen, et al., Improving the resolution in proton-detected through-space heteronuclear multiple quantum correlation NMR spectroscopy., *J. Magn. Reson.* 245 (2014) 38–49.
- [79] S.E. Ashbrook, S. Wimperis, Rotor-synchronized acquisition of quadrupolar satellite-transition NMR spectra: practical aspects and double-quantum filtration., *J. Magn. Reson.* 177 (2005) 44–55.
- [80] Q. Wang, J. Trébosc, Y. Li, J. Xu, B. Hu, N. Feng, et al., Signal enhancement of J-HMQC experiments in solid-state NMR involving half-integer quadrupolar nuclei., *Chem. Commun.* 49 (2013) 6653–5.

Chapter 6: Revisiting NMR composite pulses for broadband ^2H excitation

In solid-state Nuclear Magnetic Resonance (NMR), deuterium quadrupolar echo spectroscopy is a powerful tool for investigating structure and dynamics. This method allows for measuring quadrupolar coupling parameters from static powder patterns facilitating the study of dynamics, hydrogen bonding, ligand identification and chemical exchange in a variety of systems^[1-4].

Although the quadrupolar couplings of spin-1 ^2H nuclei are far smaller than those of most half-integer spin nuclei, their values (typically in the range of $C_Q=e^2qQ=50-180$ kHz)^[5,6] are comparable with the maximum RF field strength that can be achieved by modern NMR probes. Therefore, high RF fields for efficient excitation are strongly desired to cover the wide spectral widths encountered in deuterium experiments. To uniformly excite the wide spectral widths, several composite pulses have been developed.^[7-11] Siminovitch et al. have also adapted a composite pulse approach to reduce the RF field requirements in the deuterium quadrupolar echo experiments.^[12] In their study, four different composite 90° pulses (COM-I, II, III and IV, Table 1) were compared and analyzed. In addition, T.M. Barbara has shown how phase distortions may be manifested in composite pulses due to finite pulse width effects^[13]. However, the issue of phase cycling was not addressed in these two works^[12,13]. Recently, a new analysis showed the importance of phase cycling both the pulses and the receiver for suppressing spectral artifacts due to finite pulse widths^[14]. Indeed, in the case of quadrupolar echo using two single pulses, the evolution of the spin system under both RF and quadrupolar interactions was shown to give rise to spectral distortions that may be decreased by phase cycling.

6.1 Pulse sequence and its implementation with composite pulse

Here, we would like to revisit the previous four composite pulses (COM-I, II, III and IV) and we combine them with the 8-step phase cycle developed for deuterium

quadrupolar echo experiments^[14]. Numerical simulations and experiments were performed to investigate the performances of these composite pulses with a 2-, 4- or 8-step phase cycling scheme. It is shown that the 8-step phase cycling minimizes the distortions, which allows for accurate lineshape measurements.

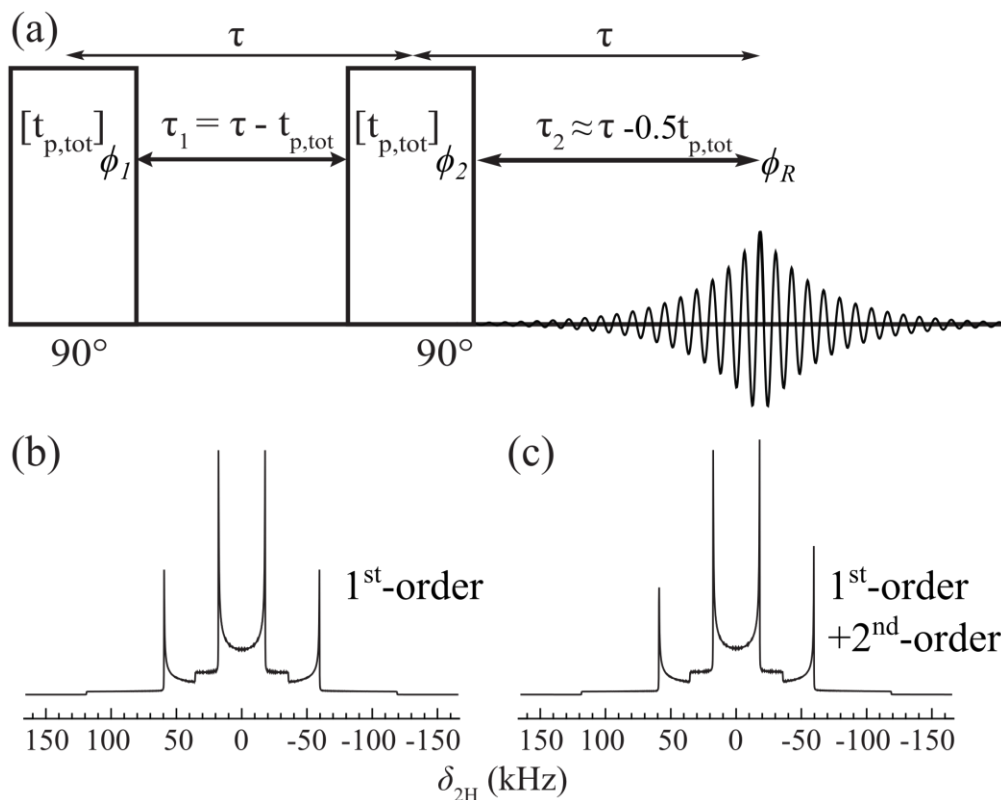


Fig.1. The quadrupolar echo pulse sequence investigated in this work. In the experiment, the echo is formed at τ_2' after the second 90° pulse. Simulated ^2H quadrupolar echo using two ideal 90° pulses with first-order only (b) or with both 1st - and 2nd -order (c) quadrupolar interactions taken into account are shown as references for the simulation section. In this ideal case, the echo is not distorted and is formed at $\tau_2' = \tau_1'$ after the second 90° pulse.

The basic principle of the conventional two-pulse quadrupolar echo sequence is shown in Fig.1. The quadrupolar interaction is refocused by the two 90° pulses and an echo is formed at time τ_2' after the second pulse (Fig.1). As the signal need not be recorded immediately after the second pulse, the instrumental limitation imposed by the finite recovery time of the receiver and probe ringing effects may be overcome. In this sequence, the nuclear spins evolve under both the RF and the quadrupolar interaction, which are often of comparable sizes, hence leading to a distorted echo occurring at τ_2' rather than τ_1' .^[15] In practice, the signal is sampled after the second pulse but before the

echo peak and is then left shifted in order to place the first data point at the peak of the echo before Fourier transformation.

The composite 90° pulses studied in this paper, denoted as COM-i ($i = \text{I-IV}$), are shown in Table 1. Here we have always used two identical composite pulses in each sequence. The origin of the quadrupolar dephasing is always close to the center of each RF excitation period. Since the duration of these composite pulses are different, the echo spacing τ_1' has to be calculated to retain the same magnetization evolution time for each composite pulse which can be expressed as

$$\tau_1' = \tau_1 - t_p^{\text{tot}} \quad (1)$$

In the above expression τ_1 is fixed in each experiment and t_p^{tot} is the total length of single or composite 90° pulses. Under these conditions the echo delay τ_1' is shortest in the case of COM-III due to the fact that the total length of this composite pulse, t_p^{tot} , lasts for $12 \cdot t_{90}$, where t_{90} correspond to the nominal 90° pulse length for the quadrupolar echo sequence with single 90° pulse (referred as SP). t_p^{tot} lasts $3 \cdot t_{90}$, $6 \cdot t_{90}$, $6 \cdot t_{90}$ for COM-I, COM-II, COM-IV, respectively.

The 8-step phase cycling scheme developed for spin-1 quadrupolar echo spectroscopy,^[14] shown in Table 2 (shown in the section 4), has been used for the current study. We have also compared the results obtained with the full 8-step phase cycling with those achieved with the 2- and 4-step phase cycling consisting of the first 2 and 4 steps shown in Table 2.

Table.1. The four composite 90° pulses used to replace the two single 90° pulses in the quadrupolar echo sequence in Fig.1. Nominal pulse flip angles are given in degrees and a bar denotes a 180° phase shift. The total pulse length, t_p^{tot} , is given as a function of the nominal 90° pulse length, t_{90} .

Sequence	Composite 90° pulse	t_p^{tot}
COM-I	$135 \overline{90} 45$	$3t_{90}$
COM-II	$90 \overline{180} 90 \overline{135} 45$	$6t_{90}$
COM-III	$135 \overline{180} 90 \overline{135} 45 \overline{90} 180 \overline{90} 135$	$12t_{90}$
COM-IV	$135 \overline{180} 90 \overline{135}$	$6t_{90}$

6.2 Numerical simulations

Simulations of powder sample spectra were carried out using the SPINEVOLUTION software^[16] with 501,500 (α_{CR} , β_{CR}) polar angles defining the quadrupolar tensors with respect to the laboratory frame, which were selected according to the ASG algorithm to profit of its interpolation procedure.^[17] In the simulations, we have introduced a static field of 9.395 T (61.402 MHz for ^2H) and two deuterium atoms with $\eta_Q = 0$, $C_Q = 48$ or 160 kHz, and the same orientation of the quadrupolar tensor. Both 1st- and 2nd-order quadrupolar terms were always taken into account, except in Fig.1b where the spectrum was simulated with 1st-order only to be shown as a reference. Dipolar coupling and chemical shift anisotropy were ignored in these simulations, as they are much smaller than the dominating quadrupolar coupling. For each simulated spectrum, the signal was sampled with a dwell time of 3 μs directly after the second single or composite 90° pulse, and then left-shifted to place the first data point at the top of the echo before Fourier transformation.

We show in Fig.1b the spectrum simulated using two ideal 90° pulses with only the 1st-order interaction taken into account; both pairs of horns are then equally intense. For each pair, the separation is equal to $0.75C_Q(1 - \eta_Q)$, thus leading to 36 and 120 kHz in the figure.^[18] However, when the 2nd-order terms are taken into account, the spectrum becomes asymmetric (Fig.1c), as always observed experimentally, especially at low magnetic fields.

Fig.2 shows the echo spectra simulated using two composite or single 90° pulses with $\nu_1 = 40$ kHz and with (Fig.2a) or without (Fig.2b) the 8-step phase cycling. The figure shows that the peaks of all the spectra obtained with this phase cycling scheme are more symmetric than without phase cycling, due to the fact that the finite pulse width effect is better suppressed (the details of how this distortion arises is discussed in Chapter 7). COM-II and -IV yield spectra with a flat baseline, and the feature of outer edge (as indicated by an arrow) is more apparent with COM-II. We also note that using two 90° single pulses (SP) leads to poor excitation of the deuterons having a large C_Q value, as the intensities of the outer horns at ± 60 kHz are then almost three times smaller than with composite pulses. These results indicate that proper phase cycling is important to

suppress the finite pulse width effects in quadrupolar echo experiments with both composite and single pulses, and that moderate RF fields may achieve efficient excitation.

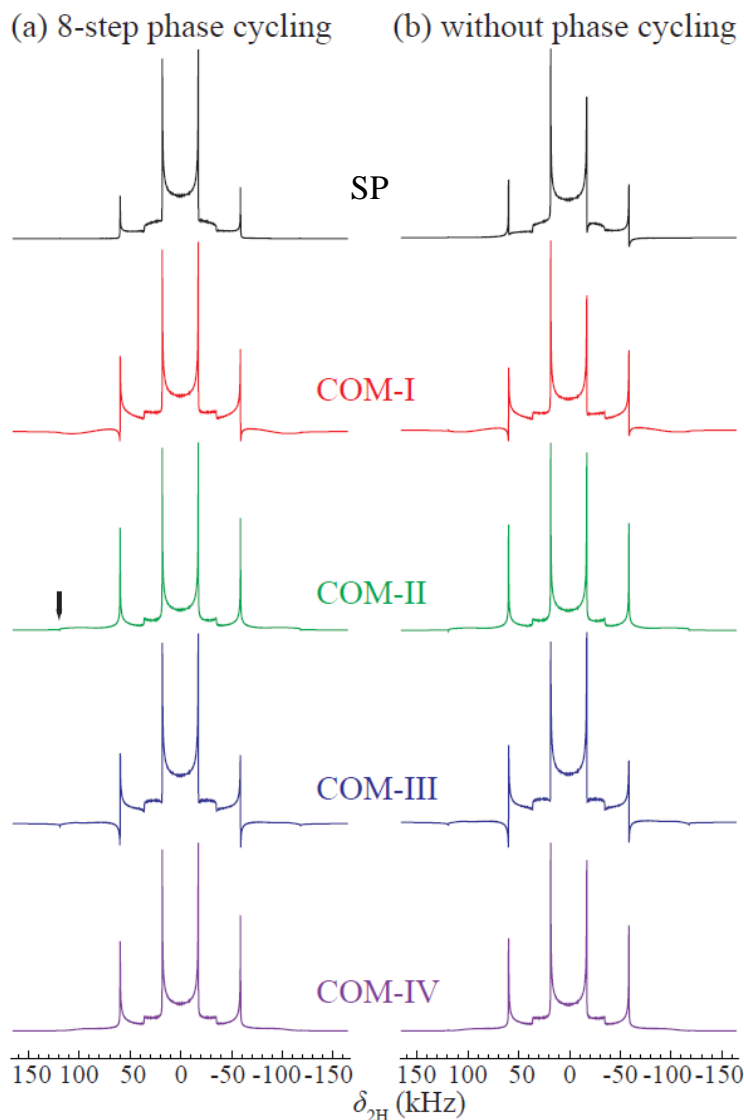


Fig.2. Quadrupolar echo spectra simulated with two single (SP, black), COM-I (red), COM-II (green), COM-III (blue), and COM-IV (purple) 90° pulses using either a 8-step phase cycling scheme (a) or without phase cycling (b). In these simulations, the RF field amplitude was set to $\nu_1 = 40$ kHz.

6.3 Experimental

Experiments were performed at room temperature on a Bruker Avance III 7.046 T spectrometer operating at a ^2H Larmor frequency of 46.051 MHz. Perdeuterated palmitic

acid (PA- d_{31}) sample was purchased from Cambridge Isotopes and was packed into a 4 mm rotor, but experiments were performed with a static sample. The spectra were collected by accumulating 1000 scans with a recycle delay of 16 s and a dwell time of 1.6 μ s. The RF amplitude (ν_1) and echo delay (τ_1) are indicated in the figure captions. Suitable left shifting was applied before Fourier transformation.

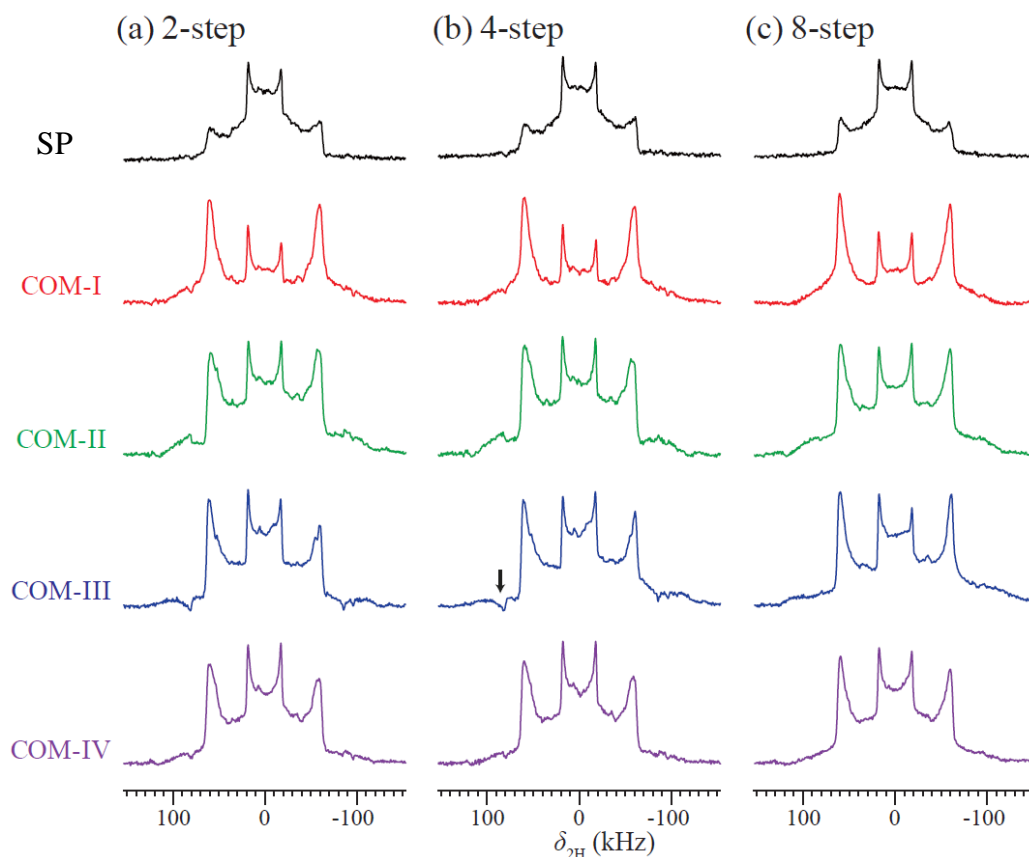


Fig.3. Quadrupolar echo spectra of PA- d_{31} acquired using 2- (a), 4- (b) and 8-step (c) phase cycling scheme with two single (SP, black), COM-I (red), COM-II (green), COM-III (blue), and COM-IV (purple) 90° pulses. The RF field was $\nu_1 = 35.7$ kHz and the echo spacing τ_1 was fixed to 100 μ s.

The choice of the phase cycling was analyzed by comparing the spectra recorded with an incomplete 2- or 4-step phase cycling and the complete 8-step phase cycling scheme (Fig.3) using the moderate RF field of $\nu_1 = 35.7$ kHz. Two overlapping powder patterns are observable, with a splitting of 41 and 125 kHz. These two deuteron sites correspond to the methyl group associated with motional averaging and the chain species experiencing the largest quadrupolar interaction, respectively. Based on these splitting values the quadrupolar couplings for the two sites were determined to be $C_Q = 55$ and 167

kHz.

We found that the resulting powder patterns are more symmetric using the 8-step phase cycling rather than the two incomplete phase-cycling schemes. However, this improvement is less apparent in the case of COM-II and -IV. Comparing these two composite pulses, the symmetry of the outer horns is slightly better with COM-II. With COM-III, both horns are distorted which may be related to larger finite pulse width effects related to the longer composite pulse duration. We note that with COM-I, the signal corresponding to $C_Q = 55$ kHz is reduced in the center of the spectra compared with the echo signal recorded with two single pulses, which has also been reported in a previous study.^[12] We also note that the single pulses lead to poor excitation of the spins having the largest quadrupolar coupling constant, as the intensity of the outer horns at ± 60 kHz is almost three times smaller than with composite pulses, which is consistent with our simulations.

Referring to Fig.3a and 3b with the 2- and 4-step phase cycling (first 2 and 4 steps of Table 2, respectively), a pair of artifacts is introduced for COM-II, -III and -IV at the frequency of ± 85 kHz (as indicated by an arrow for COM-III), and several burs in the center of the spectra are also present. These artifacts and small dips are removed by employing the 8-step phase cycling (Fig.3c), resulting in spectra with much smoother inner horn and baseline without artifacts. All these results confirm that adapting the 8-step phase cycling results in undistorted composite pulse quadrupolar echo spectra. Globally, we found that COM-II and -IV, with a slight advantage for COM-II, performed the best among the four different composite pulses investigated.

To analyze in more details the efficiency of composite pulse excitation, we implemented the quadrupolar echo sequence with COM-II and -IV and with single 90° excitations, using the 8-step phase cycling scheme under different RF fields, as shown in Fig.4.

With the weak RF field of $\nu_1 = 18$ kHz, only one specie can be observed using two single pulses (Fig.4a). However, the signal arising from the large quadrupolar interaction related to chain deuterons may be also observed using COM-II and -IV. Although the powder pattern is then distorted, this weak RF field may facilitate the analysis of temperature sensible protein systems, since it is possible to estimate the C_Q from these

distorted spectra.

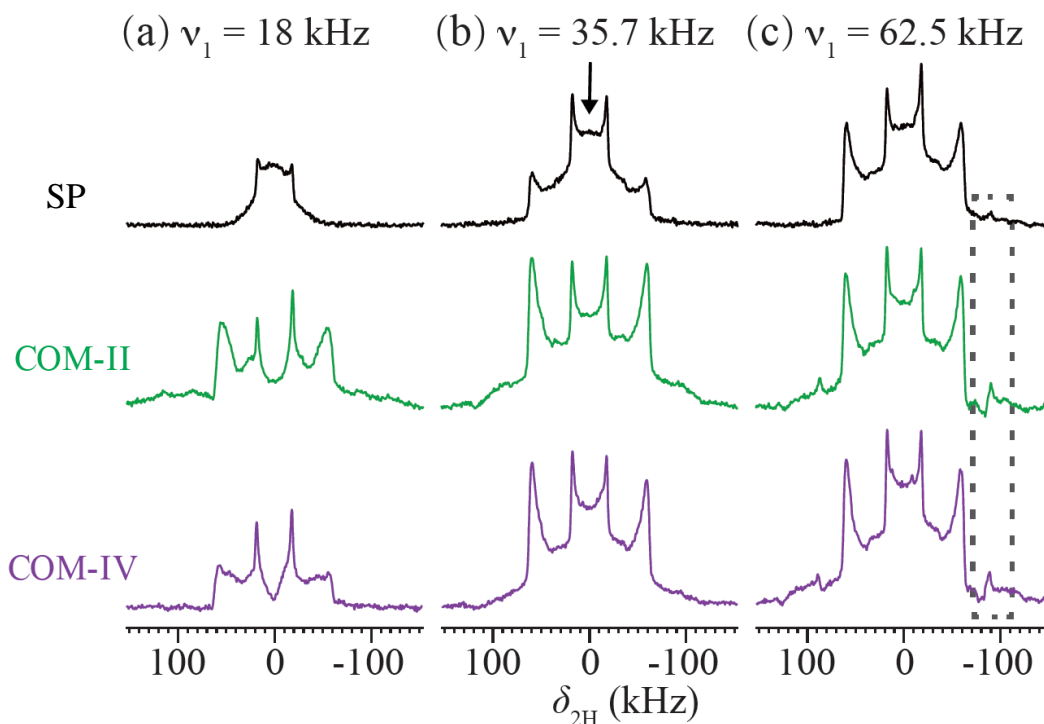


Fig.4. Quadrupolar echo spectra of PA- d_{31} acquired using 8-step phase cycling scheme with two single (SP, black), COM-II (green) and COM-IV (purple) pulses. The RF field) was $\nu_1 = 18$ kHz (a), 35.7 kHz (b), 62.5 kHz (c), and the echo spacing τ_1 was fixed to 180 (a), 100 (b), 60 (c) μs , respectively. Due to the decrease of the rf field (ν_1), the each spacing τ_1 has to increase to ensure that $\tau_1' = \tau_1 - t_p^{\text{tot}} > 0$.

With the moderate RF field of $\nu_1 = 35.7$ kHz, the signal of the outer horn is still weak using two single pulses (Fig.4b). The central part of the powder pattern (as indicated by an arrow) is smoother with COM-II and -IV, while it looks flat with the single pulses.

With the large RF field of $\nu_1 = 62.5$ kHz, artifacts are encountered as shown in the dashed box of Fig.4c. These additional artifacts might be due to higher phase transients and probe ring-down effects associated with higher RF field, which may be only partially compensated by the 8-step phase cycling.

6.4 Conclusions

In this work we have reported on the performance of composite pulses in deuterium quadrupolar echo experiments. Simulations and experiments have confirmed that finite pulse width effects are partially removed by proper phase cycling. It is shown that

COM-II and -IV are superior to the other composite 90° pulses studied as they reduce the requisite RF fields for uniform excitation, but also give undistorted spectra without baseline artifacts. COM-III was found to yield a distorted powder pattern due to its much longer pulse duration. Our results show that the full 8-step phase cycling is robust in mitigating undesired finite pulse width effects that result in spectral distortions and should be applicable for quadrupolar echo spectroscopy based on composite pulses.

References:

- [1] C. Tardy-Laporte, A.A. Arnold, B. Genard, R. Gastineau, M. Moran çais, J.-L. Mouget, R. Tremblay, I. Marcotte, A ^2H solid-state NMR study of the effect of antimicrobial agents on intact *Escherichia coli* without mutating., *Biochim. Biophys. Acta*, 1828 (2013) 614-622.
- [2] B. Walaszek, A. Adamczyk, T. Pery, X. Yeping, T. Gutmann, S. Amadeu Nde, S. Ulrich, H. Breitzke, H.M. Vieth, S. Sabo-Etienne, B. Chaudret, H.H. Limbach, G. Buntkowsky, ^2H solid-state NMR of ruthenium complexes, *J. Amer. Chem. Soc.*, 130 (2008) 17502-17508.
- [3] B. Kwon, A.J. Waring, M. Hong, A ^2H solid-state NMR study of lipid clustering by cationic antimicrobial and cell-penetrating peptides in model bacterial membranes, *Biophysical journal*, 105 (2013) 2333-2342.
- [4] M.N. Kinde-Carson, C. Ferguson, N.A. Oyler, G.S. Harbison, G.A. Meints, Solid state ^2H NMR analysis of furanose ring dynamics in DNA containing uracil, *J. Phys. Chem. B*, 114 (2010) 3285-3293.
- [5] I. del Rosal, T. Gutmann, L. Maron, F. Jolibois, B. Chaudret, B. Walaszek, H.H. Limbach, R. Poteau, G. Buntkowsky, DFT ^2H quadrupolar coupling constants of ruthenium complexes: a good probe of the coordination of hydrides in conjunction with experiments, *Phys. Chem. Chem. Phys.*, 11 (2009) 5657-5663.
- [6] C.A. Michal, J.C. Wehman, L.W. Jelinski, Deuterium Quadrupole-Coupling and Chemical-Shielding Tensors in the Model Dipeptide Glycylglycine Monohydrochloride Monohydrate, *J. Magn. Reson. Series B*, 111 (1996) 31-39.
- [7] X. Shi, J.L. Yarger, G.P. Holland, ^2H - ^{13}C HETCOR MAS NMR for indirect detection of ^2H quadrupole patterns and spin-lattice relaxation rates, *J. Magn. Reson.*, 226 (2013) 1-12.
- [8] D. Carnevale, G. Bodenhausen, Composite pulses for efficient excitation of half-integer quadrupolar nuclei in NMR of static and spinning solid samples, *Chem. Phys. Lett.*, 530 (2012) 120-125.

-
- [9] Y. Millot, P.P. Man, Determination of quadrupole parameters with a composite pulse for spurious signal suppression, *J. Magn. Reson.*, 150 (2001) 10-16.
- [10] T. Fujiwara, K. Nagayama, Numerical design of broadband composite pulses for quadrupole-echo experiments in $I = 1$ systems, *J. Magn. Reson.*, (1969-1992), 93 (1991) 563-571.
- [11] W. Dongsheng, L. Gengying, W. Xuwen, Composite pulse quadrupole echo without phase distortion, *J. Magn. Reson.*, (1969-1992), 74 (1987) 464-468.
- [12] D.J. Siminovitch, D.P. Raleigh, E.T. Olejniczak, R.G. Griffin, Composite pulse excitation in quadrupole echo spectroscopy, *J. Chem. Phys.*, 84 (1986) 2556.
- [13] T.M. Barbara, Analytical expressions and lineshape simulations for Levitt-Suter-Ernst composite-pulse quadrupolar echo sequences, *J. Magn. Reson.*, (1969), 67 (1986) 491-500.
- [14] E.S. Mananga, Y.S. Rumala, G.S. Boutis, Finite pulse width artifact suppression in spin-1 quadrupolar echo spectra by phase cycling, *J. Magn. Reson.*, 181 (2006) 296-303.
- [15] X. Ma, C. Sun, G.S. Boutis, Investigation of the effect of a variety of pulse errors on spin $I = 1$ quadrupolar alignment echo spectroscopy, *J. Magn. Reson.*, 211 (2011) 134-142.
- [16] M. Veshtort, R.G. Griffin, SPIN-EVOLUTION: a powerful tool for the simulation of solid and liquid state NMR experiments, *J. Magn. Reson.*, 178 (2006) 248-282.
- [17] D.W. Alderman, M.S. Solum, D.M. Grant, Methods for analyzing spectroscopic line shapes. NMR solid powder patterns, *J. Chem. Phys.*, 84 (1986) 3717.
- [18] L.A.O. Dell, Direct detection of nitrogen-14 in solid-state NMR spectroscopy, *Progress in Nuclear Magnetic Resonance Spectroscopy*, 59 (2011) 295-318.

Chapter 7: Revisiting NMR composite pulses for broadband ^2H excitation: Theoretical calculation by average Hamiltonian theory

In Chapter 6, we have shown that COM-II ($90 \overline{180} 90 \overline{135} 45$) with an 8-step phase cycling could reduce the requisite RF fields for uniform excitation, and thus yield undistorted spectra for accurate line-shape measurements. The performance of COM-II was slightly better than COM-IV, in particular in the outer edges of the quadrupolar echo spectra. Here we chose to analyze COM-II in this chapter by average Hamiltonian theory. Analytical results, to first order of the Magnus expansion, highlight the performance of this composite pulse with an 8-step phase cycling scheme. By applying the fictitious spin-1 operators, this chapter highlights the mechanism of the 8-step phase cycling that minimizes spectral distortions.

7.1 Analytical calculations of COM-II

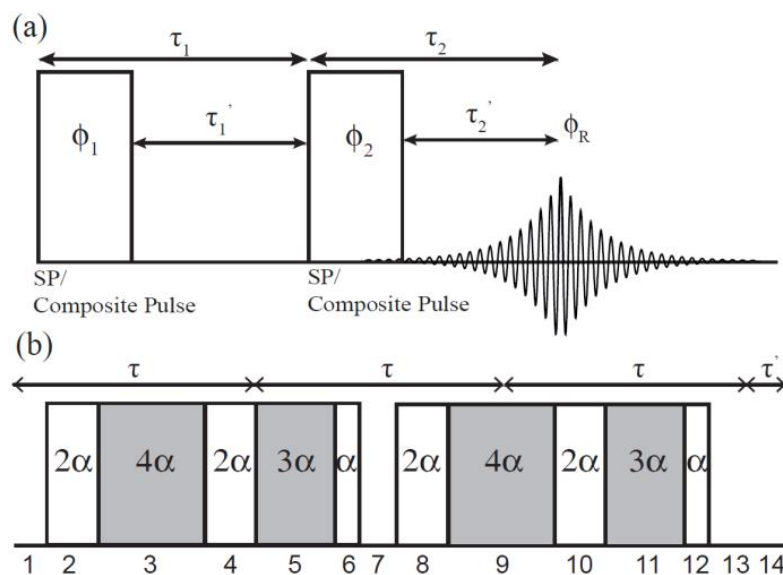


Fig. 1 (a) Pulse sequence of ^2H quadrupole echo experiment. The echo is formed at τ_2' after the second 90° pulse due to finite pulse width effect. (b) COM-II pulse, white rectangles denotes pulses with 0° phase, filled rectangles denotes pulses with a 180° phase shift. The cycle shown here corresponds to the first row in Table 1. 2α corresponds to the length of 90° pulse.

The quadrupolar echo pulse sequence is shown in Fig. 1a. The quadrupolar interaction is refocused by two 90° single pulses or composite pulses and an echo is formed at time after the second 90° pulse (τ_2' in Fig. 1). In this pulse sequence, the nuclear spins evolve under both the RF and quadrupolar interaction. Large quadrupolar interactions comparable to the RF field lead to a distorted echo occurring at τ_2' rather than τ_1' . In addition, as we show below, spectral distortions arise from the composite evolution of the spins under both the RF and internal Hamiltonians. In practice, the free induction decay (FID) is sampled before the echo peak and is left shifted in order to place the first data point at the peak of the echo before Fourier transformation.

Step	ϕ_1	ϕ_2	ϕ_R
1	x	y	-y
2	x	-y	-y
3	-x	y	y
4	-x	-y	y
5	y	x	x
6	y	-x	x
7	-y	x	-x
8	-y	-x	-x

Table 1 The 8-step phase cycling scheme investigated in our work. The phases ϕ_1 and ϕ_2 correspond to the phase of 1st and 2nd single or composite 90° pulse in Fig.1, and ϕ_R corresponds to the receiver phase. The 2-step cycle refers to the first two rows, and the 4-step cycle the first four rows in the table respectively.

Below we provide analytical results, based on average Hamiltonian theory^[1] and focus the discussion on COM-II which provided the highest performance amongst the composite pulses we investigated^[2]. In this treatment, we take only the first order quadrupolar interactions and ignore the chemical shift anisotropy and dipolar interactions. Further, in our analysis, we make use of the fictitious spin-1 operators^[3] which are defined as

$$I_{p,1} = \frac{1}{2}I_p \quad (1)$$

$$I_{p,2} = \frac{1}{2}(I_q I_r + I_r I_q) \quad (2)$$

$$I_{p,3} = \frac{1}{2}(I_r^2 - I_q^2) \quad (3)$$

with $p = x, y, z$ and $(p, q, r) = (x, y, z)$ with cyclic permutations. In this formalism, the Hamiltonian of the quadrupolar interaction in the principal axis frame may be written as

$$H_{\omega_Q} = \omega'_Q R_{2,0} \frac{1}{\sqrt{6}} [12I_{z,1}I_{z,1} - I \cdot I] = \omega_Q [12I_{z,1}I_{z,1} - I \cdot I] \quad (4)$$

In the above expressions, $R_{2,0}$ is given by $R_{2,0} = \sqrt{\frac{3}{2}} [P_2(\cos(\theta)) + \frac{\eta}{2} \cos(2\theta) \sin^2(\phi)]$ and the constant $\omega'_Q = \frac{e^2 q Q}{2I(2I-1)\hbar}$. Therefore, ω_Q is given by $\omega_Q = \frac{e^2 q Q}{4I(2I-1)\hbar} [P_2(\cos(\theta)) + \frac{\eta}{2} \cos(2\theta) \sin^2(\phi)]$. $P_2(\cos(\theta))$ is the second-order Legendre polynomial of $\cos(\theta)$, θ and ϕ are two of the three Euler angles.

In the average Hamiltonian treatment^[1] the density matrix at a given time t_c , termed a cycle, may be evaluated as

$$\rho(t_c) = U_{RF} U_{int} \rho(0) U_{int}^{-1} U_{RF}^{-1} \quad (5)$$

where the propagator U_{RF} is given by the Dyson series and U_{int} is given by the Magnus expansion

$$U_{int}(t, 0) = \exp[-it_c (\overline{H_{int}^0} + \overline{H_{int}^1} + \dots)] \quad (6)$$

In what follows we restrict the discussions to the leading order term in the Magnus expansion which is given by

$$\overline{H_{int}^0} = \frac{1}{t_c} \int_0^{t_c} \tilde{H}_{int}(\tau) d\tau \quad (7)$$

Table 2 provides the integrated toggling frame Hamiltonians for sequence COM-II, and Table 3 highlights the average Hamiltonians for all combinations of the COM-II quadrupolar echo sequence. Here we restricted the computations of spin state at 3τ . A schematic of the composite pulse is provided in Figure 1b with the various durations denoted as δ_n ($n=1:14$). In our parameterization, the entire pulse sequence is of duration $T=3\tau$ and a 90° pulse width has duration 2α .

Interval	Time	$\overline{H_{\omega_Q}}$
δ_1	$0 \leq t \leq \tau - 8\alpha$	$\frac{\omega_Q}{T} (12I_{z,1}I_{z,1} - I \cdot I)(\tau - 8\alpha)$

δ_2	$\tau - 8\alpha \leq t$ $\leq \tau - 6\alpha$	$\frac{2\alpha\omega_Q}{T} (6I_{z,1}I_{z,1} + 6I_{x,1}I_{x,1} + \frac{12}{\pi} (I_{z,1}I_{x,1} + I_{x,1}I_{z,1}) - I \cdot I)$
δ_3	$\tau - 6\alpha \leq t$ $\leq \tau - 2\alpha$	$\frac{4\alpha\omega_Q}{T} (6I_{z,1}I_{z,1} + 6I_{x,1}I_{x,1} - I \cdot I)$
δ_4	$\tau - 2\alpha \leq t \leq \tau$	$\frac{2\alpha\omega_Q}{T} (6I_{z,1}I_{z,1} + 6I_{x,1}I_{x,1} - \frac{12}{\pi} (I_{z,1}I_{x,1} + I_{x,1}I_{z,1}) - I \cdot I)$
δ_5	$\tau \leq t \leq \tau + 3\alpha$	$\frac{3\alpha\omega_Q}{T} ((6 - \frac{4}{\pi})I_{z,1}I_{z,1} + (6 + \frac{4}{\pi})I_{x,1}I_{x,1}$ $- \frac{4}{\pi} (I_{z,1}I_{x,1} + I_{x,1}I_{z,1}) - I \cdot I)$
δ_6	$\tau + 3\alpha \leq t$ $\leq \tau + 4\alpha$	$\frac{\alpha\omega_Q}{T} ((6 - \frac{12}{\pi})I_{z,1}I_{z,1} + (6 + \frac{12}{\pi})I_{x,1}I_{x,1} + \frac{12}{\pi} (I_{x,1}I_{z,1}$ $+ I_{z,1}I_{x,1}) - I \cdot I)$
δ_7	$\tau + 4\alpha \leq t$ $\leq 2\tau - 4\alpha$	$\frac{\omega_Q}{T} (12I_{x,1}I_{x,1} - I \cdot I)(\tau - 8\alpha)$
δ_8	$2\tau - 4\alpha \leq t$ $\leq 2\tau - 2\alpha$	$\frac{2\alpha\omega_Q}{T} (6I_{x,1}I_{x,1} + 6I_{y,1}I_{y,1} + \frac{12}{\pi} (I_{x,1}I_{y,1} + I_{y,1}I_{x,1})) - I$ $\cdot I)$
δ_9	$2\tau - 2\alpha \leq t$ $\leq 2\tau + 2\alpha$	$\frac{4\alpha\omega_Q}{T} (6I_{y,1}I_{y,1} + 6I_{x,1}I_{x,1} - I \cdot I)$
δ_{10}	$2\tau + 2\alpha \leq t$ $\leq 2\tau + 4\alpha$	$\frac{2\alpha\omega_Q}{T} (6I_{x,1}I_{x,1} + 6I_{y,1}I_{y,1} - \frac{12}{\pi} (I_{x,1}I_{y,1} + I_{y,1}I_{x,1}) - I$ $\cdot I)$
δ_{11}	$2\tau + 4\alpha \leq t$ $\leq 2\tau + 7\alpha$	$\frac{3\alpha\omega_Q}{T} ((6 - \frac{4}{\pi})I_{x,1}I_{x,1} + (6 + \frac{4}{\pi})I_{y,1}I_{y,1}$ $- \frac{4}{\pi} (I_{x,1}I_{y,1} + I_{y,1}I_{x,1}) - I \cdot I)$
δ_{12}	$2\tau + 7\alpha \leq t$ $\leq 2\tau + 8\alpha$	$\frac{\alpha\omega_Q}{T} ((6 - \frac{12}{\pi})I_{x,1}I_{x,1} + (6 + \frac{12}{\pi})I_{y,1}I_{y,1} + \frac{12}{\pi} (I_{x,1}I_{y,1}$ $+ I_{y,1}I_{x,1}) - I \cdot I)$
δ_{13}	$2\tau + 8\alpha \leq t$ $\leq 3\tau$	$\frac{\omega_Q}{T} (12I_{y,1}I_{y,1} - I \cdot I)(\tau - 8\alpha)$
δ_{14}	$3\tau \leq t \leq 3\tau + \tau'$	$\frac{\omega_Q}{T} (12I_{y,1}I_{y,1} - I \cdot I)\tau'$

Table 2. Integrated toggling frame Hamiltonians, based on equation 7, for the [y,x] cycle of COM-II for each time duration indicated. The final expressions for each step of the 8-step phase cycle are provided in Table 3. In the table, the term α defines the $\pi/2$ pulse width duration, $2\alpha = \pi/2$.

ϕ_1	ϕ_2	$\bar{H}_{\omega_Q}^0$
x	y	$-\frac{4\omega_Q}{\pi T} [AI_{z,1}^2 - BI_{y,1}^2 + CI_{x,1}^2]$
x	-y	$-\frac{4\omega_Q}{\pi T} [AI_{z,1}^2 - BI_{y,1}^2 + CI_{x,1}^2]$
-x	y	$-\frac{4\omega_Q}{\pi T} [AI_{z,1}^2 - BI_{y,1}^2 + CI_{x,1}^2]$
-x	-y	$-\frac{4\omega_Q}{\pi T} [AI_{z,1}^2 - BI_{y,1}^2 + CI_{x,1}^2]$
y	x	$-\frac{4\omega_Q}{\pi T} [AI_{z,1}^2 + CI_{y,1}^2 - BI_{x,1}^2]$
y	-x	$-\frac{4\omega_Q}{\pi T} [AI_{z,1}^2 + CI_{y,1}^2 - BI_{x,1}^2]$
-y	x	$-\frac{4\omega_Q}{\pi T} [AI_{z,1}^2 + CI_{y,1}^2 - BI_{x,1}^2]$
-y	-x	$-\frac{4\omega_Q}{\pi T} [AI_{z,1}^2 + CI_{y,1}^2 - BI_{x,1}^2]$

Table 3 Integrated first order terms of the Magnus expansion over the time $T=3\tau$ (δ_{14} is not included here), based on equation 7, for the various two-pulse echo combinations for the COM-II composite pulses. In the table, $A = 2\alpha(1 + \pi)$, $B = 4\pi\alpha$ and $C = 2\alpha(\pi - 1)$.

Referring to Table 3, it is noteworthy to consider the zeroth order term of the Magnus expansion for any of the sequences and evaluate this term in the limiting case when the pulse duration $\alpha=0$. In this case, any term given in Table 3 is zero and from Eq. 5 we find that the density matrix at $t=3\tau$ is simply $I_{y,1}$ (for the [x,y] cycle) corresponding to full refocusing of the ensemble.

Using the results from Table 3 and Eq. 5 we have evaluated the density matrices for each of the eight cycles for COM-II. Table 4 highlights the results from this computation and shows that the general form is given by $\rho \propto -DI_{y,1} - EI_{y,2}$ (D and E are defined in Table 4). Taking the limit again for $\alpha=0$ corresponding to δ -function RF pulses yields $\rho \propto I_{y,1}$ corresponding to complete refocusing of the magnetization. We note that the terms $I_{y,2}$ from any of the $[\pm x, \pm y]$ cycles ($I_{x,2}$ for the $[\pm y, \pm x]$ cycles) in Table 4 do not commute with the quadrupolar Hamiltonian and evolves to a detectable signal which results in a spectral distortion. The spectral distortion arises from the fact that the factor E in front of the term $I_{y,2}$ for all $[\pm x, \pm y]$ cycles ($I_{x,2}$ for all $[\pm y, \pm x]$ cycles) is a sine modulation in ω_Q whereas the term D multiplying $I_{y,1}$ for all $[\pm x, \pm y]$ cycles ($I_{x,2}$ for all

$[\pm y, \pm x]$ cycles) is a cosine modulation in ω_Q . The frequency dependence of the term E is asymmetric with ω_Q , and as a consequence, the superposition of D and E results in a spectrum that will be asymmetric in frequency and appear distorted.

ϕ_1	ϕ_2	$\rho(3\tau)$
x	y	$-DI_{y,1} - EI_{y,2}$
x	-y	$-DI_{y,1} - EI_{y,2}$
-x	y	$DI_{y,1} + EI_{y,2}$
-x	-y	$DI_{y,1} + EI_{y,2}$
y	x	$DI_{x,1} - EI_{x,2}$
y	-x	$DI_{x,1} - EI_{x,2}$
-y	x	$-DI_{x,1} + EI_{x,2}$
-y	-x	$-DI_{x,1} + EI_{x,2}$

Table 4 Density matrices, calculated using the results from Table 3 (to leading order of the Magnus expansion) for the two-pulse echo combinations with the COM-II composite pulses. $D = \cos(\chi)$, $E = \sin(\chi)$ and $\chi = \frac{6\alpha\omega_Q(3\pi-1)}{\pi}$.

Referring to Table 4 we find that the addition of the cycles $[x,y]$ and $[x,-y]$, does not cancel the spectral distortion. In addition, the first 4-steps of the phase cycle given in Table 2 will not cancel the undesired terms $I_{y,2}$ either. Our previous experimental and simulation results verified this result^[2]. However, the addition of 2-steps for phase cycling, such as $[x,y]$ and $[-y,x]$ will suppress terms denoted E in the density matrix yielding only the terms D which only has a cosine modulation with respect to ω_Q . Moreover, one possible 4-step phase cycling scheme for suppressing the spectral distortion would be the combination of $[x,y] + [x,-y] + [-y,x] + [-y,-x]$ cycles (note that the receiver would have to be cycled as $[-y,-y, -x,-x]$ in this case). A second combination for a 4-step phase cycle would be the superposition of $[-x,y] + [-x,-y] + [y,x] + [y,-x]$ cycles with the receiver set to $[y,y,x,x]$. The full eight step phase cycling combines both of these 4-step cycles and suppresses the sine terms E multiplying $I_{x,2}$ and $I_{y,2}$ in the density matrices. However, the 2-step or 4-step phase cycles would not be expected to perform as robust as the full 8-step cycle as cancellation of receiver imbalance in the channels or phase transients may not be fully suppressed. For this

reason, it is preferable to implement the full 8-step cycling for cancelation of finite pulse width effects and instrumental artefacts especially when high RF power is being applied.

7.2 Numerical simulations

To further investigate the validity of our theoretical calculations, simulations were performed by the use of SIMPSON^[4] software. Only one ^2H nucleus with quadrupolar coupling up to second order was considered in the simulations. The static magnetic field was set to 9.4 T, and the quadrupolar coupling constant C_Q was set to 160 kHz with the asymmetry parameter η_Q set to 0. The powder averaging was performed using 256 $(\alpha_{\text{CR}}, \beta_{\text{CR}})$ pairs $\times 1 \gamma_{\text{CR}}$ angles, which was selected according to the REPULSON algorithm^[5].

We show in Fig. 2 the simulated FID signals recorded right after the second 90° COM-II pulse by using RF field of 40 kHz. The 8-step phase cycling scheme was used. It is clear that the COM-II pulse generates normal echo signal. We point out that the evaluating the time for each peak (τ_2') is straightforward with the consideration of the time-span of δ_{14} and we obtain $\tau_2' = (6 - 2/\pi)\alpha \sim 5.36 \alpha$. We have found that the calculated τ_2' value through our analytical expressions agrees well with our simulations in Fig 2.

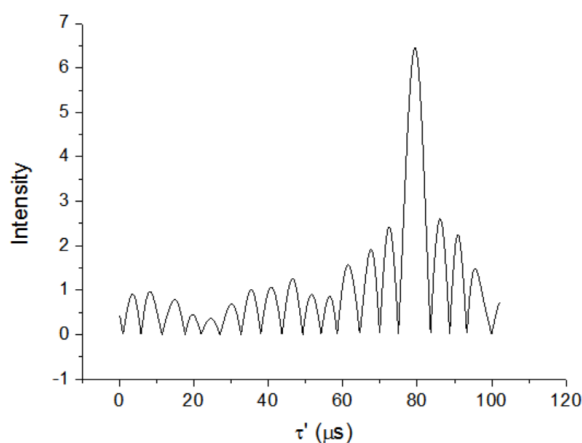


Fig.2 Simulated time domain signal recorded right after the second 90° COM-II pulse using RF field of 40 kHz. 8-step phase cycling was used to accumulate the signals.

We show in Fig. 3 the dependence of echo peak amplitude on the RF field used for single pulses and COM-II pulses. It appears that the amplitude of echo peak is always

greater using COM-II pulses regardless of the RF field. This must be due to the fact that composite pulse allows achieving broadband excitation, and it indicates that the composite pulse could be preferable in ^2H quadrupolar echo spectroscopy.

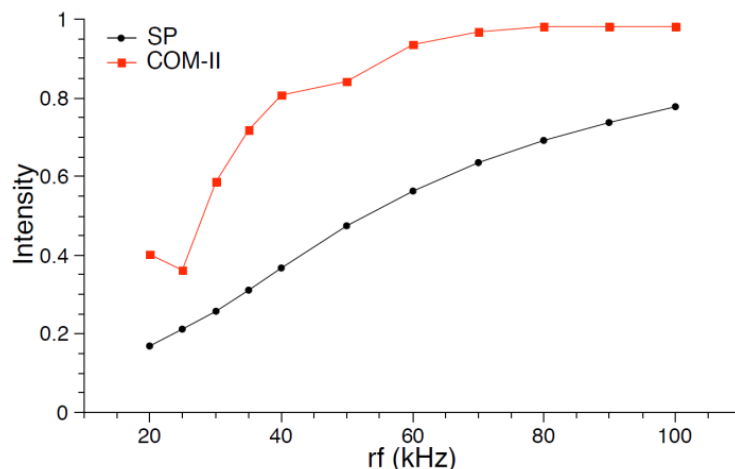


Fig.3 The dependence of the echo peak amplitude on the RF field applied for single 90° pulse (SP) or COM-II pulses (b). The echo peak amplitudes were extracted from corresponding time domain signals and were normalized with respect to that simulated using ideal pulses.

Lastly, we point out a subtle point regarding the application of composite pulses, as discussed in detail in references^[6, 7] when fast exchange may take place on the time scale of the echo experiment. Composite pulse excitation may lead to additional line-shape distortions in situations of exchange—such artefacts cannot be suppressed by phase cycling. For such spin systems, it behoves the experimenter to investigate the acquired quadrupolar echo spectra as a function of echo spacing and/or pulse duration if composite pulses are applied whose duration is comparable to exchange times.

7.3 Conclusions

In this chapter, we have provided analytical results based on the leading order term in the average Hamiltonian theory for COM-II ($90 \overline{180} 90 \overline{135} 45$), which we found to be the most robust sequence investigated in our recent work on ^2H quadrupolar echo spectroscopy.^[2] We also show that a full 8-step phase cycle is robust in cancelling undesired terms in the density matrix that contribute to spectral distortions and should be applicable for quadrupolar echo spectroscopy based on composite pulses. Our simulations and computations fully confirm the previous experimental results. Detailed theoretical

analysis could be further explored with the newly developed approach termed the Floquet-Magnus expansion^[8].

References:

- [1] U. Haeberlen, J.S. Waugh, Coherent Averaging Effects in Magnetic Resonance, *Physical Review*, 175 (1968) 453-467.
- [2] M. Shen, R. Roopchand, E.S. Mananga, J.-P. Amoureux, Q. Chen, G.S. Boutis, B. Hu, Revisiting NMR composite pulses for broadband ²H excitation, *Solid State Nuclear Magnetic Resonance*, (2014), *in press*.
- [3] S. Vega, A. Pines, Operator formalism for double quantum NMR, *The Journal of Chemical Physics*, 66 (1977) 5624.
- [4] M. Bak, J.T. Rasmussen, N.C. Nielsen, SIMPSON: A General Simulation Program for Solid-State NMR Spectroscopy, *Journal of magnetic resonance*, 147 (2000) 296-330.
- [5] D.W. Alderman, M.S. Solum, D.M. Grant, Methods for analyzing spectroscopic line shapes. NMR solid powder patterns, *J. Chem. Phys.*, 84 (1986) 3717.
- [6] D.J. Siminovitch, D.P. Raleigh, E.T. Olejniczak, R.G. Griffin, Composite pulse excitation in quadrupole echo spectroscopy, *J. Chem. Phys.*, 84 (1986) 2556.
- [7] T.M. Barbara, M.S. Greenfield, R.L. Vold, R.R. Vold, Deuterium quadrupole echo NMR spectroscopy. I. Effects of chemical exchange during single and composite pulses, *Journal of Magnetic Resonance* (1969), 69 (1986) 311-330.
- [8] A.D. Bain, R.S. Dumont, Introduction to Floquet theory: The calculation of spinning sideband intensities in magic-angle spinning NMR, *Concepts in Magnetic Resonance*, 13 (2001) 159-170.

Chapter 8: Resume

The main achievements have been made in this thesis comprise:

1) The development of methodology for the homo-nuclear correlation experiments under fast MAS in high magnetic field.

In Chapter 2, a new method for probing ^{13}C - ^{13}C and ^{31}P - ^{31}P homo-nuclear proximities under fast MAS in very high magnetic field is discussed. This method combines the fp-RFDR technique with a nested (XY8) 4 super-cycling. It facilitates the enhancement of ^{13}C - ^{13}C long-range correlations in uniformly labeled samples and ^{31}P - ^{31}P correlations in inorganic compound.

In Chapter 3, modulation-sideband recoupling conditions of the ^{13}C - ^{13}C Second-order Hamiltonian among Analogous nuclei plus (SHA+) is discussed, and it is shown that this sequence can be used in two different recoupling regimes. The second regime, $\nu_R < \Delta\nu_{\text{iso}}^{\text{max}}$, as first discovered in our work, can be used *selectively* to observe long-range constraints under fast MAS in high magnetic field.

2) The development of methodology for the Hetero-nuclear Correlation experiments under fast MAS in high magnetic.

In Chapter 4, it is shown that the spectral resolution along the indirect dimension of proton-detected HMQC spectra can be enhanced by applying decoupling schemes during the t_1 period. The performance of different decoupling schemes have been compared under fast and very-fast MAS.

In Chapter 5, it is demonstrated that the frequency-selective radio-frequency (rf) long pulses allow one to achieve an efficient excitation of nuclei experiencing large anisotropic NMR interactions. In *D*-HMQC experiment, the efficiency of selective excitation is comparable to that of broadband excitation given the rf field delivered by common solid-state NMR probes.

3) The development of methodology for the ^2H Quadrupole Echo experiment.

In Chapter 6, a revision of four well-known composite pulses (COM-I, II, III, and IV) for broadband excitation in deuterium quadrupolar echo (solid-echo) spectroscopy is presented. It is shown that COM-II and -IV are superior to the other composite 90° pulses

studied as they reduce the requisite RF fields for uniform excitation, but also give undistorted spectra without baseline artifacts. It is also proved that the full 8-step phase cycling is robust in mitigating undesired finite pulse width effects that result in spectral distortions.

In Chapter 7, a theoretical analysis of COM-II with 8-step phase cycling by average Hamiltonian theory is given, which allows us to understand the experiment results we obtained in Chapter 6. By applying the fictitious spin-1 operators, this chapter highlights the mechanism of the 8-step phase cycling that minimizes spectral distortions.

There is no doubt that the methods developed in this thesis could be applied on the characterization of many intriguing solid materials, such as membranes, catalysts and many other functional nanomaterials. Advanced Solid-State NMR permits the determination of structure and dynamics in atomic level. Efforts will be made towards this direction.

Paper list

- [1] Zhang, S.; Liu, Q.; Shen, M.; Hu, B.; Chen, Q.; Li, H.; Amoureux, J.-P. A Facile Route for Preparing a Mesoporous Palladium Coordination Polymer as a Recyclable Heterogeneous Catalyst. *Dalton Trans.* **2012**, *41*, 4692.
- [2] Shen, M.; Hu, B.; Lafon, O.; Tréboss, J.; Chen, Q.; Amoureux, J.-P. Broadband Finite-Pulse Radio-Frequency-Driven Recoupling (fp-RFDR) with (XY8)⁴ Super-Cycling for Homo-Nuclear Correlations in Very High Magnetic Fields at Fast and Ultra-Fast MAS Frequencies. *Journal of Magnetic Resonance* **2012**, *223*, 107–119.
- [3] Shen, M.; Liu, Q.; Tréboss, J.; Lafon, O.; Masuda, Y.; Takegoshi, K.; Amoureux, J.-P.; Hu, B.; Chen, Q. Exploring Various Modulation-Sideband Recoupling Conditions of SHA+ Sequence at Fast MAS. *Solid State Nuclear Magnetic Resonance* **2013**, *55-56*, 42–47.
- [4] Yu, G.; Shen, M.; Wang, M.; Shen, L.; Dong, W.; Tang, S.; Zhao, L.; Qi, Z.; Xue, N.; Guo, X.; Ding, W.; Hu, B.; Peng, L. Probing Local Structure of Layered Double Hydroxides with ¹H Solid-State NMR Spectroscopy on Deuterated Samples. *J. Phys. Chem. Lett.* **2014**, *5*, 363–369.
- [5] Liu, Q.; Peng, B.; Shen, M.; Hu, B.; Chen, Q. Polymer Chain Diffusion and Li⁺ Hopping of Poly(Ethylene Oxide)/LiAsF₆ Crystalline Polymer Electrolytes as Studied by Solid State NMR and Ac Impedance. *Solid State Ionics* **2014**, *255*, 74–79.
- [6] Qian, Y.; Shen, M.; Amoureux, J.-P.; Noda, I.; Hu, B. The Dependence of Signal-to-Noise Ratio on Number of Scans in Covariance Spectroscopy. *Solid State Nuclear Magnetic Resonance* **2014**, *59-60*, 31–33.
- [7] Shen, M.; Tréboss, J.; Lafon, O.; Pourpoint, F.; Hu, B.; Chen, Q.; Amoureux, J.-P. Improving the Resolution in Proton-Detected Through-Space Heteronuclear Multiple Quantum Correlation NMR Spectroscopy. *Journal of Magnetic Resonance* **2014**, *245*, 38–49.
- [8] Li, S.; Pourpoint, F.; Tréboss, J.; Zhou, L.; Lafon, O.; Shen, M.; Zheng, A.; Wang, Q.; Amoureux, J.-P.; Deng, F. Host–Guest Interactions in Dealuminated HY Zeolite Probed by ¹³C–²⁷Al Solid-State NMR Spectroscopy. *J. Phys. Chem. Lett.* **2014**, *5*, 3068–3072.
- [9] Liu, Q.; Li, C.; Wei, L.; Shen, M.; Yao, Y.; Hu, B.; Chen, Q. The Phase Structure, Chain Diffusion Motion and Local Reorientation Motion: ¹³C Solid-State NMR Study on the Highly-Crystalline Solid Polymer Electrolytes. *Polymer* **2014**, *55*, 5454–5459.
- [10] Shen, M.; Roopchand, R.; Mananga, E. S.; Amoureux, J.-P.; Chen, Q.; Boutis, G. S.; Hu, B. Revisiting NMR Composite Pulses for Broadband ²H Excitation. *Solid State Nuclear Magnetic Resonance* **2015**, *66-67*, 45–48.

-
- [11] Ming Shen, Julien Trebosc, Luke O'Dell, Olivier Lafon, Frederique Pourpoint, Bingwen Hu, Qun Chen. Comparison of various NMR methods for the indirect detection of nitrogen-14 via protons in solids. *Journal of Magnetic Resonance* **2015**, 258, 86–95.
- [12] Ming Shen, Rabia Roopchand, Eugene S. Mananga, Jean-Paul Amoureux, Qun Chen, Gregory S. Boutis, Bingwen Hu, Theoretical calculation of a composite pulse for ^2H broadband excitation by average Hamiltonian theory. *Chinese Journal of Magnetic Resonance*. In press.
- [13] Ming Shen, Julien Trebosc, Olivier Lafon, Zhehong Gan, Frederique Pourpoint, Bingwen Hu, Qun Chen, and Jean-Paul Amoureux. Solid-state NMR indirect detection of nuclei experiencing large anisotropic interactions using frequency-selective pulses. Submitted to the *Solid State Nuclear Magnetic Resonance*

Résumé

Mon travail de thèse a porté sur le développement de méthodes avancées de RMN des solides. Nous avons notamment introduit de nouvelles méthodes de corrélation homonucléaire compatibles avec une rotation rapide de l'échantillon et des champs magnétiques élevés. Nous avons montré que la robustesse de la technique fp-RFDR peut être améliorée par l'utilisation d'un supercyclage (XY8)⁴. Cette méthode a été employée pour sonder les proximités ^{13}C - ^{13}C and ^{31}P - ^{31}P dans les solides. Nous avons aussi introduit expériences de corrélation ^{13}C - ^{13}C du deuxième ordre avec assistance des protons, appelées SHA+, afin d'observer les proximités ^{13}C - ^{13}C à longue distance dans les solides. Au cours de ma thèse, nous avons aussi amélioré les méthodes de corrélation hétéronucléaire pour l'observation indirecte des noyaux ^{14}N via les protons. Nous avons montré que la résolution spectrale dans la dimension indirecte des spectres HMQC peut être accrue par l'utilisation de séquences de découplage homonucléaire pendant le temps t_1 . Nous avons aussi proposé l'utilisation d'impulsion sélective de la bande centrale pour l'excitation des noyaux ^{14}N dans les expériences HMQC $^1\text{H}\{^{14}\text{N}\}$. L'efficacité de ces impulsions sélectives de la bande centrale est comparable aux méthodes d'excitation large bande, compte tenu des champs radiofréquence produits par les sondes RMN pour l'étude des solides. La dernière partie de mon travail de thèse a porté sur l'amélioration des séquences d'écho quadripolaire pour l'acquisition des spectres ^2H de solides. Les distorsions de ces spectres ont été réduites par l'introduction de nouvelles impulsions composites.

Abstract

My PhD work has focused on the development of advanced solid-state NMR methods. We have notably developed homo-nuclear correlation methods compatible with high MAS frequencies and high magnetic fields. First, we have shown that the robustness of finite pulse Radio Frequency Driven Recoupling (fp-RFDR) technique can be improved by the use of nested (XY8) $_4^1$ super-cycling. Such method has been employed to probe ^{13}C - ^{13}C and ^{31}P - ^{31}P proximities in solids. Second, we have also introduced a second-order proton-assisted ^{13}C - ^{13}C correlation experiment, denoted “Second-order Hamiltonian among Analogous nuclei plus” (SHA+), to observe long-range ^{13}C - ^{13}C proximities in solids at fast MAS and high magnetic field. During my PhD, we have also improved the heteronuclear correlation methods for the indirect observation of ^{14}N nuclei via protons. We have shown that the spectral resolution along the indirect dimension of proton-detected Heteronuclear Multiple Quantum Correlation (HMQC) spectra can be enhanced by applying homonuclear dipolar decoupling schemes during the t_1 period. We have also proposed the use of centerband-selective radio-frequency (rf) pulses for the excitation of ^{14}N nuclei in $^1\text{H}\{^{14}\text{N}\}$ HMQC experiment. The efficiency of these centerband-selective pulse is comparable to that of broadband excitation given the rf field delivered by common solid-state NMR probes. The last part of my PhD focuses on the improvement of the quadrupolar echo sequence for the acquisition of the ^2H spectra of solids. The distortions of such spectra were reduced by the introduction of novel composite pulses.